

301

UNIVERSITY OF ILLINOIS AT URBANA-CHAMPAIGN
THE GRADUATE COLLEGE
THE INTERSTELLAR MEDIUM ALONG THE LINE OF SIGHT TOWARD X PER

1983

IN PARTIAL FULFILLMENT OF THE REQUIREMENTS FOR THE DEGREE OF DOCTOR OF PHILOSOPHY IN ASTRONOMY

BY

DAVID JEFFREY LIEN

B.S., University of Wisconsin, 1977
M.S., University of Illinois, 1979

THESIS

Submitted in partial fulfillment of the requirements
for the degree of Doctor of Philosophy in Astronomy
in the Graduate College of the
University of Illinois at Urbana-Champaign, 1983

Urbana, Illinois

University of Illinois at Urbana-Champaign

DEPARTMENTAL FORMAT APPROVAL

THIS IS TO CERTIFY THAT THE CONTENT, FORMAT, AND QUALITY OF PRESENTATION OF
THE THESIS SUBMITTED BY David Jeffrey Lien AS ONE OF
THE REQUIREMENTS FOR THE DEGREE OF Doctor of Philosophy
IS ACCEPTABLE TO THE Department of Astronomy
Department/Division/Unit

14 Dec 1982

Date of Approval

Richard M. Kutner

Departmental Representative

PREFACE

Fourteen years ago (half of my life), a very good friend of mine invited me to look through his small 1" refractor at Saturn. Having nothing else to do, I accepted. By the end of the summer, I had devoured most of the astronomy books in the local Public Library. I will always thank Russell Schmunk for his invitation. A few years later, I had the opportunity to attend an introductory astronomy course at the local University. I wish to thank Dr. Arthur Norberg for his patience and encouragement.

By this time I had decided to pursue a career in Astronomy, although I had absolutely no idea of what an Astronomer actually did for a living, besides looking through large telescopes. However, this did not deter me and I steadfastly clung to the hopes of joining their ranks. It is during these, my early High School years, that I must give credit to my parents. Despite the fact that my father, the late Dr. Arnold J. Lien, wanted me to go into business or accounting (something to make bucks at), both my parents accepted my desire to pursue my own career. For their help, encouragement, financial, and spiritual support, I will always be in debt.

I entered the University of Wisconsin at Madison, Wisconsin still not knowing exactly what an Astronomer does. I wish to thank Drs. Anderson, Cassinelli, Mathis, and Nordsieck for their help in my astronomical education. As a graduate student at the University of

PREFACE

Illinois at Urbana-Champaign, I had the opportunity to work for and with a great ensemble of talent. Particularly, I wish to thank Dr. Lewis Snyder for his assistance, both financial and astronomical, in leading me towards the material which is contained in this volume. I especially wish to thank Dr. Richard Crutcher, for without his help, I wouldn't be writing this.

I have made many friends and acquaintances during my tenure in Urbana-Champaign. Foremost among them is Dr. Phil Jewell, who now knows more about the details of UV and optical absorption line studies of the ISM than he probably really cares to. For this I am deeply grateful. And of course, thanks are due to the Basement Crew.

Most of all, I wish to thank my wife, Molly. Without her, I probably would have gone into shipbuilding.

TABLE OF CONTENTS

CHAPTER	PAGE
1. INTRODUCTION	1
1.1 The Nature of the ISM	1
2. STELLAR PROPERTIES OF X PER	9
3. OBSERVATIONS	11
3.1 Radio Observations	11
3.2 Optical Observations	16
3.3 UV Observations	17
3.4 Literature References	31
3.4.1 Radio	31
3.4.2 Optical	44
3.4.3 UV	44
3.5 Extinction	46
4. ANALYSIS	49
4.1 Curve of Growth Analysis	49
4.2 Curve of Growth for X Per	63
4.3 Profile Fitting	72
5. OBSERVATIONAL RESULTS	79
5.1 Hydrogen	79
5.2 Highly Ionized Species	83
5.3 Dominant Stage Ions	93
5.3.1 Column Densities	95

CHAPTER	PAGE
5.4 Neutral Species	103
5.4.1 Ionization Equilibrium and its Affect on the Curve of Growth	104
5.4.2 Column Densities	110
5.5 CO	113
5.5.1 Radio CO	113
5.5.2 UV CO	114
5.6 Diatomic Carbon	123
5.7 CN	128
5.8 CH	131
5.9 CH+	138
5.10 OH	138
5.11 H ₂ O	139
5.12 Unidentified Lines	140
5.13 Line Searches	147
6. DISCUSSION	149
6.1 Depletions	149
6.2 Temperature	165
6.3 Densities	169
6.3.1 Electron Density	169
6.3.2 Hydrogen Density	176
6.4 Isotopic Ratio	187
6.5 Abundances	189
7. A DIFFUSE CLOUD MODEL	193

CHAPTER	PAGE
8. SUMMARY AND CONCLUSIONS	222
8.1 Summary	222
8.2 Conclusion	227
 APPENDICES	
A. Radio Data Reduction	228
B. IUE Satellite and Data Reduction	239
C. Molecular Band Structure	249
D. Photoionization and Recombination in the ISM	263
 BIBLIOGRAPHY	 269
 VITA	 277

LIST OF TABLES

TABLE		PAGE
3-1	Radio Emission Line Observations of X Per	12
3-2	Radio Calibration Sources	14
3-3	Optical Absorption Line Observations	18
3-4	IUE Spectra	21
3-5	UV Atomic Equivalent Widths	25
3-6	UV Molecular Equivalent Widths	32
3-7	UV Unidentified Absorption Lines	34
3-8	Published Radio Emission Line Observations	43
3-9	Published Optical and UV Absorption Line Observations ...	45
5-1	Atomic Column Densities	85
5-2	Fractional Atomic Abundances	91
5-3	Photoionization Ratios and Fractional Curves of Growth ..	107
5-4	Optically Thin Column Densities for ^{12}CO and ^{13}CO	118
5-5	Diatomic Carbon D-X Column Densities	129
5-6	CH Ultraviolet Absorption Lines	137
5-7	UV Molecular Line Search	148
6-1	Solar Atomic Abundances	150
6-2	Depletions From Dominant Stage Ions	151
6-3	Depletions From Neutral Species	157
6-4	Fractional Atomic Abundance in Grains	161
6-5	Chemical Composition of Terrestrial Minerals	163
6-6	Electron Density From Ionization Equilibrium	171
6-7	Column Densities of Unobservable Ions	174

TABLE	PAGE
6-8 Atomic Collisional Excitation Parameters	179
6-9 C I Multiplets	184
6-10 C I Relative Line Strengths	184
6-11 Fractional Molecular Abundances	191
7-1 IS Diffuse Cloud Model	204
D-1 Photoionization and Recombination Rates	265
D-2 Ionization Equilibrium Parameters	268

LIST OF FIGURES

FIGURE	PAGE
1-1 Observed Depletions Towards ζ Oph, \circ Per, and ζ Per	4
3-1 Observed Radio Emission Line Profiles for ^{12}CO and ^{13}CO .	15
3-2 Optical Atomic and Molecular Absorption Line Profiles ...	19
3-3 Absorption Line Profiles of Mg I at 2852 \AA and 1707 \AA ...	24
3-4a ^{12}CO Line Profiles	35
3-4b ^{13}CO Line Profiles	36
3-4c Diatomic Carbon F-X (0,0) Line Profile	37
3-4d H_2O C-X Line Profiles	38
3-4e Line Profiles of Two Unidentified Lines at 2510 \AA	39
3-4f Line Profile of Unidentified Line at 1543.2 \AA	40
3-4g Line Profile of Unidentified Line at 1510.4 \AA	41
3-4h Line Profile of Unidentified Line at 1419.5 \AA	42
3-5 Absolutely Calibrated SWP Low Dispersion Spectrum (5 - 8 μm^{-1})	47
3-6 5 to 8 μm^{-1} Extinction Curve for X Per	48
4-1 Comparison of Equation 4-20 and Published Values	58
4-2 Theoretical Curve of Growth For $b = 1$ and $b = 10$ km/s ...	59
4-3 95/5 Composite Curve of Growth	62
4-4a Dominant Stage Ions and $b = 10$ km/s Curve of Growth	67
4-4b Mg I and Cl I Data With a 95/5 Curve of Growth	68
4-5 Si II Data Fit to a 95/5 Curve of Growth	71
4-6a The 1657 \AA Multiplet of C I: Observed, Theoretical, and Convolved	76
4-6b 3-0 Band of ^{12}CO : Observed, Theoretical, and Convolved ..	77

FIGURE	PAGE
4-6c 0-0 F-X C ₂ : Observed, Theoretical, and Convolved	78
5-1 Empirical Curve of Growth for the Highly Ionized Species	84
5-2 Ionization Potentials for H - Zn	94
5-3 Curve of Growth for Dominant Stage Ions	96
5-4 90/10 and 95/5 Theoretical Curves of Growth	111
5-5 Mg II Curve of Growth Compared with Theoretical Curves ..	99
5-6 Theoretical Curves of Growth for C II*	102
5-7 Empirical Curve of Growth for the Neutral Species	112
5-8 T_{R1}^* versus T_{R2}^* for X Per Compared with Theory	115
5-9 Theoretical and Observed ¹² C ¹⁸ O Line Profiles	121
5-10 Theoretical and Observed Curves of Growth for CO	122
5-11 Theoretical and Observed Curves of Growth for F-X Diatomic Carbon	124
5-12 Expected Rotational Lines for the D-X System of Diatomic Carbon	126
5-13 Theoretical and Observed F-X C ₂ Line Profiles	127
5-14 Energy Levels for the B-X System of CN	130
5-15 Energy Levels for the Visible Systems of CH	132
5-16 Individual Spectra Near the H ₂ O C-X Band	141
5-17 Expected Position of the R(0) A-X line of CS	145
6-1 Observed Depletions	153
6-2 Depletion Differences Between X Per and ζ Oph	154
6-3 Theoretical Diatomic Carbon Line Profiles	168
6-4 Theoretical and Observed C ₂ Line Profiles for T = 20 K ..	170
6-5 Theoretical and Observed C I Line Profiles	186
7-1 Column Densities From H ₂ Rotational Levels	208

FIGURE	PAGE
7-2 n_e , n_{HI} , and n_{H2} as a Function of A_V	210
7-3 Neutral Column Densities	211
7-4 C I and C II Fine Structure Column Densities	213
7-5 Theoretical and Observed C I Line Profiles	215
7-6a Heating Rates as a Function of Depth Into the Cloud	216
7-6b Cooling Rates as a Function of Depth Into the Cloud	217
7-7 Predicted and Empirical Temperature Distribution	219
7-8 n_H as a Function of Distance From the Cloud Center	220
A-1 τ_1 / τ_2 as a Function of Temperature	236
A-2 T_{R1}^* versus T_{R2}^*	238
B-1 Idealized Representation of the KCl Target	246
C-1 Vector Representation of Hund's Case (a)	252
C-2 Vector Representation of Hund's Case (b)	253
C-3 Transition From Case (a) to Case (b)	254

1. INTRODUCTION

1.1 Diffuse Interstellar Clouds

Most of our understanding of the nature of diffuse clouds has come from detailed observations towards a few clouds. With the advent of the Copernicus satellite, four comprehensive studies have been done as have a larger number of less complete studies. The diffuse interstellar medium (ISM) towards Alpha Vir (York and Kinahan, 1979), Gamma Vel (Morton and Bhavsar, 1979), Gamma Cas (Ferlet, Vidal-Madjar, Laurent, 1980), 15 Mon (Shull, 1980), Chi Oph (Frisch, 1979, 1980), Lambda Sco (York, 1975a), Delta Sco (Smith, 1974), and Gamma Ara (Morton and Hu, 1975) have had partial analyses. A more complete analysis was done on Zeta Pup (Morton, 1978), but the three major and comprehensive studies have been of the clouds towards Zeta Oph (Herbig, 1968; Morton, 1975), Zeta Per (Snow, 1977), and Omicron Per (Snow, 1975, 1976). After Morton published his paper on Zeta Oph, a number of subsequent papers came out which either modified the original conclusions or added new data. Discussions of O I (de Boer, 1979), C I (de Boer and Morton, 1974), CO (ultraviolet [UV], Smith, Krishna Swamy, Stecher, 1978; Wannier, Penzias, and Jenkins, 1982; radio, Crutcher, 1976; Liszt, 1979; Crutcher and Watson, 1981), K I (Crutcher, 1978), Na I (Crutcher, 1976), C₂ (UV, Snow, 1978), OH (UV, Crutcher and Watson, 1976), H I (H-alpha, Reynolds and Ogden, 1982), Rb I (Jura and Smith, 1981), Sc II (Snow and Dodgen, 1980), other velocity components (Snow and Meyers, 1979), ¹²CH⁺, and

$^{13}\text{CH}^+$ (Vanden Bout and Snell, 1980, 1981), weak near-UV lines (Shulman, Bortolot, and Thaddeus, 1974), and a detailed model of the diffuse cloud (Black and Dalgarno, 1977) have been published. For Zeta Per, the UV observations (Snow, 1977) give parameters similar to the Zeta Oph cloud. Observations of C_2 (IR, Hobbs, 1979a; Chaffee et al. 1980), Ti II (Hobbs, 1979b), CH and CH^+ (Federman, 1980), O I (de Boer, 1981), Na I and Ca II (Hobbs, 1974), and the near UV lines (Chaffee, 1974) have been made. A detailed model of the Zeta Per cloud (Black, Hartquist, and Dalgarno, 1978) has also been made. The UV observations towards the cloud in front of Omicron Per (Snow, 1976, 1977) have been augmented by observations of C_2 (IR, Hobbs, 1981), O I (de Boer, 1981), and radio CO observations (Crutcher, 1976).

For the various clouds, usually more than one velocity component exists. The theoretical models for Zeta Oph and Zeta Per suggest that both clouds have a cold, dense inner core, and a warm, diffuse outer shell. The range of temperature and density for Zeta Oph is $(n, T) = (2500 \text{ cm}^{-3}, 22 \text{ K})$, and $(500 \text{ cm}^{-3}, 110 \text{ K})$ (Black, Hartquist, and Dalgarno, 1978), for the inner and outer region, respectively. Crutcher and Watson (1981) note that the data are also consistent with one cloud, having $(n, T) = (200 \text{ cm}^{-3}, 65 \text{ K})$, and that the newer data appear to require that there be no cold, very dense core. The inner and outer values for the Zeta Per cloud are $(267 \text{ cm}^{-3}, 45 \text{ K})$, and $(110 \text{ cm}^{-3}, 120 \text{ K})$, respectively (Black and Dalgarno, 1977).

Figure 1-1 shows the range of depletions for the three stars, Zeta Oph, Zeta Per, and Omicron Per. It is immediately obvious that some elements have essentially a solar abundance (S, O, N, Ar), whereas other elements have very large depletions (Ti, Fe, Al). In other surveys, it was found that, in general, O (de Boer, 1981) and Zn (York and Jura, 1981) have roughly solar abundances whereas Fe (Savage and Bohlin, 1979) has very large depletions. The initial results of a C I survey by Jenkins and Shaya (1979) suggest that carbon can be depleted by up to a factor of ten over the solar value, although Liszt (1981) shows that if C I is compared with $N(H_2)$ and not $N(H_{tot})$, then carbon is essentially undepleted. Since the C I and the H_2 are probably coexistent, this is probably a good assumption to make. Crutcher (1975) also argued that C may be essentially undepleted. The problem of too few grains for too much depletion (Greenberg, 1974) has been solved, in the sense that the initial suggestions of large depletions of carbon and oxygen were incorrect.

The three clouds, which have similar color excesses ($E(B-V)=.3$), also have approximately 50% of the hydrogen in diatomic form. The rise in the far-UV extinction curve in all three clouds is also similar. The velocity parameters "b" ($\sqrt{2}$ times the Maxwellian velocity dispersion) for the two regions (Zeta Oph and the two Perseus stars) have values of (0.9 km/s; 6.5 km/s) for Zeta Oph, and (1.5 km/s; 10 km/s) for the two Perseus stars, where the values in parentheses are the velocity parameters for the neutral and ionized species, respectively. Hobbs (1974, 1979a) and Liszt (1979) point out that higher spectral resolution

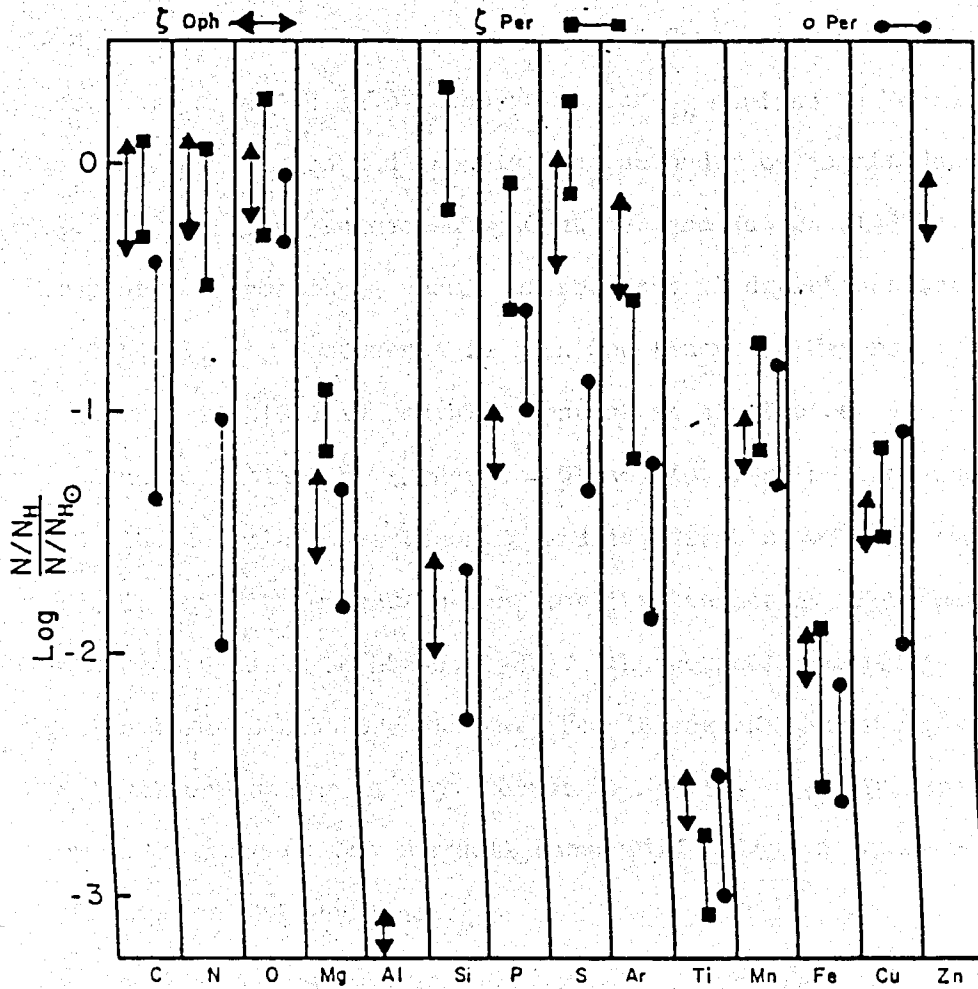


Figure 1-1. The observed depletions (log) towards ζ Oph, o Per, and ζ Per.

indicates that smaller velocity parameters should be used for the neutral components for both Zeta Per (Hobbs, 1979) and Zeta Oph (Liszt, 1979). Using ionization equilibrium considerations, Morton (1975) found that $n_e = 0.7 \text{ cm}^{-3}$ for Oph; although, if Crutcher and Watson (1981) are correct, $n_e = 0.8 \text{ cm}^{-3}$. The value for n_e derived by Morton from neutral and singly ionized iron is over an order of magnitude smaller (closer to the value suggested by Crutcher and Watson [1981]). This discrepancy is probably a result of the unequal depletions between the different velocity components in Zeta Oph (Snow and Meyers, 1979). The ratio of $N(\text{C I})/N(\text{CO})$ is roughly constant at a value of ≈ 10 over large variations in extinction (Federman, Glassgold, Jenkins, and Shaya, 1980). The correlation between CO and A_v , first noted by Dickman (1976), is found to extend to very small values of A_v (Federman, Glassgold, Jenkins, and Shaya, 1980). Theoretical abundances for simple molecules towards Zeta Oph and Zeta Per (Black, Hartquist, and Dalgarno, 1978; Black and Dalgarno, 1977) agree reasonably well with the observations, except for the well known difficulty in accurately predicting the CH^+ abundance.

Because of the possibility of observing the effects of nucleosynthesis in the relative abundance of a particular isotope, various isotopes of a number of molecules have been searched for. In particular, ^{12}CO and ^{13}CO are very ubiquitous, and $^{12}\text{CH}^+$ and $^{13}\text{CH}^+$ can be observed. Unfortunately, there exists a chemical fractionation process by which the $^{13}\text{CO} / ^{12}\text{CO}$ ratio can increase over the true isotopic C ratio (Watson, Anicich, and Huntress, 1976). Towards Zeta

Oph, the $^{12}\text{CO} / ^{13}\text{CO}$ ratio is 55 ± 11 (Wannier et al. 1982) or >50 (Crutcher and Watson, 1981), and the $^{12}\text{CH}^+ / ^{13}\text{CH}^+$ ratio is $77 (+17, -12)$ (Vanden Bout and Snell, 1980, 1981). This suggests that perhaps chemical fractionation has occurred.

There are still a number of uncertainties about the physical structure of diffuse clouds, particularly as the clouds become more opaque. A number of uncertainties arise because of the integral nature of the observations. If the diffuse cloud can be characterized by a constant density, pressure, and radiation field, then the observed column densities can be used to accurately calculate these same physical properties. Any variation of these parameters will be reflected by a modification of the column densities of the atoms and molecules. It is not immediately obvious whether the derived temperature and densities will reflect the true physical conditions. Additionally, other processes may be affecting the local density of a particular species. For example, the accretion rate onto IS grains may be a function of depth into the cloud and may also be different for each stage of ionization. The depletion of an element can be inferred from both the dominant stage ions and the neutral species. These may be different if the neutral and ionized species are weighted differently.

Another problem concerns the velocity parameter of the gas. If the bulk of the material is in one region of space at a relatively high density, then why do the neutral and singly ionized species show different velocity parameters? The neutral species can exist in the

intercloud medium (ICM), hence the reason cannot be that all the neutrals are only in the center of the cloud.

The existence of molecules in diffuse clouds has been attributed to ion-molecule reactions. This suggests that as the cloud gets darker and the density gets higher, more molecules will be found. Hence it is important to not only find them, but to attempt to infer where they are in the cloud.

To answer some of these questions, I have observed the diffuse cloud along the line of sight towards X Per. This analysis differs from previous studies in that I am using the combined data from the UV, optical, and radio to analyze the physical parameters of the cloud. Previous studies have primarily focused either on the UV and optical, or on the radio. Additionally, the extinction towards X Per is almost a factor of two greater than the most heavily reddened stars previously analyzed in detail.

In Chapter 2, I discuss the stellar properties of X Per. Chapter 3 presents the UV, optical, and radio data. Chapter 4 discusses the various analytical techniques which were used to derive the atomic and molecular column densities (Chapter 5) and some of the physical parameters of the diffuse cloud (Chapter 6). Chapter 6 includes the analysis of the depletions, the electron and hydrogen densities, the kinetic temperature: it also discusses the isotopic ratios of carbon and oxygen.

I have developed a model for the diffuse cloud towards X Per. This model accurately predicts the column densities of all observed ions and neutrals as well as the diatomic hydrogen column density, the atomic fine structure population, and the mean electron density. The few discrepancies can all be explained. This model is presented in Chapter 7. I conclude with a summary and discussion of the results in Chapter 8.

2. STELLAR PROPERTIES OF X PER

2.1 Stellar Parameters

X Per (HD24534) is a variable 6th magnitude star with an intensity variation of about 0.6 magnitude (Moffat, Haupt, and Schmidt-Kaler, 1977). It has been classified as a Be star, with a spectral type of either B0 (Ramsey, 1950; Mendoza, 1958; Brucatan and Kristian, 1972) or Ope (Delhaye and Blaauw, 1953; Hiltner, 1954; Harris, 1956; Cohen, 1973; Moffat, Haupt, and Schmidt-Kaler, 1977). X Per is unusual in that the variation in magnitude is much larger than found in normal Be stars (Moffat, Haupt, and Schmidt-Kaler, 1977). Only Gamma Cas has a similar magnitude of variation. Because of the uncertainty in the spectral classification, the E(B-V) color excess is not well known. The color excesses in the literature range from 0.55 (Moffat, Haupt, and Schmidt-Kaler, 1977) to 0.62 (Harris, 1956; Cohen, 1973). The rotational velocity of X Per is 450 km/s (Hutchings, 1977). X Per is also a spectroscopic binary, with a period of 584 days (Hutchings, 1977; Kemp, 1982)

Braes and Miley (1972), Brucatan and Kristian (1972), and Van den Bergh (1972) have shown that X Per lies very close to the center of the error box for the X-ray source 3U 0352+30. The total X-ray luminosity of X Per is 5×10^{33} erg/s (Garavoglia and Treves, 1976; Mushotzky, Roberts, Baiy and Peterson, 1977; Moffat, Haupt, and Schmidt-Kaler,

1973; Mason et al. 1976; Frontera, Fuligni, Morelli, and Ventura, 1979). The X-ray flux is also variable, with a period of 13.924 minutes (Mason et al. 1976).

A recent model for the X Per system suggests that the 13.982 minute period represents half the rotational period of an X-ray pulsar, which is orbiting X Per with a period of 584 days.

The current picture of the X Per system (White et al. 1982) is a widely separated binary containing a B0 star with a stellar wind and an accreting neutron star. The observed X-ray spectrum can be fit by a 10 keV thermal model. The mass loss rate derived by White et al. (1982) is $\dot{M} \approx 8 \times 10^{-8} V_3 M_\odot$ per year, where V_3 is the terminal velocity of the wind in units of 10^3 km/s.

The stellar UV spectrum of X Per shows an ionization structure expected for a 30,000 K atmosphere. Lines arising from He II, C II, C IV, N III, N IV, N V, Mg II, Al III, Si III, Si IV, Mn IV, Fe III, Fe IV, and Fe IV have been identified. None of the line profiles show any evidence for mass loss. Optical stellar lines (Moffat et al. 1973) include H I, He I, He II, C II, N II, N III, O II, O III, Ne II, Mg II, Al III, Si III, Si IV, S II, S III, A II, and Fe III.

3. INTERSTELLAR OBSERVATIONS

This chapter describes the radio (3.1), optical (3.2), and UV (3.3) observations taken for this work. Section 3.4 describes the previously published IS observations of the ISM towards X Per.

3.1 Radio

Microwave emission lines from the J=1-0 rotational transition of ^{12}CO and ^{13}CO , the J=2-1 rotational transition of ^{12}CO , and the $X^2\Pi_{3/2}$ F=2-1 hyperfine transition of the ground rotational state of OH were observed towards X Per. Upper limits were placed on emission from the J=1-0 rotational transitions of HCO^+ and HCN, and the C 85 α recombination line. Table 3-1 lists the atom or molecule, the transition, observed radiation temperature, LSR velocity, line width, integration time, spectral resolution, and the telescope used to obtain the data.

The data on the J=1-0 rotational transition of ^{12}CO and ^{13}CO were obtained using the 11 m radio telescope at Kitt Peak. Orthogonal senses of polarization were directed into either the 250 kHz filter bank or the 100 kHz filter bank. Frequency switching was used instead of position switching, primarily because of the spatial extent of the molecular

TABLE 3-1
RADIO EMISSION LINE OBSERVATIONS OF X PER

Mole.	Trans.	T_R^* (K)	σ (K)	Δv (km/s)	V_{LSR} (km/s)	Telescope	Int. (min)	Res. (km/s)
^{12}CO	J=1-0	3.4	0.12	2.08	7.75	NRAO ^a 11 ^m	30	0.26
^{12}CO	J=2-1	1.8	0.2	1.9	7.73	MWO ^b 5 ^m	30	0.08
^{13}CO	J=1-0	0.36	0.05	1.63	7.95	NRAO ^a 11 ^m	60	0.27
OH^c	F=2-1	0.09	0.05	1.2	7.9	NRAO ^a 140'	NA	NA
$\text{C85}\alpha$	n=86-85	---	0.005	---	---	NRAO ^a 140'	120	0.14
HCN	J=1-0	---	0.13	---	---	NRAO ^a 11 ^m	45	0.34
HCO^+	J=1-0	---	0.08	---	---	NRAO ^a 11 ^m	30	0.34

^aNational Radio Astronomy Observatory

^bMillimeter Wave Observatory, University of Texas at Austin

^cR. M. Crutcher, private communication (1982)

cloud around the Per OB2 association (Sancisi et al.). The spectra were calibrated using a mechanical chopping vane (Ulich and Haas, 1976; Kutner and Ulich, 1981, hereafter KU). Additional calibration checks were made by observing several standard sources. The X Per data were then scaled by the ratio of the true antenna temperature to the observed antenna temperature of the standard source. Table 3-2 lists the standard sources used, along with their antenna temperatures.

The 11 m radio telescope was also used in the aforementioned observing mode to put upper limits on the J=1-0 rotational transitions of HCO⁺ and HCN. These limits are reported in Table 3-1.

The J=2-1 rotational transition of ¹²CO was observed using the 4.9 m radio telescope of the University of Texas' Millimeter Wave Observatory. The 62.5 kHz filter bank was used in frequency switching mode, and was calibrated by using a mechanical chopping vane. The J=1-0 ¹²CO and ¹³CO and the J=2-1 ¹²CO emission lines are shown in Figure 3-1.

The NRAO 140' radio telescope at Green Bank, W. Va., was used to observe the X²Π_{3/2} F=2-1 hyperfine transition of OH and to obtain an upper limit on the C 85α recombination line. These data are also presented in Table 3-1.

TABLE 3-2
RADIO CALIBRATION SOURCES

Source	α (1950)	δ (1950)	T_R^* (K)	σ (K)	V_{LSR} (km/s)	Δv (km/s)
^{12}CO						
W3(OH)	$2^{\text{h}}23^{\text{m}}16^{\text{s}}.7$	$61^{\circ}38'54''$	16.1	1.3	-47.4	6.8
M17SW	$18^{\text{h}}17^{\text{m}}26^{\text{s}}.5$	$-16^{\circ}14'54''$	39.5	0.5	19.4	26.7
W51	$19^{\text{h}}21^{\text{m}}27^{\text{s}}.0$	$59^{\circ}39'00''$	28.4	2.1	57.1	12.5
^{13}CO						
M17SW	$18^{\text{h}}17^{\text{m}}26^{\text{s}}.5$	$-16^{\circ}14'54''$	13.7	1.1	19.4	5.6
W3(OH)	$2^{\text{h}}23^{\text{m}}16^{\text{s}}.7$	$61^{\circ}38'54''$	7.1	0.6	-47.4	6.4

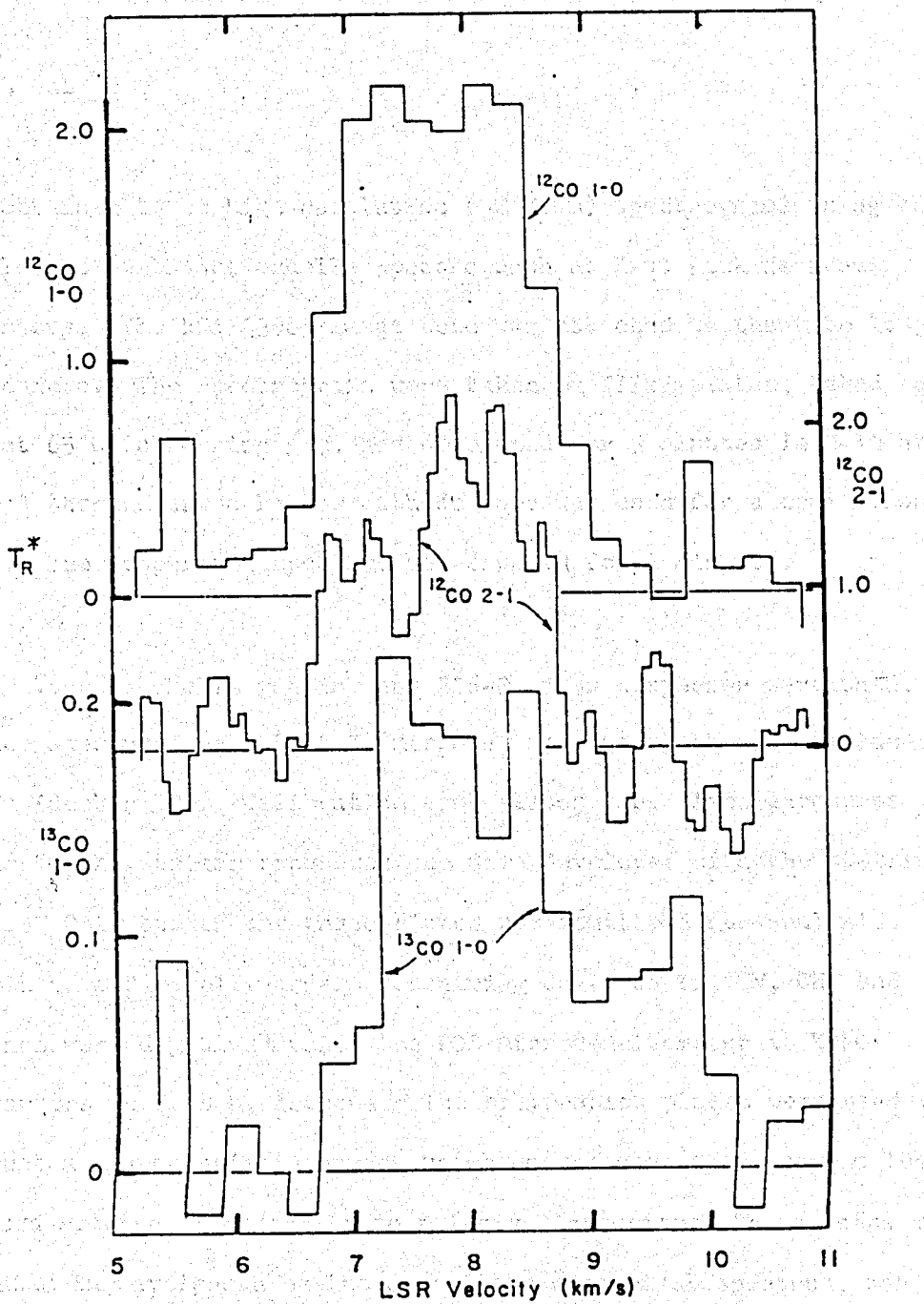


Figure 3-1. The $J=1-0$ rotational transitions of ^{12}CO and ^{13}CO and the $J=2-1$ rotational transition of ^{12}CO toward X Per. The ordinate of the latter is on the right.

3.2 Optical

I obtained three high resolution ($\approx 2 \text{ \AA/mm}$) spectrograms using the 4 m telescope with the echelle spectrograph at Kitt Peak National Observatory. The RCA 33063 image tube was attached to the blue long focus camera. The spectrograms were taken on IIIaJ plates, baked for 2 hours at 65 C in forming gas, and developed for 5 minutes in D-19 at 20 C. A thorium-argon hollow cathode tube was used for a comparison source. The comparison spectrum was exposed for 3 minutes.

The 79-63° echelle grating and 226-2 cross disperser were used. The entrance aperture was set at 70 microns, and the spectra were widened to 1.55 mm (decker #3). Calibration spot plates were given exposures similar to the stellar exposures and were developed with the stellar spectra. Only two of the three plates were suitable for analysis. The spot plates and echelle orders containing Ca I, Ca II, CN, CH, and CH⁺ lines were digitized using the PDS microdensitometer at KPNO headquarters in Tucson, Arizona. The calibration plates were used to construct a characteristic curve, which was then used to convert the digitized spectra from density to relative intensity. The spectra were calibrated in wavelength by the use of the comparison spectrum, and the relative intensity was plotted against the wavelength for each of the orders mentioned above.

The equivalent widths were extracted from the plots with a planimeter, and are presented in Table 3-3. The error in the equivalent width is the equivalent width of a noise feature which appeared to have a 1- variation in intensity. Figure 3-2 shows the intensity tracings for all the lines listed in Table 3-3.

3.3 Ultraviolet

The UV data were obtained with the International Ultraviolet Explorer (IUE) satellite. A detailed description of the satellite and the data is presented in Appendix B.

Ten SWP and eight LWR (short wavelength prime and long wavelength redundant cameras, respectively; cf Appendix B for a detailed description of the IUE) high dispersion spectra of X Per were obtained. The image sequence numbers, dates, exposure times, and other salient data are listed in Table 3-4. These spectra were processed as described in Appendix B. The data from each useable order were shifted in wavelength and co-added.

Each summed order was then searched for possible IS lines. Lines whose identification as real features were in doubt were examined in detail by the identification methods discussed in Appendix B. The equivalent width for each line which passed the identification test was then extracted. A cubic spline was fit to a number of points which were

TABLE 3-3
OPTICAL ABSORPTION LINE OBSERVATIONS

Mole/Line ID	Lambda (Å)	Equivalent Width				f-value
		EW Plate 1	1σ	EW Plate 2	1σ	
CN $B^2\Sigma^+ - X^2\Sigma^+$						
$R_1(0)+R_{Q_{21}}(0)$	3874.608	20.9	1.1	20	1.5	0.0173
$P_1(1)+P_{Q_{12}}(1)$	3875.763	11.1	0.9	7.3	1.0	0.0058
$R_2(1)+R_1(1)+R_{Q_{21}}(1)$	3873.998	6.4	0.9	7.3	1.1	0.0115
$R_1(2)+R_2(2)+R_{Q_{21}}(2)$	3873.369	1.3	1.1	1.0	1.0	0.0104
$P_1(2)+P_2(2)+P_{Q_{12}}(2)$	3876.310	1.0	1.1	--- ^a	--- ^a	0.0069
CH $A^2\Delta - X^2\Pi_{1/2}$						
$R_{1e2e}(1)+R_{1f2f}(1)$	4300.32	33.1	1.4	---	---	0.0120
$B^2\Sigma^- - X^2\Pi_{1/2}$						
$P_{Q_{12}}(1)+R_2(1)$	3886.65	14.2	1.1	---	---	0.0032
CH ⁺ $A^1\Pi - X^1\Sigma^+$						
R(0)	4232.54	<10	3.1	---	---	0.0136
CaI	4226.728	10.1	2.0	---	---	1.75
CaII	3933.663	184.6	1.6	---	---	0.6819
	3968.468	133.2	1.7	---	---	0.3305

^a no tracings available

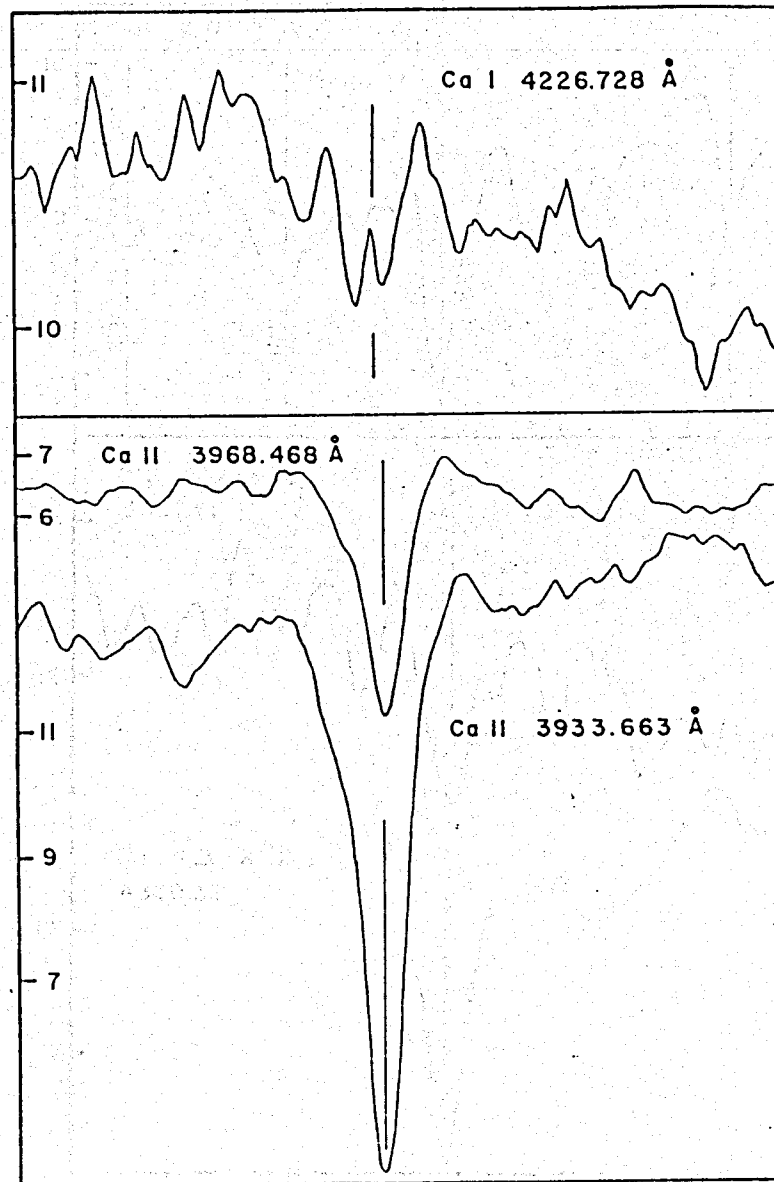


Figure 3-2 The line profiles of the observed optical atomic and molecular transitions. Relative intensity scales for each line are on the left side of each figure: a) Ca II 3933 Å; b) Ca II 3968 Å; c) Ca I 4226 Å;

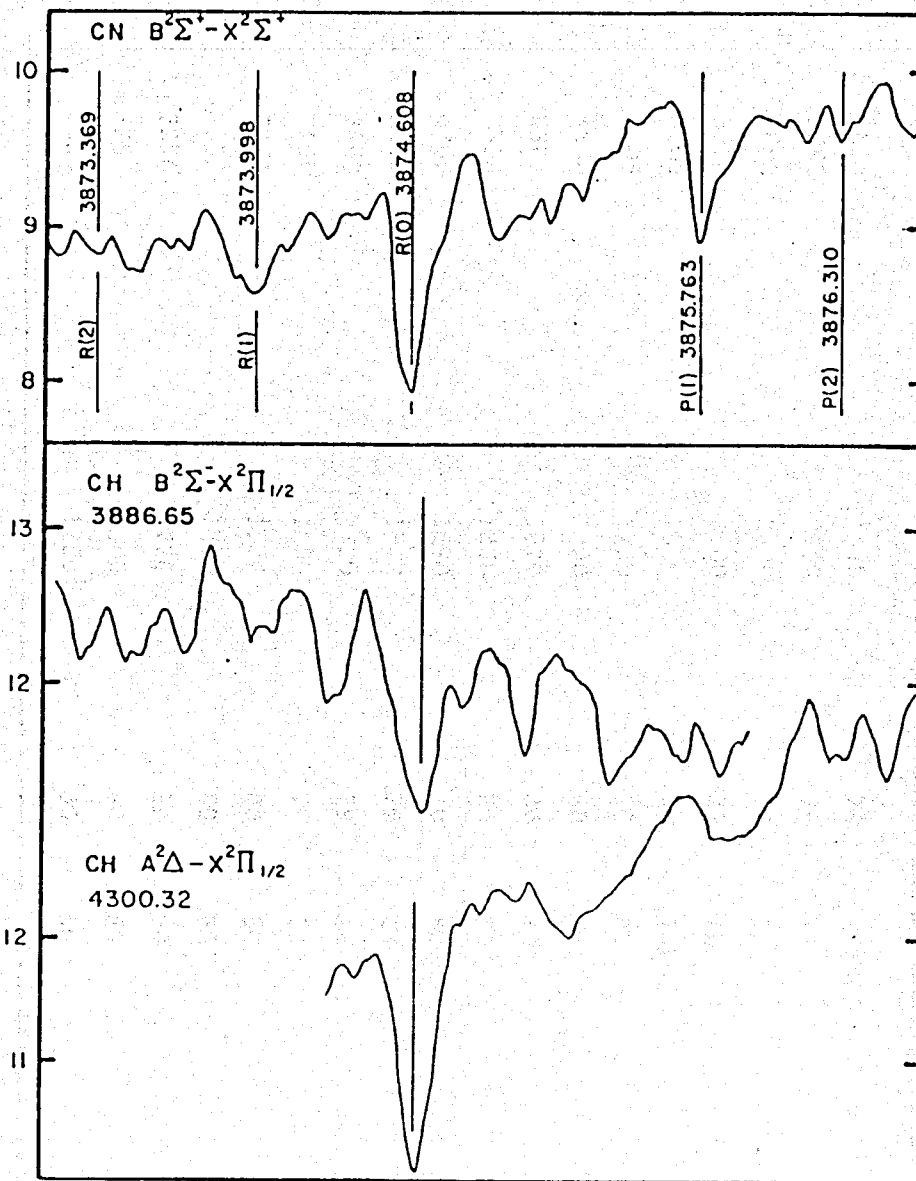


Figure 3-2 The line profiles of the observed optical atomic and molecular transitions. Relative intensity scales for each line are on the left side of each figure: d) CN 3874 Å; e) CH 4300 Å; f) CH 3886 Å.

TABLE 3-4
IUE SPECTRA

Image Sequence Number (ISN)	Exposure (s)	Year	Day
SWP 2834	1440	78	275
3892	2400	79	12
3893	2400	79	12
3894	2400	79	12
6805	1319	79	282
8305	2700	80	80
8306	1800	80	80
8307	1620	80	80
8308	1200	80	80
8309	1620	80	80
LWR 3462	1800	79	12
3463	2700	79	12
3464	1800	79	12
7252	1500	80	80
7253	1200	80	80
7254	720	80	80
7255	500	80	80
7256	1200	80	80

chosen as representative of continuum values. The equivalent width of a line is the area of the region bounded by the absorption feature and the continuum and is expressed in wavelength units. Numerically, it is the sum of a set of trapezoids constructed from adjacent discrete wavelength points. Let C_i and D_i represent the intensities at the i^{th} wavelength of the continuum and data, respectively. The equivalent width can then be written as

$$W = \sum_{i=1}^{n-1} \Delta\lambda_i \frac{(C_i - D_i + C_{i+1} - D_{i+1})}{(C_i + C_{i+1})} \quad (3-1)$$

where $\Delta\lambda_i = \lambda_{i+1} - \lambda_i$. D_i and C_i are in units of FN (flux number).

To a first approximation, equation 3-1 can be rewritten as

$$W = \sum_{i=1}^{n-1} \frac{(C_i - D_i)}{C_i} \quad (3-2)$$

The first order error estimate is then (Bevington, 1978)

$$(dW_i)^2 = \left(\frac{\partial W_i}{\partial \Delta\lambda_i} d\Delta\lambda_i\right)^2 + \left(\frac{\partial W_i}{\partial C_i} dC_i\right)^2 + \left(\frac{\partial W_i}{\partial D_i} dD_i\right)^2 \quad (3-3)$$

and

$$(dW)^2 = \sum_{i=1}^n (dW_i)^2 \equiv \sigma_W^2 \quad (3-4)$$

Evaluating the partial derivatives and substituting them into equation

3-3 yields

$$(dW_i)^2 = (d\Delta\lambda_i)^2 \left(\frac{C_i - D_i}{C_i}\right)^2 + (dC_i)^2 \left(\frac{D_i}{C_i}\right)^2 \Delta\lambda_i^2 + (dD_i)^2 (C_i)^{-2} \Delta\lambda_i^2 \quad (3-5)$$

The photometric noise (N) for a given flux (FN) is approximately $N = \alpha/\sqrt{FN}$, where $\alpha = 10$. Hence, $d^2C_i = 100 \times C_i$, and $d^2D_i = 100 \times D_i$.

Equation 3-5 is then

$$(dW_i)^2 = (d\Delta\lambda_i)^2 \left(1 - \frac{C_i}{D_i}\right)^2 + \alpha^2 \Delta\lambda_i^2 \left(\frac{D_i^2}{C_i^3} + \frac{D_i}{C_i^2}\right) \quad (3-6a)$$

$$(dW_i)^2 = \alpha^2 \Delta\lambda_i^2 \frac{D_i}{C_i^2} \left(1 + \frac{D_i}{C_i}\right) \quad (3-6b)$$

where I have assumed that the error in the wavelength is much smaller than any other source of error. For weak lines, $C_i = D_i$, and equation 3-6 takes the simple form

$$(dW)^2 = \sum_{i=1}^n (2\alpha^2 \Delta\lambda_i^2) / C_i \quad (3-7)$$

The UV equivalent widths were calculated using equation 3-1, and the errors were calculated using equation 3-6 and 3-4), where $\Delta\lambda = 0.007$. Figure 3-3 shows the 2852 Å and 1707 Å lines of Mg I as examples of strong and weak lines, respectively. The 2-σ error is shown for each line.

Table 3-5 contains the equivalent widths of all atomic species observed with the IUE. Also included are the laboratory wavelengths, the oscillator strengths (if known), and the calculated error. Lines

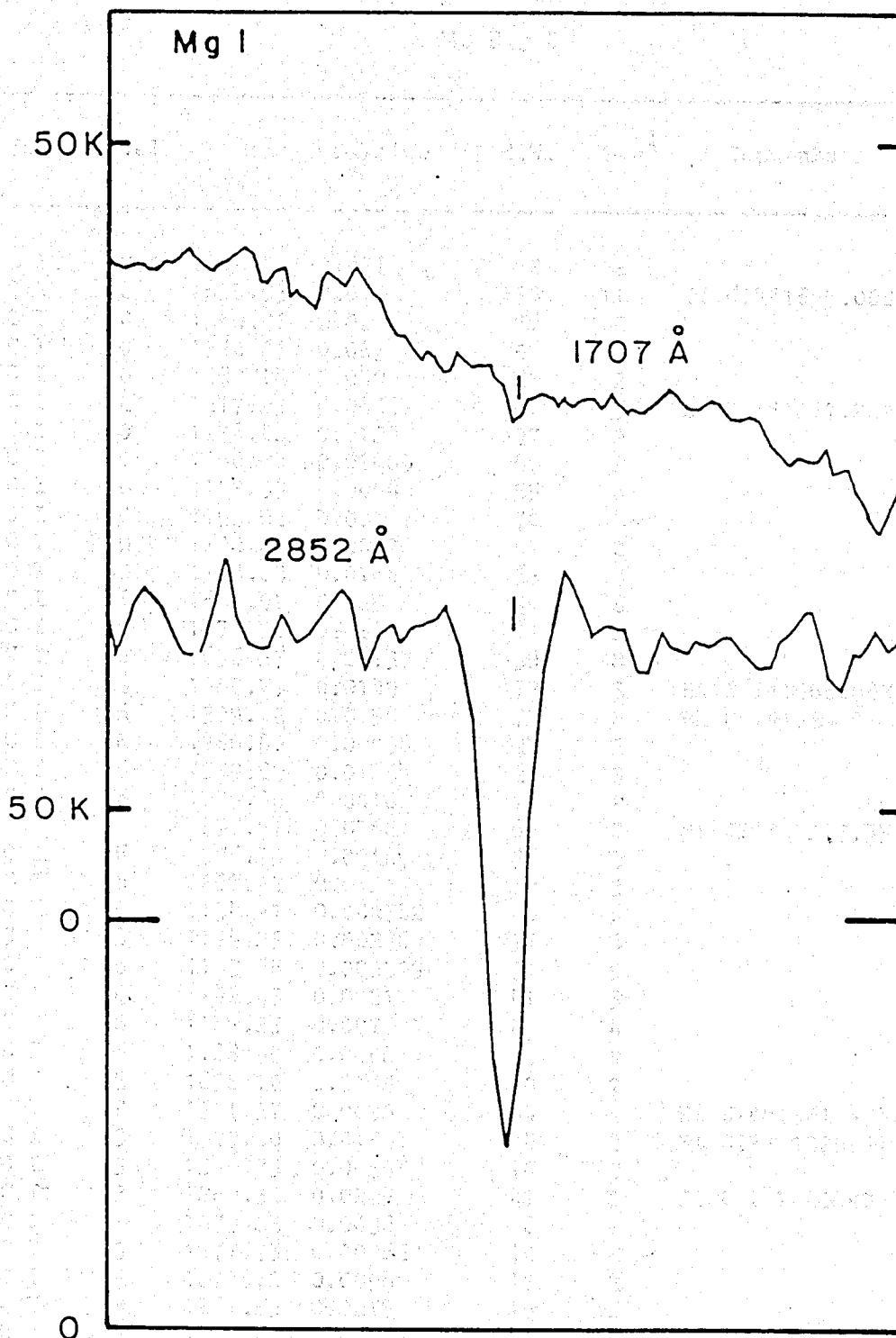


Figure 3-3. The Mg I lines at 2852 Å and 1707 Å showing examples of strong and weak lines. The vertical bars represent twice the standard deviation of the noise (2σ).

TABLE 3-5

Ion	Level	$\lambda(\text{\AA})$	f-Value	E.W.	$1-\sigma^1$	Comments
B II	0	1362.46	0.827	2	2	
C I	0	1656.93	0.075	133	11	Bl CI**1657.008
C I	0	1560.31	0.06	77	3	
C I	0	1328.83	0.063	51	2	
C I	0	1280.14	0.049	41	2	
C I	0	1277.25	0.0646	101	3	Bl C I*1277.282
C I	0	1276.48	0.0124	37	2	
C I	0	1260.74	0.02869	40	2	
C I	0	1193.93	0.0094	55	6	
C I	0	1193.03	0.081	70	5	
C I	0	1192.22	0.0027	51	2	
C I	0	1188.83	0.0168	33	3	
C I	16	1657.91	0.025	49	8	
C I	16	1657.38	0.0188	47	8	
C I	16	1656.27	0.0313	30	8	
C I	16	1560.71	0.0149	73	3	Bl C I*1560.683
C I	16	1329.12	0.0158	73	2	Bl C I*1329.1, 1329.086
C I	16	1280.60	0.00998	27	2	
C I	16	1279.89	0.0125	28	3	
C I	16	1279.06	0.0016	15	2	
C I	16	1277.51	0.0162	65	2	Bl CI** 1277.55
C I	16	1276.75	0.0016	31	3	
C I	16	1261.12	0.012	82	3	
C I	16	1194.41	0.000782	40	6	
C I	16	1194.23	0.00236	17	6	
C I	16	1193.68	0.003919	31	5	
C I	16	1192.45	0.0021	41	5	
C I	16	1189.25	0.007	44	4	
C I	16	1188.99	0.0056	38	4	
C I	43	1658.12	0.0188	30	7	
C I	43	1561.37	0.0059	54	4	Bl CI**1561.438, 1561.341
C I	43	1329.60	0.0158	44	3	Bl CI** 1329.578
C I	43	1280.85	0.0075	14	2	
C I	43	1280.33	0.0225	41	2	Bl C I 1280.404
C I	43	1279.23	0.0038	6	2	
C I	43	1277.95	0.00062	10	2	
C I	43	1277.72	0.0098	17	2	
C I	43	1261.55	0.0215	15	2	
C I	43	1261.43	0.0072	14	2	
C I	43	1194.69	0.008	21	4	

¹ Equivalent widths less than $2-\sigma$ are not considered detections.

TABLE 3-5 (CONT.)

Ion	Level	λ (Å)	f-Value	E.W.	$1-\sigma$ ¹	Comments
C I	43	1189.45	0.0042	8	2	
C II	0	1334.53	0.1287	288	3	
C II	0	2324.69	0.00000007	10	10	
C II	63	1335.71	0.1159	170	4	Bl CII** 1335.662
C IV	0	1550.77	0.0952	39	3	
C IV	0	1548.20	0.1911	71	3	
N I	0	1200.71	0.0594	144	5	
N I	0	1200.22	0.1144	136	5	
N I	0	1199.55	0.178	199	5	
N IV	0	1486.50	0.00000077	5	5	
N V	0	1242.80	0.0783	2	2	
N V	0	1238.82	0.1569	2	2	
O I	0	1302.17	0.0503	242	8	
O I	158	1304.86	0.051	2	2	
O I	226	1306.03	0.0506	2	2	
O I	0	1355.60	0.00000063	5	5	
Mg I	0	2852.13	1.81	240	4	
Mg I	0	2025.82	0.112	41	4	
Mg I	0	1827.54	0.0238	18	5	
Mg I	0	1747.81	0.00898	14	3	
Mg I	0	1707.10	0.00433	8	3	
Mg I	0	1683.51	0.00246	4	3	
Mg II	0	2802.70	0.3061	496	5	
Mg II	0	2795.53	0.6091	521	5	
Mg II	0	1240.40	0.00032290	14	2	
Mg II	0	1239.93	0.00064530	30	2	
Al I	0	3082.15	0.1794	5	5	
Al I	0	2652.48	0.014	5	5	
Al I	0	2567.98	0.0455	3	2	
Al I	0	2367.05	0.1209	5	5	
Al I	0	2263.46	0.0148	5	5	
Al II	0	1670.79	1.83	205	4	
Al II	0	1862.80	0.2772	76	4	
Al II	0	1854.72	0.5569	110	4	
Si I	0	2514.32	0.1584	25	6	
Si I	0	2207.98	0.0412	18	1	
Si I	0	1977.58	0.0308	5	5	
Si I	0	1845.52	0.152	11	8	

¹ Equivalent widths less than $2-\sigma$ are not considered detections.

TABLE 3-5 (CONT.)

Ion	Level	λ (Å)	f-Value	E.W.	$1-\sigma$ ¹	Comments
Si I	0	1841.15	0.0136	7	7	
Si I	0	1255.28	0.218	5	5	
Si I	0	1562.05	0.0001	7	3	
Si I	0	1568.62	0.0001	6	3	
Si I	0	1572.71	0.0001	9	3	
Si I	0	1614.57	0.0174	5	5	
Si I	77	2211.74	0.017	10	6	
Si I	77	2210.89	0.0508	18	7	
Si I	77	1847.47	0.114	4	3	
Si I	77	1846.11	0.0	5	3	
Si I	77	1843.77	0.0	4	3	
Si II	0	1808.00	0.0036	75	3	
Si II	0	1526.72	0.1303	208	4	
Si II	0	1304.37	0.0918	172	3	
Si II	0	1260.42	0.9525	269	3	
Si II	0	1193.28	0.5077	265	1	
Si II	0	1190.42	0.2931	200	5	
Si II	28	1264.73	0.827	5	2	
Si II	28	1197.39	0.15	9	3	
Si II	0	1206.51	1.695	19	1	
Si IV	0	1402.77	0.2236	24	3	
Si IV	0	1393.76	0.4502	43	3	
P I	0	1787.68	0.051	3	2	
P I	0	1782.87	0.102	4	4	
P I	0	1774.99	0.1537	6	3	
P I	0	1679.71	0.0247	5	5	
P I	0	1674.61	0.0168	5	5	
P I	0	1671.68	0.0082	6	3	
P II	0	1532.51	0.00951	6	3	
P II	0	1301.87	0.0381	16	3	
P III	0	1334.87	0.0294	5	5	
S I	0	1900.27	0.000036	8	5	
S I	0	1807.34	0.1116	49	6	
S I	0	1474.57	0.001232	5	5	
S I	0	1474.39	0.0163	84	5	
S I	0	1474.01	0.075	11	6	
S I	0	1473.00	0.017	15	3	
S I	0	1425.24	0.00215	13	2	Bl S I 1425.229
S I	0	1425.23	0.03	13	2	Bl S I 1425.24
S I	0	1425.07	0.1918	18	3	

1

Equivalent widths less than $2-\sigma$ are not considered detections.

TABLE 3-5 (CONT.)

Ion	Level	λ (Å)	f-Value	E.W.	$1-\sigma$ ¹	Comments
S I	0	1401.54	0.0161	5	2	
S I	0	1316.62	0.000411	43	6	Bl S I 1316.61, 1316.57
S I	0	1303.42	0.0293	14	4	
S I	0	1296.14	0.0408	19	4	
S I	0	1295.66	0.1233	21	4	
S I	0	1247.17	0.0	9	2	
S I	0	1262.83	0.0	5	2	
S I	0	1270.78	0.0073	19	3	
S I	0	1381.57	0.000093	8	2	
S I	0	1388.46	0.00016	10	2	
S I	0	1444.32	0.000814	9	3	
S II	0	1259.52	0.0121	133	4	
S II	0	1253.81	0.0099	106	3	
S II	0	1250.59	0.0054	79	3	
S III	0	1190.21	0.0224	83	8	
S V	0	1199.13	0.0	12	4	
Cl I	0	1379.53	0.0031	6	2	
Cl I	0	1347.24	0.114	25	4	
Cl I	0	1188.77	0.074	20	4	
Ca I	0	2721.65	0.2	9	3	
Ca II	0	1341.89	0.00080980	9	3	
Ti II	0	1903.46	0.0	14	6	
Ti II	0	1298.67	0.1	6	2	
Ti II	0	1295.88	0.071	3	2	
V II	0	2677.01	0.0	33	5	
Cr I	0	2365.91	0.0046	3	2	
Cr I	0	2366.81	0.0041	28	5	
Cr I	0	2364.73	0.0057	20	5	
Cr I	0	2094.93	0.00099	31	6	
Cr I	0	2095.39	0.00073	17	5	
Cr I	0	2095.88	0.00053	15	5	
Cr II	0	2065.46	0.08	13	5	
Cr II	0	2061.54	0.12	13	5	
Cr II	0	2055.59	0.17	6	5	
Mn II	0	2605.70	0.158	79	3	
Mn II	0	2593.73	0.223	114	3	

1

Equivalent widths less than $2-\sigma$ are not considered detections.

TABLE 3-5 (CONT.)

Ion	Level	λ (Å)	f-Value	E.W.	$1-\sigma$ ¹	Comments
Mn II	0	2576.11	0.288	113	4	
Mn II	0	1201.12	0.058	16	5	
Mn II	0	1197.17	0.096	24	5	
Fe I	0	2966.90	0.0439	5	5	
Fe I	0	2719.03	0.1207	14	3	
Fe I	0	2522.85	0.2767	25	5	
Fe I	0	2483.27	0.5536	22	3	
Fe I	0	2166.80	0.1478	10	6	
Fe I	0	2132.00	0.0052	10	6	
Fe II	0	2599.40	0.2249	332	4	
Fe II	0	2585.88	0.0573	235	6	
Fe II	0	2382.03	0.328	288	5	
Fe II	0	2373.73	0.0395	166	7	
Fe II	0	2366.86	0.000117	3	2	
Fe II	0	2343.50	0.108	246	7	
Fe II	0	2260.08	0.00698	69	7	
Fe II	0	2249.18	0.00129	32	6	
Fe II	0	1608.46	0.22	118	4	
Co I	0	2365.06	0.012	4	3	
Ni I	0	2320.03	0.6808	4	4	
Ni I	0	2310.95	0.0	6	4	
Ni I	0	2207.74	0.0	20	6	
Ni II	0	1773.96	0.0	5	3	
Ni II	0	1741.56	0.0	15	3	
Ni II	0	1809.60	0.0	18	4	
Ni II	0	1703.41	0.0	7	2	
Ni II	0	1467.85	0.0	2	2	
Ni II	0	1393.33	0.54	6	2	
Ni II	0	1370.20	0.1	24	7	
Ni II	0	1317.38	0.0	15	2	
Ni II	0	1317.22	0.121	14	2	
Cu I	0	2181.72	0.0713	5	5	
Cu I	0	2178.94	0.13	16	5	
Cu II	0	1358.76	0.54	9	2	
Cu II	0	1472.40	0.0	5	3	
Zn I	0	2138.56	1.459	8	8	
Zn I	0	1589.76	0.0	11	3	
Zn II	0	2062.02	0.202	49	4	
Zn II	0	2025.51	0.405	73	5	
Ga II	0	1414.40	1.69	12	2	

¹ Equivalent widths less than $2-\sigma$ are not considered detections.

TABLE 3-5 (CONT.)

Ion	Level	λ (A)	f-Value	E.W.	$1-\sigma^1$	Comments
Ge II	0	1237.10	0.8718	19	3	
Ge II	0	1602.50	0.1309	5	5	
Xe I	0	1469.60	0.28	5	2	
As II	0	1263.78	0.	6	2	
Br I	0	1488.60	0.0001	8	3	

¹ Equivalent widths less than $2-\sigma$ are not considered detections.

LIBRARY OF THE L. H. WOODS - GEORGETOWN

which were searched for but not detected are indicated in Table 3-5 by equal equivalent widths and errors, where the quoted errors are $1-\sigma$ errors. Table 3-6 lists the same information for all molecular lines or bands observed with the IUE, and Table 3-7 lists the same information for a number of unidentified UV transitions. Figure 3-4(a-h) shows the observed profiles for the data presented in Tables 3-6 and 3-7.

3.4 Data in Literature

3.4.1 Radio

The line of sight towards X Per was included in the H I survey of the Per OB2 association (Sancisi et al. 1974). The peak temperature, LSR velocity and column density were interpolated from H I maps presented by Sancisi, et al. (1974), and are presented in Table 3-8.

CO towards X Per was first detected by Knapp and Jura (1976). Their results are also presented in Table 3-8. Knapp and Jura (1976) also observed the four cardinal points at a distance of 2 arcminutes from X Per. The line widths remained constant, and there was a slight variation in T_R ($\approx 20\%$). To a first approximation, the cloud in front of X Per does not show small-scale structure. This assumption is very useful, as it implies that the radio and UV data are measuring the same physical conditions and it aids in the radio data reduction in the sense

TABLE 3-6
UV MOLECULAR ABSORPTION LINE OBSERVATIONS

Mole/Line ID Vib. Band	Lambda (Å)	Eq. Width (mÅ)	2-σ Error (mÅ)	f-value
$^{12}\text{CO} \quad A^1\Pi - X^1\Sigma^+$				
0-0	1544.45	125	8	0.02
1-0	1509.75	123	8	0.038
2-0	1477.57	140	6	0.0429
3-0	1447.36	125	6	0.036
4-0	1419.04	102	6	0.0251
5-0	1392.53	79	6	0.0155
6-0	1367.62	78	6	0.00848
7-0	1344.18	88	10	0.00437
8-0	1322.15	50	4	0.00217
9-0	1301.40	28	6	0.00108
10-0	1281.87	34	6	0.0005
11-0	1263.43	23	4	0.00025
12-0	1246.06	14	6	0.00013
13-0	1229.67	21	6	0.000068
$^{13}\text{CO} \quad A^1\Pi - X^1\Sigma^+$				
1-0	1510.45	108	6	0.038
2-0	1478.68	39	6	0.0429
3-0	1449.04	33	8	0.036
4-0	1421.21	28	6	0.0251
5-0	1395.15	18	6	0.0155
6-0	1370.61	12	6	0.00848
7-0	1347.51	8	4	0.00437
8-0	1325.76	<10	4	0.00217
9-0	1305.25	<10	6	0.00108

TABLE 3-6 (CONT.)

Mole/Line ID	Lambda	Eq. Width	2- σ Error	f-value
Vib. Band	(\AA)	($\text{m}\text{\AA}$)	($\text{m}\text{\AA}$)	
C_2	$\text{F}^1\Pi_u - \text{X}^1\Sigma_g^+$			
0-0	1341.63	35	8	0.104
1-0	1314.25	--	5	0.063
H_2O	$\bar{\text{C}}^1\text{B}_1 - \bar{\text{X}}^1\text{A}_1$			
000-000	1239.728 ^a	5	4	0.018
000-000	1240.949 ^b	7	4	0.0082

^a $1_{10}^{-0}00$ rotational transition

^b $0_{00}^{-1}10$ rotational transition

LIBRARY OF THE UNIVERSITY OF CALIFORNIA

TABLE 3-7
UV UNIDENTIFIED ABSORPTION LINES

Wavelength (\AA)	Wavenumber (cm^{-1})	Eq. Width ($\text{m}\text{\AA}$)	2- σ Error ($\text{m}\text{\AA}$)	Log Nf (cm^{-2})
2512.76	39784.9	25	6	11.65
2510.98	39813.1	10	6	11.25
1543.12	64803.61	39	4	12.27
1510.45	66205.44	70	-	12.54 ^a
1419.49	70447.84	33	4	12.27

^ablend with ^{13}CO at 1510 \AA

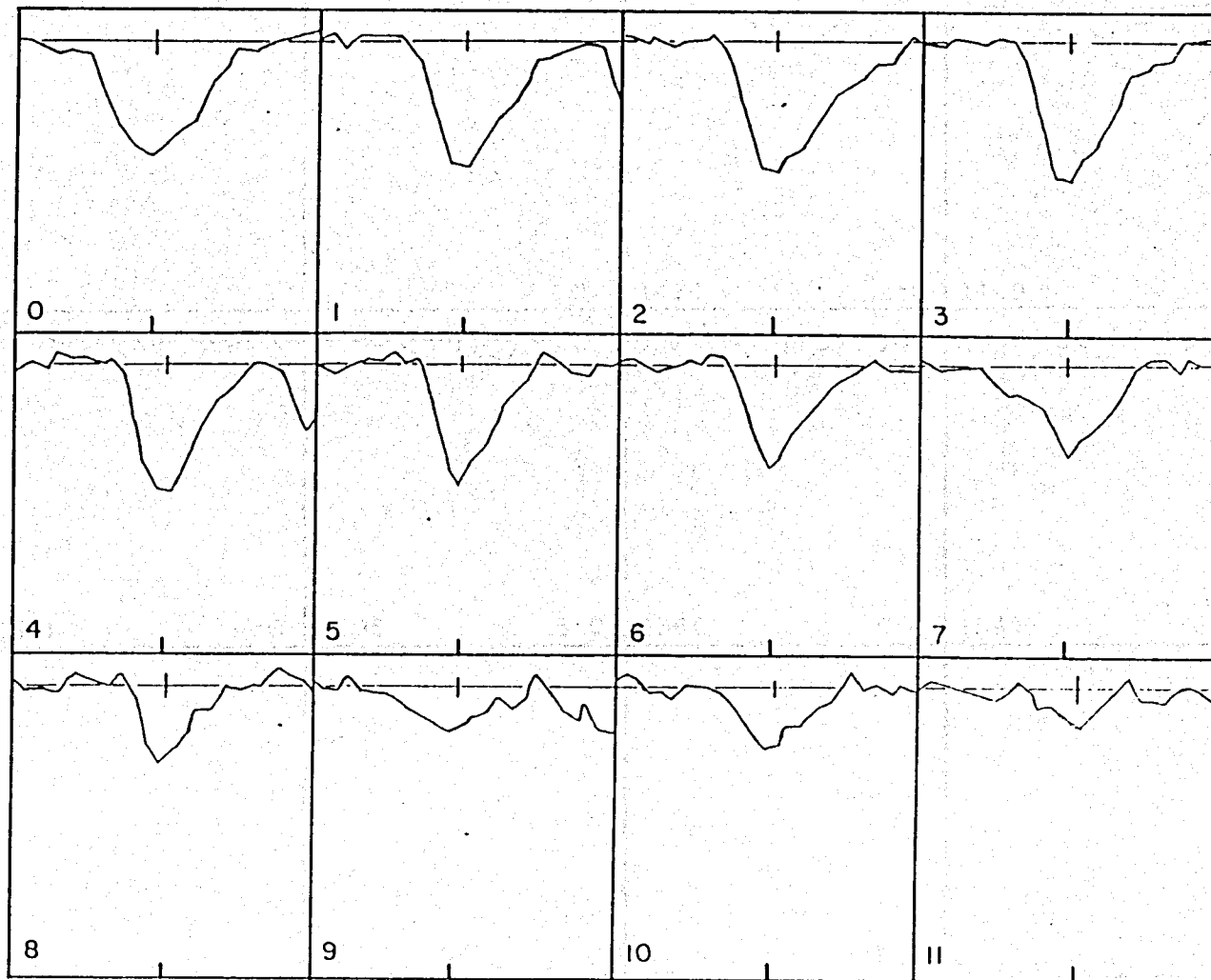


Figure 3-4a. Normalized ^{12}CO line profiles for the first 12 vibrational bands of the A-X electronic transition ($v' = 0-11$). The thin horizontal line in each box represents a relative intensity of 1.0. The expected position of the R(0) line for each band is shown; the length of the line represents twice the standard deviation of the noise. The width of each box is 1 Å.

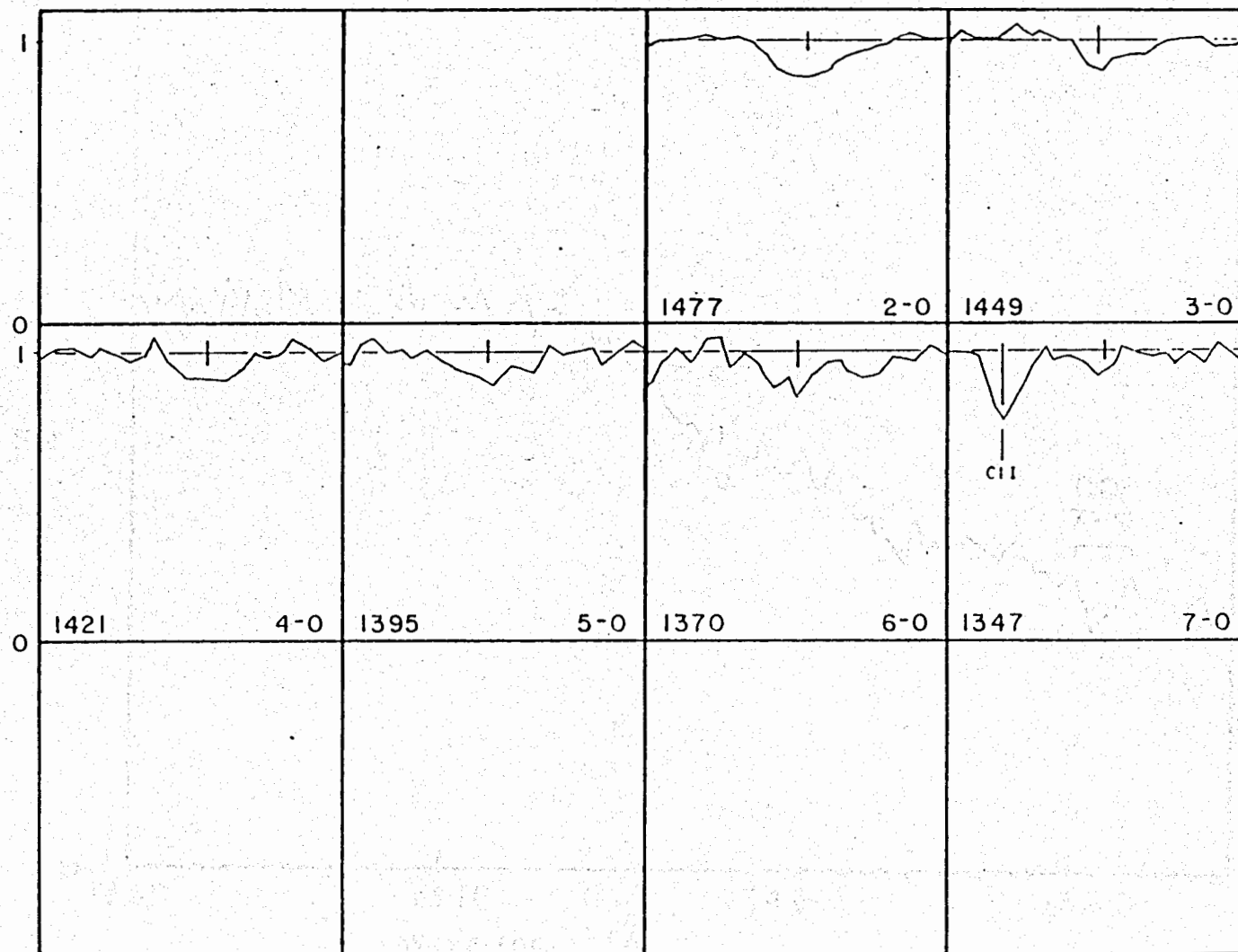


Figure 3-4b. The same as Figure 3-4a, except for ^{13}CO .

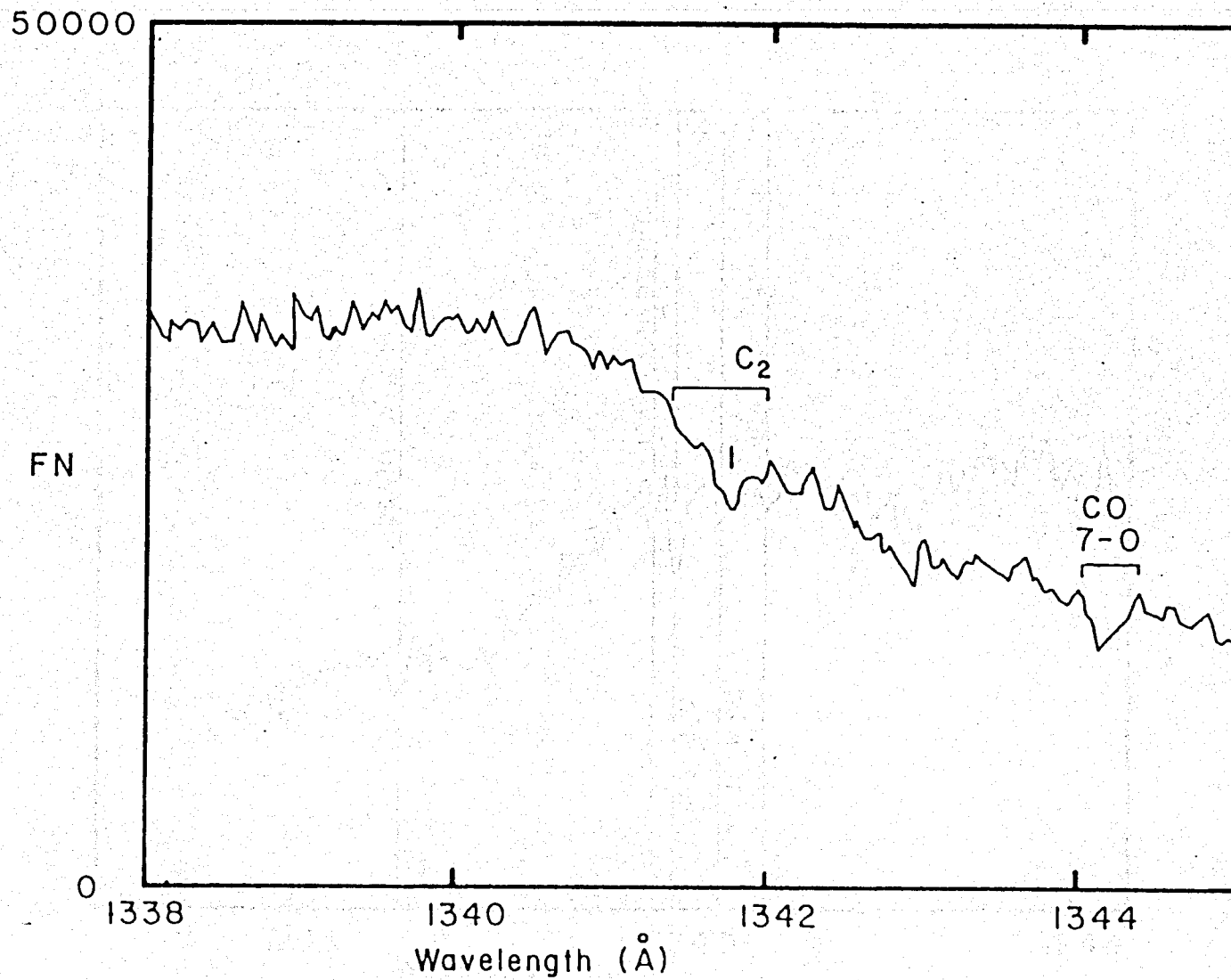


Figure 3-4c. The expected position and extent of the (0-0) band of the F-X system of C_2 . The vertical bar represents a $2\text{-}\sigma$ variation in the noise. The (7-0) band of ^{12}CO is also indicated.

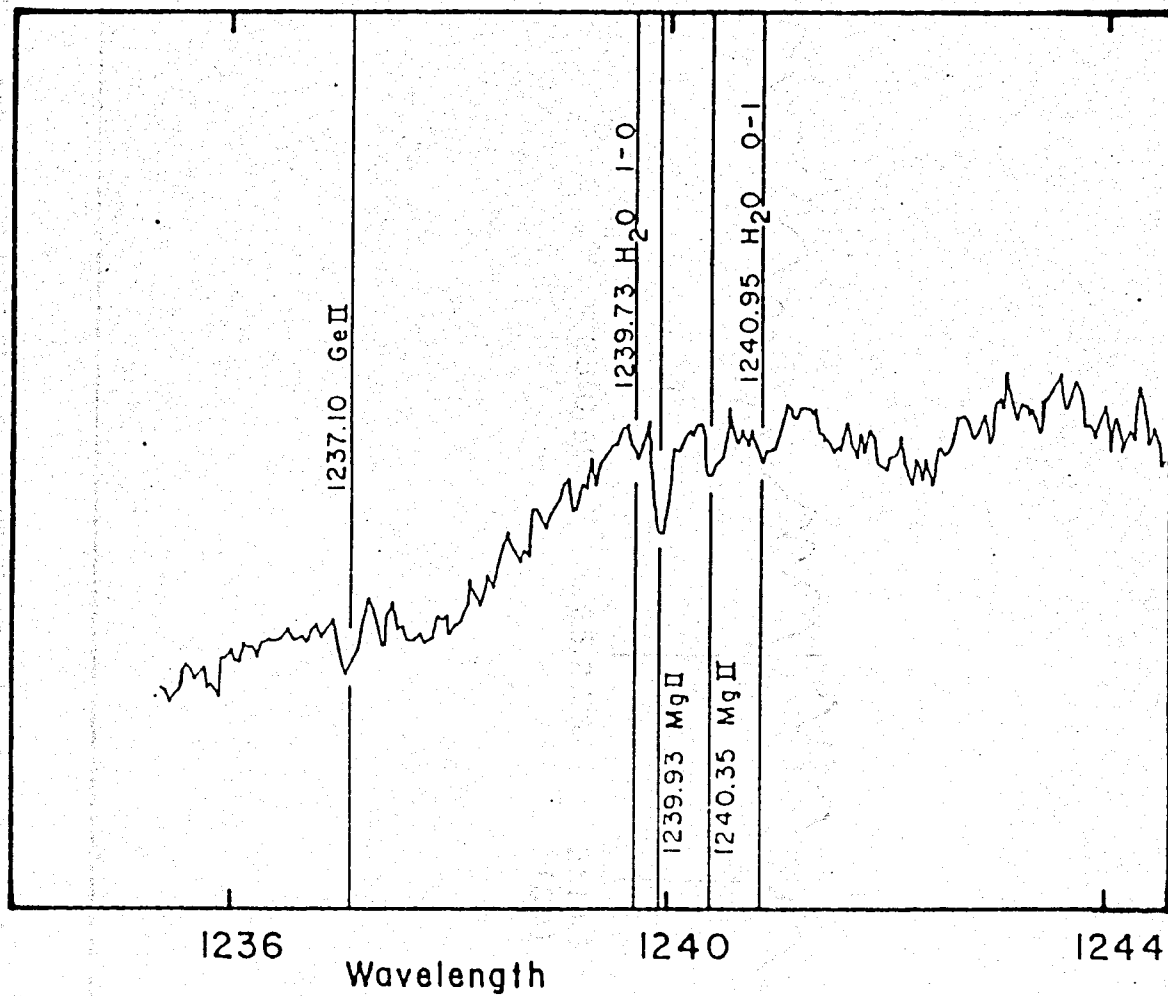


Figure 3-4d. The expected positions of the $1_{10} - 0_{00}$ and the $0_{00} - 1_{01}$ rotational lines of the $\bar{C}-\bar{X}$ system of H_2O . Also shown are the Mg II 1240 Å doublet and the Ge II line at 1237.1 Å.

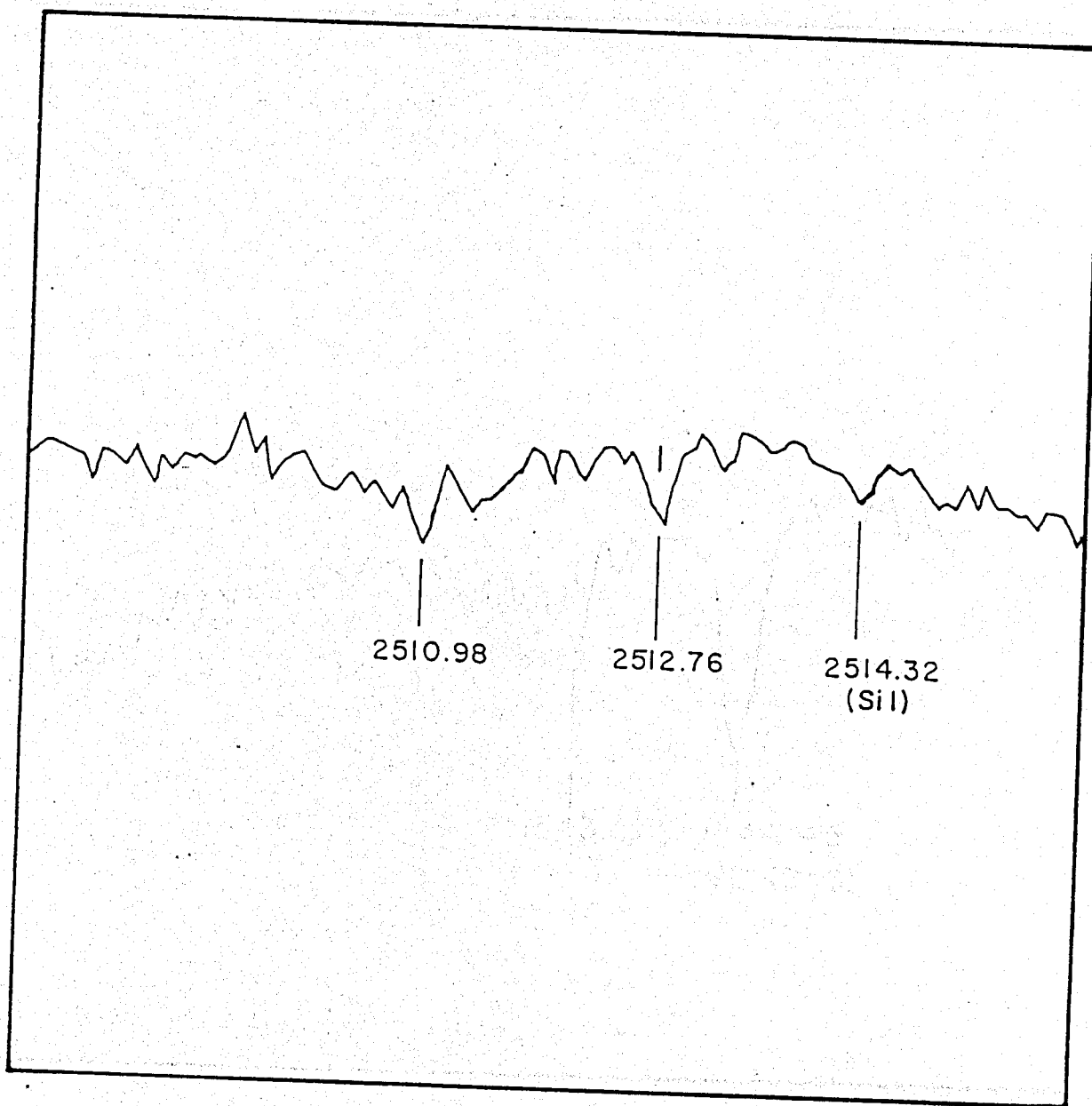


Figure 3-4e. Two unidentified lines at 2511.0 Å and 2512.8 Å. Also shown is the Si I line at 2514.3 Å. The vertical bar represents a 2- σ variation in the noise.

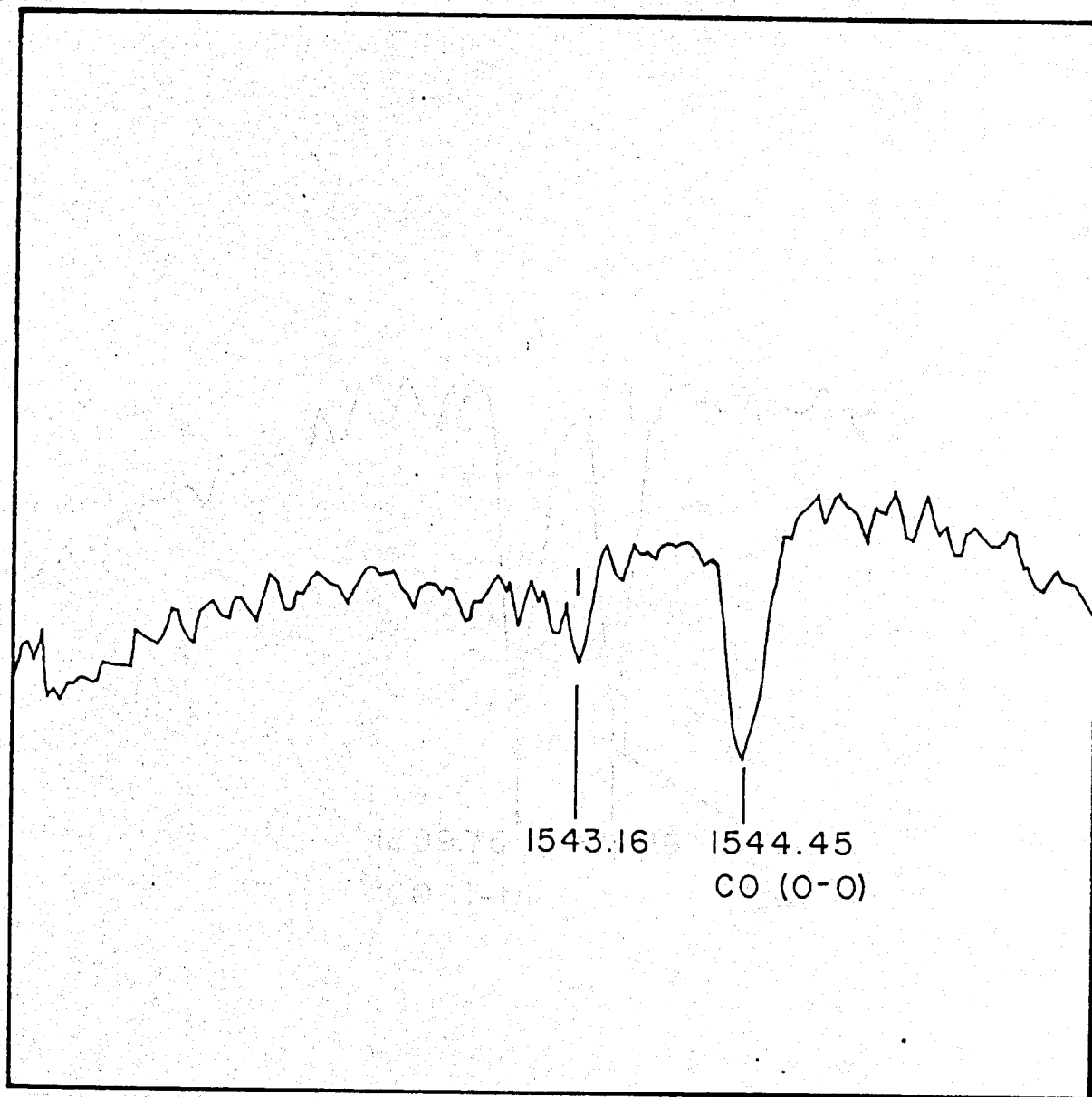


Figure 3-4f. An unidentified line at 1543.2 cm^{-1} . Also shown is the 0-0 ^{12}CO band.

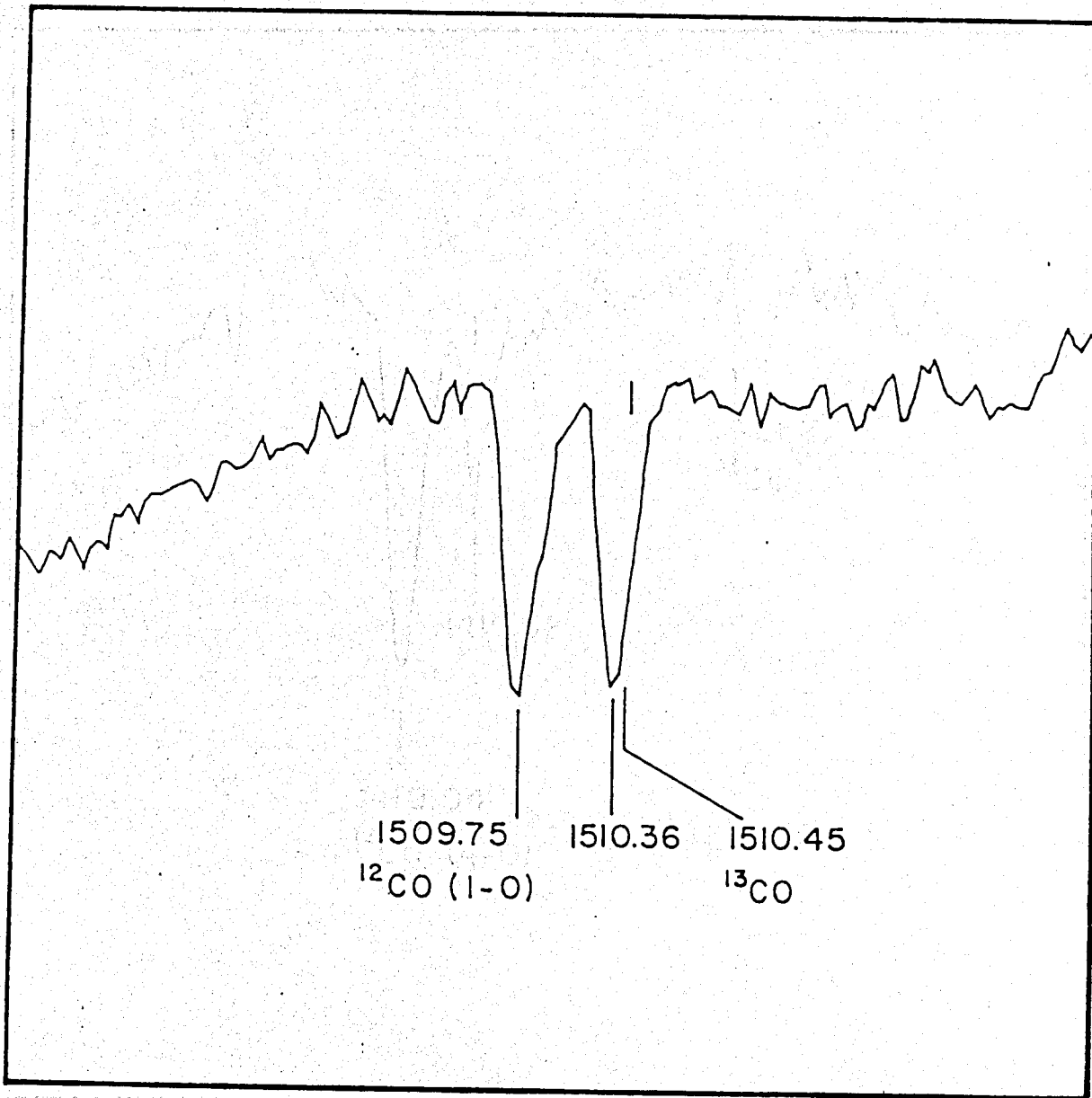


Figure 3-4g. An unidentified line at 1510.4 Å. Also shown is the 1-0 ^{12}CO band. The expected position of the head of the 1-0 ^{13}CO band is also indicated.

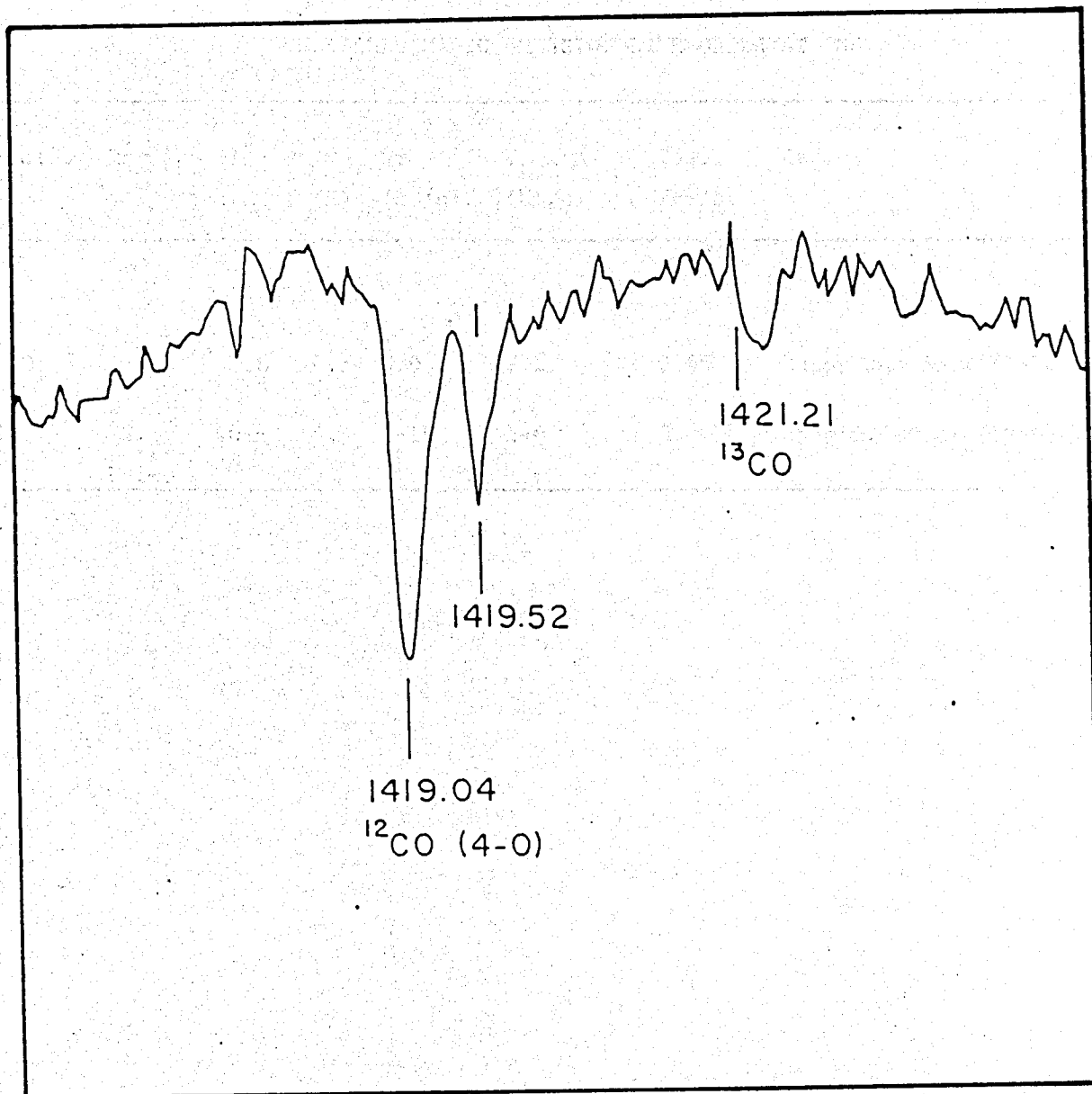


Figure 3-4h. An unidentified line at 1419.5 Å. Also shown are the 4-0 bands of ^{12}CO and ^{13}CO .

TABLE 3-8
PUBLISHED RADIO EMISSION LINE OBSERVATIONS

Species	Trans.	T_R^* (K)	σ (K)	Δv (km/s)	V_{LSR} (km/s)	Res. (km/s)	Ref.
^{12}CO	J=1-0	2.6	0.5	0.9	7.2	0.65	Knapp and Jura (1976)
HI	$^2\text{S}_{1/2}$ F=1-0	40.	4.	8-10	5-6	2	Sancisi et al (1974)

that the beam couples smoothly to the source (cf. Appendix A.).

3.4.2 Optical

Optical absorption lines of K I, Ca II, Na I, CH and CH⁺ have been observed towards X Per. Table 3-9 lists the species, wavelength, and the published values of the equivalent width, its error and the column density. The 4232 Å line of CH⁺ was only marginally detected by Adams (1948) and Cohen (1973).

3.4.3 Ultraviolet

The UV spectrometer aboard the Copernicus satellite (Rogerson et al. 1973) was used to measure the equivalent width of neutral hydrogen (Lyman α) and the J=0 and J=1 rotational lines of the A-X transition of H₂. (White et al. 1976). Only the column densities of the H₂ lines were given: they are $N(J=0) = 6.0 \pm 1.5 \times 10^{20} \text{ cm}^{-2}$ and $N(J = 1) = 5.0 \pm 1.5 \times 10^{20} \text{ cm}^{-2}$, respectively. The atomic hydrogen column density was derived from the FWHM (Full width at half maximum) of Ly α , where the equivalent width is related to the FWHM by

TABLE 3-9
PUBLISHED OPTICAL AND UV ABSORPTION LINE OBSERVATIONS

Species	Lambda (\AA)	Eq. Width ($\text{m}\text{\AA}$)	Error	Log N (cm^{-2})	Reference
HI	1216	8000	2 \AA	20.3 \pm 0.1	White et al (1976)
H ₂ J=0	--	--	--	20.78 \pm 0.11	White et al (1976)
J=1	--	--	--	20.70 \pm 0.11	White et al (1976)
CaII	3933	150	15%	12.5	Cohen (1972); b=5 km/s
	3968	110	15%	12.5	Cohen (1972); b=5 km/s
CH A-X	4300	20	15%	13.3	Cohen (1972)
CH ⁺ A-X	4232	12	10 $\text{m}\text{\AA}$	12.7	Cohen (1972)
KI	7698	124	12 $\text{m}\text{\AA}$	12.03 \pm 0.9	Chaffee and White (1982)
	7664	177	10 $\text{m}\text{\AA}$	12.03 \pm 0.9	Chaffee and White (1982)

$$W = 1.48 \times \text{FWHM}$$

(3-8)

(Lorentz broadening only). The equivalent width of Ly α is $8 \pm 2 \text{ \AA}$, corresponding to a neutral hydrogen column density of $2.0 \pm 0.5 \times 10^{20} \text{ cm}^{-2}$.

3.5 Extinction

Figure 3-5 shows the absolutely calibrated short wavelength low resolution spectrum of X Per. Ly α can clearly be seen at 1215 \AA , as can the Si IV doublet at 1400 \AA .

Figure 3-6 shows the extinction curve for X Per, plotted as $E(\lambda-V)/E(B-V)$ for $E(B-V) = 0.6$. HD 36512 (BOV, $V = 6.04$, $E(B-V) = 0.02$) was used as the comparison star for Figure 3-6. Also shown in Figure 3-6 is the "standard" IS extinction curve of Savage and Mathis (1979). The dashed line is this same curve decreased by an amount corresponding to the amount the extinction curve for X Per would increase if $E(B-V) = 0.52$.

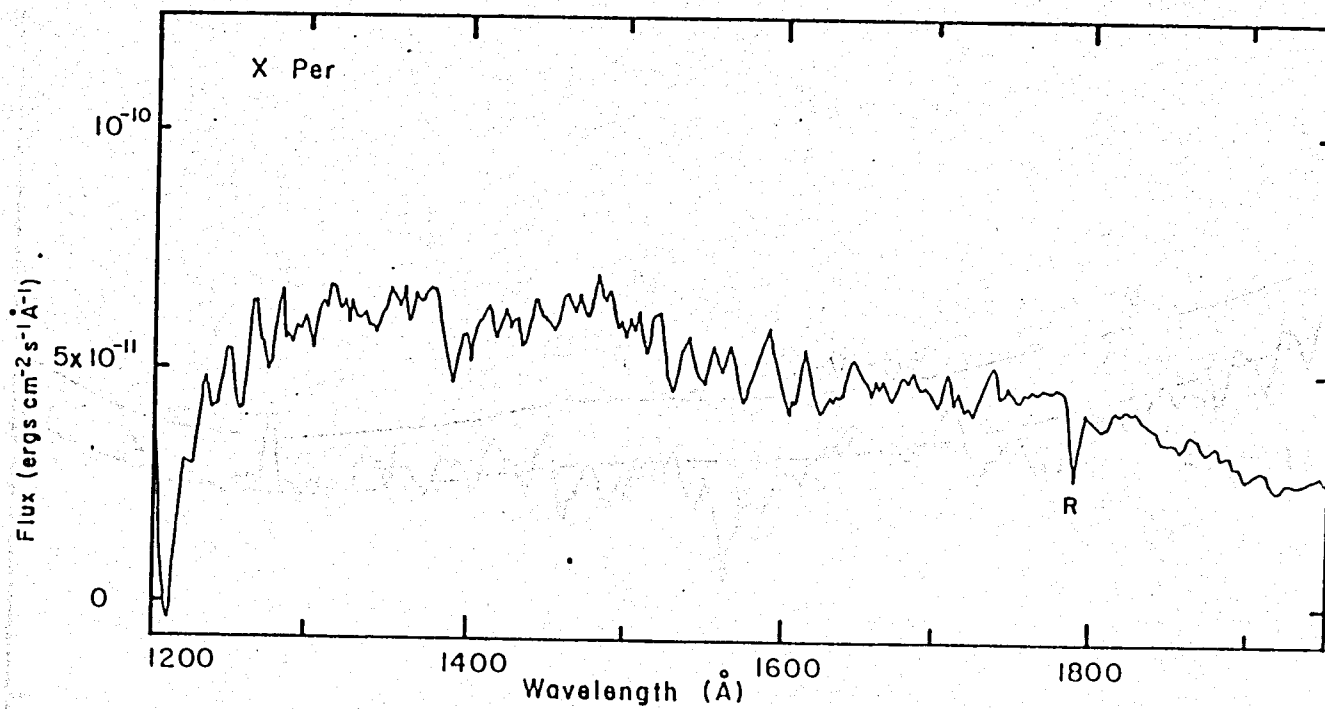


Figure 3-5. Absolutely calibrated (ergs cm⁻²s⁻¹Å⁻¹) SWP spectrum of X Per. Line from Si IV (1400 Å) and Ly α (1215 Å) are clearly seen. R signifies the position of a reseau.

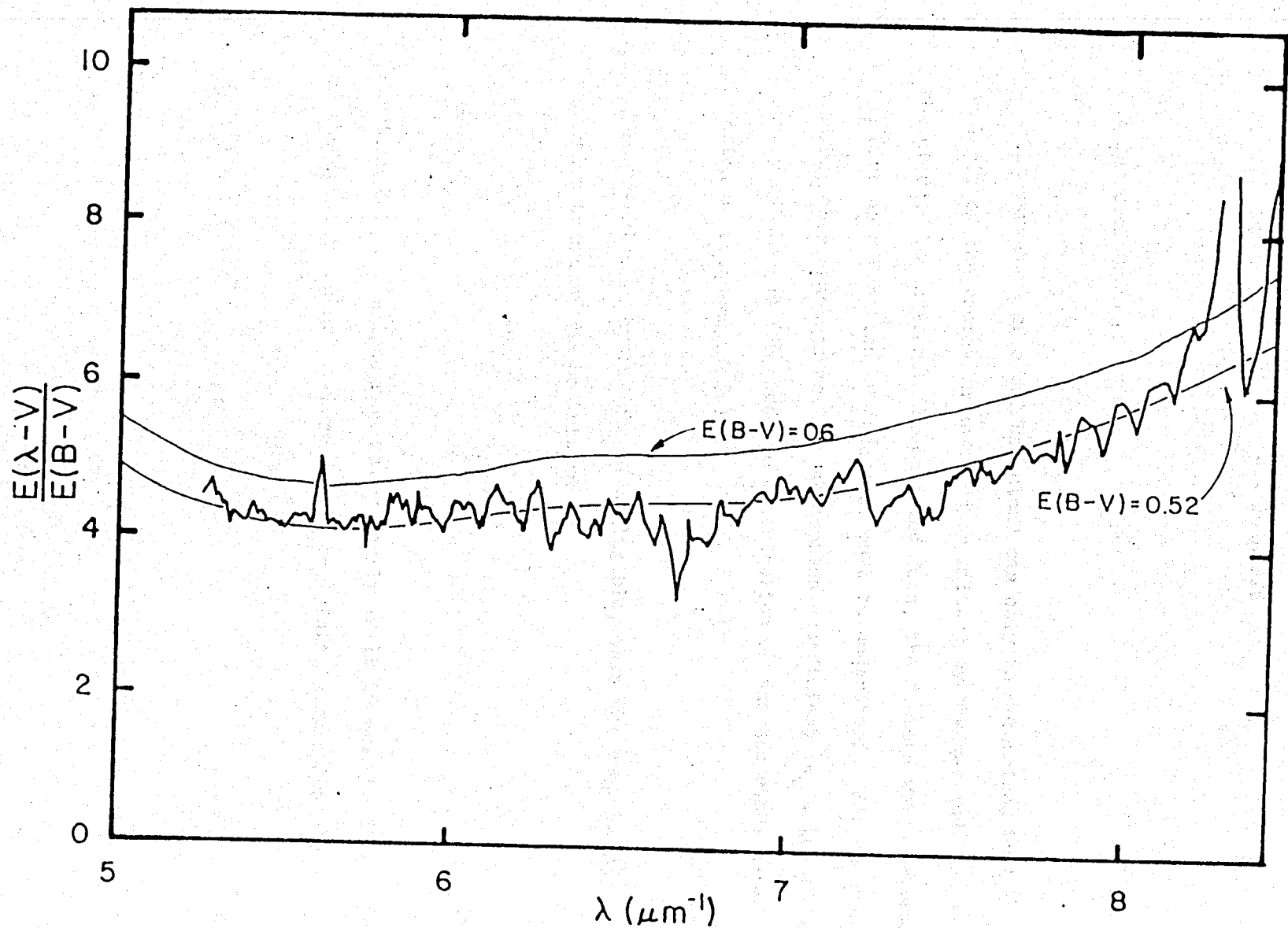


Figure 3-6. Extinction curve for X Per from $5 \mu\text{m}^{-1}$ to $8.5 \mu\text{m}^{-1}$. Also shown are the mean galactic extinction curves for $E(B-V) = 0.6$ and $E(B-V) = 0.52$.

4. ANALYSIS

4.1 Curve of Growth

The structure of a diffuse cloud can only be determined by the analysis of the radiation absorbed or emitted by the gas and dust within the cloud. To interpret the observed data, the factors which determine the flux as a function of frequency must be understood. For absorption studies, these factors are the absorption coefficient (κ_ν), the column density of the gas (N), and the distribution of the absorbers as a function of frequency ($\phi(\nu)$).

If re-emission by the gas is negligible, then the equation of radiative transfer can be written as

$$\frac{dI_\nu}{ds} = -\kappa_\nu I_\nu \quad (4-1)$$

Equation 4-1 can be integrated very easily if it is expressed in terms of the optical depth, τ , where $d\tau = \kappa_\nu ds$. This integration yields

$$I_\nu(\tau_\nu) = I_\nu(0) e^{-\tau_\nu} \quad (4-2)$$

where

$$\tau_{\nu} = \int_0^x \kappa_{\nu} ds \quad (4-3)$$

The absorption coefficient can be rewritten as

$$\kappa_{\nu} = nS_{\nu} = n(\phi_{\nu})S_0 \quad (4-4)$$

where n is the volume density of the absorber, S_0 is the atomic absorption coefficient, and $\phi(\nu)$ is the normalized line profile ($\int \phi(\nu) d\nu = 1$). In terms of basic atomic parameters,

$$\int \kappa_{\nu} d\nu = \frac{\pi e^2}{mc} fn = n \int S_{\nu} d\nu = nS_0 \int \phi_{\nu} d\nu \quad (4-5)$$

Thus

$$S_0 = \frac{\pi e^2}{mc} f \quad (4-6)$$

where f is the oscillator strength, and the other symbols have their usual meaning. Finally, the optical depth, τ_{ν} , can be rewritten in terms of the column density, N :

$$\tau_{\nu} = \int \kappa_{\nu} ds = \int nS_0 \phi_{\nu} ds = S_0 \phi_{\nu} \int n ds = \frac{\pi e^2}{mc} fN\phi_{\nu} \quad (4-7)$$

The normalized observed flux is

$$\frac{I_{\nu}(\tau_{\nu})}{I_{\nu}(0)} = e^{-\frac{\pi e^2 f N \phi_{\nu}}{mc}} \quad (4-8)$$

If $\phi(\nu)$ and $I_{\nu}(0)$ are known, then a measurement of $I_{\nu}(\tau_{\nu})$ can be translated into a column density. Unfortunately, the resolution of most spectrographs is usually not high enough to measure $I_{\nu}(\tau_{\nu})$. However, the equivalent width (W) defined as

$$W_{\nu} = \int \frac{I_{\nu}(0) - I_{\nu}(\tau_{\nu})}{I_{\nu}(0)} d\nu = \int \left(1 - \frac{I_{\nu}(\tau_{\nu})}{I_{\nu}(0)}\right) d\nu = \int (1 - e^{-\tau_{\nu}}) d\nu \quad (4-9)$$

is easy to measure. The equivalent width is usually measured in wavelength units, W_{λ} , where

$$W_{\lambda} = \frac{\lambda^2}{c} W_{\nu} \quad (4-10)$$

To derive the column density from an equivalent width measurement, the frequency distribution function ($\phi(\nu)$) of the absorbers must be known. The three distribution functions normally used in IS studies are the Gaussian or Doppler profile, the Lorentz profile, and the Voigt profile, which is a convolution of a Lorentzian and a Doppler profile. The distribution function for Doppler broadening is

$$\phi_{\nu} = (\sqrt{2\pi} \sigma)^{-1} e^{-\frac{1}{2} \left(\frac{\nu - \nu_0}{\sigma}\right)^2} \quad (4-11)$$

where σ is the dispersion of the gaussian. If σ is written in terms of the velocity (v), and defining $b = \sigma\sqrt{2}$, then

$$\phi_v = (\sigma\sqrt{\pi})^{-1} e^{-\left(\frac{v-v_0}{b}\right)^2} \quad (4-12)$$

b is referred to as the velocity parameter, and k is the conversion factor between velocity and frequency units. The full width at half maximum of a Doppler profile is

$$\text{FWHM} = 2b\sqrt{\ln 2} = 2\sigma\sqrt{2\ln 2} \quad (4-13)$$

The equivalent width is then

$$W = \int \left(1 - e^{-\frac{S_0 N}{b\sqrt{\pi}} e^{-\left(\frac{v-v_0}{b}\right)^2}}\right) dv \quad (4-14)$$

where b has been converted to frequency units. If $\tau_v \ll 1$, the exponent can be expanded, and the integral solved:

$$W_v = \int (1 - e^{-\tau_v}) dv \approx \int \tau_v dv = \frac{S_0 N}{b\sqrt{\pi}} \int e^{-\left(\frac{v-v_0}{b}\right)^2} dv = S_0 N \quad (4-15)$$

In wavelength units,

$$W_\lambda = \frac{\lambda^2}{c} S_0 N = \frac{\pi e^2}{mc^2} N \lambda^2 f \quad (4-16a)$$

$$W_\lambda = 8.85 \times 10^{-21} N f \lambda^2 \text{ (Å)} \quad (4-16b)$$

When $\tau_\nu > 1$, equation 4-14 must be numerically integrated. For very large optical depths, the line profile is saturated in the core, and the broadening mechanism is due to natural broadening (Lorentzian profile) instead of Doppler broadening. The Lorentz line profile is

$$\phi_\nu = \frac{\omega_L/\pi}{(\nu-\nu_0)^2 + \omega_L^2/2} \quad (4-17)$$

where $\omega_L = \Gamma/2$ = FWHM of the Lorentz profile, and

$$\Gamma = t_u^{-1} + t_l^{-1} \quad (4-18)$$

t_u^{-1} and t_l^{-1} are the lifetimes of the upper and lower electronic states, respectively.

For intermediate optical depths, the line profile is the convolution of the Lorentz and Doppler profiles, called the Voigt profile.

Following the development of Armstrong (1967), the Voigt profile is

$$\phi_H(\nu) = 1/\alpha_D \left(\frac{\ln 2}{\pi}\right)^{1/2} H(x,y) \quad (4-19a)$$

where

$$H(x,y) = x/\pi \int_{-\infty}^{\infty} \frac{e^{-t^2}}{(x^2 + (y-t)^2)} dt \quad (4-19b)$$

$$x = \frac{\alpha_L}{\alpha_D} (\ln 2)^{1/2} \quad (4-19c)$$

$$y = \left(\frac{v-v_0}{\alpha_D} \right) (\ln 2)^{1/2} \quad (4-19d)$$

Also,

$$\alpha_D = \text{HWHM} = v_0 / c \{ \ln 2 (2kT/m + V^2) \}^{1/2} \quad (4-19e)$$

The normalization of equation 4-19a is

$$\int_{-\infty}^{\infty} \phi_H(v) d(v-v_0) = 1 \quad (4-19f)$$

The Voigt function, $H(x,y)$, does not have an analytic solution.

However, it does describe the line profile under a wide variety of astrophysical situations. Because of this, a number of methods have been found to efficiently numerically integrate $H(x,y)$ (Whiting, 1968; Penner, 1969; Drayson, 1976; Pierluissi et al. 1977; and Humlicek, 1979). Armstrong (1967) gives a good review of the various forms which are used to approximate $H(x,y)$ and discusses the various computational procedures. To calculate the equivalent width for a Voigt profile, $\phi_H(v)$ must be evaluated at each frequency, which involves an integral from plus to minus infinity. Theoretically, the integral over frequency (equation 4-9) is from zero to infinity. Tabulations of $H(x,y)$ and equivalent widths for various values of x and y have been published (Van de Hulst and Reesinck, 1947; Posener, 1959; Jansson and Korb, 1968).

Rodgers and Williams (1974) and Hill (1979) have parameterized the equivalent width, as a function of N and b , in terms of the expected Doppler and Lorentz equivalent widths (Rodgers and Williams, 1974) or in terms of the optically thin limit (Hill, 1979). These tabulations are only useful if the absorbing region can be parameterized by a single value of x (equation 4-19b).

Towards X Per, the Mg I curve of growth suggests that the neutral magnesium has more than one velocity parameter, hence tabulated values for either the equivalent width or the normalized line profile cannot be used. Equation 4-19a must then be numerically integrated. A very clever empirical approximation to the Voigt profile has been developed by Whiting (1968). He found that the normalized Voigt profile could be characterized by a linear function of the Doppler and Lorentz profiles. A least-squares fit to the tabulated data of Posener (1959) showed that the normalized line profile can be written as

$$\frac{I(\lambda)}{I(0)} = (1 - \omega_L/\omega_D) e^{-2.772 \left(\frac{\lambda - \lambda_0}{\omega_V}\right)} + \omega_L/\omega_D (1 + 4 \left\{ \frac{\lambda - \lambda_0}{\omega_V} \right\}^2)^{-1} \quad (4-20)$$

$$+ 0.016 (1 - \omega_L/\omega_D) (\omega_L/\omega_D) e^{-0.4 \left(\frac{\lambda - \lambda_0}{\omega_V}\right)^{2.25}} - 10 \left(10 + \left\{ \frac{\lambda - \lambda_0}{\omega_V} \right\}^{2.25} \right)^{-1}$$

Equation 4-20 approximates the true Voigt profile to better than 5%.

For convenience, I will rewrite the important definitions:

$$\omega_L = \frac{\Gamma/2\pi}{c \times 10^{13}} \lambda^2 \quad (\text{\AA}) \quad (4-21a)$$

$$\omega_D = 2\sqrt{\ln 2} \ b \ \lambda_o / c \quad (4-21b)$$

$$\omega_V = \frac{1}{2} (1.0692\omega_L + \sqrt{0.86639\omega_L^2 + 4\omega_D^2}) \quad (\text{\AA}) \quad (4-21c)$$

$$I_{\lambda_o} = \frac{\pi e^2}{mc} Nf \ (\omega_V \{1.065 + 0.447 \ \omega_L / \omega_V + 0.058 \{ \omega_L / \omega_V \}^2\})^{-1} \quad (4-21d)$$

The number 2.772 is $(2\sqrt{\ln 2})^2$, and comes from changing b to ω_V . The number 1.065 is $\pi/2\sqrt{\ln 2}$.

In the limit $\omega_L = 0$,

$$I_{\lambda} = \frac{\pi e^2}{mc} \frac{Nf}{b\sqrt{\pi}} e^{-\left(\frac{\lambda - \lambda_o}{b}\right)^2} \quad (4-22)$$

If $\omega_V = \omega_L$,

$$\frac{I_{\lambda}}{I_{\lambda_o}} = \left(1 + 4 \left(\frac{\lambda - \lambda_o}{\omega_V}\right)^2\right)^{-1} \quad (4-23)$$

This is equivalent to equation 4-17:

$$\phi(v) = \frac{\omega_L}{2\pi (\lambda - \lambda_0)^2 + (\omega_L/2)^2} \quad (4-24a)$$

$$\phi(v) = \frac{1}{\pi} \frac{1}{\omega_L/2} \frac{1}{(1 + \frac{(\lambda - \lambda_0)^2}{(\omega_L/2)^2})} \quad (4-24b)$$

$$\phi(v) = \frac{1}{\omega_L/2} \left| 1 + 4 \left(\frac{\lambda - \lambda_0}{\omega_L} \right)^2 \right|^{-1} \quad (4-24c)$$

and $1/(\omega_L \pi/2)$ is absorbed into $\phi(v)$ to form I_λ/I_0 . In fact, the constant in the denominator when $\omega_V = \omega_L$ is $\omega_L \pi/2 = 1.57 L$.

I have compared the equivalent widths derived from equation 4-20 with very accurate published tables of equivalent widths (Jansson and Korb, 1968). Figure 4-1 shows the curve of growth from Jansson and Korb (filled circles) and the curve of growth calculated from equation 4-20 for FWHM = 2km/s ($b = 1.2$ km/s). The agreement is excellent. I have used equation 4-20 for all line profile calculations.

The curve of growth is a graphical representation of the relationship between the equivalent width and the column density of the material along the line of sight. The unknown parameters are the column density and the line broadening parameter. An important step in this work is the use of the radio line widths of CO and OH to infer the form of the line profile. A series of curves of growth can be constructed by numerically integrating equation 4-9 for various velocity parameters. Figure 4-2 is an example of the results for $b = 10$ km/s and $b = 1$ km/s.

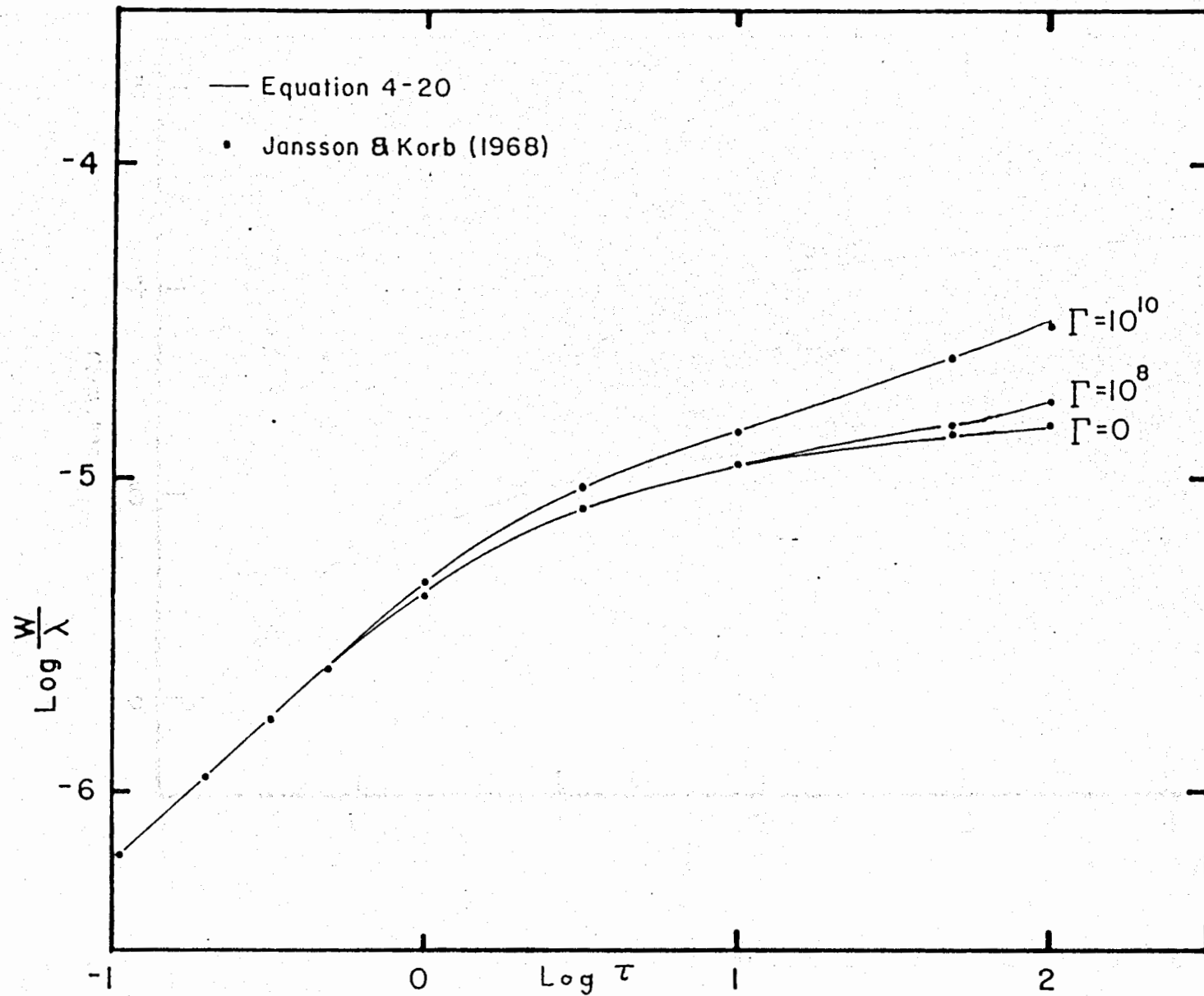


Figure 4-1. Comparison between the curves of growth calculated from equation 4-20 and published equivalent widths (filled circles). Three different damping parameters are shown.

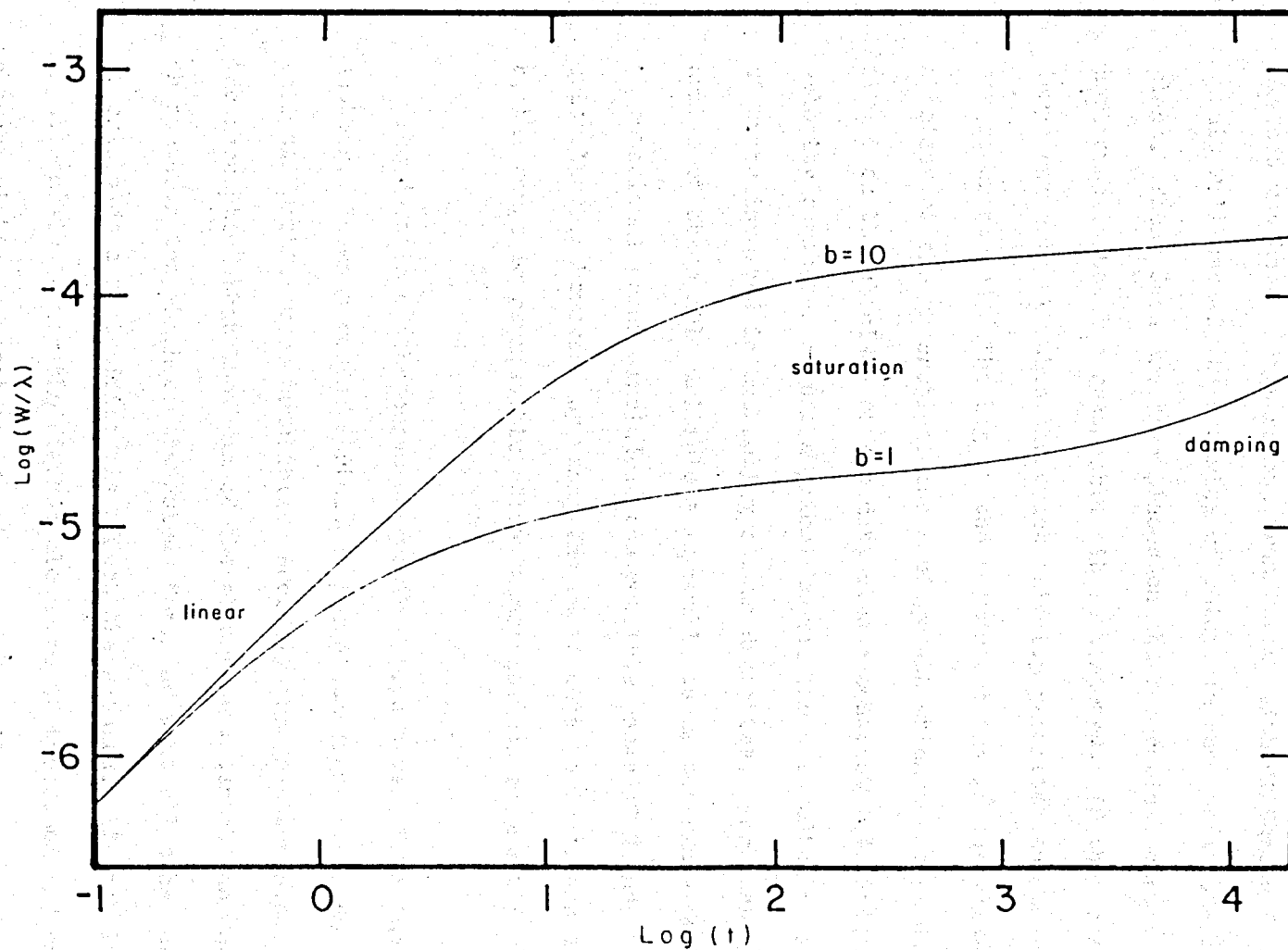


Figure 4-2. Theoretical curves of growth for velocity parameters of $b = 1$ km/s and $b = 10$ km/s. A damping constant of 10^7 s^{-1} was used.

To use a curve of growth, the observational points are plotted as $\log(f\lambda)$ on the abscissa, and $\log(W/\lambda)$ on the ordinate. Since a given element may have more than one transition, with differing f values, the result will usually be a series of points in the $\log(W/\lambda) - \log(f\lambda)$ plane. These data are then placed on the theoretical curves and slid horizontally until a reasonable fit is achieved. If the data have a large range in $f\lambda$, then the exact velocity parameter and column density can be extracted. The log of the column density is the value on the abscissa of the theoretical curve of growth which corresponds to $\log f\lambda = 0$ on the abscissa of the data plus a constant (14.824). Since the velocity parameter is not a priori known, there is often a large amount of error involved in extracting column densities. For most atoms, the number of observable multiplets is small, as is the range of $f\lambda$. With observational errors included, the possible range of N and b are often quite large. However, by using the radio data to constrain the range of b , the range in permissible column densities can be greatly reduced.

The details of the curve of growth analysis vary from one study to another. In many cases, certain ad hoc assumptions are made to make the analysis problem more tractable. Probably the greatest single error is the assumption that the bulk of the absorbing material has one set of characteristics which can be solved for, and that all other absorbing materials do not significantly affect the results. If each line of sight contained only the diffuse cloud and if the cloud had one characteristic temperature, density, and Maxwellian velocity distribution, then the extraction of column densities from the curve of

growth would be straightforward. This is usually not the case. As an illustrative example, assume that the diffuse cloud consists of a few smaller cloudlets, each with a different radial velocity and a different velocity parameter. All the cloudlets have the same temperature, density, and composition. As long as the total optical depth from all clouds is small, the total equivalent width is the sum of the equivalent widths from each cloud. However, as the product of the column density and the oscillator strength (Nf) increases, the cloudlets with the smallest velocity parameter will become optically thick and will no longer significantly add to the total equivalent width. Eventually, all the cloudlets will become optically thick, and the total observed equivalent width will remain approximately constant with increasing Nf . If the difference in radial velocities of the cloudlets is greater than or equal to the FWHM of the cloudlets, then the observed velocity parameter is just the sum of the individual velocity parameters. If the velocity spacing between the cloudlets is less than the FWHM, then the effective velocity parameter will be intermediate between the sum of the individual b values and the largest single b value. This was quantified by York (1975b), who showed the effects of varying the separation between the cloudlets and of varying the amount in each cloudlet. Although York (1975b) calculated the resultant curve of growth for a variety of velocity parameters, all the cloudlets for each model had the same velocity parameter. Figure 4-3 shows a theoretical curve of growth assuming that 95% of the material has a velocity parameter of 1 km/s, the other 5% having $b = 10$ km/s. Qualitatively, Figure 4-3 can be described as two normal curves of growth, with the one with $b = 10$ km/s

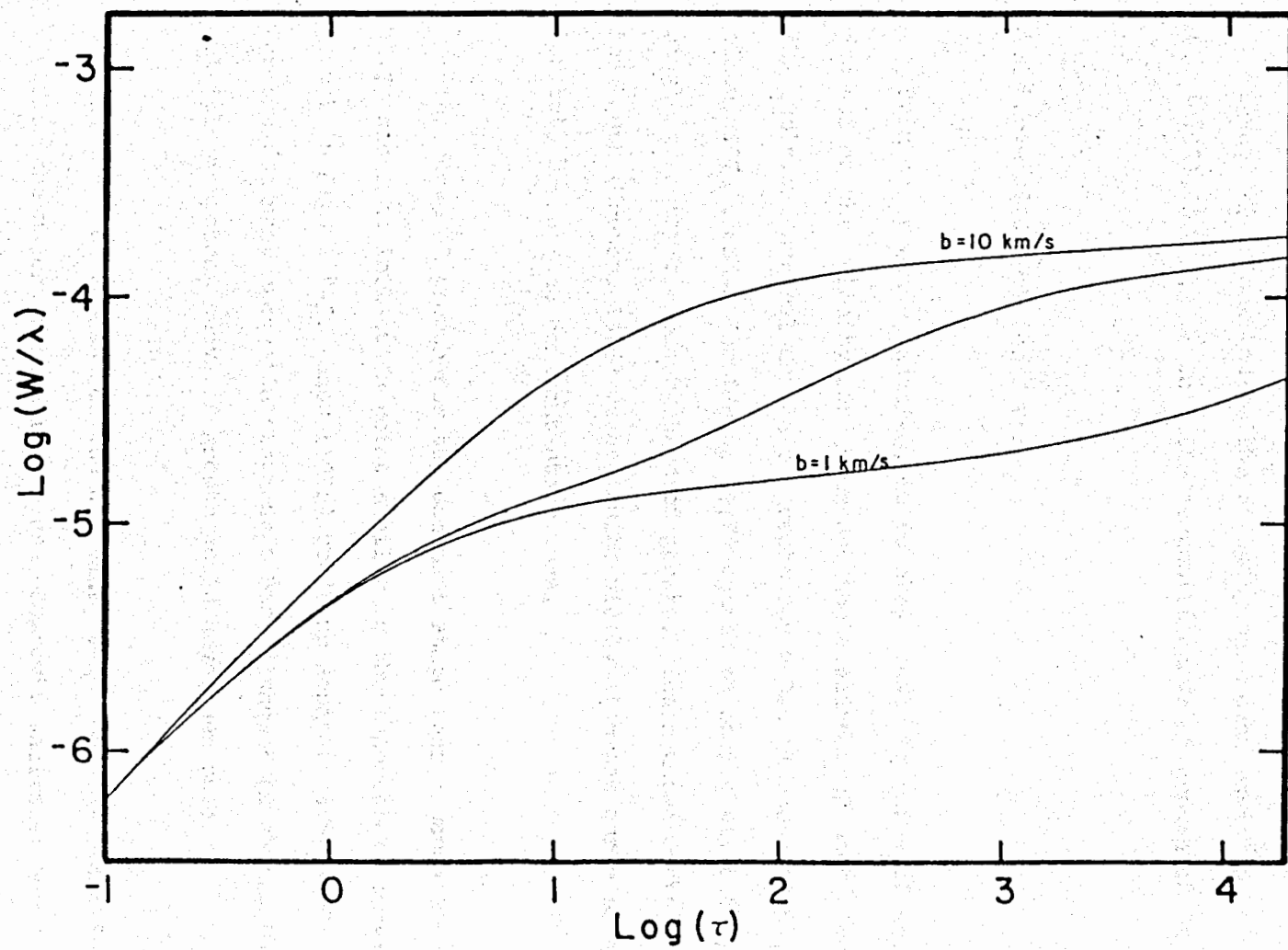


Figure 4-3. The same as Figure 4-2, along with a 95/5 curve of growth.

shifted to the right by an amount approximately equal to the inverse of the log of the fraction in the 10 km/s component. The 10 km/s component in Figure 4-2 is shifted to the right by an amount equal to $(\log(0.05))^{-1} = 1.3$ to form the composite curve of growth of Figure 4-3.

4.2 Curve of Growth for X Per

From the previous section, it is clear that the curve of growth depends on the velocity parameter and the abundance of each cloudlet. The empirical neutral curves of growth for ζ Oph (Morton, 1975), \circ Per (Snow, 1976), and ζ Per (Snow, 1977) cannot be completely fit by a single velocity component curve of growth. The neutral curve of growth for ζ Oph (Morton, 1975) meshes quite nicely with the curve of growth for both H_2 and the dominant stage ions.

The curve of growth for the dominant stage ions towards ζ Per (Snow, 1977) shows an inflection point similar to the theoretical curve of growth in Figure 4-3. Snow (1976) used two separate curves of growth for the dominant stage ions towards \circ Per, although he stated that a multiple component curve of growth could have been used.

The curve of growth for the dominant stage ions towards \circ Per typifies the major problem in a curve of growth analysis: how to identify the existence of a multiple velocity parameter component curve of growth. To completely identify the curve of growth in Figure 4-3,

four points are needed: one on the linear portion of the 1 km/s component, one on the saturated part of the 1 km/s component, one on the linear part of the 10 km/s component, and the last one on the saturated part of the 10 km/s component. This corresponds to a range in $f\lambda$ of five orders of magnitude. Excluding forbidden lines, none of the elements observable with the IUE have this range in $f\lambda$. This is a major problem, because the 10 km/s part of the curve of growth in Figure 4-3 is almost indistinguishable from the 10 km/s curve of growth of Figure 4-2. However, the abundances derived from the two curves of growth will vary by a factor of 20! From Figure 4-3, the range in $\log(W/\lambda)$ covered by the saturated part of the 1 km/s component is very small; hence the probability of a particular line being within this range is small. For example, Snow (1976) found that the dominant stage ions towards α Per could be fit by two separate velocity parameters of 4 km/s and 9 km/s. In this case, none of the elements which are described by the 9 km/s curve of growth have lines which lie below the saturated part of the 4 km/s curve of growth. None of the elements described by the 4 km/s curve of growth have lines which lie significantly above the saturated part of the 4 km/s curve of growth, although the Fe II curve of growth appears to turn off the saturated part of the 4 km/s curve of growth.

An important question in determining the proper curve of growth is the spatial distribution of the material with the different velocity parameters. For example, the line of sight towards stars with relatively little reddening show $b \approx 6-15$ km/s, which suggests that perhaps the intercloud medium contributes to the curve of growth.

Assuming $n_H = 0.1 \text{ cm}^{-3}$, then $n_H(\text{ICM}) = 1.1 \times 10^{20} \text{ cm}^{-2}$ towards X Per (360 pc, Blaauw, 1954). Assuming $n_H = 5.6 \times 10^{21} E(B-V)$ (Savage and Mathis, 1979), $n_H(\text{ICM})/n_H = 0.04$ for $E(B-V) = 0.52$. For the line of sight towards X Per then, the curve of growth could be described as being a superposition of the curves of growth for the diffuse cloud and the ICM.

The relative amount of ICM will decrease as the color excess increases, although this is clearly dependent on the distance to the star. If a normal 10 km/s curve of growth is used instead of the multiple component curve of growth, the derived column density will be lower than the true column density, and this difference will increase as the fraction of the material in the ICM decreases. The erroneous conclusion would be that the depletion of all elements increases as a function of color excess.

The problem then is to identify the proper curve of growth to use for each ion of each element. The column density in each component is a convolution of the mass distribution, ionization structure, and depletion of the element. These parameters can change between b-components. Since the distribution of the dominant stage ions closely mimics the mass distribution of the element, then the curve of growth for all the dominant stage ions will be the same. This generalization will not work if the depletions within the different b-components differ between elements. The construction of an empirical curve of growth using the curves of growth for the individual elements is therefore

justified for dominant stage ions.

Figure 4-4a shows an empirical curve of growth for the dominant stage ions towards X Per. The empirical curve of growth can be fit by a theoretical curve of growth with $b = 10$ km/s. The fit is quite good. The only discrepancies are the weak Mn II lines near 1200 \AA . These lines are weak and probably have larger errors than shown due to the sensitivity of the echelle orders and the order overlap problem (cf Appendix B). There is no overlap between the ions which determine the saturated 10 km/s component and the lowest section of the linear part of the curve of growth. This problem is similar to the aforementioned Per curve of growth.

Figure 4-4b shows the curve of growth for Mg I and Cl I. There is a clear indication of multiple velocity parameter components. The solid line through the data is a theoretical curve of growth with $b = 1$ km/s for 95% of the material and $b = 10$ km/s for the other 5%. Henceforth, I will use the notation N/M to denote the percentages in the 1 km/s component (N) and in the 10 km/s component (M). The theoretical curve of growth in Figure 4-4b is a 95/5 curve of growth. I have used a 95/5 curve of growth to extract the equivalent widths of the dominant stage ions. The rest of this section will explain how this choice was made.

The existence of a 10 km/s component to the dominant stage ion curve of growth is evident from Figure 4-4a. Both Fe II and Si II have equivalent widths which lie on both the saturated and linear sections of

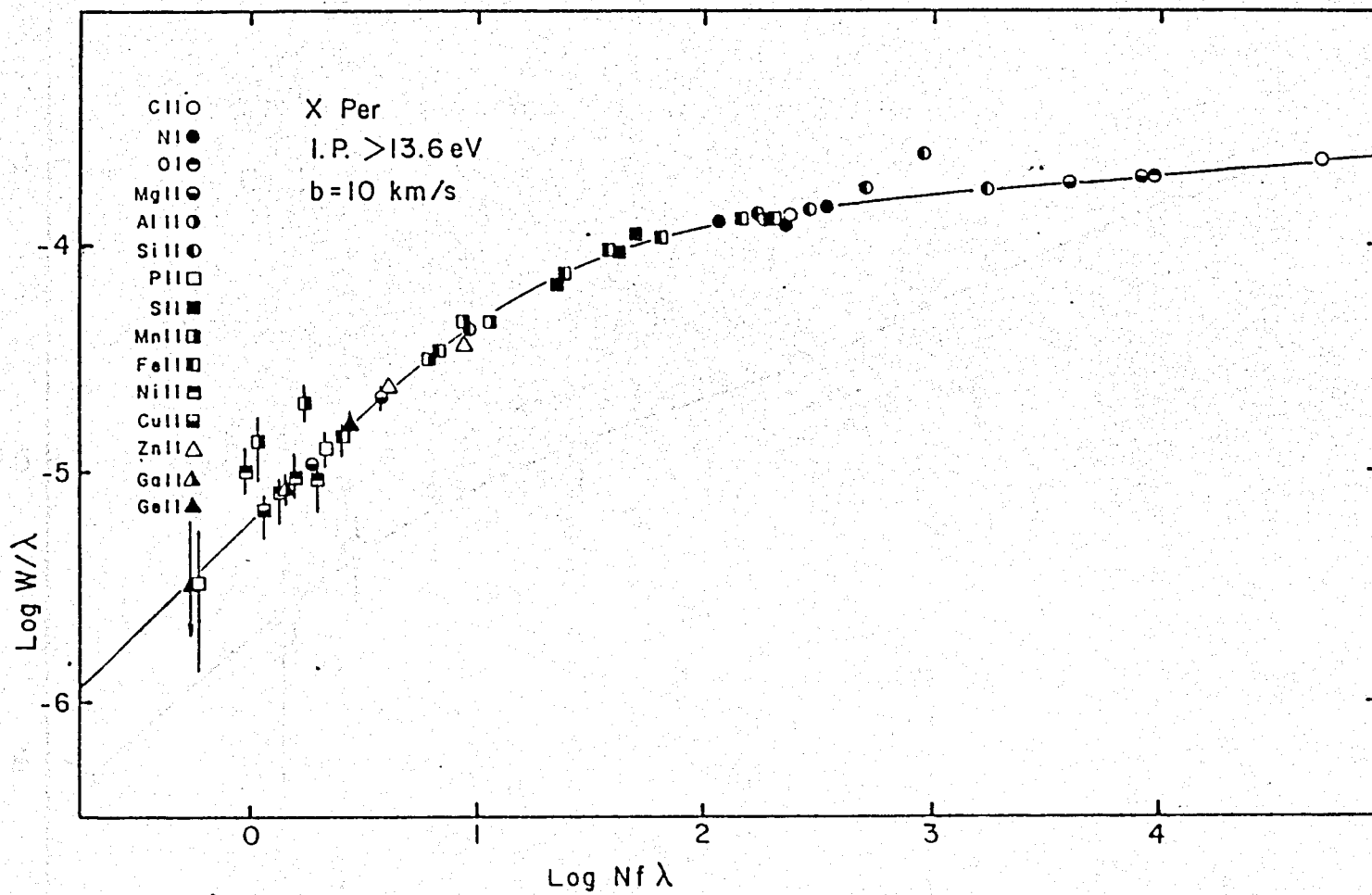


Figure 4-4a. The empirical curve of growth for the dominant stage ions with the condition that they correspond to a 10 km/s curve of growth (line).

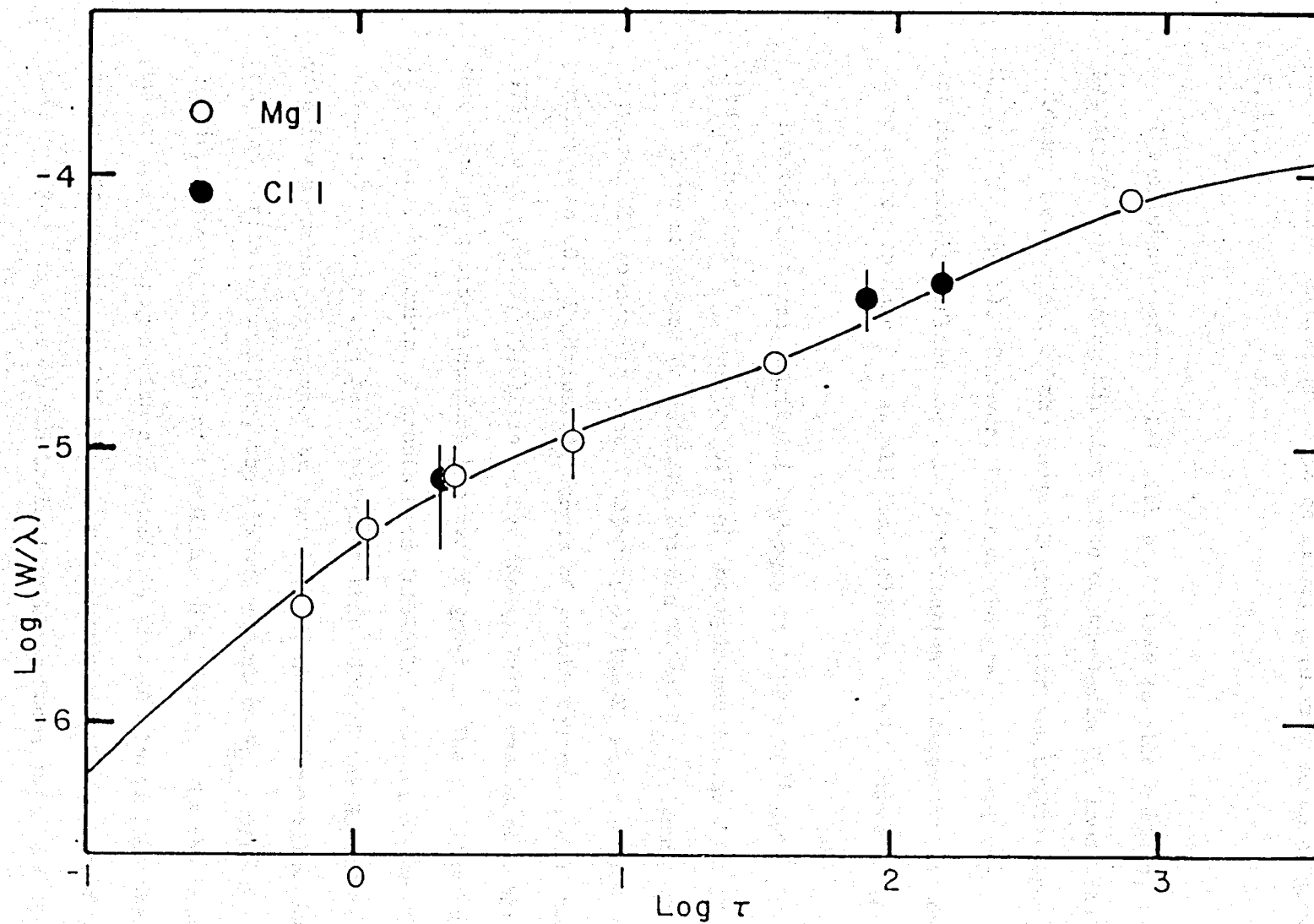


Figure 4-4b. Mg I (open circles) and Cl I (filled circles) curve of growth. The thin line corresponds to a 95/5 curve of growth.

the 10 km/s curve of growth. The empirical curve of growth for the highly ionized species can also be fit by a 10 km/s curve of growth (cf 5.2).

The existence of material with $b = 1$ km/s is also obvious, the primary evidence being the line width of the radio CO lines. Additional evidence is provided by the curve of growth for the neutral species (eg Mg I, Figure 4-4b). However, the distribution of neutral magnesium does not necessarily reflect the mass distribution of magnesium, hence there is no reason to assume that all ions will fit a 95/5 curve of growth.

The total column density of hydrogen is $2.52 \times 10^{21} \text{ cm}^{-2}$ (cf 5.1), with a fraction $f = 2N_{\text{H}_2}/N_{\text{H}} = 0.88$ of the hydrogen in the form of H_2 . Since there is a good correlation between CO and H_2 (Dickman, 1976), it is reasonable to suggest that a majority of the H_2 has the same velocity parameter as CO. Empirical H_2 curves of growth towards ζ Oph (Morton, 1975), σ Per (Snow, 1976), and ζ Per (Snow, 1977) cannot be completely described by a single component curve of growth. The published curves suggest that the curve of growth does initially saturate at small velocity parameters. I have estimated that $\approx 80\%$ of the H_2 has the velocity parameter suggested by the curve of growth before the turnoff from saturation. For X Per, the minimum amount of N_{Htot} with $b = 1$ km/s is 70%, assuming that 80% of the H_2 has $b = 1$ km/s. The the total percentage of hydrogen with $b = 1$ km/s is probably larger, as there is atomic hydrogen mixed with the molecular hydrogen. The curve of growth towards X Per can thus be constrained to lie between 70/30 and 100/0.

As the percentage in the 10 km/s component decreases, the range in $f\lambda$ which the saturated part of the 10 km/s curve of growth covers decreases. The maximum curve of growth allowed by the observed $f\lambda$ range of Si II and Fe II is 99/1.

Since sulfur and zinc are generally thought to be undepleted in diffuse clouds, the reverse question can be asked: what fraction must be in the 10 km/s component for these elements to have solar abundances? The answer is 95/5 for S II and 93/7 for Zn II. This line of reasoning is not actually proof, as sulfur and zinc may be depleted.

The Si II curve of growth provides the best evidence for a 95/5 curve of growth. The 1190 Å and 1194 Å lines of Si II have large natural damping constants ($\Gamma \approx 4 \times 10^9 \text{s}^{-1}$), whereas the other lines have $\Gamma < 10^9 \text{s}^{-1}$. Figure 4-5 shows the observed curve of growth for Si II. The solid lines are for a 95/5 theoretical curve of growth. Because of the difference in damping constants, there are two curves of growth: one for the 1190 Å and 1194 Å lines and the second for all the other lines. The damping part of the curve of growth is relatively unaffected by the contributions from different b-components, and hence the column density of Si II is determined by the strengths of the 1190 Å and 1194 Å lines. The 1808 Å line of Si II lies on the linear part of the 10 km/s curve of growth. Once the total column density of Si II is set, the theoretical curve of growth must pass through this line. Only a 95/5 curve of growth will fit all the Si II data for the assumed column density. Errors in the oscillator strength of the 1808 Å line result

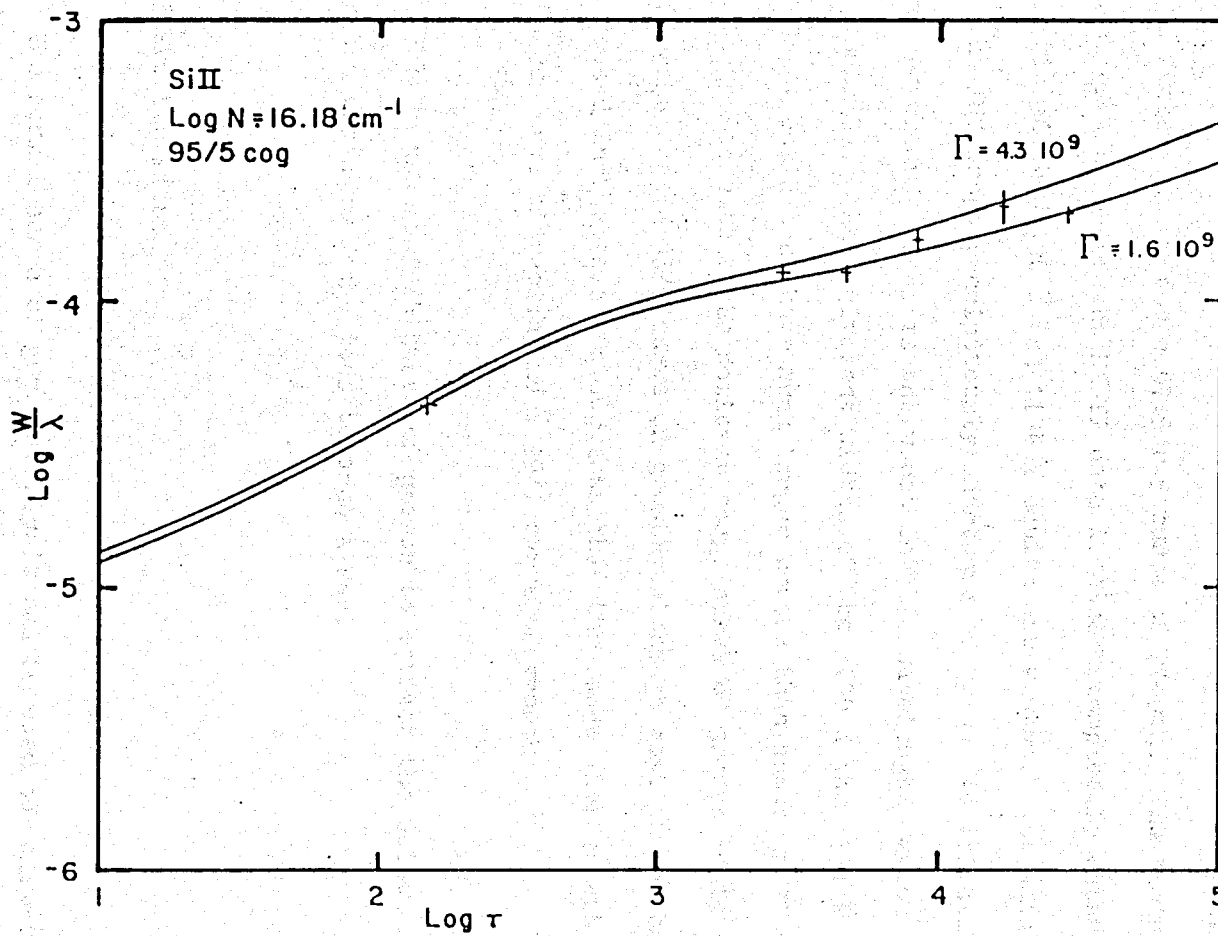


Figure 4-5. 95/5 curve of growth with the empirical Si II curve of growth. The theoretical curve of growth for the two most important damping parameters are shown. The vertical line represents a $2\text{-}\sigma$ variation in the equivalent width.

in a range from 93/7 to 96/4 for the curve of growth. For points which lie on the linear or saturated part of the 10 km/s component of the curve of growth, the column density decreases by a factor of two if the curve of growth is reduced to a 90/10 curve of growth, and it increases by a factor of two for a 97.5/2.5 curve of growth. The choice of a 95/5 curve of growth for the Si II data is almost completely determined by the fit of the 1190 Å and 1194 Å equivalent widths. The sensitivity of the IUE drops precipitously shortward of Ly α . Additionally, the order-overlap problem is the worst in this wavelength region (cf Appendix B). The equivalent widths of the 1190 Å and 1194 Å lines of Si II could thus have much larger errors than shown in Figure 4-5. It is possible that the dominant stage curve of growth could be very different from a 95/5 curve of growth, although most of the data presented in this section suggests that the range lies somewhere between a 80/20 curve of growth and a 99/1 curve of growth.

I have used a 95/5 curve of growth to extract the column densities for the dominant stage ions towards X Per.

4.3 Profile Fitting

The normal curve of growth analysis can be used to extract the column density of an element as long as the line(s) being used in the analysis are free of overlapping absorption from another line of the same multiplet or another element. In cases where more than one line

lies within one resolution element of the spectrograph, other methods must be used to derive the column density. I will not address the general problem of overlapping absorption lines from different species. Rather, I will briefly describe what can be done when the overlap is due to lines within a given multiplet having an intrinsically small separation (C I), or due to the rotational structure of simple molecules (CO, C₂).

The ground state of the neutral carbon atom is split into three fine-structure components. The two upper levels are separated by an equivalent energy of 24 K and 63 K for J=1 and J=2 respectively. For a given multiplet of carbon, many of the fine structure lines are blended, not only with lines arising from the same level, but often with lines arising from a different level. The level populations are determined by the temperature and density of the cloud (Bahcall and Wolf, 1968; de Boer and Morton, 1974; Smeding and Pottasch, 1979). Since the relative populations are not initially known, the curve of growth method will not yield useful results. However, the overlap can be explicitly handled by calculating what the line profile would look like under different physical conditions.

If the separation between successive rotational lines in a molecular band is equal to or less than the resolution of the spectrograph, then the individual rotational lines will be blended together, unless only the lowest rotational level is populated. The wavenumber of a rotational line is (Herzberg, 1950)

$$\nu = T'_e + G'(v') + F'(J') - T''_e - G''(v'') - F''(J'') \quad (4-25)$$

The difference between successive Q branch rotational lines is

$$\Delta\nu = F'(J+1) - F''(J+1) - \{F'(J) - F''(J)\} \quad (4-26)$$

Since $F(J) = B J(J+1)$, equation 4-26 can be rewritten as

$$\Delta\nu = 2(J+1)(B' - B'') \quad (4-27)$$

The rotational lines in the vibrational band will be unresolved for

$$|B' - B''| < (2R \lambda (J+1) \times 10^{-8})^{-1} \quad (4-28)$$

where R is the resolution of the spectrograph, and λ is in Angstroms.

$\Delta\lambda = |B' - B''| = 0.32$ for the (0-0) band of the A-X transition of CO. The SWP spectrograph has a resolution of 1.2×10^4 , hence the righthand side of equation 4-28 is 1.39. The vibrational band is not resolved into rotational lines, as observed. For C_2 , the Q branch does not exist ($\Sigma - \Sigma$ transition), and since the nuclear spin of the carbon atom is zero, odd J levels do not exist. The difference between the R(0) and R(2) line can be found by substituting the appropriate J' and J'' in equation 4-26. The left hand side of equation 4-28 will then be $10B' - 6B'' = 7.3 \text{ cm}^{-2}$ for the (0,0) band of the D-X transition and $10B' - 6B'' = 6.5 \text{ cm}^{-2}$ for the (0,0) band of the F-X transition. The corresponding values

for the spectrograph are 3.3 cm^{-2} and 6.2 cm^{-2} , respectively. The D-X transition is resolvable, whereas the F-X transition is almost resolvable.

The physical parameters needed to calculate a theoretical line profile are the velocity parameter (b), the column density of each level (N_i), and the instrumental response function. Appendix B discusses the instrumental response function. Given that b and N_i are known for all levels, the optical depth (τ_i) can be calculated using the methods described in section 4.1. The normalized line profile is then $\exp(-\Sigma\tau_i)$ at each wavelength. The separation between adjacent wavelength steps is less than or equal to one tenth the dispersion of the line profile ($b/2$). The theoretical profile is then convolved with the instrumental response function, and the result is plotted.

Figure 4-6 shows examples of the theoretical, convolved and observed line profiles for the 1657 \AA multiplet of C I (Figure 4-6a), the 3-0 vibrational band of CO at 1477 \AA (Figure 4-6b), and the 0-0 vibrational band of C_2 at 1341 \AA (Figure 4-6c).

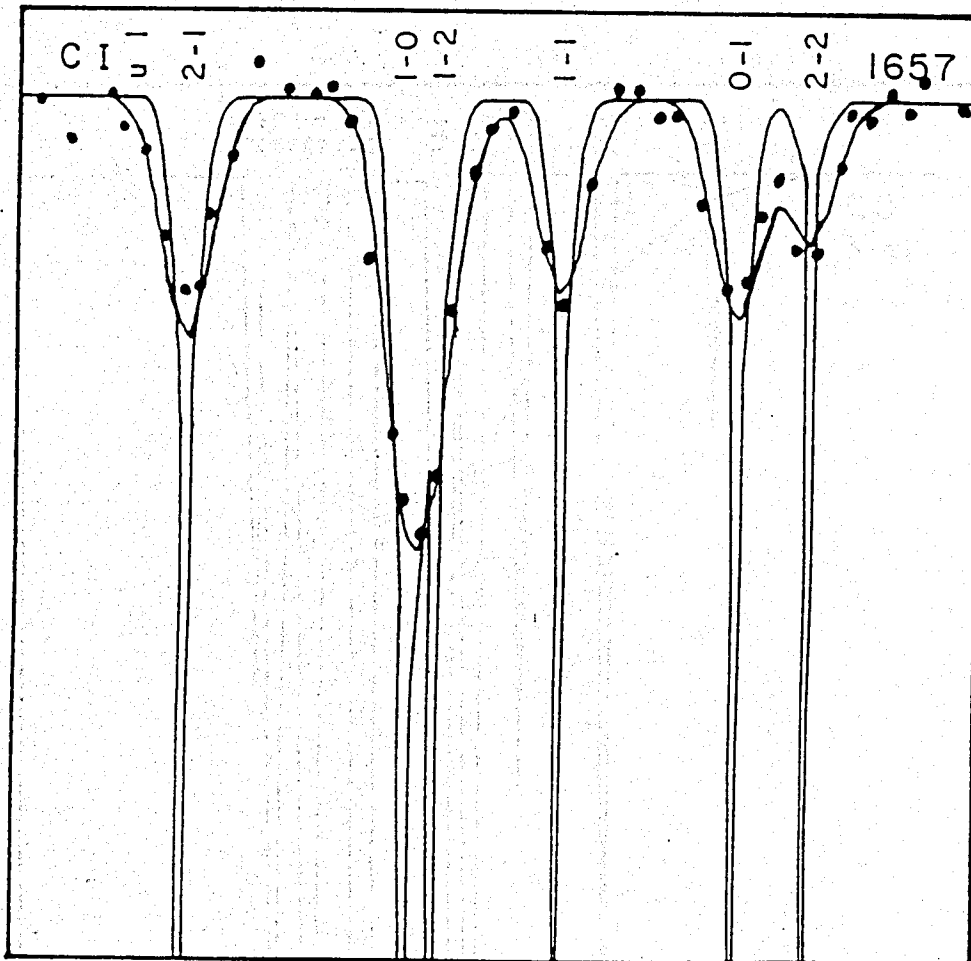


Figure 4-6a. Theoretical, convolved and observed (filled circles) line profiles for the 1657 Å multiplet of C I. The individual transitions are labeled with the upper and lower J value.

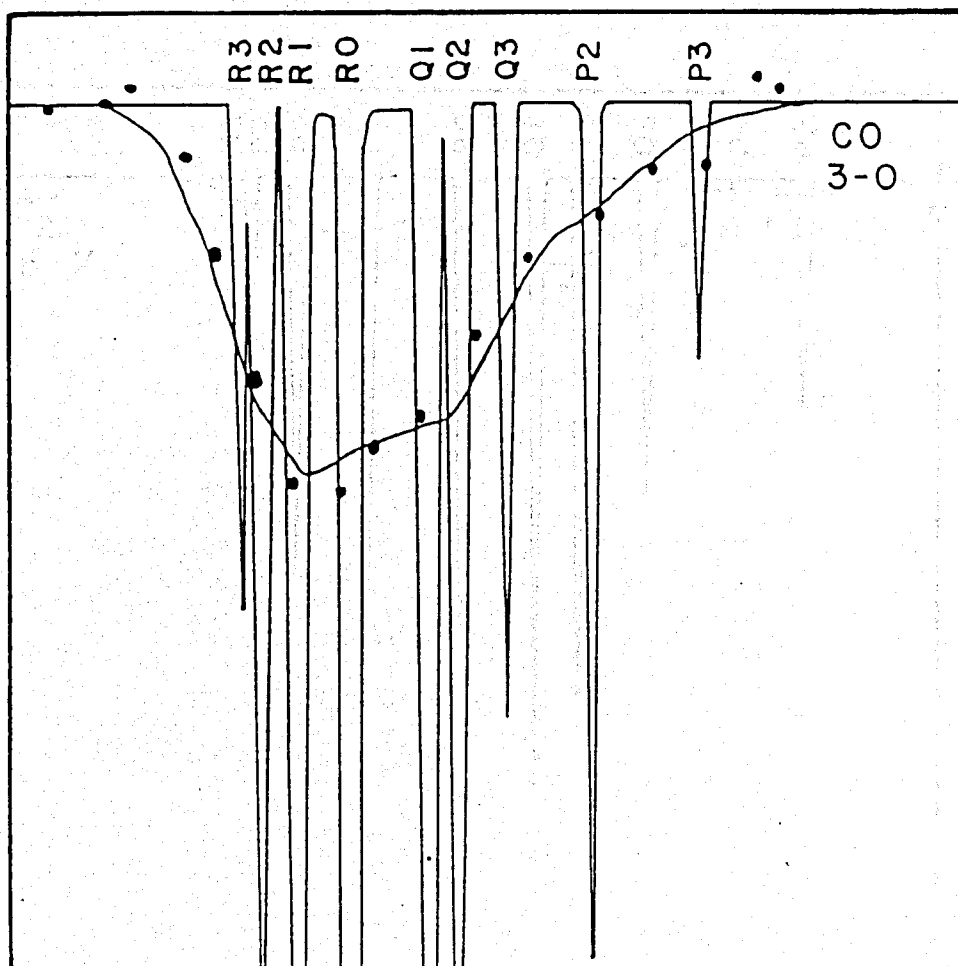


Figure 4-6b. The same as Figure 4-6a, except for the 3-0 band of the A-X system of ^{12}CO .

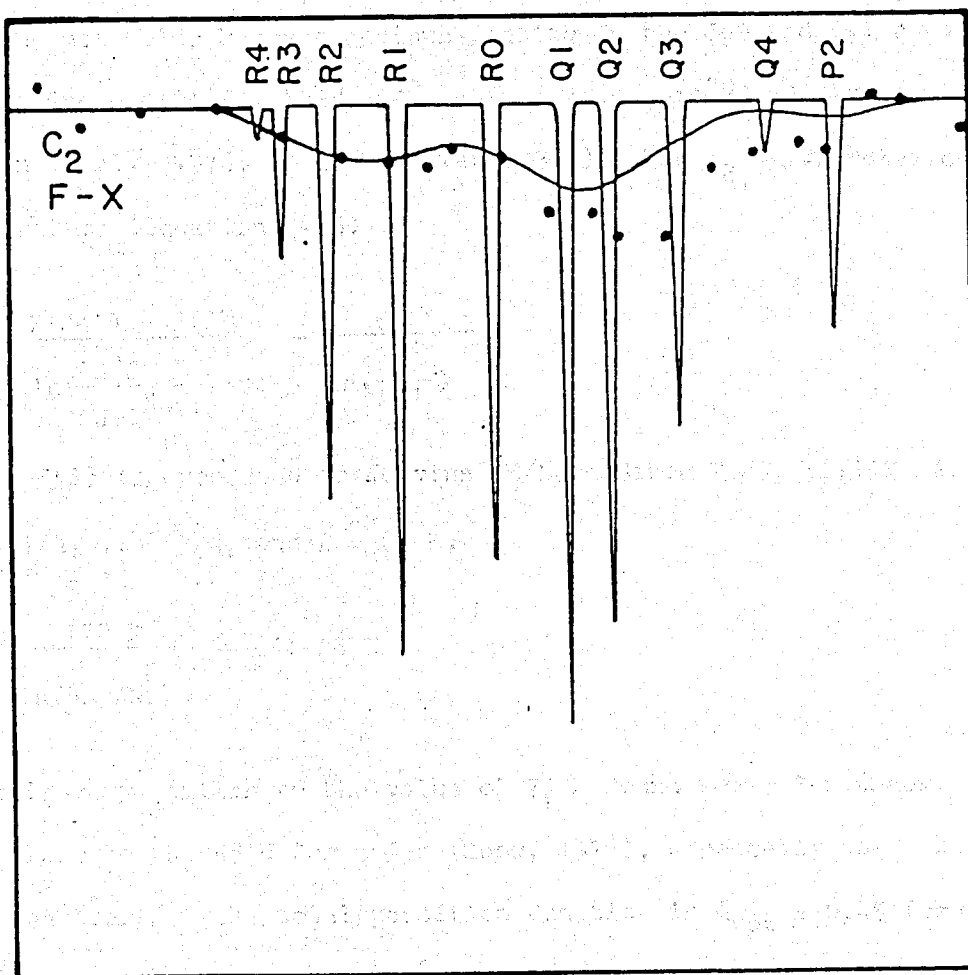


Figure 4-6c. The same as Figure 4-6a, except for the 0-0 vibrational band of the F-X electronic system of C_2 .

5. OBSERVATIONAL RESULTS

5.1.1 Hydrogen

The molecular hydrogen column density in the $J=0$ and $J=1$ rotational levels are $6.0 \pm 1.5 \times 10^{20} \text{ cm}^{-2}$ and $5.0 \pm 1.5 \times 10^{20} \text{ cm}^{-2}$, respectively (Mason et al. 1976; cf 3.4 and Table 3-9). The H_2 $J=1-0$ rotational temperature (equation C-16) is

$$T = \frac{F(J+1) - F(J)}{\ln\left(\frac{\phi_J N_J}{\phi_{J+1} N_{J+1}}\right)} = \frac{F(1)}{\ln\left(\frac{\phi_0 N_0}{\phi_1 N_1}\right)} \quad (5-1)$$

where $F(J)$ is expressed in Kelvins (E/k). Since $F(J)=J(J+1)B=2B$,

$\phi_0 = 1/4$, $\phi_1 = 3/4$, and $B = 85 \text{ K}$,

$$T = \frac{170 \text{ K}}{\ln(9N_0/N_1)} = 71 \pm 8 \text{ K} \quad (5-2)$$

This is very similar to the value of 75 K found for ζ Per (Snow, 1977) and close to the 48 K for \circ Per (Snow, 1976), especially when the errors are considered. The total partition function is $Q_{\text{rot}} = 0.45$ (equation C-9), of which less than 0.1% comes from $J=2$ and above. The total column density is then just the sum of the $J=0$ and $J=1$ rotational levels: $N_{\text{H}_2} = 1.1 \pm 0.2 \times 10^{21} \text{ cm}^{-2}$.

The neutral atomic hydrogen column density is $3.2 \pm 0.2 \times 10^{20}$ cm^{-2} from my IUE data, and $2.0 \pm 0.5 \times 10^{20}$ cm^{-2} from Mason et al. (1976). For my data, the major uncertainty is the placement of the continuum, which is difficult to ascertain due to the rapidly changing response of the detector near 1215 \AA and the echelle blaze response. However, my data has a higher S/N (≈ 50) than the measurement of Mason et al. (1976; S/N ≈ 10). If the atomic hydrogen 21 cm line is optically thin, then $N_{\text{H I}} = 7.5 \pm 0.5 \times 10^{20}$ cm^{-2} (Sancisi et al. 1974). The optical depth in the 21 cm line implied by my UV measurements is (Spitzer, 1978)

$$\tau = 5.49 \times 10^{-14} \frac{N(\text{HI})}{T_e \sigma \sqrt{\pi}} = 0.14 \quad (5-3)$$

for $\sigma = 0.94 \text{ FWHM}$, $\text{FWHM} = 10.0$ km/s, and $T_e = 70$ K. The 21 cm line is therefore optically thin.

The equivalent width of Ly α is large enough that the column density is independent of the velocity parameter, or any combination of velocity parameters as long as the maximum b is less than about 50 km/s. Thus, material in the 1 km/s component is not "hidden" in the 10 km/s component. The equivalent width corresponding to the radio H I column density is 23 \AA . Even with a large error in the continuum, the equivalent width of Ly α is $\lesssim 20 \text{ \AA}$. Since only the column density was published, and not the profile, I assume that the factor of two difference between the column densities is either due to errors in the radio analysis or due to H I behind X Per. Clumping within the radio

beam could also increase the observed 21 cm hydrogen column density. I will use the hydrogen column density derived from my UV measurements of Ly α ($\log N_{\text{H I}} = 20.51 \text{ cm}^{-2}$).

The total hydrogen column density is

$$N_{\text{H}} = N_{\text{H I}} + N_{\text{H}_2} = 2.52 \pm 0.3 \times 10^{21} \text{ cm}^{-2} \quad (5-4)$$

and

$$f = \frac{2N_{\text{H}_2}}{N_{\text{H}}} = 0.87 \pm 0.10 \quad (5-5)$$

The average total hydrogen column density is (Savage and Mathis, 1979)

$$N_{\text{H}} = \frac{5.8 \times 10^{21}}{E(B-V)} \text{ cm}^{-2} \text{ mag}^{-1} = 3.0 \times 10^{21} \text{ cm}^{-2} \quad (5-6)$$

for $E(B-V) = 0.52$ (cf 3.5)

If the average hydrogen volume density in the ICM is 0.1 cm^{-3} (Myers, 1978), then the column density of atomic hydrogen towards X Per is ($D = 360 \text{ pc}$, Blaauw, 1950) $n_{\text{H}} = 1.1 \times 10^{20} \text{ cm}^{-2}$. One-third of the atomic hydrogen may be in the ICM.

Limits on the velocity parameter of the H_2 can be inferred from the CO data. Dickman (1976) has shown that CO is a good tracer of H_2 , hence it is reasonable to assume that the CO and H_2 velocity parameters should be similar. Observationally however, the H_2 has a larger velocity parameter than both the CO and the neutral elements. For example, the data towards ζ Oph (Morton, 1975) are $b(\text{CO}) = 0.9$ km/s (Crutcher, 1976), $b(\text{neutrals}) = 0.9$ km/s, and $b(H_2) = 3.8$ km/s. A similar pattern exists towards σ Per (Snow, 1976), where $b(\text{CO}) = 0.9$ km/s (Crutcher, 1974), $b(\text{neutrals}) = 1.5$ km/s, and $b(H_2) = 3.0$ km/s. It is possible that more than 50% of the H_2 can have $b=b(\text{CO})$ without causing a major shift in the curve of growth.

The result of this section is that the total column density of hydrogen towards X Per is $2.5 \pm 0.3 \times 10^{21}$ cm^{-2} , with $\approx 90\%$ of the hydrogen in the form of H_2 . The velocity parameter of the H_2 is assumed to be the same as the velocity parameter of the CO ($b = 1$ km/s), although higher velocity parameters are not ruled out. The atomic hydrogen has $b \approx 8-10$ km/s, with smaller velocity parameters also possible.

5.2 Highly Ionized Species

Absorption lines of C IV, Si III, Si IV S III, and Al III were observed. The previous ionization stage of all of these ions have ionization potentials greater than 13.6 eV. Figure 5-1 shows the empirical curve of growth derived from the observations, along with a theoretical curve of growth with $b = 10$ km/s. The empirical curve of growth was derived by finding the smoothest curve which fit all the data, particularly the C IV, Si IV and Al III doublets. Table 5-1 lists the column densities derived from Figure 5-1. The errors were determined by finding the maximum and minimum column densities which fit the 10 km/s curve of growth. The velocity parameter can also have values from 9.5 km/s to 11 km/s and still be consistent with the data.

The equivalent widths of Si III and C IV in Figure 5-1 are weak enough to show the effects of the two component curve of growth shown in Figure 4-3. There is no indication in the data that a curve of growth with more than $\approx 50\%$ of the material having $b = 1$ km/s is needed. If a 50/50 curve of growth were used, the column densities in Table 5-1 would increase by a factor of 2 (0.3 dex).

A number of other lines of sight have Si II and C IV absorption features (Black et al. 1980, hereafter BDHR; Cowie et al. 1981, hereafter CTY) BDHR and CTY point out that if the C:Si:O ratio is solar, then the Si IV and C IV lines are too strong to arise from the same gas which produces the O VI absorption ($T > 10^5$ K).

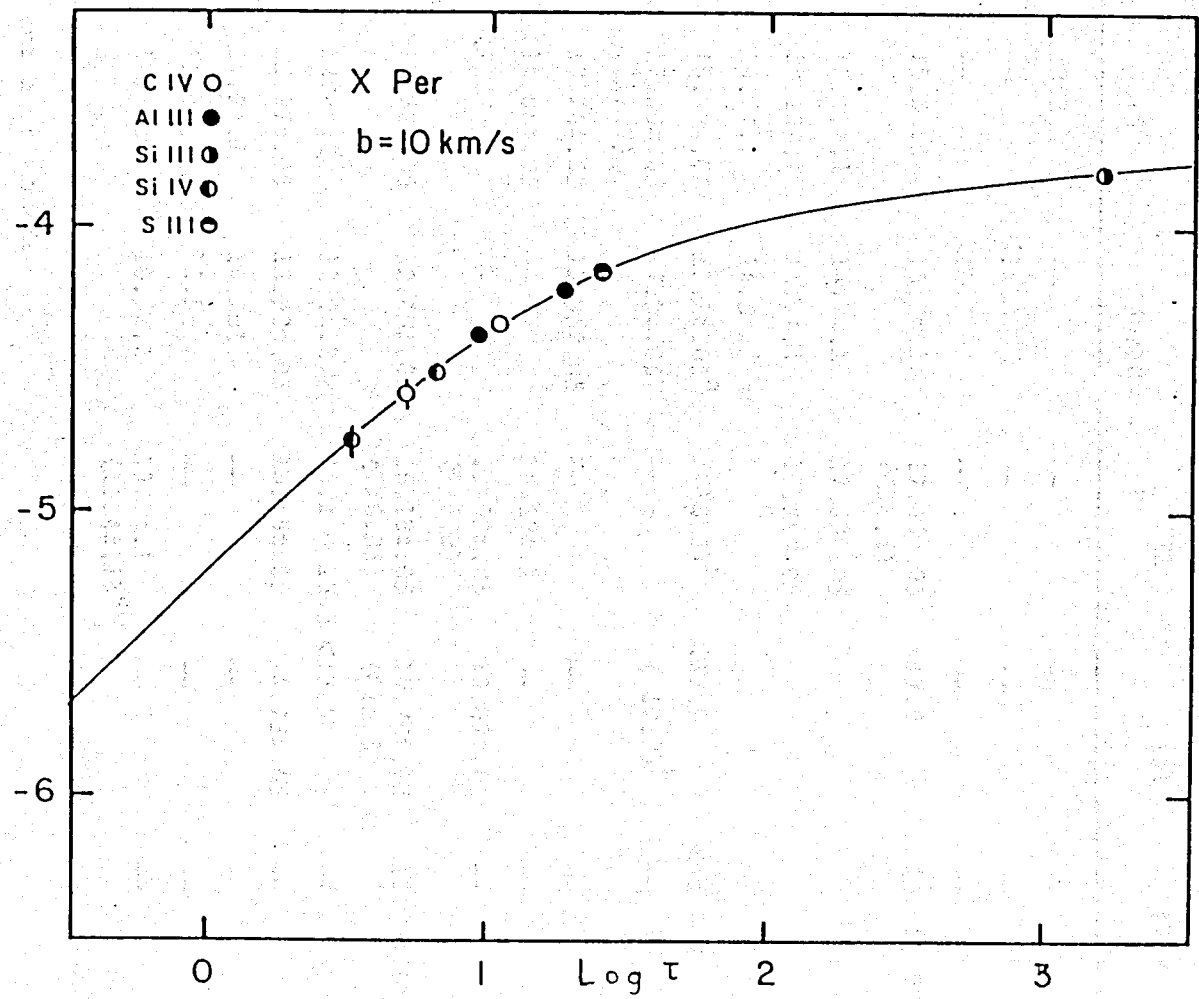


Figure 5-1. Empirical curve of growth for the highly ionized species toward X Per. Also shown is a theoretical curve of growth with $b = 10$ km/s.

TABLE 5-1
ATOMIC COLUMN DENSITIES

Element	Log Column Density (cm^{-2})				
	Ionization Stage				
	95/5	I 90/10	II	III	IV/V
Li	<13.3	—	—	—	—
Be	—	<11.4	—	—	—
B	—	<11.6	—	—	—
C _{Tot}	15.5±.1	15.2±.1	17.65±.05 (<18.5)	<17.9	13.45±.05 IV
C ^o	15.12±.1	14.7±.1	17.63±.05		
C [*]	15.12±.1	14.7±.1	16.25±.05		
C ^{**}	14.7±.1	14.5±.1			
N	16.42±.05	17.1±.05 ^a	(<18.2) ^b	<17.9	<12.3 V
O	17.50±.05 (<17.7)	17.9±.05 ^a	—	(17.7) ^b	—
Na	13.26±.05	12.95±.05	—	—	—
Mg	14.08±.05	—	16.33±.2	—	—
Al	<12.3	—	15.02±.05 (<16.3)	13.07±.05	—
Si	12.72±.05	12.43±.05	16.18±.05 (<16.35)	14.70±.15 (<15.8)	12.85±.05 IV
P	12.4±.2	12.0±.2	14.1 - 13.5	<13.5	—
S	13.92±.05	13.92±.05	16.65±.05	14.75±.08	—
Cl	14.2±.1	14.2±.1	—	—	—
K	12.8±.1	12.5±.1	—	—	—
Ca	10.6±.1	10.6±.1	13.7±.1 (13.4±.1) ^c	—	—

^a100/0 curve of growth

^bLimits derived from fine structure lines

^c90/10 curve of growth

TABLE 5-1 (CONT.)

Element	Log Column Density (cm^{-2})				
	Ionization Stage				
	95/5	I 90/10	II	III	IV/V
Sc	—	—	<11.9	<12.4	—
Ti	—	—	<11.7	12.7 ± .2	—
V	<11.6	—	13.8 ± .15	—	—
Cr	<13.6	—	12.7 ± .25	—	—
Mn	<11.1	—	14.3 ± .1	—	—
Fe	12.32 ± .08	12.32 ± .08	15.58 ± .06	—	—
Co	<11.7	—	<11.5	—	—
Ni	<11.5	—	13.5 ± .2	—	—
Cu	<12.3	—	12.3 ± .1	—	—
Zn	<11.7	—	13.97 ± .05	—	—
Ga	—	—	12.0 ± .1	—	—
Ge	—	—	13.1 - 12.6	—	—

BDHF and CTY suggest that the observed abundances are due to photoionized gas, and that they are not associated with the coronal component of the ISM. The photoionization occurs around the hot background star used as the background continuum. CTY also suggest the possibility that the line of sight passes through the Stromgren sphere of another star, causing the absorption; or that the star is an X-ray source, which Auger-ionizes C II and Si II to produce C IV and Si IV. An atom undergoes an Auger or radiationless ionization when a K or L shell electron is photoejected by the absorption of an X-ray, and the subsequent decay of an outer shell electron into the hole releases enough energy to eject a second electron. The modification to the ISM by a galactic X-ray source has also been discussed by McCray, Wright, and Hatchett (1977) and Kallman and McCray (1982, hereafter KM).

If the C IV and Si IV were produced in an H II region, then $N(\text{C IV})/N(\text{Si IV}) < 1$ for all stellar effective temperatures less than 50,000 K. The observations towards X Per ($T_{\text{EFF}} = 30000$ K) give $N(\text{C IV})/N(\text{Si IV}) = 4 \pm 0.2$. The predicted column densities of C IV and Si IV for a B0 star with $n_e = 1 \text{ cm}^{-3}$ are $N(\text{C IV}) = 5.7 \times 10^{12}$ and $N(\text{Si IV}) = 7.8 \times 10^{13}$ (CTY). The column densities scale as $n_e^{1/2}$. For $n_e = 1 \text{ cm}^{-3}$, the Stromgren radius is 1.5×10^{20} cm, which gives an emission measure of $\text{EM} = \int n_e^2 dl = 50 \text{ cm}^{-6} \text{ pc}$. The Palomar Sky Survey, which is sensitive to emission measures of this magnitude, does not show any evidence for an H II region along the line of sight towards X Per, although extinction by the cloud in front of the star might account for this. There is a small patch of nebulosity approximately $1'$ away from X

Per (cf Brucato and Kristian, 1972 for a magnified PSS print of X Per), however, the star does not show any evidence for an H II region surrounding it. Additionally, the emission measure of the entire region surrounding X Per is $10 \text{ cm}^{-6} \text{ pc}$ (Reynolds and Ogden, 1982). This suggests that n_e is less than 1 cm^{-3} , which would lead to lower column densities of C IV and Si IV. If the star were also an X-ray source with a soft X-ray flux of 2000ϕ (ϕ is a scaling factor) photons cm^{-2} per second per keV at 296 eV and 15000ϕ photons cm^{-2} per second per keV at 125 eV, then $N(\text{C IV})/N(\text{Si IV}) = 3.3$ for an effective stellar temperature of 30000 K and $n_e = 1 \text{ cm}^{-3}$ (CTY). However, the predicted column density is an order of magnitude lower than observed. In the case of a soft X-ray flux, the column density scales as $n_e^{-1/2}$. By decreasing the electron density, the column density of C IV and Si IV would increase, while the emission measure would decrease. However, the column density scales as the X-ray flux scaling factor. For X Per, $\phi = 10^{-3}$ to 10^{-4} (White et al. 1982). The electron density would then have to be prohibitively small to reproduce the observed column densities.

McCray, Wright, and Hatchett (1977) suggested that a galactic X-ray source would create a zone of highly ionized material around it. They showed that the column density of the ions scaled as $K(nL_x)^\alpha$, where n is the hydrogen volume density, L_x is the X-ray luminosity, and α and K are constants for each ion. Further refinements in the theory were presented by KM. The ratio of C IV to Si IV is independent of the density and the X-ray luminosity ($\alpha = 0.5$ for all elements, KM), and depends solely on the ratio $AK_{\text{C IV}}/AK_{\text{Si IV}}$, where A is the abundance of

the element with respect to hydrogen. The value for K depends on the input X-ray spectrum. For a 10 keV thermal spectrum (The X-ray spectrum of X Per can be described by a 10 keV thermal spectrum; White et al. 1982, cf 2.1) and solar abundances, the ratio of $AK_{C IV}/AK_{Si IV}$ is 2.5, which is close to the observed value of 4 considering the number of assumptions made. A 10 KeV thermal also gives $N(N V)/N(C IV) = 0.13$, which is consistent with the observed upper limit of 0.22. Hence, for volume densities between 1 and 1000, the model of KM predicts the quite accurately the ratios of C IV, Si IV and N V.

The column density is predicted by the equation

$$N_i = A_i K_i \left(\frac{L_x n}{10^{38}} \right)^{1/2} \text{ cm}^{-2} \quad (5-7)$$

Given that L_x is $5.0 \times 10^{33} \text{ ergs cm}^{-3} \text{ s}^{-1}$ and the observed column densities (Table 5-1), equation 5-7 can be solved for the hydrogen volume density, n :

$$n = \left(\frac{N_i}{A_i K_i} \right)^2 L_x (-38) \text{ cm}^{-3} \quad (5-8)$$

The value of K changes as a function of density, so the process of solving equation 5-8 is an iterative one. The result is that the $n_{C IV} = 13 \text{ cm}^{-3}$, $n_{Si IV} = 27 \text{ cm}^{-3}$, and $n_{N V} < 13 \text{ cm}^{-3}$. The densities will increase as the element becomes more depleted. Given the generalizations of the theory (McCray, 1982), the densities are essentially the same. The only possible problem is if the gas is

totally ionized, as the emission measure data would prohibit large densities, unless a very small distance was involved. The closest theoretical model of KM to the X Per conditions suggest that the gas around the star is fully ionized out to 10^{16} cm. One can envisage a situation in which the edge of the cloud is far enough from the star that a negligible H II region forms, but where the modification to the ionization structure of C, N, and Si are such as to produce the observed column densities. Clearly, more work needs to be done on the problems of a X-ray source modifying the ISM.

An alternate proposal is that the gas is collisionally ionized at a temperature of 50000 K (Bruhweiler et al. 1980). Table 5-2 lists $-\log(N_i/N)$, where N is the total column density in the 10 km/s component ($0.05N_I + 0.05 N_{II} + N_{III} + N_{IV}$). Theoretical ratios (Shull and van Steenberg, 1982) are also listed for relevant temperatures. The ionization fraction for each element matches quite closely to the theoretical fractions for $\log T \approx 4.5$ to 4.7 K. This was also the conclusion presented by Bruhweiler et al. (1980). Although these data are consistent with the ICM being collisionally excited at 50000 K, other observational evidence suggests that this is not the case.

If the gas were collisionally ionized at $T = 50000$ K, then the velocity parameter range should change by almost a factor of two between Fe II and Mg II. The exact decrease depends on the amount of turbulent broadening. The total velocity parameter is

TABLE 5-2
FRACTIONAL ATOMIC ABUNDANCES

Element	Log $\frac{N_{\text{Tot}}}{N_i}$					Observed Theory	Log T_{eff} (K)
	I	II	III	IV	V		
C	2.40	0.0	-0.25	4.2			
	2.34	0.11	0.64	4.57		4.6	
N	0.0					<4.1	
	2.2	0.10	0.72	4.48		6.0	4.6
Si	3.85	0.0	1.47	3.32			
	3.34	0.56	0.14	3.72		4.7	
S	2.54	0.0	1.91				
	1.86	0.05	1.04			4.4	

$$b = (b_{\text{kin}}^2 + b_{\text{turb}}^2)^{1/2} \text{ km/s} \quad (5-9)$$

where $b^2 = 2kT/m$. For carbon at $T = 50000 \text{ K}$, $b_{\text{kin}} = 8.3 \text{ km/s}$. The observed velocity parameter of 10 km/s sets b_{turb} :

$$b_{\text{turb}} = (b^2 - b_{\text{kin}}^2)^{1/2} = 5.6 \text{ km/s} \quad (5-10)$$

From equation 5-9, the expected velocity parameter for Fe is $b_{\text{Fe}} = 6.8 \text{ km/s}$. The curve of growth clearly shows a contribution at $b = 10 \text{ km/s}$. This strongly suggests that the gas is not collisionally ionized at $T = 50000 \text{ K}$.

Although the ionization structure of C and Si match quite nicely with the theoretical calculations, this is not the case for Mg. The ratio Mg I/Mg II for $T > 50000 \text{ K}$ is $\log(\text{Mg I/Mg II}) < -2.33$, whereas the absolute minimum observed value is -2.25 . Although the observational errors encompass the theoretical value, two problems exist. The first is that the analysis of the dominant stage ions (5.3) suggest that the Mg II abundance is less than that needed to produce the agreement. Hence, the Mg I/Mg II ratio increases to an absolute maximum of $\log(\text{Mg I/Mg II}) = -1.5$, where all the Mg II is in the ICM. This ratio is too large to be collisionally ionized for $T \approx 10000 \text{ K}$. Even if the minimum value is correct, the implication is that Mg III is the dominant stage of ionization, not Mg II. For $T = 50000 \text{ K}$, $\text{Mg III/Mg II} = 1000$, which implies that the column density of Mg III is more than 30 times the solar abundance of Mg, and all of it is in the ICM, which, if it has

5% of the mass, contains more than 600 times the solar abundance of Mg. Since Mg is thought to be depleted in the ICM (Bruhweiler and Kondo, 1982), the existence of a collisionally ionized gas at $T = 50000$ K is highly improbable.

The main results for this section are the identification of the highly ionized species and their connection with the 10 km/s velocity parameter component. Additionally, I have shown that a modification of the ICM is needed to give the observed C IV/Si IV ratio, and that a collisionally ionized gas at $T = 50000$ K can be ruled out. The most probable cause of the enhanced C IV/Si IV ratio is through the modification of the ionization structure by X-rays, presumably from the stellar X-ray source. However, the theory has not been developed far enough to be conclusive.

5.3 Dominant Stage Ions

Diffuse clouds are opaque to all wavelengths with energies greater than 13.6 eV but are transparent to most photons with energies less than 13.6 eV. Since a number of elements have ionization potentials less than 13.6 eV, they will exist primarily in a singly (or doubly, eg Ti and Ca) ionized form in the diffuse ISM. Only in very dense IS clouds, where the grains and other absorption mechanisms cut off all ionizing photons, will the dominant stage of ionization be the neutral species. Figure 5-2 shows the ionization potentials for the first 26 elements and

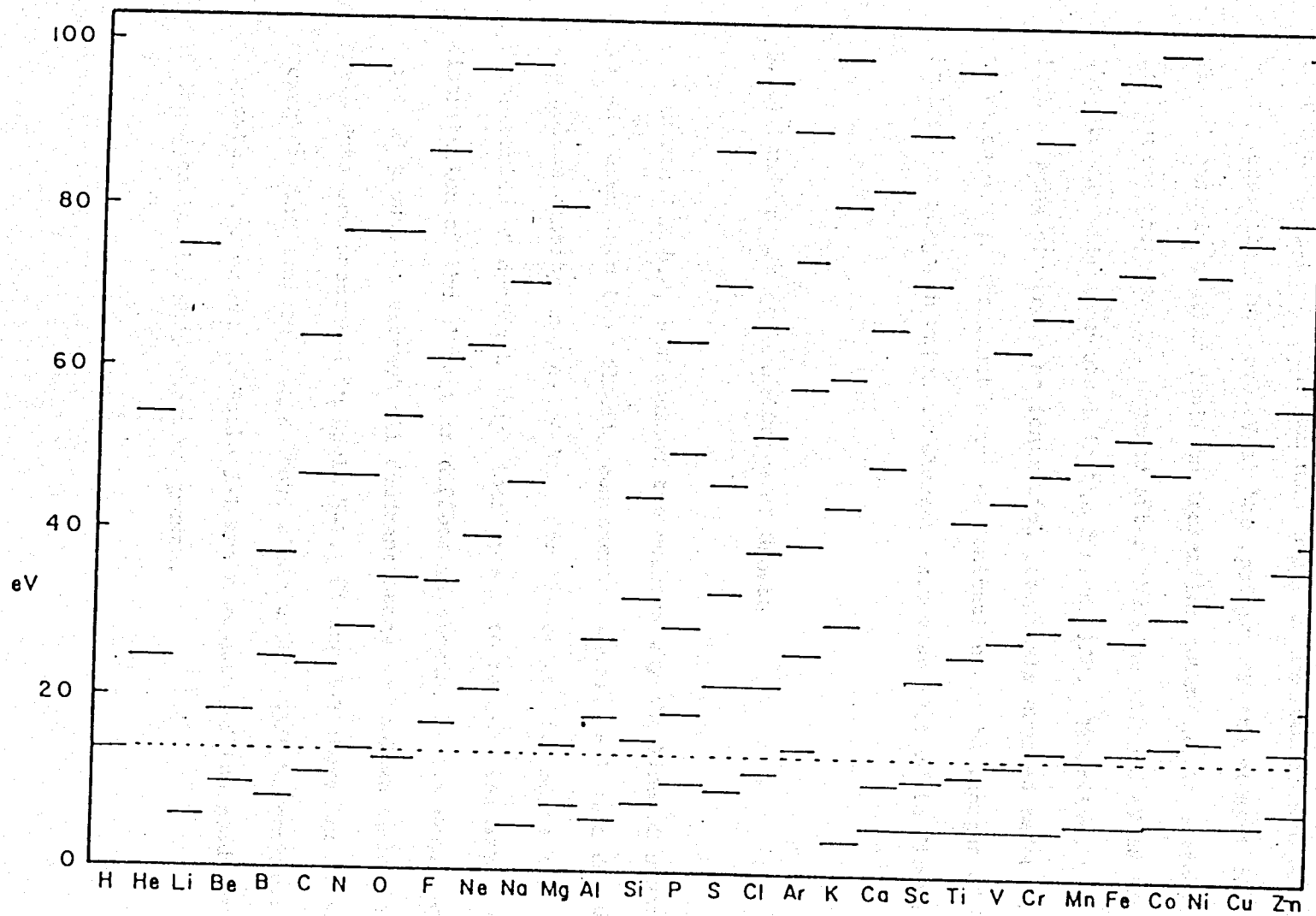


Figure 5-2. Ionization potentials for H through Zn. The thin line at 13.6 eV corresponds to the ionization potential of H. Except for dust absorption, all photons with $E < 13.6$ eV are unimpeded in the general ICM.

where the ionization potential is less than 100 eV. A horizontal line is drawn at 13.6 eV. The dominant stage of ionization can be found by going vertically from 0.0 eV at the position of the element of interest. The element is neutral until an ionization potential is crossed. If the ionization potential is crossed after the line at 13.6 eV is crossed, the element will be neutral in the diffuse ISM. Otherwise, the atom has lost as many electrons as ionization potentials crossed before 13.6 eV is reached. The dominant stage of ionization can be thought of as the ionization stage in which an element exists at 13.6 eV in Figure 5-2.

5.3.1 Dominant Stage Ions: Curve of Growth

In section 4.2, I discussed the reasons why the line of sight could be separated into two velocity components, where $b = 1$ km/s for 95% of the column density and $b = 10$ km/s for the other 5%. Since the distribution of dominant stage ions appear to reflect the mass distribution of the element in diffuse IS clouds, I have used the 95/5 curve of growth to extract all dominant stage ion column densities. These data are presented in Table 5-1. Figure 5-3 shows the curve of growth for the dominant stage ions, along with a 95/5 theoretical curve of growth. The errors in Table 5-1 are a measure of the goodness of fit of the data to the 95/5 curve of growth.

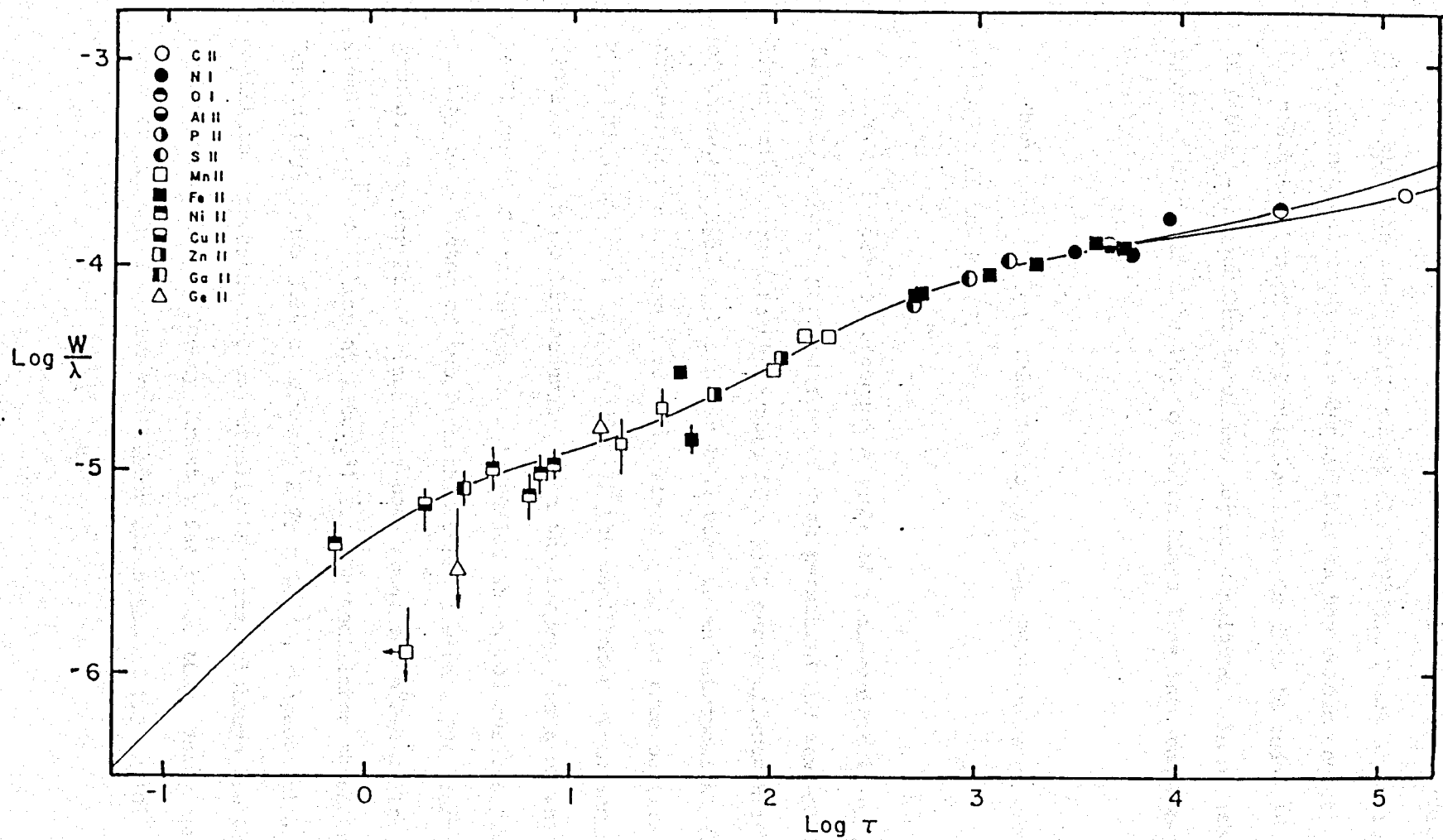


Figure 5-3. Empirical curve of growth for the dominant stage ions. A 95/5 theoretical curve of growth is also shown. The data for Si II, Mg II are shown elsewhere. The curves of growth for C II and O I are shown explicitly.

A number of dominant stage ions have forbidden lines which might be observable with the IUE (Cowan et al. 1982). These lines were searched for and not detected. The upper limit on the column density implied by the non-detection of the forbidden lines is also included in parenthesis in Table 5-1 under the tabulated column densities. In no case is the upper limit implied by the forbidden lines less than the observed column density.

There are two ions which do not fit the 95/5 curve of growth very well: Fe II and Mg II.

Kurucz (1982) has produced a table of semi-empirical log gf values for Fe II. There are a number of weak permitted and semi-forbidden lines which should be observable if a 95/5 curve of growth is used. One of these, at 2366 Å, has never been seen in an astronomical source before, and questions have been raised as to its true oscillator strength (Lugger et al. 1982). If the oscillator strengths of Kurucz (1982) are reasonably accurate, then the largest fraction which the Fe II curve of growth can have is 90/10, which reduces the total column density by a factor of two from that derived with a 95/5 curve of growth. Two new Fe II lines have been seen: the a^6D-z^4D line at 2249.18 Å and the a^6D-z^4F line at 2260.081 Å. The oscillator strengths from Kurucz (1982) are 3.24×10^{-3} and 2.79×10^{-3} , respectively. The oscillator strengths are essentially the same, although the observed equivalent widths differ by almost a factor of two. Using the 95/5 curve of growth, I derive oscillator strengths of 1.29×10^{-3} and

6.98×10^{-3} for the 2249 Å and 2260 Å lines, respectively. Accurate laboratory oscillator strengths would be extremely useful, as they would help determine the exact fraction in each velocity parameter cloud.

The ratio of the equivalent widths of the 1240 Å doublet of Mg II is ≈ 2 , which suggests that they are on the linear portion of the curve of growth. However, the equivalent widths of the two lines place them above the 1 km/s turnover from thick to thin. These data are consistent with a composite curve of growth in which no more than 50% of the Mg II has $b = 1$ km/s. indicates a factor of ten reduction in the abundance of Mg II in the 1 km/s cloud. This is either a true depletion or an artificial one caused by a shift from Mg II to Mg I as the dominant stage of ionization. The Mg II curve of growth is shown in Figure 5-5 where the observational data are shown twice: once for the best fit to the 95/5 curve of growth ; again for the best fit to a 0/100 curve of growth. The column density derived from the 0/100 curve of growth is also listed in Table 5-1. If all of the observable Mg II were in the 10 km/s cloud, the total abundance in the 10 km/s cloud would still be less than the solar abundance, and is $\delta_{\text{Mg II}} = -0.12$,

where $\delta_i = \log(N_i/N_H) - \log(N_i/N_H)_\odot$. The magnesium abundance in the 10 km/s cloud would be solar if 75% of the magnesium is Mg III, the other 25% being Mg II. Since the ionization potential of Mg II is very close to that of Si II (Figure 5-2), the relative amount of Mg III should be comparable to the relative amount of Si III, which is less than 10% of the Si in the 10 km/s cloud. This suggests that Mg III will

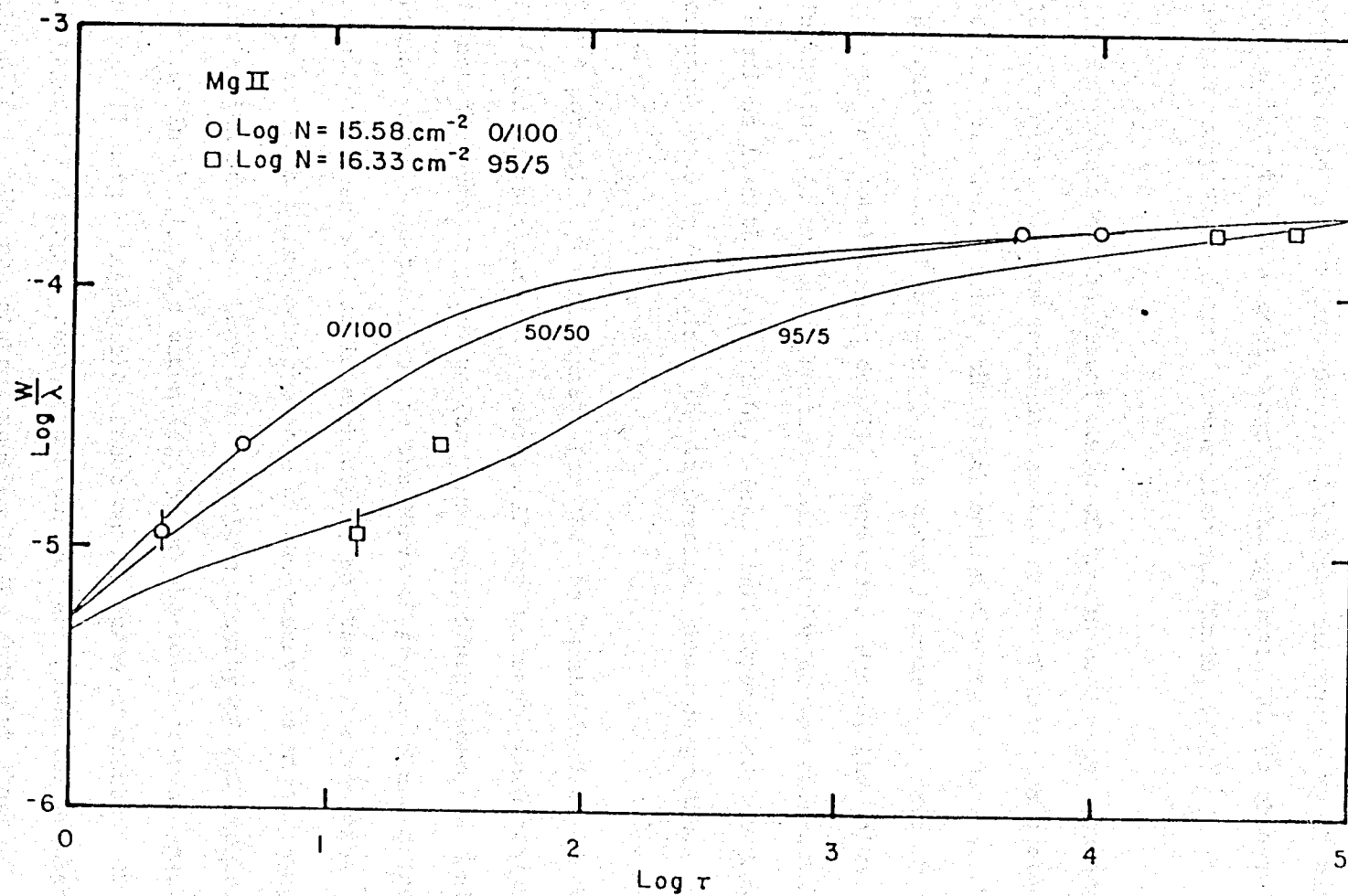


Figure 5-5. Theoretical curves of growth for fractions of 0/100, 50/50, and 95/5. The observed MgII data are shown for two separate column densities.

not be abundant enough to reduce the depletion to 0. The suggested depletion in the 10 km/s cloud, if all the observable Mg II exists in it, is less than the depletions in the general ICM, as observed towards a few nearby white dwarfs (Bruhweiler and Kondo, 1982).

Regardless of the actual curve of growth used, the abundance in the 10 km/s cloud remains constant: as the ratio of the 1 km/s cloud to the 10 km/s cloud decreases, the total column density decreases. However, the relative amount in the 10 km/s cloud increases at exactly the same rate as the total column density decreases. Hence, the column density in the 10 km/s component remains constant for curves of growth with fractions less than 99.95/0.05. This limit depends on the damping constant used to calculate the theoretical curve of growth.

A potential problem exists for the the identification of the correct fraction for the curve of growth. If the dominant stage of ionization is not the same for the two (or more) components, then the ionization balance must be determined, as the curve of growth is a measure of the relative number of ions in each cloud, not the relative mass. For the line of sight towards X Per, none of the observable higher stages of ionization have more than 10% the column density of the implied column density in the 10 km/s cloud (eg, 5% of the total column density), and hence all have a negligible effect on the curve of growth. Oxygen and nitrogen (also argon, neon, and fluorine) are potential problems. In the diffuse ISM, the neutral species is the dominant stage of ionization. However, this may not be the case for the ICM (and

especially for an H II region), where N II and O II will be the dominant stage of ionization. Indeed, both N I and O I are compatible with both a 95/5 and a 100/0 curve of growth (the upper limit on O I is set by the absence of the 1355 Å intersystem line). The column densities for O I and N I using a 100/0 curve of growth are also included in Table 5-1. The errors quoted in Table 5-1 are a measure of the goodness of fit of the data to the 95/5 curve of growth. The errors will, of course, be larger if I make some guess as to the error in using the 95/5 curve of growth.

Absorption from the $P_{3/2}$ level of C II (referred to as C II*) is observed, whereas the similar transition in Si II is not seen. Since these levels are populated by collisions, the ratio of the column densities from the $P_{1/2}$ and $P_{3/2}$ levels can be used to put limits on the temperature and density (cf 6.2 and 6.3). The problem is choosing the proper curve of growth for the C II* line. The curve of growth for any excited state will reflect the velocity parameter distribution of the pressure convolved with the distribution of the ionization stage. Si II has a number of observable UV multiplets, hence observations of the fine structure lines arising from the $P_{3/2}$ level of Si II could be used to construct a curve of growth to be used with Si II. Unfortunately, absorption from the $P_{3/2}$ level of Si II is not observed. Figure 5-6 shows the curve of growth for C II* with cloud fractions of 0/100, 95/5, 99/1 and 100/0. The horizontal line corresponds to the observed equivalent width of 170 ± 4 mÅ. The C II* absorption line at 1335 Å consists of two lines: $P_{3/2} - D_{5/2}$ at 1334.6627 Å and

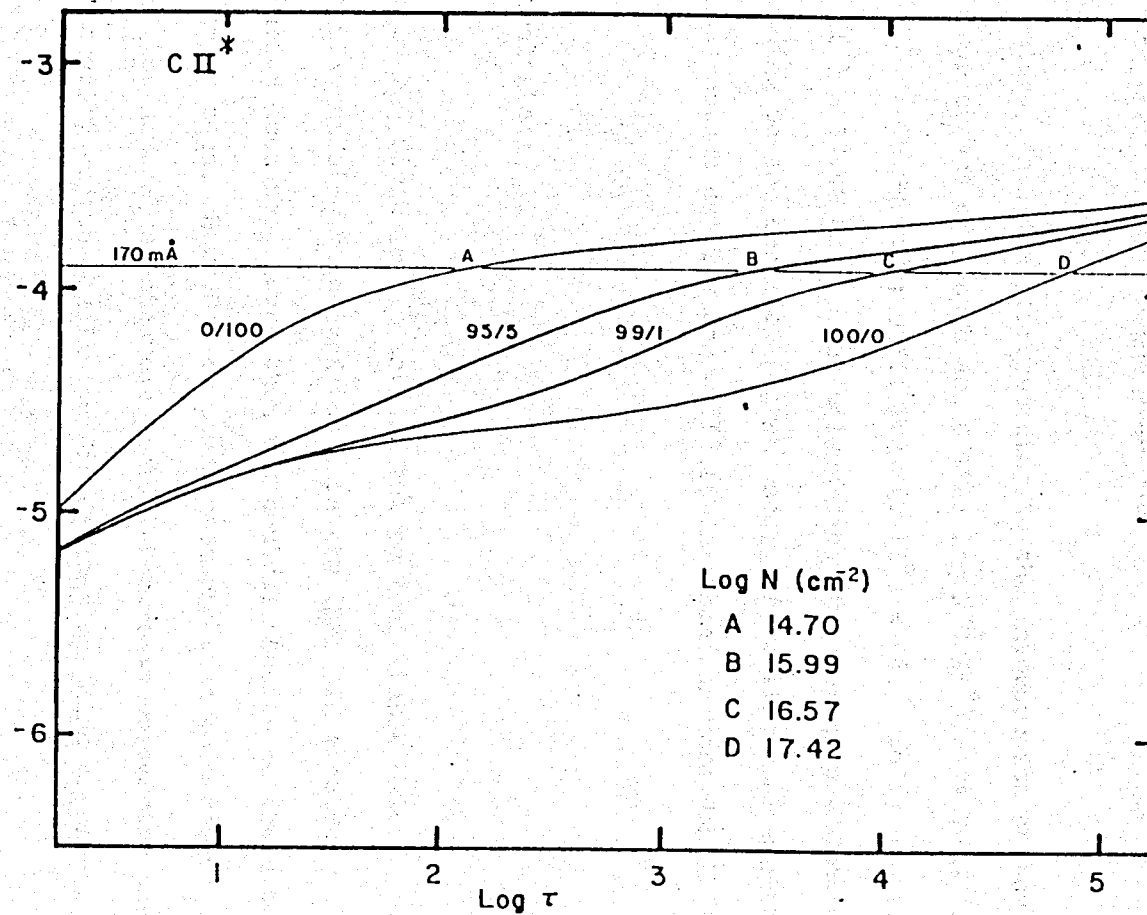


Figure 5-6. Column density of C II^* as a function of the theoretical curve of growth. Four different curves of growth and respective column densities are shown.

$P_{3/2} - D_{5/2}$ at 1335.7077 \AA . The lines are separated by 10.3 km/s , and thus are unresolved by the IUE. The oscillator strengths are 0.0118 and 0.1159 , respectively. The curve of growth was calculated with the line profile techniques discussed in 4.3.

The column densities corresponding to the intersection of the line and the four curves of growth are 0/100: $\log N(\text{C II}^*) = 14.7 \text{ cm}^{-2}$; 95/5: $\log N(\text{C II}^*) = 15.99 \text{ cm}^{-2}$; 99/1: $\log N(\text{C II}^*) = 16.57 \text{ cm}^{-2}$; and 100/0: $\log N(\text{C II}^*) = 17.42 \text{ cm}^{-2}$. The column density changes by a factor of 500 depending on the curve of growth used. The collisional excitation and assumed column density for C II^* is discussed in more detail in 6.3.

5.4 Neutral Atoms

Most of the first 30 elements in the periodic table exist predominantly as singly ionized atoms in the ISM. If electron recombination does not occur, then the neutral species of these atoms will never be seen. However, electron recombination does occur, and the amount of the neutral species can yield information concerning the electron density and the radiation field along the line of sight.

5.4.1 Ionization Equilibrium

The density of the neutral species and their first ions are related through the equilibrium of ionization and recombination rates.

Mathematically, this can be written

$$\Gamma n_i = n_e n_{i+1} \alpha(T) \quad (5-11)$$

where n_1 and n_2 are the volume densities (cm^{-3}) of the neutral species and its first ion, n_e is the electron density (cm^{-3}), Γ is the photoionization rate (s^{-1}), and α is the recombination rate ($\text{cm}^{-3}\text{s}^{-1}$). α varies roughly as $T^{-0.7}$. Appendix D discusses the calculation of the photoionization rate in more detail.

The ratio between the neutral and its first ion is

$$n_i/n_{i+1} = n_e \alpha(T)/\Gamma \quad (5-12)$$

For a given cloud, n_e is a constant, but Γ/α varies with the specific element (I am assuming that each cloud can be described by one unique value for all physical parameters). The ratio N_1/N_2 is thus different for each element. Since the conditions in the 1 km/s and 10 km/s cloud are different, it is useful to look at the behavior of the ratio of the densities of the two clouds. The ratio between the ionization ratio (equation 5-12) in the 1 km/s and 10 km/s components can be written

$$\frac{n_1(1)/n_2(1)}{n_1(10)/n_2(10)} = \frac{n_e(1)\alpha(T_1)/\Gamma_1}{n_e(10)\alpha(T_{10})/\Gamma_{10}} \quad (5-13)$$

or

$$\frac{n_1(1)}{n_1(10)} = \frac{n_e(1)}{n_e(10)} \frac{\alpha(T_1)/\Gamma_1}{\alpha(T_{10})/\Gamma_{10}} \frac{n_2(1)}{n_2(10)} \quad (5-14)$$

Note that if a depletion exists in the 1 km/s cloud, it affects both n_1 and n_2 equally, and hence the ratio N_1/N_2 is unaffected.

If the ratio of the dominant stage ions (n_2) between the two velocity parameter components reflects the mass ratio of the two components, then

$$\frac{n_1(1)}{n_1(10)} = 19 \frac{n_e(1)}{n_e(10)} \frac{\alpha(T_1)/\Gamma_1}{\alpha(T_{10})/\Gamma_{10}} \quad (5-15)$$

where 19 is 95/5. Note that the ratio $n_2(1)/n_2(10)$ may be less than 19 if the Mg II column density is different from that derived by a 95/5 curve of growth (cf 5.3.1).

As discussed in Appendix D, the value of Γ depends on the extinction. The details of the integration depend on the scattering properties of the grains and the geometry of the cloud (Roberge et al. 1981, hereafter RDF). The grain scattering properties in the far UV are very uncertain (Savage and Mathis, 1979; RDF; Anderson et al. 1982).

A major uncertainty is the choice for the temperature of the 10 km/s b-component. If the absorption occurs in the ICM, then $T \approx 7000$ to 12000 K. If the majority of the absorption occurs at lower temperatures at the edge of the cloud, then $T \approx 20$ to 120 K. The ratio of $[\alpha/\Gamma(1)]/[\alpha/\Gamma(10)]$ is

$$\frac{\alpha/\Gamma(1)}{\alpha/\Gamma(10)} = \left(\frac{T(10)}{T(1)}\right)^\eta \frac{\Gamma(10)}{\Gamma(1)} \quad (5-16a)$$

for the ICM and

$$\frac{\alpha/\Gamma(1)}{\alpha/\Gamma(10)} = \frac{\Gamma(10)}{\Gamma(1)} \quad (5-16b)$$

if the 10 km/s is part of the diffuse cloud. η is tabulated in Table D-1, and $T(1)$ and $T(10)$ are the temperatures of the 1 km/s and 10 km/s components, respectively. Equations 5-16a and 5-16b were evaluated using the photoionization rates of RDF (model 2 and model 3 only, cf Appendix D) for $T(1) = T(10)$ and $T(10) = 200T(1)$ ($T(1) = 50$ K, $T(10) = 10^4$ K; or $T(10) = 50$ K) and are listed in Table 5-3. Γ is assumed to be equal to its unshielded ICM value for both temperatures (Γ_0 , cf Appendix D, Table D-1).

Both Mg I and Cl I seem to fit a 95/5 curve of growth (Figure 4-4b), hence

TABLE 5-3

PHOTOIONIZATION RATIOS AND FRACTIONAL CURVES OF GROWTH

Element	$(200)^n$	Γ_0/α		$(200)^n \Gamma_0/\alpha$		Percent in 1 km/s comp.			
		Model:		Model:		Model:		Model:	
		2	3	2	3	2	3	2	3
		T(1)=T(10)		T(10)=200T(1)		T(1)=T(10)		T(10)=200T(1)	
C	27.3	4.39	1.44	119.8	39.3	97.6	95.3	92.3	85.5
Na	53.2	6.12	2.89	325.6	153.7	98.3	97.6	97.3	95.8
Mg	92.8	2.03 (0.49) ^a	1.35 (0.74) ^a	188.4 (0.0053) ^a	125.3 (0.0079) ^a	95.0	95.0	95.0	95.0
Si	24.2	2.44	1.25	59.0	30.3	95.8	94.6	85.6	82.0
S	28.2	4.02	1.42	113.4	40.0	97.4	95.2	91.9	85.7
Cl	40.8	7.41 (0.13) ^a	1.68 (0.59) ^a	302.3 (.0033) ^a	68.5 (.015) ^a	98.6	95.9	96.8	91.1
K	59.1	2.37	1.37	140.1	81.0	95.7	95.1	93.4	92.4
Ca	117.7	2.61	1.93	307.2	227.2	96.0	96.4	96.9	97.1
Ca ⁺	69.3	5.25	1.64	363.8	113.7	98.0	95.8	97.3	94.5
Fe	112.3	2.11	1.18	237.0	132.5	95.2	94.3	96.0	95.2
					mean	96.8	95.5	94.3	91.4
					s.d.	1.4	0.9	3.7	5.2

$$\frac{n_e(1)}{n_e(10)}$$

$$\frac{n_e(1)}{n_e(10)} \frac{\alpha(T_1)/\Gamma_1}{\alpha(T_{10})/\Gamma_{10}} = 1 \quad (5-17)$$

Table 5-3 also lists (in parenthesis, under their respective values of $[\alpha/\Gamma(1)]/[\alpha/\Gamma(10)]$) the values of $n_e(1)/n_e(10)$ for Mg I and Cl I. The largest discrepancy is for $T(1) = T(10)$ (model 2) where the derived value of $n_e(1)/n_e(10)$ for Mg I is four times the value derived for Cl I. Chlorine may be a bad example, as its photoionization edge occurs at 950 Å. The exact fraction in each stage of ionization thus depends on the specific details of the grain properties and the IS radiation field in the region where the least is known.

Using equation 5-15 and the $n_e(1)/n_e(10)$ from the Mg I calculations (Table 5-3), the percentage in the 1 km/s cloud can be calculated by

$$P(1) = \frac{100}{1 + n_1(10)/n_1(1)} \quad (5-18)$$

These values are listed in Table 5-3 for $T(1) = T(10)$ and $T(10) = 200T(1)$ evaluated for models 2 and 3. The fractional abundance in the 1 km/s component is independent of the exact Mg II curve of growth, since the product

$$\frac{n_2(1)}{n_2(10)} \frac{n_e(1)}{n_e(10)} = \frac{n_1(1)}{n_1(10)} \left(\frac{\alpha/\Gamma(1)}{\alpha/\Gamma(10)} \right)^{-1} \quad (5-19)$$

is a constant for the particular model and temperatures chosen, although $n_e(1)/n_e(10)$ increases by the ratio $19 n_2(1)/n_2(10)$.

The non-detection of the 4044 Å doublet of K I and the 2800 Å doublet of Na I limit their respective curves of growth to less than 95/5 and 99/1. The Na I limit is met by all combinations of models and temperatures. The K I curve of growth for $T(1) = T(10)$ is 95.6/4.3 or 95.1/4.9 for models 2 and 3, respectively but is less than 95/5 for both models and $T(10) = 200T(1)$. This suggests that the temperature of the 10 km/s component is closer to the temperature of the diffuse cloud than to the temperature of the ICM.

Qualitatively, the percentages in the 1 km/s component can be described as follows. The decrease in the percentage going from model 2 to model 3 is because of the increase in the forward scattering and albedo of the grains, and hence the center of the cloud is brighter for model 3 than for model 2. As the temperature increases in the 10 km/s component, recombination becomes more efficient, increasing the neutral fraction in the 10 km/s component. This reduces the percentage of the observed neutral species in the 1 km/s component. The best model appears to be model 3 with $T(10) = T(1)$, particularly in meeting the requirements of the Na I and K I curve of growth. Both models can be made to fit the constraints exactly if the temperature of the 10 km/s component is allowed to rise above the temperature of the 1 km/s component.

The "mean" curve of growth from all elements for each model and temperature is included in Table 5-3. From these averages, I have concluded that the neutral curve of growth lies somewhere between a

90/10 and a 95/5 curve of growth. There is a factor of two difference in the column densities derived from these two curves of growth, providing that the data for an individual curve of growth does not lie on the linear portion of the 1 km/s curve of growth. Figure 5-4 shows both a 90/10 and a 95/5 curve of growth.

5.4.2 Neutral Column Densities

I have extracted the column densities of the neutrals using both a 95/5 and a 90/10 curve of growth. These data are listed in Table 5-1. Equivalent entries indicate that the element has at least one line which lies on the linear part of the 1 km/s curve of growth. The quoted errors are errors in the fit to the particular curve of growth. Figure 5-7 shows the 95/5 curve of growth and the data fit to it.

The curve of growth used to extract the column density of the fine structure levels of C I is again not well defined (cf 5.3), as the relative population in the two components is a function of the density in the two components. Unlike C II, the fine structure levels of C I are not easily populated by collisions with electrons. If the 10 km/s component is almost fully ionized, then the amount of C I in the J=1 and J=2 levels will be almost negligible unless the density is extremely large, which does not appear to be the case. An upper limit on the curve of growth is set by the fact that the largest relative population of the J=1 level to the J=0 level is set by statistical equilibrium, and

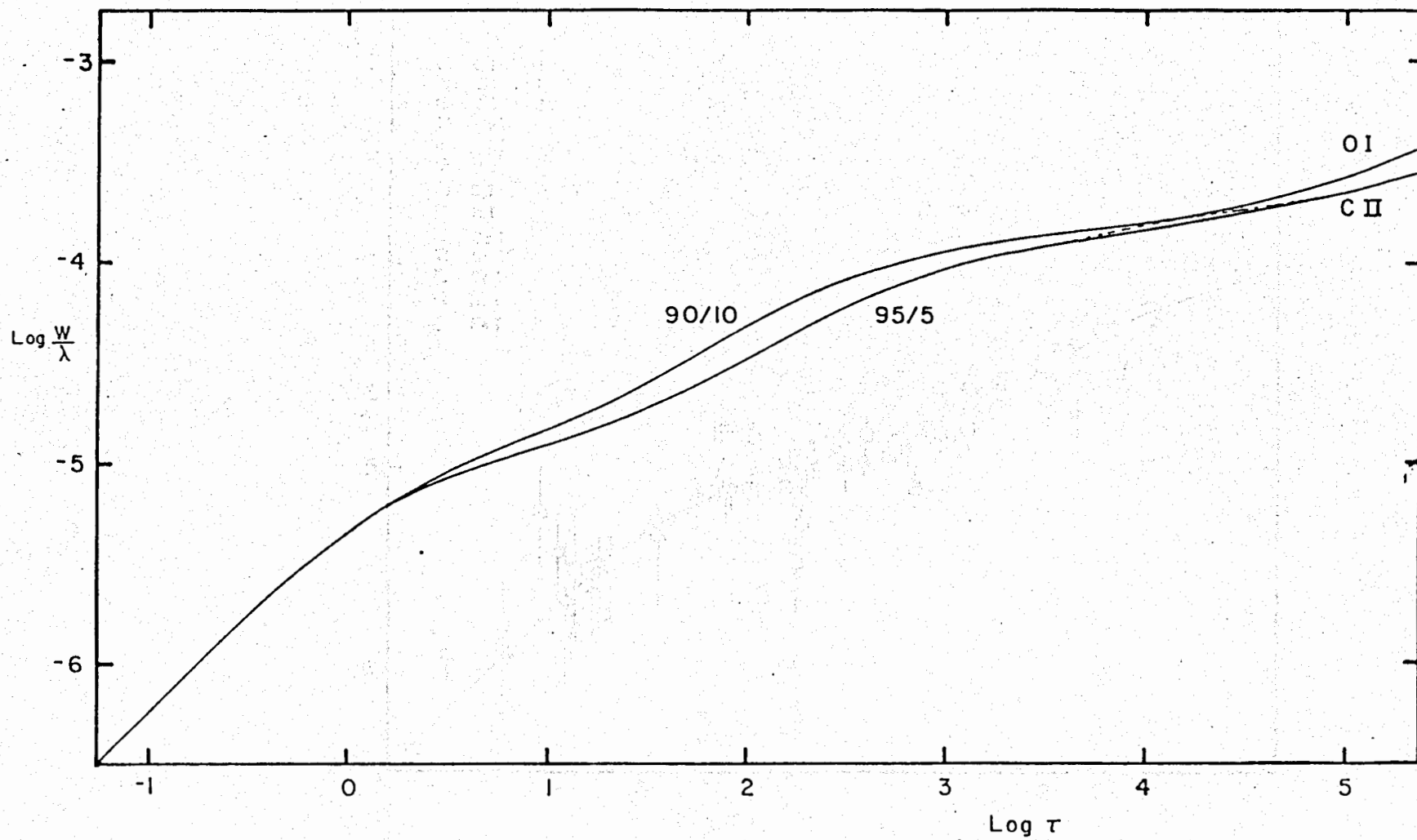


Figure 5-4. 95/5 and 90/10 curves of growth. The damping is shown for C II and O I.

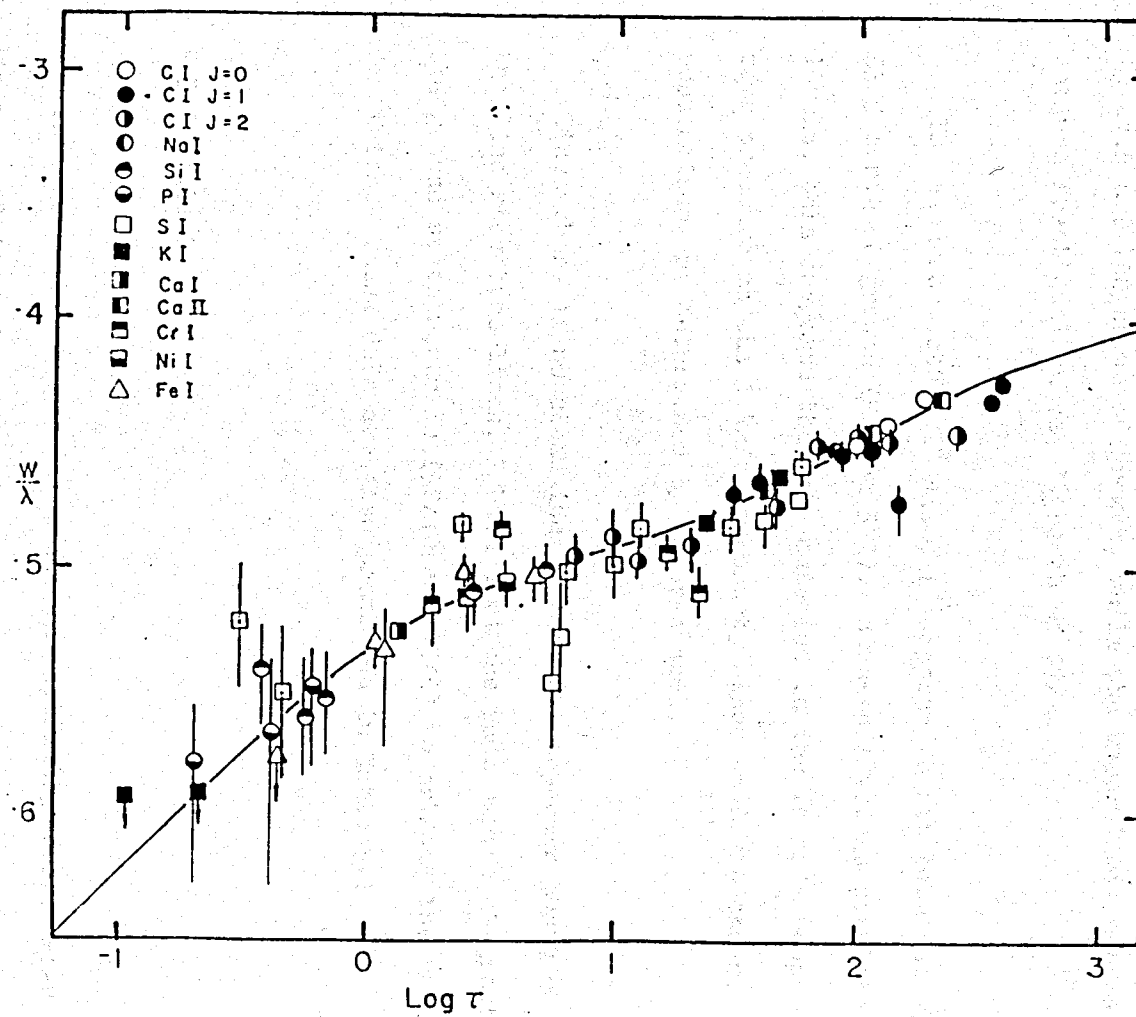


Figure 5-7. Empirical curve of growth for the neutral species toward X Per. Also shown is a 95/5 curve of growth. The data for Mg I and Cl I are shown in Figure 4-4b.

is the ratio of the degeneracies (3). The minimum ratio of $n(J=1)/n(J=0)$ is set by the IS radiation field (de Boer and Morton, 1974), and is $n(J=1)/n(J=0) = 0.02$. This lower limit cannot be reached by even a 0/100 curve of growth, while the upper limit corresponds to a maximum fractional curve of growth of 97/3.

The data for both $C\ I^*$ and $C\ I^{**}$ appear to fit both the 90/10 and 95/5 curve of growth (Figure 5-7). Since collisions populate these levels, this suggests that the material in the 10 km/s component has the same pressure as the 1 km/s component, since to first order, the level populations are determined by the pressure.

Since there is no clear indication of the proper curve of growth for the fine structure lines, I have used the same curves of growth as for the ground state neutrals (90/10 and 95/5) to extract the column densities. These data are also presented in Table 5-1.

5.5.1 Radio CO

The excitation temperatures for the optically thick $J=1-0$ and $J=2-1$ lines are $T_e(J=1-0) = 6.7 \pm 0.2$ K, $T_e(J=2-1) = 5.9 \pm 0.3$ K, (equation A-18).

Figure A-1 shows that for $T_e = 5$ K, the optical depths in the J=2-1 and J=1-0 lines should be equal if the levels have the same excitation temperature. Figure 5-8 shows the relationship between T_{R1}^* and T_{R2}^* for various values of N_{CO}/V and T_e (cf Appendix A and Figure A-2). The point for the observed J=1-0 and J=2-1 is also shown. Figure 5-8 shows that the CO lines are not in thermal equilibrium, and hence no information on the column density can be derived from the radio ^{12}CO emission lines.

If the excitation of the J=1-0 ^{13}CO line is the same as the ^{12}CO J=1-0 line, then the column density of the ^{13}CO line can be found by the method described in Appendix A. From the data in Table 3-1, equation A-21b gives 0.11 as the ^{13}CO optical depth. From equation A-15c then, $N(^{13}CO) = 3.1 \times 10^{14}$ ($\log N(^{13}CO) = 14.5 \pm 0.1$)

5.5.2 UV CO Line Analysis

Twelve vibrational bands ((0,0)-(11,0)) of the $A^1\Pi - X^1\Sigma^+$ electronic system of ^{12}CO and eight vibrational bands of ^{13}CO were observed in absorption towards X Per. The structure of the A-X CO band system is very simple, consisting of one Q, P, and R branch (Simmons, Bass, and Tilford, 1969). Since the wavelength separation between rotational lines is less than the resolution of the spectrograph (cf 4.3), the individual lines in the three branches are convolved into one band. Two methods can be used to determine the column density: profile fitting (cf

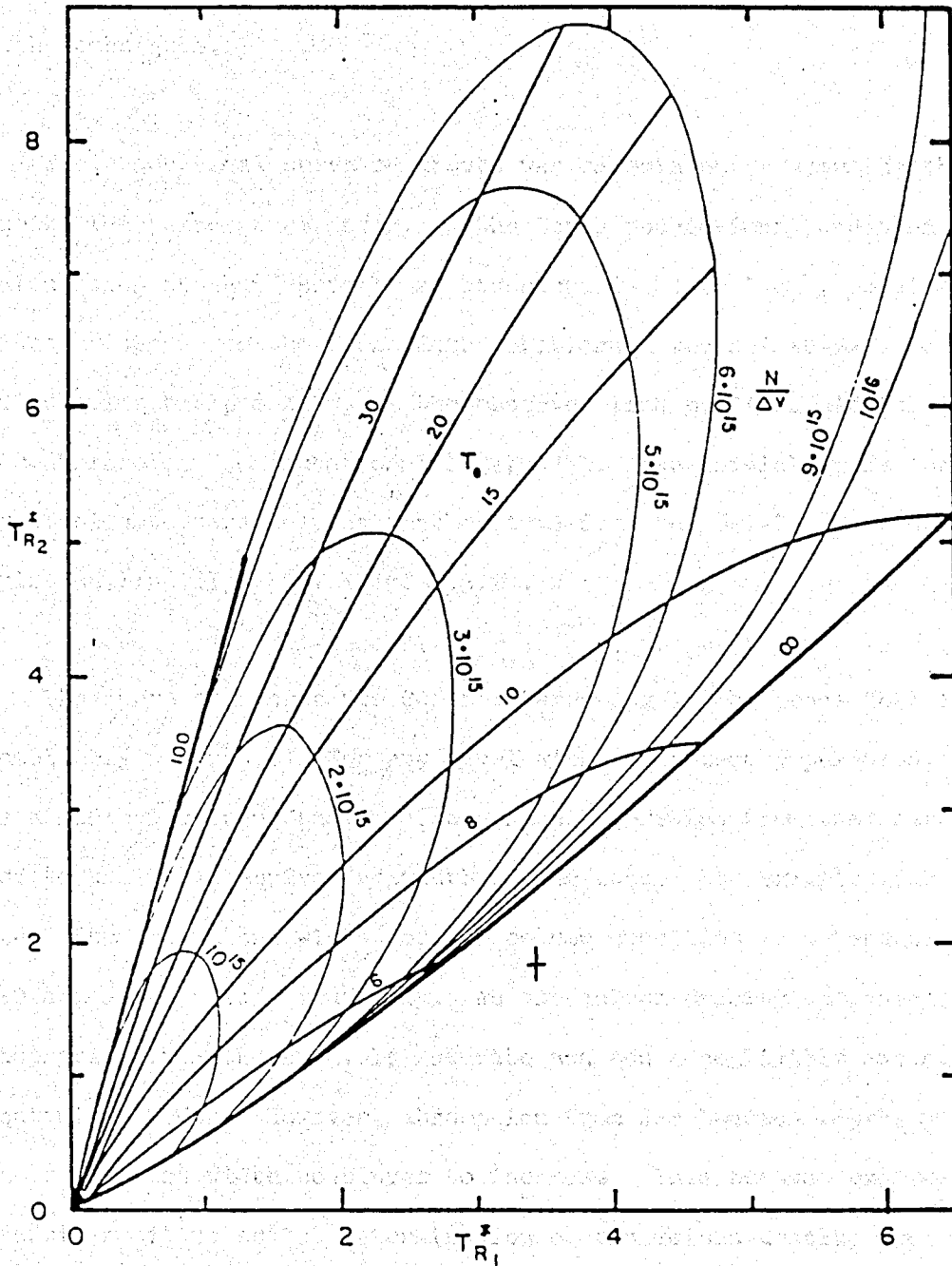


Figure 5-8. T_{R1}^* versus T_{R2}^* for different values of T_e (thick lines) and N/v (thin lines). The heaviest line on the right corresponds to an infinite column density. The observed excitation temperatures are shown as the cross, where the lengths of the lines represent a 2- σ variation in the measurement.

4.3) and normal curve of growth techniques (cf 4.1). In practice, I have found that each is inadequate in itself, mostly due to observational errors. However, a unique solution can be found using both techniques.

The theoretical curve of growth was calculated by assuming that one excitation temperature describes the level populations, and then calculating the band profile as described in 4.3. I only considered lines arising from the first four rotational levels ($J=0$ - $J=3$) in calculating the profiles, as the observed line profiles did not indicate a contribution from rotational levels $J>3$. The initial guess for the excitation temperature was that derived from the $J=1-0$ ^{12}CO radio emission line ($T_e = 6.7$ K; cf 5.5.1).

The curve of growth for CO is interesting in the sense that it never completely saturates. For any level with a non-zero population, there is a minimum column density after which absorption from that level will add to the total equivalent width of the band. For example, for $T_e = 4.5$ the equivalent width for low column densities is determined by the $J=0$ and $J=1$ levels exclusively. As the column density increases, the absorption from these levels saturate and add a negligible amount to the equivalent width. However, absorption from $J=2$ becomes important, and the equivalent width continues to increase. This becomes extremely useful, as it makes the determination of the column density much more accurate. A problem exists in that there is a range of T_e , column densities and velocity parameters which yield the same curve of growth.

The line profiles resolve this problem, as they put stringent limits on the possible values for b and T_e , as well as suggesting the need for other additional parameters (eg a component with a larger b). An initial guess for the column density can be made by calculating the column density assuming the equivalent width comes from optically thin lines. These data are presented in Table 5-4 for both ^{12}CO and ^{13}CO . The oscillator strengths are from Lassetre and Skerbele (1971). Only the last three vibrational bands of ^{12}CO and ^{13}CO appear to be optically thin, which is substantiated by the theoretical profiles. Unfortunately, these lines have the largest errors, and only a very imprecise value for the column density can be obtained.

The initial parameters suggested by the data are $b = 1$ km/s, $\log N(^{12}\text{CO}) = 15.6 - 15.8$ cm^{-2} , $T_{\text{eff}} = 4$ to 8 K, and $\log N(^{13}\text{CO}) = 14.5$ cm^{-2} . These data were used in an iterative two-fold process to determine the final column densities of ^{12}CO and ^{13}CO . The first step consists of calculating the line profile for the first eleven vibrational bands and comparing them with the observed line profiles. The line shape is a strong function of the temperature and can be used to find T_{eff} for the higher rotational levels. The shape of the band profile is a function of both the temperature and the product of the column density and the band oscillator strength (cf 4.3). For the first few vibrational bands of ^{12}CO , the line profile is determined almost completely by the effective temperature of the higher rotational states (for a constant velocity parameter). This occurs because the lower rotational levels are completely saturated and hence do not vary from

TABLE 5-4
OPTICALLY THIN COLUMN DENSITIES FOR ^{12}CO AND ^{13}CO

Band	Lambda (Å)	f-value	^{12}CO		^{13}CO	
			Eq. Width (mÅ)	Log N (cm^{-2})	Eq. Width (mÅ)	Log N (cm^{-2})
0-0	1544	0.02	133	14.50	--	--
1-0	1509	0.038	122	14.20	--	--
2-0	1477	0.0429	134	14.21	36	14.15
3-0	1447	0.036	131	14.29	37	13.64
4-0	1419	0.0251	109	14.39	24	13.74
5-0	1392	0.0155	87	14.51	24	13.96
6-0	1367	0.00848	70	14.70	24	14.23
7-0	1344	0.00437	45	14.82	24	13.31
8-0	1322	0.00217	45	15.13	10	14.47
9-0	1301	0.00108	28	15.24	10	14.79
10-0	1281	0.0005	47	15.81	--	--
11-0	1263	0.00025	16	15.66	--	--

one band to another. For higher vibrational bands, the optical depth in the higher rotational states becomes negligible, and the shape of the line profile is determined by absorption from the first two rotational levels. In principle, the rotational temperature of each level can be uniquely determined by the analysis of the line profiles. The analysis does yield the rotational temperatures of the higher rotational levels, since the line profiles for the first few vibrational levels are dependent almost exclusively on the T_{eff} for large J . For higher vibrational levels, the lines are significantly weaker. The line profiles hence are less reliable, and, although limits on the rotational temperatures can be found, the range is so large that the limits are practically useless. For the X Per line profiles, the range for the excitation temperature of the $J=1-0$ level is 2 K to 10 K. This range includes the $J=1-0$ rotational temperature determined from the radio analysis (6.7 K, of 5.5.1). The UV line profiles are consistent with a single rotational temperature of 4.5 ± 0.5 K. The rotational temperature for the lowest three rotational levels could be higher and still be consistent with the UV line profiles.

The major problem in using the line profile to determine the column density is that it is hard to get a global idea of the goodness of fit from visual comparison of the theory and data. The fit might be good for a few vibrational bands, but it is much worse for others. To circumvent this problem, I compare the theoretical and observed curves of growth since, in this case, it is easy to visually determine the global goodness of fit.

The column density derived from the curve of growth analysis of the ^{12}CO vibrational bands is $7.0 \times 10^{15} \text{ cm}^{-2}$ ($\log N = 15.85 \pm 0.05 \text{ cm}^{-2}$). Figure 5-9 shows the observed ^{12}CO line profiles (cf Figure 3-4a) plotted over the theoretical line profiles. The fit is well within the observational errors. Figure 5-10 shows the theoretical curve of growth along with the observed ^{12}CO and ^{13}CO data. The ^{13}CO equivalent width derived from this curve of growth is $1.0 \times 10^{14} \text{ cm}^{-2}$ ($\log N = 14.00 \pm 0.05 \text{ cm}^{-2}$). The error in the velocity parameter is 0.1 km/s for ^{12}CO , and 0.3 km/s for ^{13}CO . The conclusion is that, if the ^{13}CO radio column density is correct, then $\leq 1/3$ of the ^{13}CO lies in front of X Per.

The $^{12}\text{CO}/^{13}\text{CO}$ ratio is 70 ± 8 . This ratio is 23 ± 10 with the radio ^{13}CO column density. The curve of growth of diatomic hydrogen can have higher b value than the neutral species (cf 5.5.2). This suggests that there is a higher fraction of H_2 than neutrals in the higher velocity parameter component. These CO data suggest the opposite, that the percentage of neutrals in the 10 km/s component is much greater than the percentage of CO in the 10 km/s component. It appears then that although CO is generally a good tracer of H_2 , it may not be so in a detailed sense.

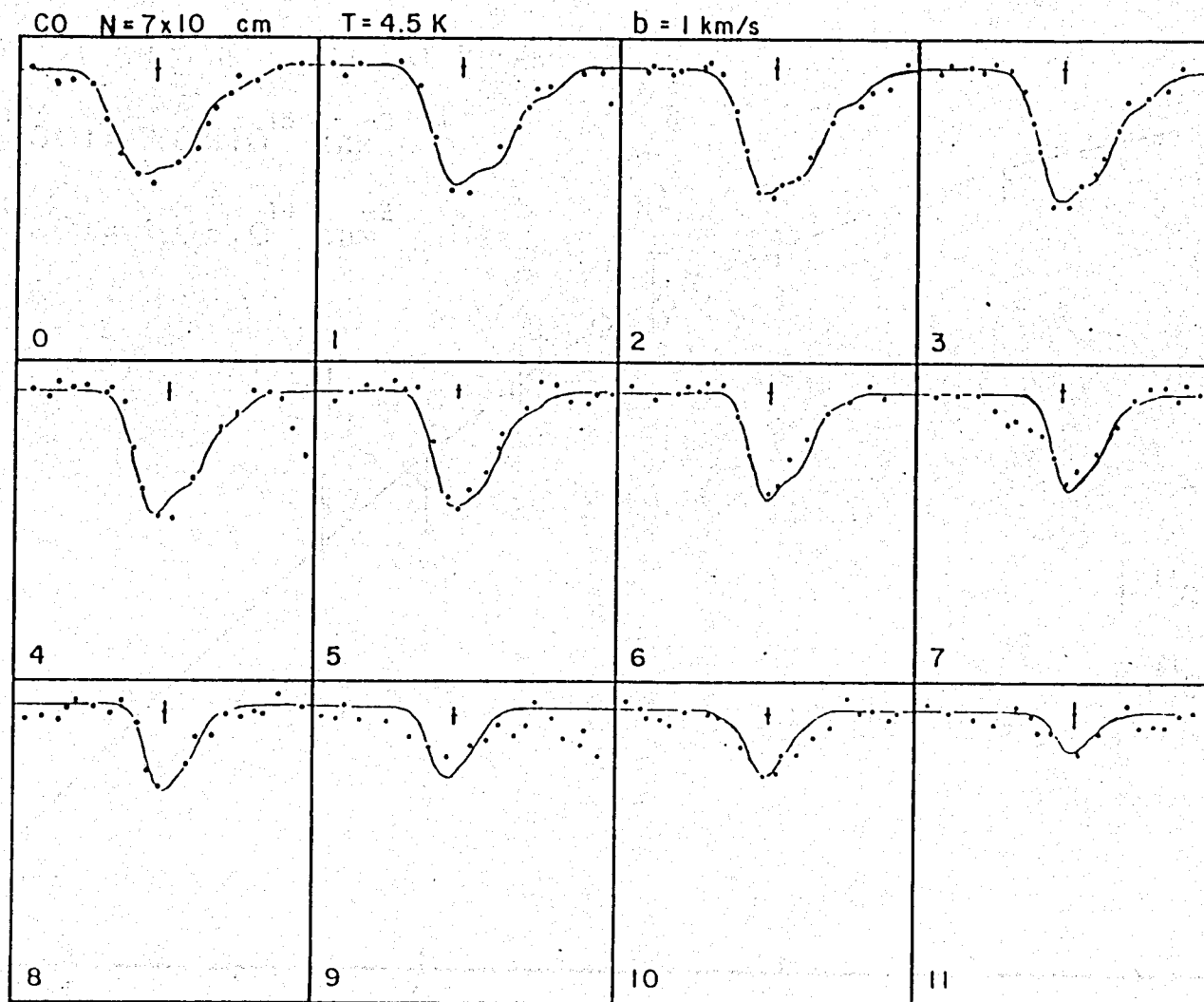


Figure 5-9. Observed (filled circles) and theoretical line profiles for the first 12 vibrational bands of the A-X system of ^{12}CO for $N = 7.0 \times 10^{15}$ cm^{-2} , $T_e = 4.5$ K, and $b = 1$ km/s.

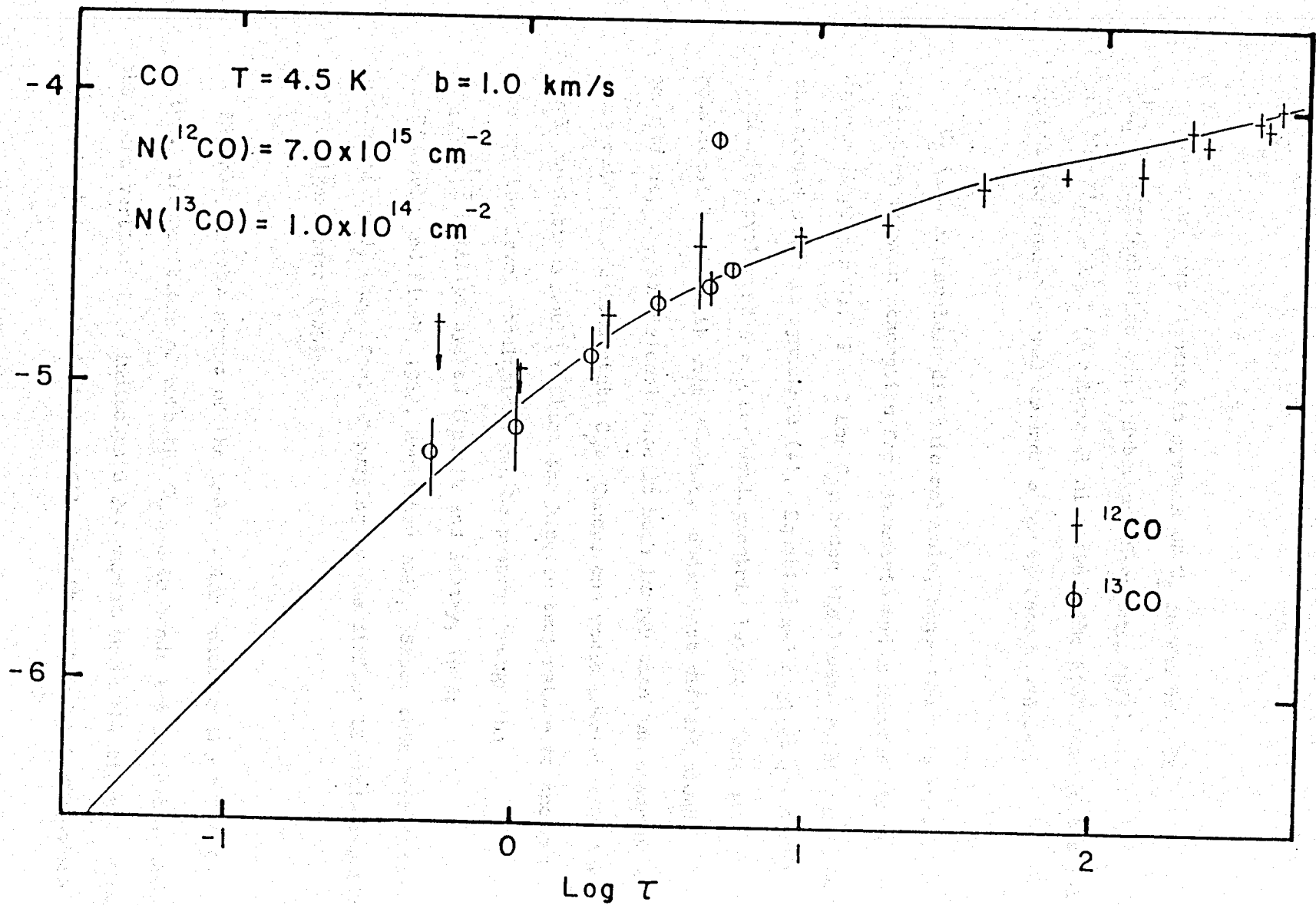


Figure 5-10. Theoretical and observed curves of growth for the A-X system of ^{12}CO (filled circles) and ^{13}CO (open circles). The length of the line through the point corresponds to a $2\text{-}\sigma$ variation in the measurement.

5.6 C_2

There are two electronic systems of C_2 in the UV. The $D^1\Sigma_u^+ - X^1\Sigma_g^+$ (Mulliken band; Huber and Herzberg, 1979) and the $F^1\Pi_u - X^1\Sigma_g^+$ (Herzberg et al. 1969) The R(0) line of the D-X system has been observed towards α Per by Snow (1976).

C_2 is a homonuclear diatomic molecule, hence there is an intensity variation between absorption from symmetric and antisymmetric rotational levels (Appendix C). $I = 0$ for C_2 , hence the lowest rotational level of the ground state is symmetric (+). Equation A-34a gives $\phi = 1$ for symmetric levels and $\phi = 0$ for antisymmetric levels. Thus only rotational levels with even J exist. Under most diffuse cloud conditions, the collisional rate is much larger than the quadrupole decay rate for excited state C_2 . Hence, one would predict that the level populations would reflect the kinetic temperature of the gas. However, the level populations can be pumped through the $A^1\Pi_u - X^1\Sigma_g^+$ Phillips system (Ballik and Ramsay, 1963; van Dishoeck and Black, 1982, hereafter vDB). Since this transition is in the infrared, the effect of pumping by the diffuse IS radiation field can be significant (vDB).

Figure 3-4c shows part of the order which contains the 0-0 F-X system. The positions of both the C_2 and CO bands are indicated, and the short vertical line indicates a $2-\sigma$ variation in the signal. Figure 5-11 shows the normalized line profile for the 0-0 and 1-0 vibrational

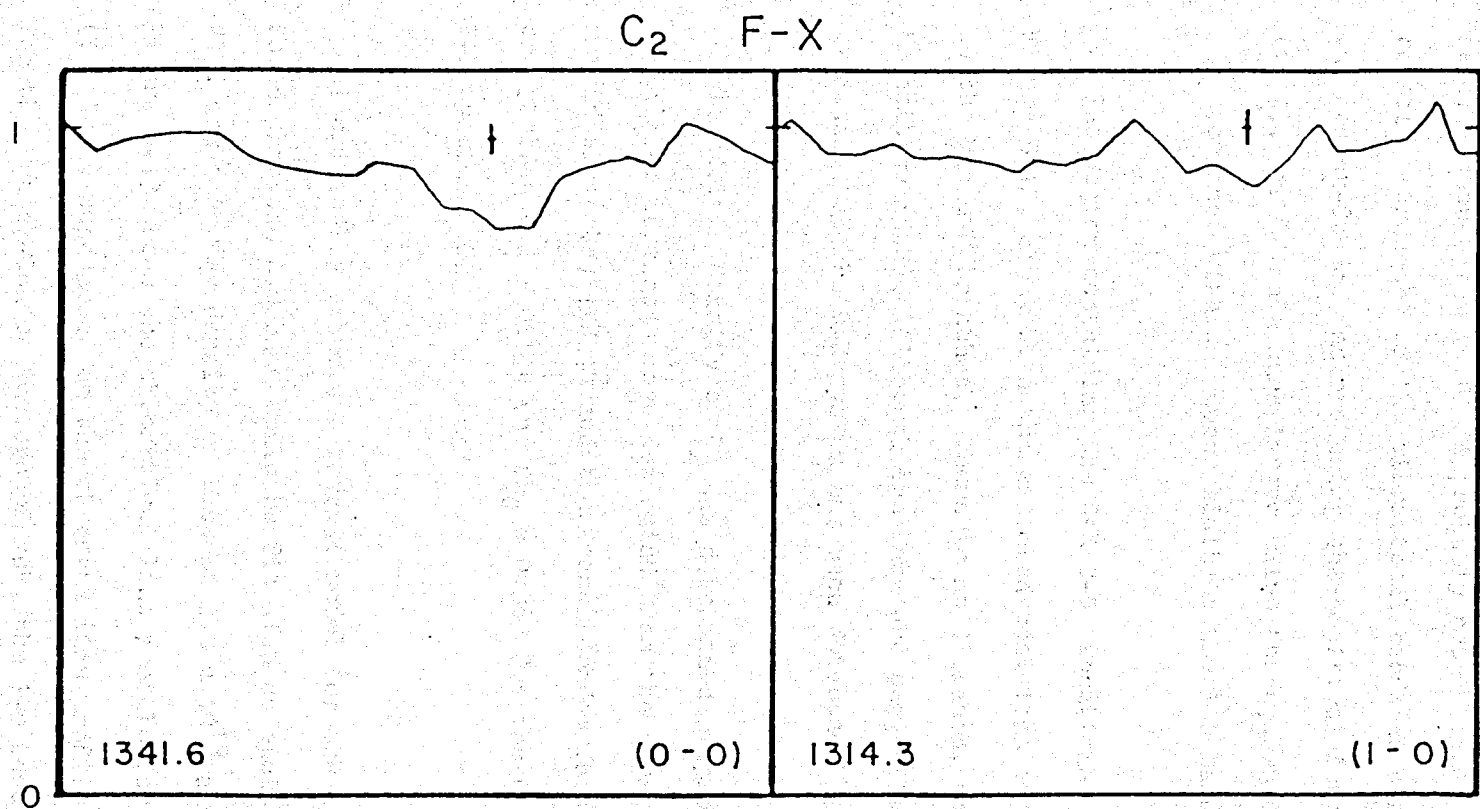


Figure 5-11. Normalized line profiles for the 0-0 and 1-0 bands of the F-X system of C_2 .

bands of the F-X electronic system of C_2 . The (0,0) band is clearly seen, although the (1;0) is probably not. This is consistent with the relative strengths of the vibrational bands as determined by calculating the Franck-Condon factors using the empirical formula of Nicholls (1973). vDB find a much larger value for q_{10} which is still marginally in accordance with the upper limit on the 1-0 band profile.

The region containing the D-X 0-0 vibrational band is shown in Figure 5-12, along with the expected positions of the first four lines in the P and R branches. There is no Q branch, as $J \neq 0$ for a $\Sigma-\Sigma$ transition (4.2). Although the data are suggestive, there is no clear evidence that the D-X system has been detected.

The column density of C_2 was determined by profile fitting. The oscillator strengths were determined from the square of the sum of dipole matrix elements, $|\Sigma R_e|^2$ and the Franck-Condon factors calculated by vDB, and yielded $f_{00} = 0.104$ and $f_{10} = 0.063$ for the 0-0 and 1-0 bands of the F-X system of C_2 .

I originally assumed a thermal model for the level populations, and found that the 0-0 band could be fit with an excitation temperature of 40 K and a column density of between 2.0×10^{13} and $4.0 \times 10^{13} \text{ cm}^{-2}$. Figure 5-13 shows the theoretical line profile for $N = 3 \times 10^{13} \text{ cm}^{-2}$ ($T = 40 \text{ K}$) superposed on the observed line profile (filled circles). For the Franck-Condon factors of vDB, the 1-0 band should be seen. The observed upper limit for the 1-0 band is consistent with the

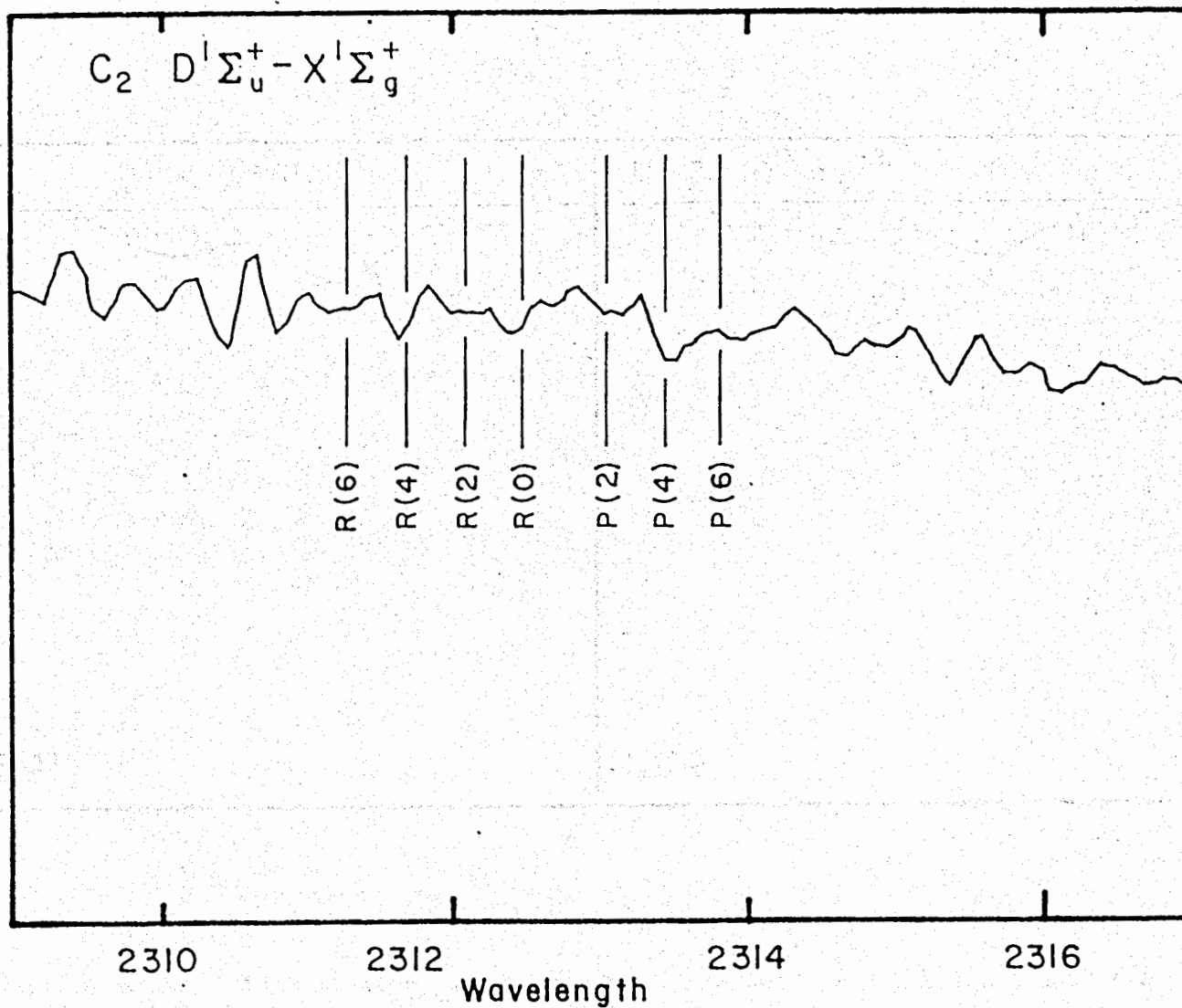


Figure 5-12. The spectrum of $X^1\Sigma_g^+$ in the region near the 0-0 band of the D-X electronic system of C_2 . The expected positions of the first seven rotational lines of this system are indicated.

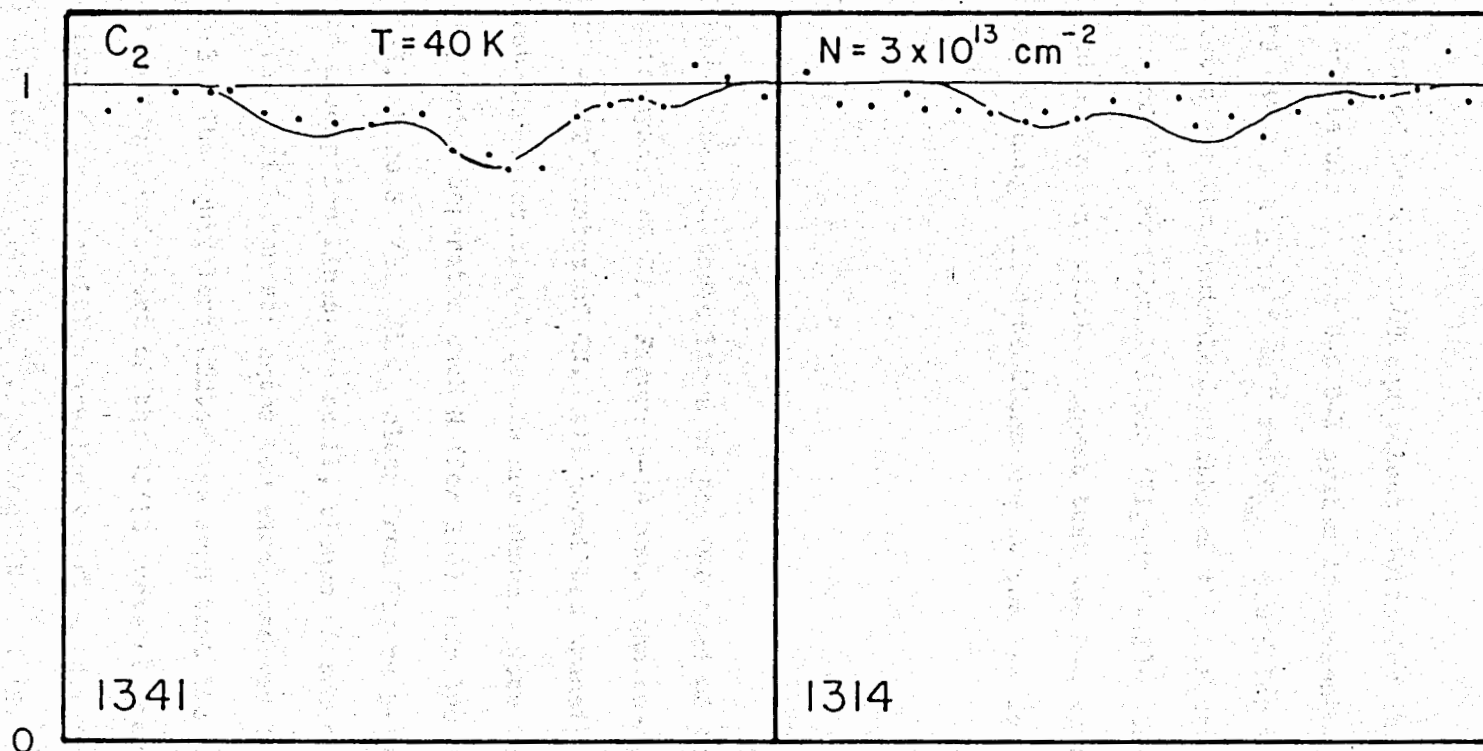


Figure 5-13. Observed (filled circles) and theoretical line profiles of the 0-0 and 1-0 bands of the F-X system of C_2 for $N = 3 \times 10^{13}\text{ cm}^{-3}$, $T = 40\text{ K}$, and $b = 1\text{ km/s}$.

Frank-Condon factors of Nicholls (1973). Quantitative laboratory work is needed for this system.

A list of the expected equivalent widths for the first four rotational levels of the 0-0 D-X system is presented in Table 5-5, assuming $N(C_2) = 4 \times 10^{13} \text{ cm}^{-2}$ and $f_{00} = 0.045$ for the D-X system (vDB). Also listed are the equivalent widths of the features near the expected positions of the rotational lines (Figure 5-12). The measured and predicted equivalent widths suggest that the D-X system may have been detected, although all detections are at the 1- σ level.

5.7 CN

I have detected three lines of the 0-0 band of the $B^1\Sigma^+ - X^1\Sigma^+$ electronic system of CN. Figure 5-14 shows the energy level diagram of the $B^1\Sigma^+ - X^1\Sigma^+$ system of CN. All permitted transitions observable from the first three rotational levels are shown. Note that it is spin splitting which separates each N (for $N \neq 0$) into two components: $J=N+S$ and $J=N-S$, where $S=1/2$. It is clear from Figure 5-14 that all of the observed absorption lines are really blends of two or three rotational lines. The oscillator strengths for each observed line are given in Table 3-3. The equivalent widths are such that the lines are all either thin or on the 1 km/s part of the 90/10 curve of growth (Figure 5-4). The derived column densities are $\log N(N=0) = 13.1 \pm 0.1, \text{ cm}^{-2}$, $\log N(N=1) = 12.67$ to $13.13, \text{ cm}^{-2}$, and $\log N(N=2) < 12.1 \text{ cm}^{-2}$. The ratio of

TABLE 5-5
 C_2 D-X COLUMN DENSITIES¹

Transition	Lambda (Å)	f-value	Eq. Width	
			Theory (mÅ)	Observation (mÅ)
R(0)	2312.45	0.045	11	12
R(2)	2312.05	0.027	22	7
R(4)	2311.66	0.025	15	14
R(6)	2311.28	0.024	5	--
P(2)	2313.04	0.018	15	10
P(4)	2313.42	0.020	12	16
P(6)	2313.82	0.021	4	4

$$N_{C_2} = 4 \times 10^{13} \text{ cm}^{-2} \quad T_{\text{Rot}} = 40 \text{ K}$$

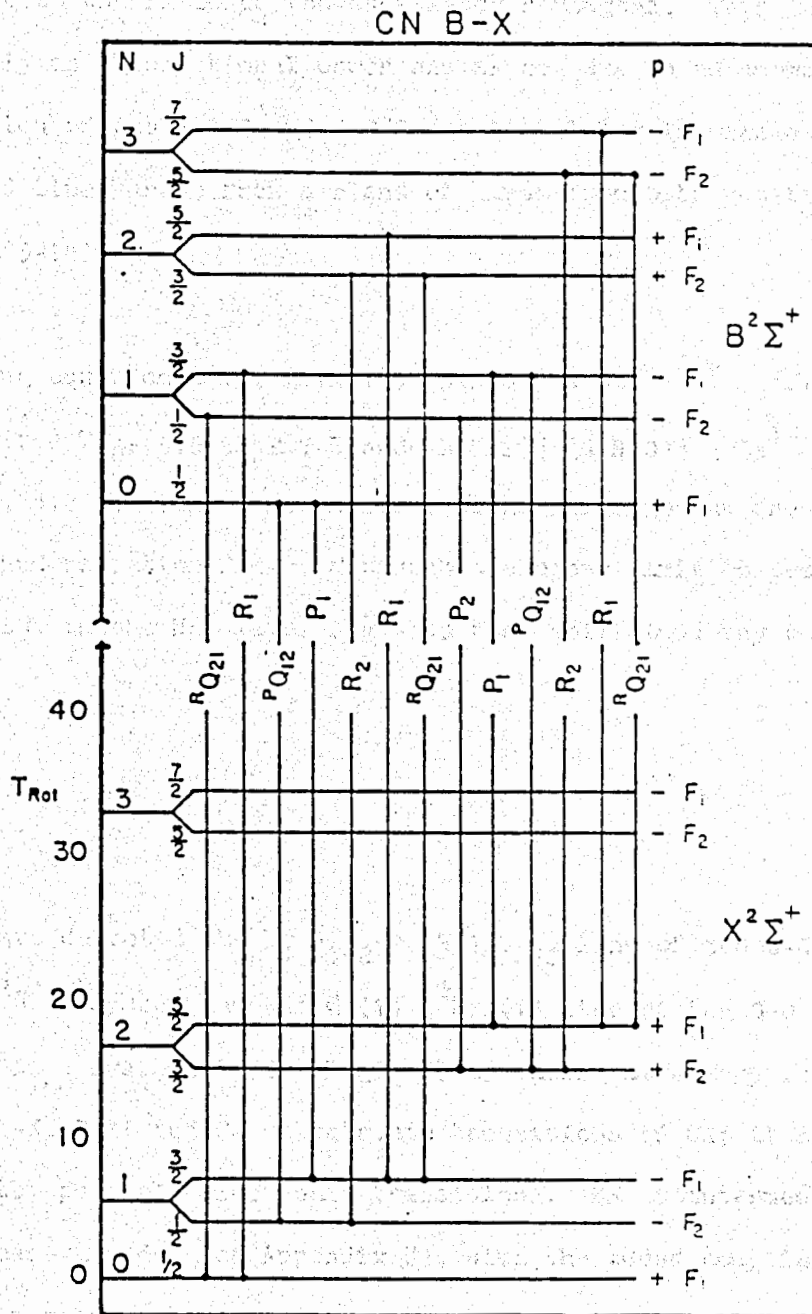


Figure 5-14. Energy level diagram for the B-X system of CN. The permitted transitions from the first few rotational levels of the ground state are indicated.

the equivalent widths of the two lines arising from the $N=1$ level are opposite to the ratio of the oscillator strengths. This is most certainly an observational error and is not due to an anomalous population of the $J=1/2$ and $J=3/2$ rotational levels, since both of the observed lines arise from a blend of lines from both rotational levels (Figure 5-14).

Using equation C-16, $[N(N=1)]/[N(N=0)] = 3e^{-5.4/T} = 1.15$ to 0.40 , which gives $T_{10} = 5.6$ to 2.7 K and $[N(N=2)]/[N(N=0)] = 5e^{-16.3/T} < 0.1$, or $T_{20} < 4.2$ K. This is consistent with excitation by the 2.8 k background radiation field, although the upper limit on the level population in the $N=1$ level suggests that collisions may be important.

5.8 CH

I have detected the $R(1)_{1e2e} + R(1)_{1f2f}$ line of the 0-0 band of the $A^2\Delta - X^2\Pi_{1/2}$ system and the $Q_2(1) + Q_{R12}(1)$ line of the 0-0 band of the $B^2\Sigma^- - X^2\Pi_{1/2}$ system of CH. Figure 5-15 shows the energy level diagram of the A-X, B-X, and C-X electronic transitions of CH; it also shows a few of the possible electronic transitions. CH is intermediate between Hund's case a and b (cf Appendix C), with the added complication of a switch in polarity of the lowest rotational level in the $^2\Pi_{1/2}$ ladder. This makes it a member of the F_2 ladder ($^2\Pi_{3/2}$). The state is split due to Λ -type doubling, and the three permitted radiofrequency transitions between the hyperfine split Λ doublet are shown. Since the

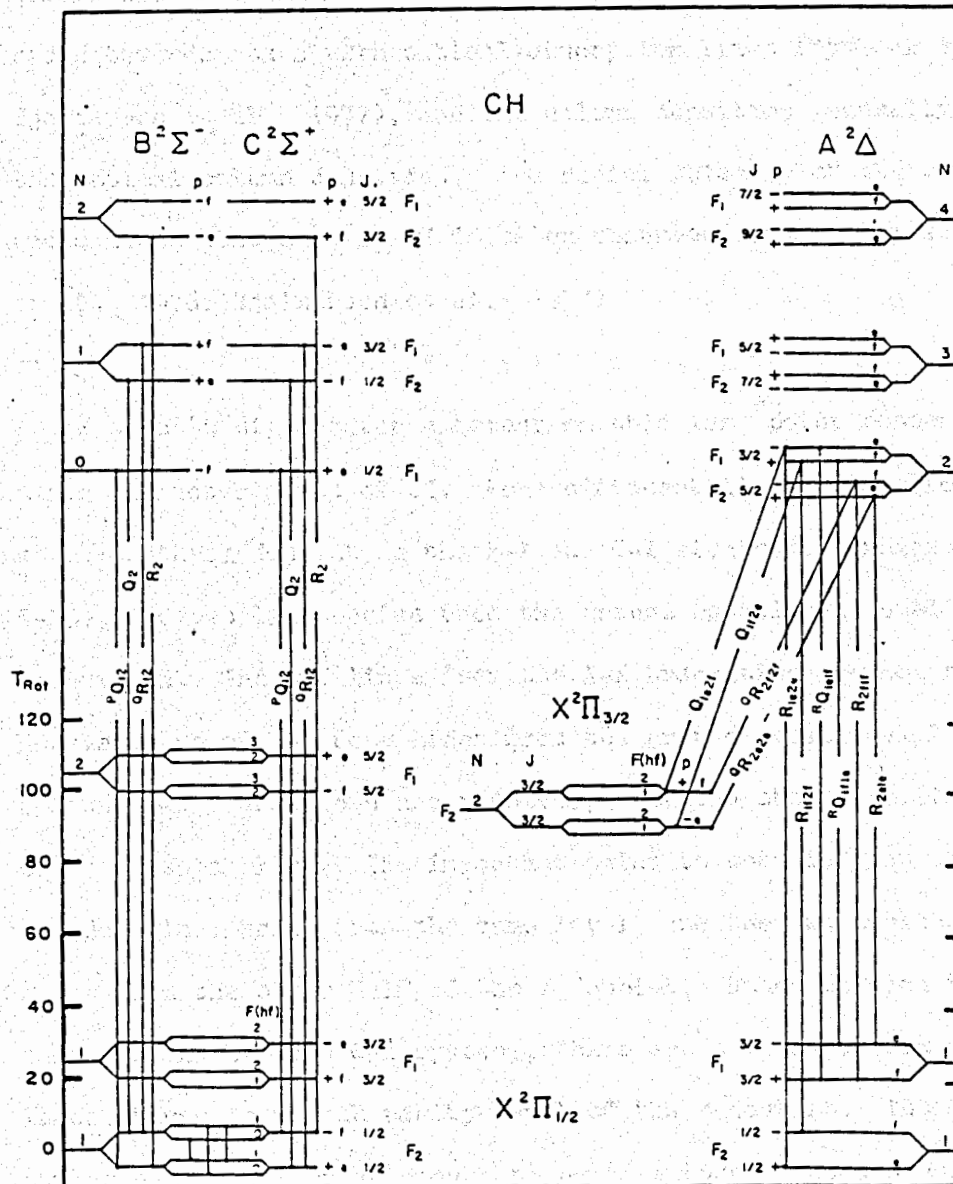


Figure 5-15. Energy level diagram for the A-X, B-X, and C-X systems of CH. The optical and radio transitions from the ground state lambda doublet are indicated.

N=1 level of the F_1 ($^2\Pi_{3/2}$) ladder is 26 K above the ground state, it is normally not populated under diffuse cloud conditions, and, indeed, absorption from this level is not seen. CH has been detected in the radio towards stars with optical absorption lines (Rydbeck et al. 1976; Hjalmarson et al. 1977), and the column densities generally agree with the optical column densities. The radial velocity of the optical and radio lines also agree. CH is often observed as a weak maser (Rydbeck et al. 1976; Hjalmarson et al. 1977).

I wish to digress for a moment on this last point concerning the maser characteristics of CH. Four different lines arise from the ground state of the Λ doublet in the B-X and C-X electronic transitions (Figure 5-15), and two lines arise from the ground rotational level in the A-X transition. The two lines from the A-X transition are not resolved. However, two of the four lines from the ground rotational level in the B-X and C-X transitions are resolved, with the other two lines being observed as a blend. The important point to note is that the two blended lines arise from the same level, and the two unblended lines arise from the other half of the Λ doublet. Hence between the two 0-0 bands of the B-X and C-X systems, there are a total of six absorption lines, three from each parity level of the Λ doublet. The oscillator strengths are different enough to be able to construct a relatively accurate curve of growth, especially if it is only the relative level population which is of interest. Thus we have in CH a way of unambiguously measuring the relative level populations of a system which is observed as a maser at radio frequencies.

This discussion raises two points about the CH column densities in the literature. The column densities derived from the 4300 Å line measures the total column density, whereas the column density derived from the 3886 Å line is only about half the total column density, as the 3886 Å line only samples the lower half of the Λ doublet.

Another problem exists in the proper oscillator strengths to use for the various lines. For the $J=1/2$ ($N=1$) level of CH, $J < \Lambda + S$ ($=1 + 1/2$), hence the degeneracy of the ground rotational state is less than $2S+1$ (Schadee, 1975; cf Appendix C for a discussion of first rotational lines). The sum of the individual Honl-London factors is 4 (equation C-3) for the $J=1/2$ level of CH. The sum rule includes a summation over parity, as each transition from each parity (Λ doublet) level is defined as a rotational line. The 4300 Å line then actually consists of two separate rotational lines, each with an oscillator strength of $f_{nv\Delta Jp} = f_{v'v''} = 4/2/2 = f_{v'v''}$ (Schadee, 1975). At the expense of being redundant, each line of the 4300 Å transition has $f = f_{v'v''}$. The total oscillator strength for the 4300 Å transition is thus twice the band oscillator strength. The value of the oscillator strength used in the literature is just one times the band oscillator strength. Hence the total column density has been overestimated by a factor of two. Similarly, the 3886 Å transition is composed of two rotational lines with individual oscillator strengths of $f(Q_2)_{nv\Delta Jp} = 2/3f_{v'v''}$ and $f(Q_{R_{12}})_{nv\Delta Jp} = 1/3f_{v'v''}$. The total oscillator strength of the 3886 Å transition is the sum of the individual oscillator strengths, or $f_{v'v''}$; again, this is twice the value quoted in the

literature. Since the 3886 Å transition results in only half the total column density, the literature values are reasonably accurate. They are twice as large due to the oscillator strength error but are half as large since they fail to consider the upper half of the Å doublet.

For X Per, the 4300 Å transition yields $\log N_{4300} = 13.57 \text{ cm}^{-2}$ and $\log N_{3886} = 13.52 \text{ cm}^{-2}$. A high dispersion spectrum of X Per was obtained with the coude spectrograph (Crutcher, 1982). The equivalent widths of the 3890 Å and 3876 Å lines of CH from this spectrum are 7.4 mÅ and 3.0 mÅ, respectively. These equivalent widths correspond to log column densities of 13.46 cm^{-2} and 13.37 cm^{-2} , respectively. Within the errors of the measurements, these column densities are the same, although the difference between the column densities of the upper and lower halves of the Å doublet may be real. The total column density is the sum of the two individual column densities, or $\log(N_{B-X}) = 13.79 \text{ cm}^{-2}$. Clearly, the total column densities from the 4300 Å and 3886 Å transitions disagree. For the column densities to agree, I find that either the band oscillator strengths for the two transitions must be equal or that the velocity parameter of the CH curve of growth is less than 1 km/s. Hinze et al. (1973) calculated theoretical oscillator strengths for the known optical systems. From their discussion, the oscillator strengths, both theoretical and experimental, are not equal. This suggests then that the velocity parameter of the CH curve of growth is less than 1 km/s. I find that for $b = 0.75 \text{ km/s}$, $\log N_{4300} = 14.0 \text{ cm}^{-2}$ and $\log N_{3886} = 13.69 \text{ cm}^{-2}$ and $\log N_{3890+3876} = 13.62$

cm^{-2} . The sum of the column densities is $\approx 14.0 \text{ cm}^{-2}$. The line width of the ^{13}CO J=1-0 line is between 0.9 and 0.8 km/s (Figure 3.1), hence it is possible for $b_{\text{CH}} \approx 0.75 \text{ km/s}$. This is further support for the existence of a velocity parameter gradient and is also consistent with most of the CH being in the central part of the cloud.

Although the line strength analysis for CH presented in this section is correct, more work needs to be done to interpret the implications of both the difference in oscillator strengths and the difference in level populations. Lines arising from the both halves of the Λ doublet have been observed towards ζ Oph (Herbig, 1968) and ζ Per (Chaffee and White, 1974). The historical error in determining the CH column density is typified by Chaffee and White (1974), who averaged the column densities derived from the two halves of the Λ doublet instead of adding them.

Herzberg and Johns (1969) have found a number of new electronic transitions of CH in the vacuum UV. They suggest that the G-X (3d complex with an unknown electronic structure) near 1370 \AA would be the strongest system in the UV. However, they were not able to make rotational line assignments, hence the lines arising from the ground rotational level are not known. Table 5-6 lists the expected positions of the IS lines arising from the J=1/2 level of the $^2\Pi_{1/2}$ ladder. These lines were searched for, but were not seen. There appears to be a weak (2- σ) line at 1369.4 \AA , which corresponds to one of the rotational lines listed by Herzberg and Johns (1969). However, since the rotational assignments of this system are unknown, no conclusions can be

TABLE 5-6
CH ULTRAVIOLET ABSORPTION LINES

System	Line	Wavelength (Å)
$D^2 \Pi_{1/2} - X^2 \Pi_{1/2}$	$R_1 (\frac{1}{2})$	1695.34
	$S_{R_{21}} (\frac{1}{2})$	1693.24
$E^2 \Pi_{1/2} - X^2 \Pi_{1/2}$	$Q_1 (\frac{1}{2})$	1557.58
	$R_1 (\frac{1}{2})$	1557.13
	$S_{R_{21}} (\frac{1}{2})$	1558.88
$F^2 \Sigma^+ - X^2 \Pi_{1/2}$	$Q_1 (\frac{1}{2})$	1549.62
	$R_1 (\frac{1}{2})$	1549.05
	$S_{R_{21}} (\frac{1}{2})$	1547.87

drawn.

5.9 CH⁺

The CH⁺ line at 4232 Å (R(0) line of the 0-0 band of the A¹Π - X¹Σ⁺ electronic system) is normally much stronger than the 4300 Å line of CH, mostly because of the oscillator strength. The column density of CH⁺ is normally less than half the column density of CH (Dickman et al. 1981). Cohen (1973) observed only a trace, and my maximum equivalent width is 10 mÅ (Table 3-3, Figure 3-2). The maximum column density is $N_{\text{CH}^+} < 5 \times 10^{12}$ ($\log N_{\text{CH}^+} < 12.7$), assuming that the line is optically thin. The CH⁺/CH ratio is consistent with that found toward other stars (Dickman et al. 1981).

5.10 OH

The radio observations of OH (Table 3-1) and the relationship $N_{\text{OH}} = 2.3 \times 10^{14} \Delta v T_R^*$ (Sancisi et al. 1974) gives $N_{\text{OH}} = 2.5 \times 10^{13} \text{ cm}^{-2}$ ($\log N_{\text{OH}} = 13.4 \pm 0.1$). Assuming that all the OH is in the ground rotational state ($J=3/2$, X²Π_{3/2}), the equivalent widths for the UV absorption lines arising from this level are 0.56 mÅ (Q₂(3/2) 0-0 D²Σ⁺ - X²Π_{3/2}, λ = 1222.07 Å) and 0.92 mÅ (Q₂(3/2) 0-0 A²Σ⁺ - X²Π_{3/2}, λ = 3079.33 Å), both of which are below the detection limits of the IUE. Indeed, a search for the 1222.07 Å and the 3079.33

\AA lines yield only upper limits for the equivalent widths (5 m \AA and 10 m \AA , respectively).

5.11 H₂O

UV absorption from the $\tilde{C}(0,0,0) - \tilde{X}(0,0,0)$ and the $\tilde{F}(0,0,0) - \tilde{X}(0,0,0)$ electronic transitions of H₂O have been searched for towards ζ Oph (Smith and Snow, 1978; Snow and Smith, 1982) and δ Sco (Smith and Snow, 1978). The only UV system of H₂O accessible to the IUE is the $\tilde{C}^1B_1 - \tilde{X}^1A_1$ system at 1240 \AA (Johns, 1963).

H₂O is split into an ortho-H₂O and a para-H₂O by symmetry, with transitions between ortho and para levels forbidden by symmetry (Green, 1980). The para-H₂O contains the ground rotational state, 0_{00} . The next rotational level, 1_{10} , is of ortho symmetry and is 34.2 K above the ground state. The population of the two levels should be thermal, as radiative transitions between the two levels are forbidden. The expected relative population is $N_o/N_p = 9e^{-34/T} = 3.8$ for $T = 40$ K. The two lines arising from these two rotational levels are the $1_{11} - 0_{00}$ (1239.728 \AA) and $0_{00} - 1_{10}$ (1240.949 \AA). Smith et al. (1981) estimate the oscillator strength for the 1239 \AA line as $f_0 = 0.018$, and measure the oscillator strength of the 1240 \AA line as $f_1 = 0.0082$. Assuming the lines are optically thin, then the ratio of the equivalent widths for $T = 40$ K is $W_1/W_0 = 1.4$.

Figure 3-4d shows the expected positions of the 1239 and 1240 lines of H_2O . The equivalent widths of the two lines are $5 \pm 4 \text{ m}\text{\AA}$ and $7 \pm 4 \text{ m}\text{\AA}$, respectively ($2\text{-}\sigma$ error). The ratio of the 1240 \AA equivalent width to the 1239 \AA equivalent width is 1.4 ± 0.7 . Figure 5-16 shows the 1240 \AA region for the individual spectra. Vertical lines are drawn at the expected positions of the two rotational lines as well as for the positions of the two lines of the Mg II 1240 \AA doublet. The S/N for each spectrum can be estimated by the strength of the Mg II lines. A feature clearly exists at 1239.73 \AA for all well exposed spectra. The 1240.949 \AA line also appears in most of the spectra. These data strongly suggest that the identification is real. The total column density of ortho- H_2O is $\log N(\text{ortho}) = 13.8 \pm 0.1 \text{ cm}^{-2}$, and the column density of para- H_2O is $\log N(\text{para}) = 13.3 \pm 0.1 \text{ cm}^{-2}$, which is approximately three times the column density of OH (5.10).

5.12 Unidentified Lines

An order by order search of the stacked spectra yielded a number of possible unidentified (U1) lines which were more than $3\text{-}\sigma$ above the noise. A more detailed analysis has shown that most of these features are due to a reseau or the superposition of many strong systematic noise features. Four lines were observed which cannot be attributed to any form of noise and are thus considered real. Table 3-7 lists the central wavelengths of the feature, the equivalent width of the line, and the log of the product of the column density times the oscillator

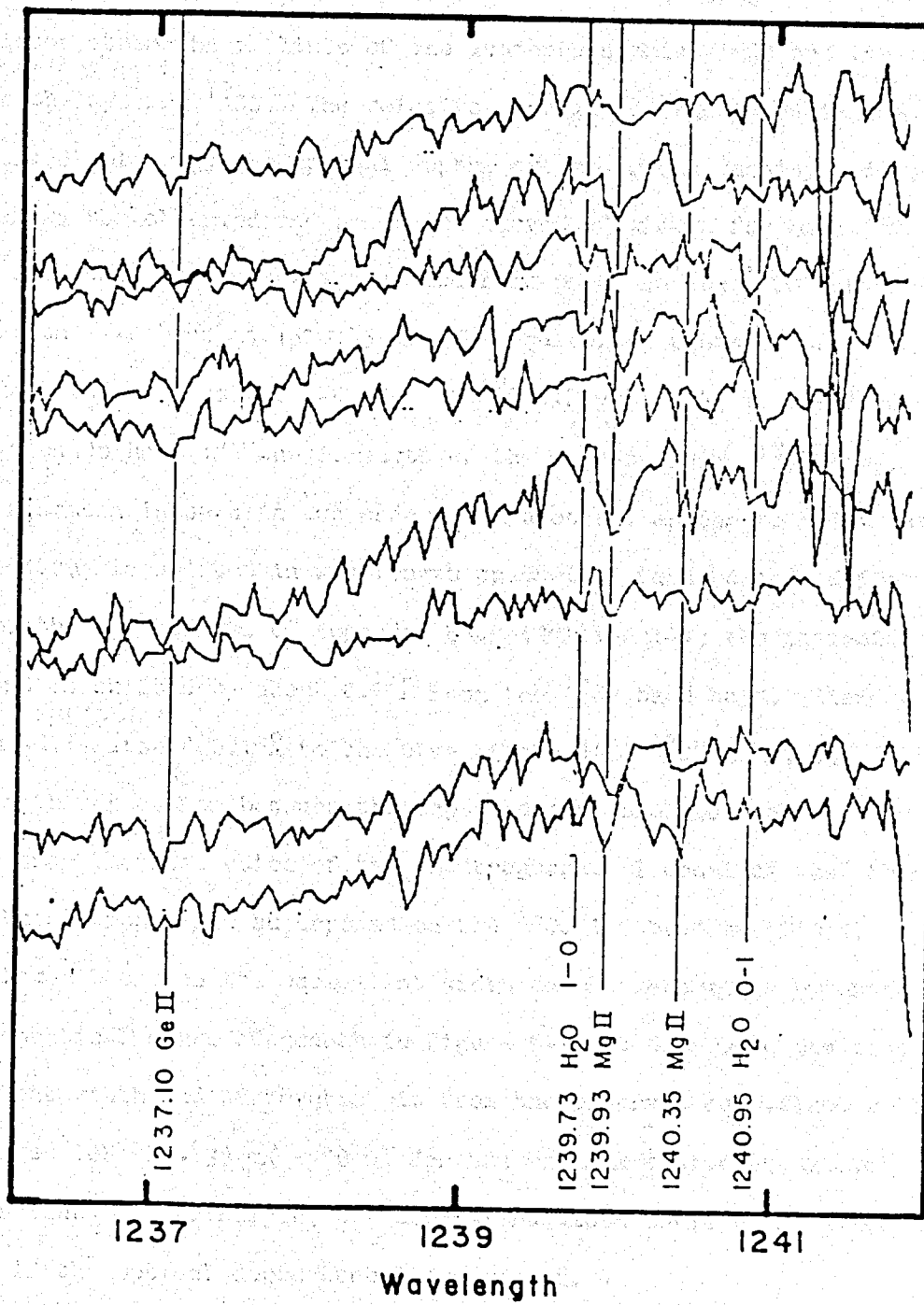


Figure 5-16. The nine SWP spectra in the region near the 1240 Å C-X system of H₂O. The stacked version is shown in Figure 3-4d.

strength- $\log Nf$. Figure 3-4(e-h) displays plots of these features. The existence of a fifth U1 can be inferred the following way. The oscillator strengths of lines of the isotopic species ^{13}CO are the same as for the species ^{12}CO . The relative strength of each band is then determined solely by the optical depth, eg the column density. Figure 5-10 shows the observed and predicted curves of growth for both ^{12}CO and ^{13}CO . Note that there is one aberrant point in the ^{13}CO curve of growth: the 1-0 band at 1510.45 Å. The equivalent width of this line is almost the same as the 1-0 band of ^{12}CO (Figure 3-4g). The ^{13}CO 2-0 and 3-0 bands have 1/4 the strength of the corresponding ^{12}CO line. This phenomena is seen in two orders and does not appear to shift when the spectrum is shifted in wavelength space (eg, focused on a different part of the KCl target, cf Appendix B). Additionally, the centroid of the band is shifted by about 0.1 Å from the ^{13}CO band head. Since the band head is itself 0.1 Å to the blue of the R(0) ^{13}CO line, the wavelength separation between the expected and observed centroids is larger than the resolution of the spectrograph. I conclude that there is another strong line superposed on the ^{13}CO 1-0 band at 1510.45 Å. A lower bound on the equivalent width can be determined by using the theoretical curve of growth in Figure 5-10 to determine the true 1-0 equivalent width and subtracting it from the observed equivalent width. This gives $108 \text{ mÅ} - 38 \text{ mÅ} = 70 \text{ mÅ}$ for the minimum equivalent width of this line. In principle, the equivalent width could be as large as 108 mÅ if the optical depth were large enough.

I have done an exhaustive literature search for molecular UV absorption features. It is surprising how little information exists about the UV spectra of most molecules. Even molecules with well studied optical spectra often have little or no UV data. Even if the UV spectrum is known, quantitative work has seldom been done.

The results of the search were negative for the 1419 Å, 2512 Å, and 2511 Å lines.

The photoelectron spectrum of CO (Asbrink et al. 1974) shows the existence of an excited state of CO^+ near 1543 Å. It is probably a Σ state. The wavenumber of the band is 64800 cm^{-1} (Huber and Herzberg, 1979), which corresponds almost exactly with the observed wavenumber, 64803.6 cm^{-1} . However, no UV absorption spectrum of this system has been obtained. If the oscillator strength of this band is 0.1, then the column density is $\log N = 13.3 \text{ cm}^{-2}$ and $N(\text{CO}^+)/N(\text{CO}) < 2.5 \times 10^{-3}$. Neither the $\text{A}^2\Pi - \text{X}^2\Sigma^+$ (4325.18 Å) or the $\text{B}^2\Sigma^+ - \text{X}^2\Sigma^+$ (2190.52 Å) (2190.52 Å) lines of CO^+ were detected. However, with oscillator strengths of 0.00035 and 0.005, respectively, the implied equivalent widths are 1.1 mÅ (4325 Å) and 4 mÅ (2190 Å). Both lines are below the detection limits of the instrument. These equivalent widths would be even smaller if the oscillator strength of the 1543 Å line were greater than 0.1.

The other possibility is that the 1543 Å and 1510 Å lines are the 0-0 and 1-0 bands of the $B^1\Sigma^+ - X^1\Sigma^+$ system of CS (Donovan, Husain, and Stevenson, 1970). The laboratory analysis shows two strong bands near the observed U1 lines. The resolution of the laboratory data is not very high, and it is not clear whether the reported wavelengths are the origins, bandheads, or simply the center of the absorption feature. If the published wavelength (1541 ± 1.5 Å) is the bandhead, then the low J levels could occur around 1543 Å. A high resolution spectra of this system would determine if indeed my U1 line is CS.

The 1-0 band of the B-X system has a published wavelength of 1510.0 Å, well within the measuremental errors of my U1 line at 1510.45 Å. However, Donovan et al. (1970) state that the 1-0 band is weaker than the 0-0 band. With a minimum equivalent width of 70 mÅ, the 1510 U1 line is twice the strength of the 1543 U1 line. If the 1543 Å and 1510 Å U1 line are due to CS, then the column density is $\log N_{CS} = 13.3$ for $f_{CS} = 0.1$. The R(0) line of the $A^1\Pi - X^1\Sigma^+$ system of CS lies at 2576.63 Å, very near the 2576.1 Å line of Mn II. Figure 5-17 shows the wavelength region near 2576 Å. The Mn II line is clearly seen, and there is a weak line at the expected position of the R(0) CS line. The equivalent width of this weak feature is 8 mÅ, which is near the 2- detection limit of the LWR camera. The strength of the 2576 Å line for $\log N = 13.3$ is 20 mÅ for $f_{A-X} = 0.0036$. The problem is that a single rotational line is not expected for the A-X system of CS. The J=1 level is 1.2 K above the J=0 level. From equation C-16, $N(J=1)/N(J=0) = 3e^{-1.2/2.8} = 1.97$: the J=1 level will

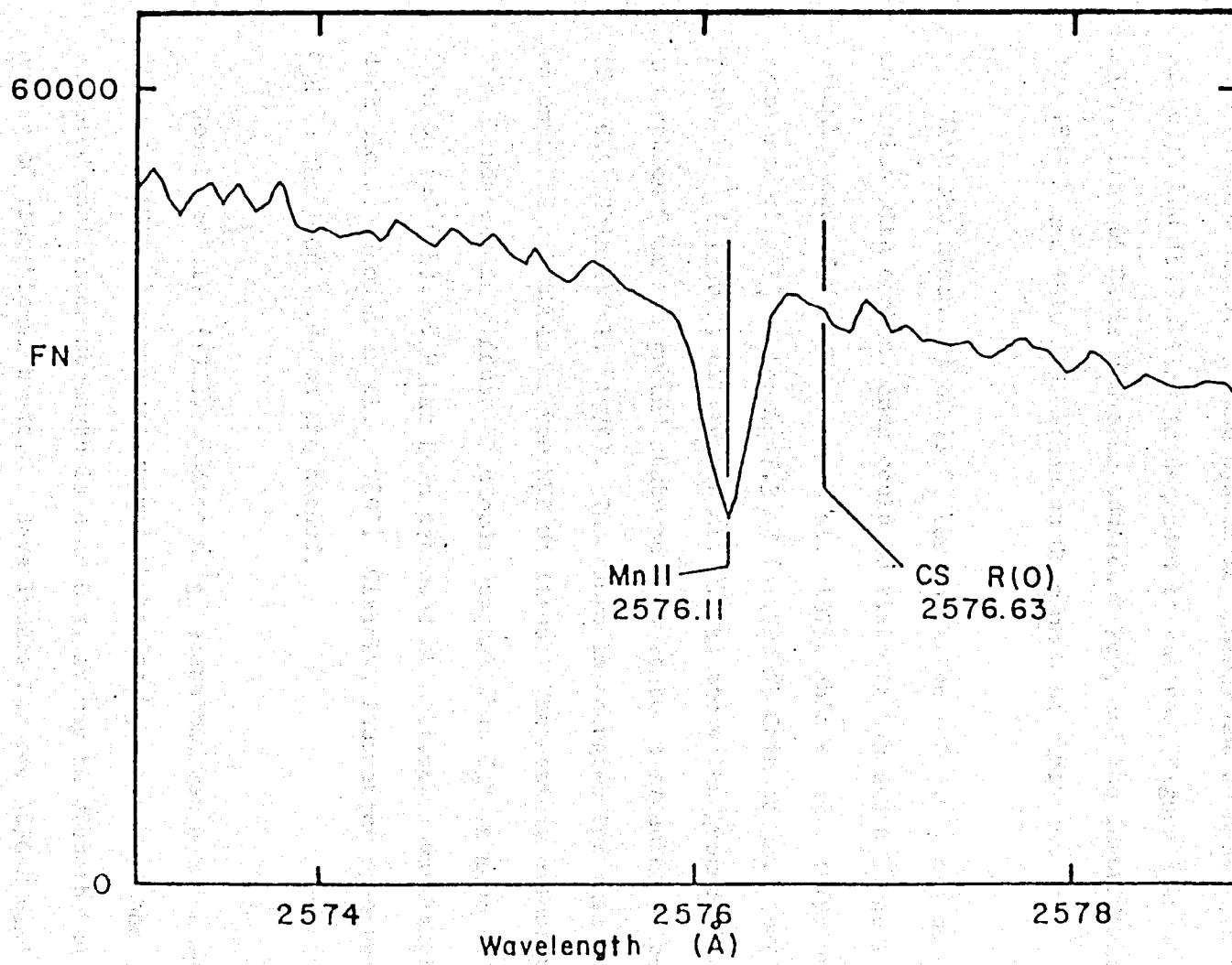


Figure 5-17. The expected position of the R(0) line of the 0-0 band of the A-X system of CS. The strong IS line is due to Mn II.

have a larger equivalent width than the $J=0$ level. Additionally, $|B'-B''| = 0.04 \text{ cm}^{-1}$, which is less than the effective wavenumber resolution of the IUE ($\approx 1.4 \text{ cm}^{-1}$, equation 4-28), and hence the band will be unresolved. A band system is clearly not seen at 2576 \AA , although the 1543 \AA line is degraded to the red (Figure 3-4f). The 2576 \AA line of CS is not seen towards X Per, and the identification of the 1543 \AA and 1510 \AA U1 lines as CS cannot be verified.

With the discovery of IS C_2 towards X Per (cf 5.6), two other molecules with carbon bonds could be visible: C_2H and C_3 . Ab initio calculations of C_2H (Hillier et al. 1975; Shih et al. 1979) show the existence of a $^2\Sigma^+$ state at $\approx 7.3 \text{ eV}$ (1700 \AA ; Shih et al. 1979) or 71900 cm^{-1} (1390 \AA ; Hillier et al. 1975) above the ground state. Absorption from the ground state to this state is expected to be strong ($f = 0.9$; Shih et al. 1979). The range in energies for this state encompasses all three of the SWP U1 lines. Theoretical calculations of the abundances in diffuse IS clouds suggest that C_2H is more abundant than CH (cf 6.5). C_2H has been detected at millimeter wavelengths in dark clouds (Wooten et al. 1980). Clearly, laboratory spectra of C_2H in the 1500 \AA region are needed.

Romelt et al. (1978) predict a $^1\Sigma_u^+$ state between 8 and 8.14 eV ($1550 \text{ \AA} - 1523 \text{ \AA}$) above the ground state for C_3 . Although the expected oscillator strength is near 0.9, it may be distributed over a number of vibrational bands. I have looked for the 4050 \AA band of C_3 on my KPNO plates of X Per, but was unable to detect it. I would

strongly suggest that a much higher S/N spectra be obtained of X Per in the visible to search for C_3 .

Clearly, high resolution laboratory spectra of these and other molecules must be obtained if the composition of the diffuse ISM is to be understood. The need for such spectra will greatly increase when the Space Telescope is launched in 1985.

5.13 Molecular Line Search

Table 5-7 lists the molecule, electronic system, wavelength, oscillator strength (if known), and upper limit on the column density for molecules with transitions in the UV. The upper limits on the column density were derived by assuming a maximum equivalent width of 5 mÅ for the SWP camera and 10 mÅ for the LWR camera, and solving equation 4-16b for the column density. If the oscillator strength is not known, then the last column in Table 5-7 contains the product Nf . For electronic transitions, the oscillator strength for permitted transitions typically ranges between 0.1 and 0.001. It is clear that a number of very important molecules have transitions in the UV, and that they are not observed because (1) the oscillator strength of the transition is too low; or (2) the column density of the molecule is not high enough to be detected.

6. DISCUSSION

6.1 Depletions

The line of sight towards X Per appears to contain $\approx 5\%$ of the material in the form of ionized or partially ionized hydrogen with a velocity parameter of 10 km/s. For silicon and sulfur, less than 10% of the material is in the higher stages of ionization (more than two electrons ejected). As discussed in 5.3, I concluded that the mass distribution follows that of the hydrogen- 95% of the material has $b = 1$ km/s, the other 5% has $b = 10$ km/s. One of the assumptions of the choice of the curve of growth was that the depletions in the two components are equal. For the most part, I will ignore the details of the structure of the 10 km/s component, as the conditions which favor the existence of higher stages of ionization are not well understood and are better handled by detailed modeling. Table 6-1 lists the recommended cosmic abundances of the elements (Engvold, 1977) in the form $A_i = \log(N_i/N_H)_0$. Except for Cl I (Table 5-1), the column density of the dominant stage ion has more than a factor of 100 times the column density of the lower stage of ionization. Depletions can thus be measured by comparing the column density of the dominant stage ions with the expected column density of the element, assuming a total hydrogen column density of $2.5 \times 10^{21} \text{ cm}^{-2}$. Table 6-2 lists the depletions of the elements, δ_i , where $\delta_i = \log(N_i/N_H) - A_i$, and $\log N_H = 21.4$. The discussion in 5.1 suggests that the error in the total hydrogen column

TABLE 6-1
SOLAR ABUNDANCES^a

Element	$\text{Log } \frac{\text{Ni}}{\text{N}_\text{H}}$	Element	$\text{Log } \frac{\text{Ni}}{\text{N}_\text{H}}$
H	0.0	Cl	-6.5
He	-1.1	Ar	-6.0
Li	-11.0	K	-6.8
Be	-10.9	Ca	-5.7
B	-9.7	Sc	-8.9
C	-3.3	Ti	-7.0
N	-4.1	V	-7.9
O	-3.2	Cr	-6.3
F	-7.4	Mn	-6.6
Ne	-4.3	Fe	-4.4
Na	-5.7	Co	-7.0
Mg	-4.4	Ni	-5.7
Al	-5.6	Cu	-7.9
Si	-4.4	Zn	-7.6
P	-6.5	Ga	-9.2
S	-4.8	Ge	-8.6

^aEngvold (1977)

TABLE 6-2
DEPLETIONS FROM DOMINANT STAGE IONS

Element	Log δ	Element	Log δ
Li	<2.9	Sc	<-0.09
Be	<0.9	Ti	-1.68
B	<-0.1	V	0.27
C	-0.47	Cr	-2.43
N	-0.90 (-0.20) ¹	Mn	-0.53
O	-0.70 (-0.30) ¹	Fe	-1.42
Mg	-0.67	Co	<-2.9
Al	-0.78	Ni	+2.18
Si	-0.82	Cu	-1.23
P	-0.83 to -1.38	Zn	0.17
S	0.05	Ga	-0.23
Cl	-0.07 ²	Ge	0.32 to -0.18
Ca	-2.28		

¹Derived from a 100/0 curve of growth

²Derived from CLI

density could be large, mostly due to the fact that the majority of hydrogen is in molecular form, and the H_2 column density was measured with rather poor S/N (Mason et al. 1976). However, a check can be made in that the depletions of both sulfur and zinc appear to be negligible (York and Jura, 1982; Snow, 1977). From Table 6-2, $\delta_S = 0.05$, and $\delta_{Zn} = 0.17$. The error in the hydrogen abundance is probably no more than 0.2 dex, assuming that these elements are undepleted. I will assume, then, that the error in the depletions is 0.15 dex, unless the error in the column density is larger. Figure 6-1 displays the data in Table 6-2. Figure 6-2 displays the difference between my depletions and those towards ζ Oph (Morton, 1975). I use the ζ Oph data instead of the \circ Per or ζ Per data (Snow, 1976; Snow, 1977) because both sets of data suggest a multiple velocity component curve of growth, and it is not clear how this affects the published depletions. I will point out, however, that the large depletions found towards \circ Per by Snow (1976) are probably due to the fact that a composite curve of growth was not used, which drastically reduced the column densities of the dominant stages. My depletions (Figure 6-2) appear to be closer to solar values than those towards ζ Oph. This may be due to an improper choice for the curve of growth, either on my part or on the part of Morton (1975). Velocity component structure (Crutcher, 1975) suggests that Morton overestimated many depletions.

As discussed in 5.3, the nitrogen and oxygen column densities may be larger if the contribution from the 10 km/s cloud is smaller for these elements. Indeed, if a 100/0 curve of growth is used, both N I and O I

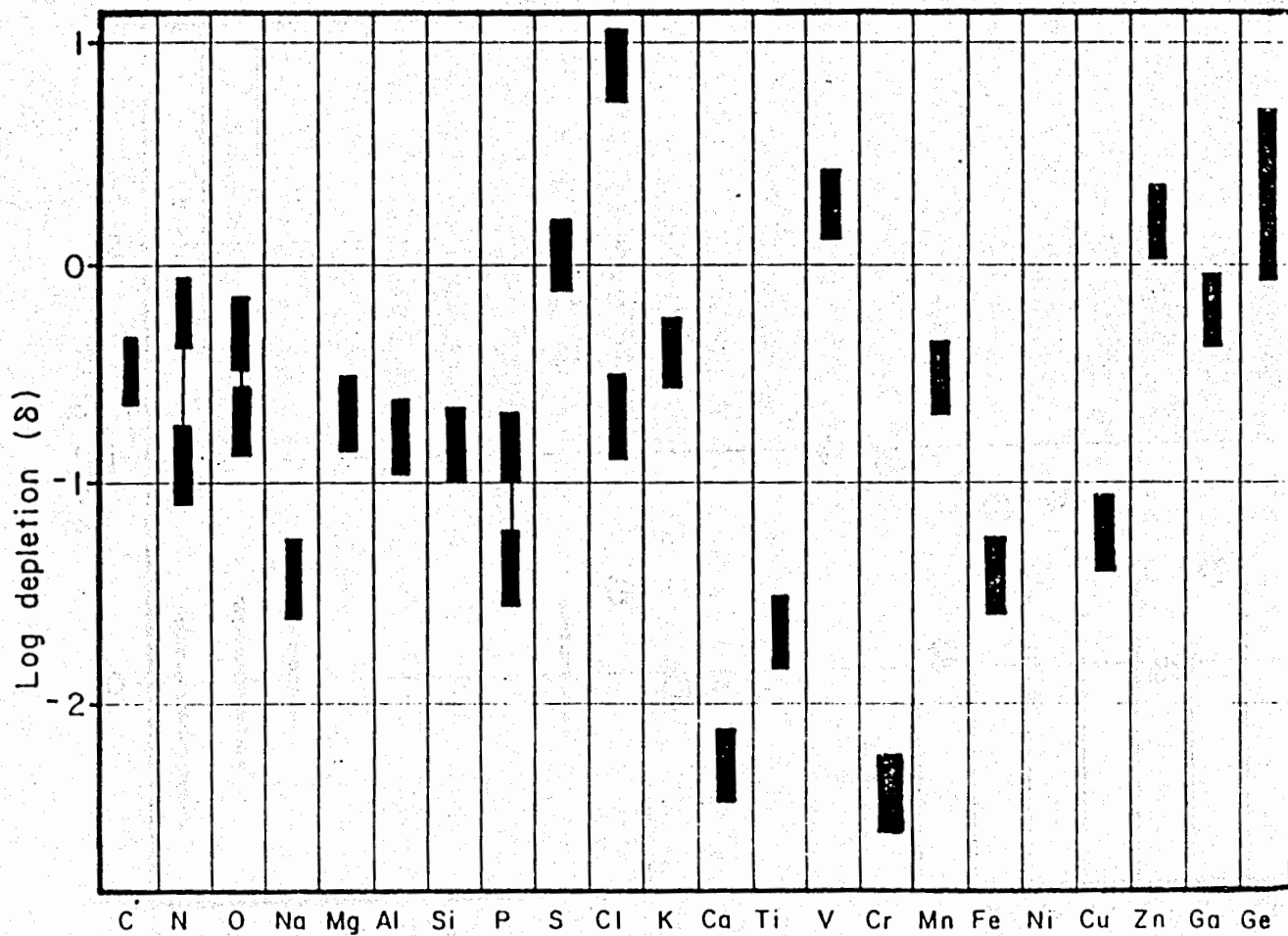


Figure 6-1. Log of the depletion of the elements toward X Per.

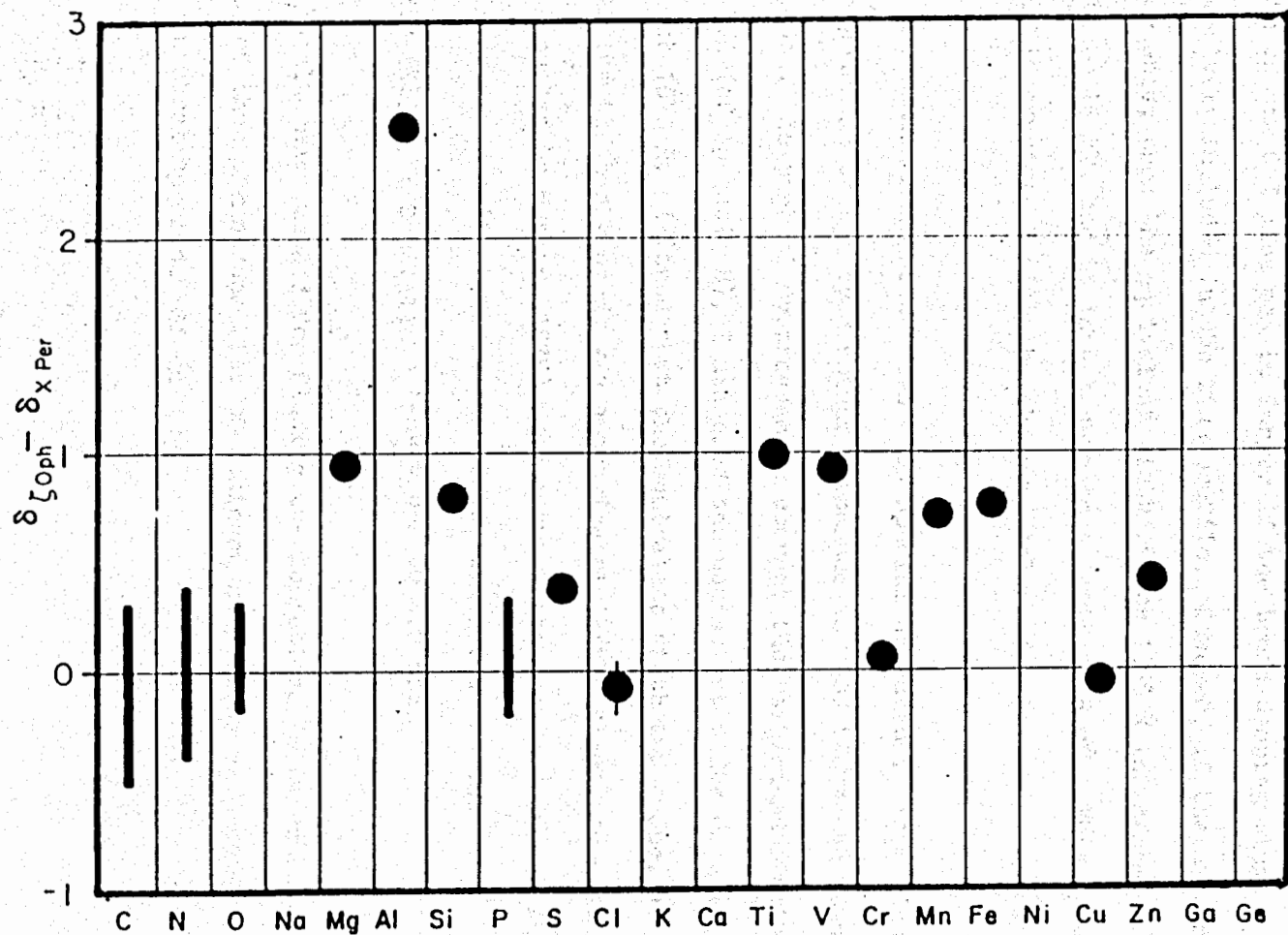


Figure 6-2. The difference between the log of the depletions toward X Per and toward ζ Oph. The mean depletions toward ζ Oph are taken from Morton (1975).

come to within a factor of 2 (0.3 dex) of being solar. The equivalent width of the O I line may be larger if the broad damping wings were not effectively included in the line profile. However, if the oxygen were undepleted, then the equivalent width of the 1355 Å inter-system line would be 16 mÅ, and it is not seen to a limit of 5 mÅ. This upper limit is consistent with the observed column density.

The aluminum abundance deserves special attention. From Figure 6-2, it appears as though my aluminum abundance is 300 times the abundance in ζ Oph. As part of my program to correct the background problem with the IUE (cf Appendix B), I measured the equivalent width of the Al II line at 1670 Å. I found that the equivalent width for ζ Oph, after modifying the background, was approximately three times the equivalent width quoted by Morton (1975). This translates to an increase in the Al II column density by a factor of 50, which reduces the $\delta_{\text{X Per (Al)}} - \delta_{\text{ζ Oph (Al)}}$ in Figure 6-2 to 0.8 dex.

An alternate method for finding the depletions is to compare the ratio of the column densities of dominant stage ions as predicted by their neutral species. Since

$$n_{\text{II}} = \frac{n_{\text{I}} \Gamma}{n_{\text{e}} \alpha} \quad (6-1)$$

then the ratio $n_{\text{IIA}}/n_{\text{IIB}}$ is

$$\frac{n_{\text{II}}(\text{A})}{n_{\text{II}}(\text{B})} = \frac{n_{\text{I}}(\text{A})}{n_{\text{I}}(\text{B})} \frac{\alpha/\Gamma(\text{A})}{\alpha/\Gamma(\text{B})} \quad (6-2)$$

Since sulfur is generally considered to be undepleted in the diffuse ISM (Snow, 1977), I have used it as the standard. Table 6-3 lists the observed values of the neutral ratio, $n_{\text{I}}/n_{\text{S I}}$, and the calculated depletion, δ , derived from equation 6-2 and the ratio of the solar abundance of sulfur to hydrogen (-4.8 dex).

Table 6-3 also lists the observed neutral ratio, $n_{\text{I}}/n_{\text{S I}}$, and the calculated depletion of the element for the diffuse IS radiation field (Γ_0) and for the radiation fields of model 2 and model 3 (RDF, cf Appendix D). The depletions all have been calculated using the column densities from the 95/5 curve of growth. The value in parentheses are the depletions derived from the column densities obtained with a 90/10 curve of growth.

The dominant stage and neutral depletions of C, Si, and S are within the estimated error (0.15 dex) of the column densities for the 95/5 curve of growth and model 3. The Ca dominant stage depletion was calculated by assuming that all of the Ca is visible as Ca II.

The Mg II and Fe II dominant stage depletions are less than the depletions estimated from the neutrals. The curve of growth for these ions, however, may be different from a 95/5 curve of growth (cf 4.2). The depletions derived from the two methods will match for magnesium if the Mg II column density is derived from a 90/10 curve of growth for

TABLE 6-3
DEPLETIONS FROM NEUTRALS

Element	Log $\frac{N_i}{N_{SI}}$	Log $\frac{\Gamma/\alpha_i}{\Gamma/\alpha_{SI}}$			Log depletion (δ)			
		Model:	0	2	3	0	2	3
C	1.55		-0.40	-0.44	-0.40	-0.35	-0.39	-0.35
	1.25					-0.65	-0.69	-0.65
Na	-0.64		-1.38	-1.25	-1.38	-1.13	-1.00	-1.13
	-0.95					-1.43	-1.30	-1.43
Mg	0.18		-0.97	-0.67	-0.95	-1.19	-0.89	-1.17
	—					—	—	—
Si	-1.18		0.66	0.88	0.72	-0.92	-0.70	-0.86
	—					—	—	—
Cl	0.30		-1.11	-1.67	-1.47	0.89	0.33	0.53
	0.20					0.79	0.23	0.43
K	-1.07		-0.98	-0.74	-0.95	-0.06	-0.18	-0.03
	-1.38					-0.36	-0.12	-0.33
Ca	-3.28		-0.24	-0.05	-0.37	-2.62	-2.43	-2.75
	—					—	—	—
Ca ⁺	-0.18		-3.09	-3.19	-3.13	-2.67	-2.77	-2.71
	-0.48					-2.37	-2.47	-2.41
Fe	-1.60		-0.67	-0.39	-0.58	-2.67	-2.39	-2.58
	—					—	—	—

model 2 or an 80/20 curve of growth for model 3. Similarly, a 70/30 curve of growth for Fe II will match the two depletions for model 2, or a 60/40 curve of growth for model 3. The observed curves of growth for Mg II and Fe II are consistent with either curve of growth. Indeed, the 60/40 Fe II curve of growth is the only one which agrees with the non-detection of the 2366 Å line of Fe II.

From the discussion of multiple component curves of growth in section 4.2, the fraction of the material in each velocity component is a function of the ionization and abundance of the element. For dominant stage ions, I pointed out that the fractional curve of growth reflects the mass distribution of the element and that, if the depletion in each velocity parameter component is the same for each element, the fractional curves of growth will be the same for all dominant stage ions. The smaller curves of growth implied for Mg II and Fe II suggest, then, that these elements are preferentially depleted within the 1 km/s component. If this is actually the case, then it appears that only magnesium and iron are actually depleted onto grains in situ in diffuse clouds. The fractional curve of growth for oxygen and carbon cannot be determined with the present data; so no conclusion can be made about the differential depletion of these elements. Silicon does not appear to have this same differential depletion. This suggests that perhaps the core of the grain is primarily made of silicates, perhaps in the atmospheres of red giants, and then coated with a layer of molecules which consist of Mg, Fe, and others (Ti, Ca, Cr, etc). Again, it is not clear as to how the oxygen and carbon depletion (if they are even

depleted, Crutcher, 1975; Liszt, 1981) fit into this scenario.

Chlorine appears to be overabundant, although the solar abundance of chlorine is not well known (Engvold, 1979). With a 95/5 curve of growth, potassium appears to be undepleted. Chaffee and White (1982) find that $\delta_K = -0.5$ over a wide range of extinctions and lines of sight although the scatter is large.

With the reasonable agreement between the neutral depletions and the dominant stage depletions, it is hard to understand the discrepancy for calcium. A major problem might be that the ionization balance between the two velocity parameter components changes such as to greatly modify the percentage of the ion in each component. Although part of the discrepancy might be due to imprecise photoionization cross sections, the more probable reason is that the distribution of the three stages of ionization between the two b-components is very different from the distribution of ions with only two possible ionization stages in the ISM. This might also be a problem for titanium, since the ionization potential of Ti II is less than 13.6 eV. Qualitatively, I would expect that the curve of growth for Ca I would be larger than 95/5 (eg 99/1), and the curve of growth for Ca II be much smaller than 95/5 (eg 40/60). This would increase the dominant stage (Ca II) depletion, making it more commensurate with the neutral depletion. For example, if Ca II is the dominant stage of ionization in both b-components, then the depletion derived from Ca I matches the observed depletion (Ca II) for Ca II curves of growth of 85/15 (model 2) or 60/40 (model 3). Observations of

the weaker UV multiplets of Ca II might solve this problem. Appendix D contains a discussion of the photoionization rate (Γ).

The depletion is a measure of the relative amount of the element in the gas phase, assuming that it should have a solar composition. The fraction of the element not in the gas phase is

$$f_g = 1 - \delta \quad (6-3)$$

where $\delta > 0$, and the value for each element is listed in Table 6-2.

f_{gr} is the fraction of the gas that is tied up in either grains or molecules. The values for f_{gr} are presented for each element in Table 6-4. The values with asterisks have been derived using the depletions calculated from the neutral species (Table 6-3). What is of interest is the absolute number of atoms of a particular element in the grains. The third column of Table 6-4 lists the number of atoms not in the gas phase per zinc atom in the gas phase. Zinc was chosen because it appears to be essentially undepleted (York and Jura, 1982). The minimum nitrogen and oxygen depletions were also used. The depletion of nitrogen and oxygen calculated from column densities derived from the 95/5 curve of growth would more than double the the number of nitrogen atoms in Table 6-4, but would only increase the number of oxygen atoms by 2/3.

It is immediately obvious that the carbon and oxygen supply the majority of the atoms in the grain and that they are approximately equal in abundance. Similarly, the relative number of atoms of N, Mg, Si, and

TABLE 6-4
 FRACTIONAL ATOMIC ABUNDANCE IN GRAINS

Element	Element	$1.0 - 10^6$	Atoms/(Zinc atom in gas)
	C	0.66	13170
	N	0.37	1170 - 2760
	O	0.50	12560 - 20110
	Fl	1.0	2
	Na ¹	0.99	79
	Mg	0.79	1252
	Al	0.83	83
	Si	0.84	1331
	P	0.85 - 0.96	11 - 12
	S	0	0
	Cl	0	0
	K ¹	0.9	6
	Ca	0.99	79
	Ti	0.98	4
	Cr	0.996	20
	Mn	0.7	7
	Fe	0.96	1525
	Cu	0.94	0.47
	Zn	0	0

¹Derived from neutrals

Fe are all the same. A third set of atoms (Ca, Na, and Al) also have equal contributions in the grains. Assuming that these three sets of elements are the primary constituents of the grains, the chemical formula would be $(\text{Ca,Na,Al})_1(\text{Mg, Si, Fe, N})_{15}(\text{C, O})_{150}$ or, ignoring the minor constituents, $(\text{Mg, Si, Fe, N})_1(\text{C, O})_{10}$. Table 6-5 lists the name and chemical composition of a number of terrestrial minerals. The largest ratio of (Mg, Fe, Si) to O is $\approx 1/4$, and not the $1/10$ that is needed; hence 60% of the O and an even larger percentage of C is still unaccounted for, assuming that the grains have compositions similar to terrestrial minerals. Greenberg (1974) discusses this problem in detail, and includes a good discussion of the optical properties that the compounds must have, and what combinations of atoms will fill these requirements. Graphite grains might account for the carbon, although the existence of graphite grains is still unsubstantiated (Czyzak et al. 1982). The abundance of CO ($\approx 1/40$ C) is not large enough to account for the remaining atoms of C and O. The upper limit on the O_2 abundance is 16.8 dex, which may contribute to the oxygen depletion if the column density is just below the upper limit. Another possible element which could tie up large amounts of C and O is carbon suboxide- C_3O_2 . C_3O_2 is interesting for a number of reasons. It contains almost equal amounts of carbon and oxygen, which could account for the similar depletions of the two elements. Two or three molecules of C_3O_2 for every mineral molecule would account for the depletions of all the major elements. It is also interesting to note that C_3O_2 exhibits continuous absorption shortward of 2300 \AA , and it has a low extinction coefficient (Thompson, 1936) which suggests that large amounts need to be present

TABLE 6-5
 CHEMICAL COMPOSITION OF TERRESTRIAL MINERALS

Name	Composition	Name	Composition
Anthophyllite	$(\text{Mg,Fe})_7\text{Si}_8\text{O}_{22}(\text{OH,F})_2$	Almandine	$\text{Fe}_3\text{Al}_2\text{Si}_3\text{O}_{12}$
Brucite	$\text{Mg}(\text{OH})_2$	Chondrite	$\text{Mg}(\text{OH,F})_2 2\text{Mg}_2\text{SiO}_4$
Cristobalite	SiO_2	Cumingtonite	$(\text{Mg,Fe})_7\text{Si}_8\text{O}_{22}(\text{OH})_2$
Enstatite	MgSiO_3	Fayalite	Fe_2SiO_4
Forsterite	Mg_2SiO_4	Geothite	$\text{FeO}(\text{OH})$
Graphite	C	Hematite	Fe_2O_3
Hydromagnesite	$\text{Mg}_4(\text{OH})_2(\text{CO}_3 3\text{H}_2\text{O})$	Lepidocrocite	$\text{FeO}(\text{OH})$
Magnesite	MgCO_3	Magnetite	Fe_3O_4
Moissanite	SiC	Olivene	$(\text{Mg,Fe})\text{SiO}_4$
Opal	$\text{SiO}_2 \cdot n\text{H}_2\text{O}$	Orthopyroxene	$(\text{Mg,Fe})\text{SiO}_3$
Pericalse	MgO	Quartz	SiO_2
Siderite	FeCO_3	Talc	$\text{Mg}_3\text{Si}_4\text{O}_{10}(\text{OH})_2$
Tridymite	SiO_2		

before it can be observed. C_3O_2 also polymerizes when exposed to UV wavelengths. Platt (1956) suggested that a large molecular aggregate grown by accretion of IS atoms and ions would be neutral, and exhibit many of the requisite properties for IS grains. Such Platt particles could in principle be composed mainly of a C_3O_2 polymer, and perhaps this is the cause of the far UV increase in the extinction curve (Savage and Mathis, 1979).

Duley (1982) has suggested that the diffuse IS features are caused by Cr^{3+} and Mn^{4+} ions at cubic sites in MgO solids. Finely divided MgO solids also show an absorption feature around 2200 Å. Both Mn and Cr are depleted by an amount which could be incorporated into the grains as defects.

The main problem with my depletion study appears to be the excess amount of carbon and oxygen depletion that I find. de Boer (1981) suggests that oxygen is not depleted towards other stars by as much as I measure towards X Per, and carbon shows similar tendencies when examined in detail (Crutcher, 1975; Liszt, 1981). Detections of the 1355 Å line of O I and the 2334 Å line of C II would go far in answering the depletion problem. Additionally, it would be very useful to obtain a better column density for both neutral and diatomic hydrogen.

6.2 Temperature

The population of the fine structure levels of C I, C II, Si I, Si II, and O I is a function of both the temperature and the density (Bahcall and Wolf, 1968, hereafter BW; Smeding and Pottasch, 1979, hereafter SP). In principle, the two effects can be separated observationally. However, in practice, the observational errors limit the analysis such that only the product of the temperature and the density (pressure) can be found, and some other way must be used to separate out the individual quantities.

The discovery of absorption from homonuclear diatomic molecules in the ISM has been very useful finding the temperature independently from the density. Electronic transitions between adjacent rotational levels in a homonuclear diatomic molecule are absolutely forbidden by symmetry rules. Electric quadropole transitions can occur between every other rotational level, but the transition probability is so small that, under diffuse cloud conditions, the collisional rate far exceeds the radiative rate. Hence, the level populations, especially between the lowest two rotational levels, is only a function of the kinetic temperature. For the diffuse clouds studied to date, this appears to be the case. However, the higher rotational levels often show an enhanced population over what is expected thermally (Spitzer, 1978). Spitzer and Zwiebel (1973) have suggested that this can be caused by a combination of photon pumping and excess energy left over from the formation of the H_2 molecule. The temperature from the lowest rotational levels ranges

between ≈ 50 K and 100 K (York, 1975b). The diatomic hydrogen observations towards X Per (Mason et al. 1976) give a rotational (kinetic) temperature of 71 ± 8 K. Unfortunately, the S/N of the H_2 data is very poor.

I have detected a different homonuclear diatomic molecule (C_2) which can be used instead of H_2 for determining the temperature, as the IUE does not cover the spectral region containing the Werner bands of H_2 . The F-X 0-0 band system at 1341.6 \AA (Figure 5-11, of 5.7) shows an unresolved vibrational band profile. Using the profile fitting techniques from 4.3, I was able to fit the F-X 0-0 line profile with a rotational temperature of 40 K and a column density of $2-4 \times 10^{13} \text{ cm}^{-2}$ ($\log N_f = 14.0 \text{ cm}^{-2}$).

Recently, van Dishoeck and Black (1982, vDB) presented a detailed analysis of the level population of C_2 . Because of the permitted electronic transition in the IR (Phillips band, A-X), the diffuse IS radiation field in the IR can significantly alter the level populations for low densities. Because of the need for an accurate temperature, I used their analysis and techniques to re-calculate the F-X band profile when the level populations are thermalized. I wrote a computer code to solve the set of linear equations

$$n_J(A_{J,J-2} + W_J I + C_{J,J+2} + C_{J,J-2}) = n_{J+2}(A_{J+2,J} + C_{J+2,J}) + n_{J-2}C_{J-2,J} + \sum_{J'} W_{J'} I n_{J'} Y(J', J) \quad (6-4)$$

for the first eleven ($J < 20$) levels of C_2 for any combination of temperature and density. n_J is the relative level population of level J . $C(K,L)$ is the collision rate, where

$$C_{J+2,J} = C_{J,J-2} \left(\frac{2J+1}{2J+5} \right) s^{-1} \quad (6-5a)$$

$$C_{J,J+2} = C_{J+2,J} \left(\frac{2J+5}{2J+1} \right) e^{-\Delta E(J+2,J)/kT} s^{-1} \quad (6-5b)$$

$$C_{2,0} = 10^4 T^{1/2} n_c \sigma_0 s^{-1} \quad (6-5c)$$

n_c is the effective density of the colliding particle ($n_{H I} + n_{H_2}$), and σ_0 is the collisional cross section in cm^{-2} . vDB find experimentally that $\sigma_0 = 2 \times 10^{16} \text{ cm}^{-2}$, which is the value that I have used. $W_J (= 5.7 \times 10^{-9} \text{ s}^{-1})$, is the rate of absorption out of level J through the Phillips band. W_J is the same for all J . I is the scaling parameter for the radiation field if it is different from that in the diffuse ISM. The Einstein A 's and radiative excitation matrix ($Y(J', J)$) are tabulated by vDB. The effect of the IR radiation field is to populate the higher rotational levels, which will broaden the line profile and decrease its maximum absorption. For example, Figure 6-3 shows the calculated F-X line profile for $T = 40 \text{ K}$ for both high and low densities. The low density line profile does not fit the data (Figure 5-11). Since the

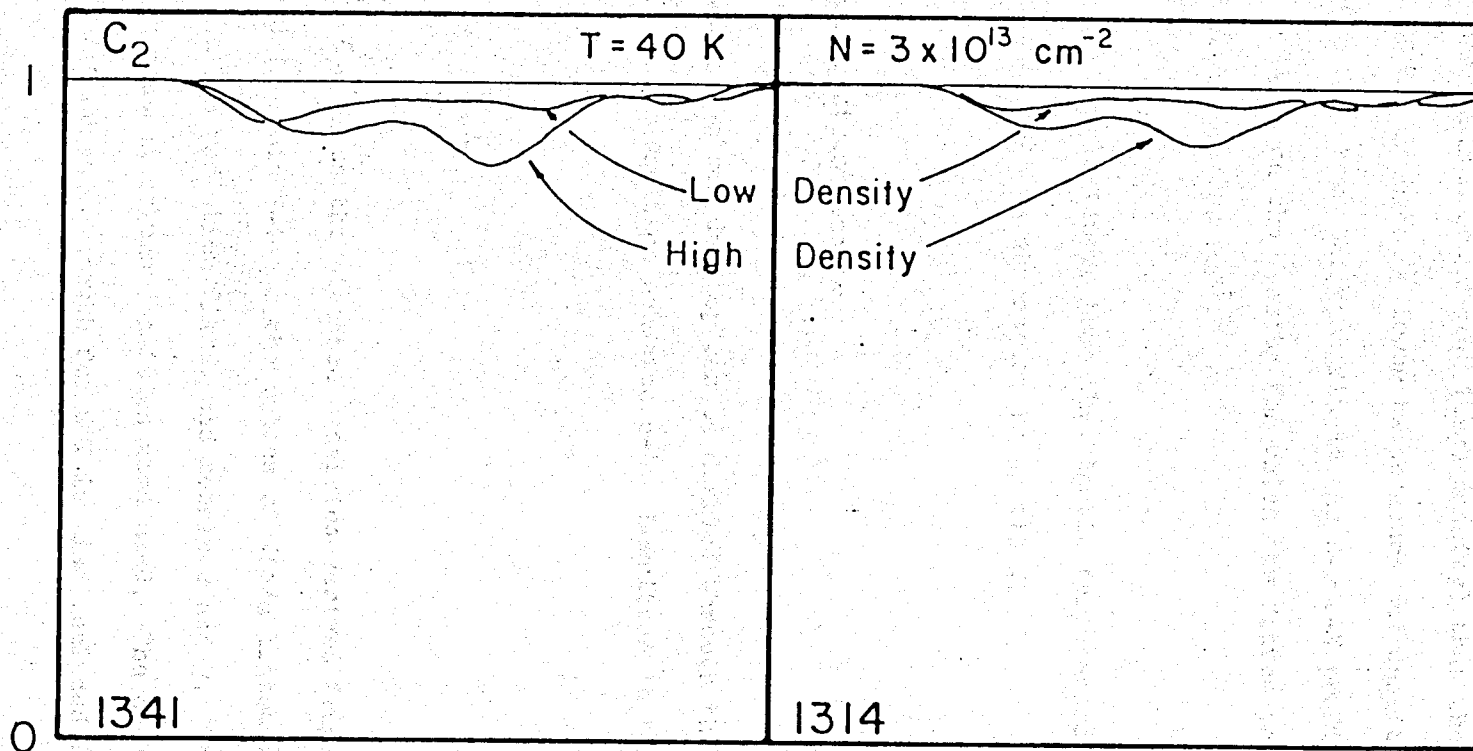


Figure 6-3. Theoretical line profiles for the 0-0 and 1-0 bands of the F-X system of C_2 for high densities ($n = 2000 \text{ cm}^{-3}$) and low densities ($n = 1 \text{ cm}^{-3}$). $N = 3 \times 10^{13} \text{ cm}^{-2}$, $T = 40 \text{ K}$, and $b = 1 \text{ km/s}$.

effect of low density is to broaden the profile, the maximum temperature for the minimum broadening (high density) that the observations allow is $T < 50$ K. However, a lower temperature and density could be acceptable. Figure 6-4 shows the best fit to the 0-0 F-X profile for $T = 20$ K. The lower limit on the density for which the fitted profile is still acceptable is 400 cm^{-3} .

The conclusion is that the kinetic temperature in the cloud containing the C_2 absorption is 40 ± 10 K.

6.3.1 Electron Density

The electron density can be derived through the ionization equilibrium equation equation 6-1. Rewritten in terms of n_e , equation 6-1 is

$$n_e = \frac{n_{\text{I}}}{n_{\text{II}}} \frac{\Gamma}{\alpha} \quad (6-6)$$

Table 6-6 lists the electron densities derived from the column densities listed in Table 5-1 and the values of $\langle \Gamma \rangle / \alpha$ listed in Appendix D for the diffuse ICM radiation field, and models 2 and 3. The 95/5 curve of growth neutral column densities were used. The electron density from the 90/10 curve of growth for C I is also included in Table 6-6.

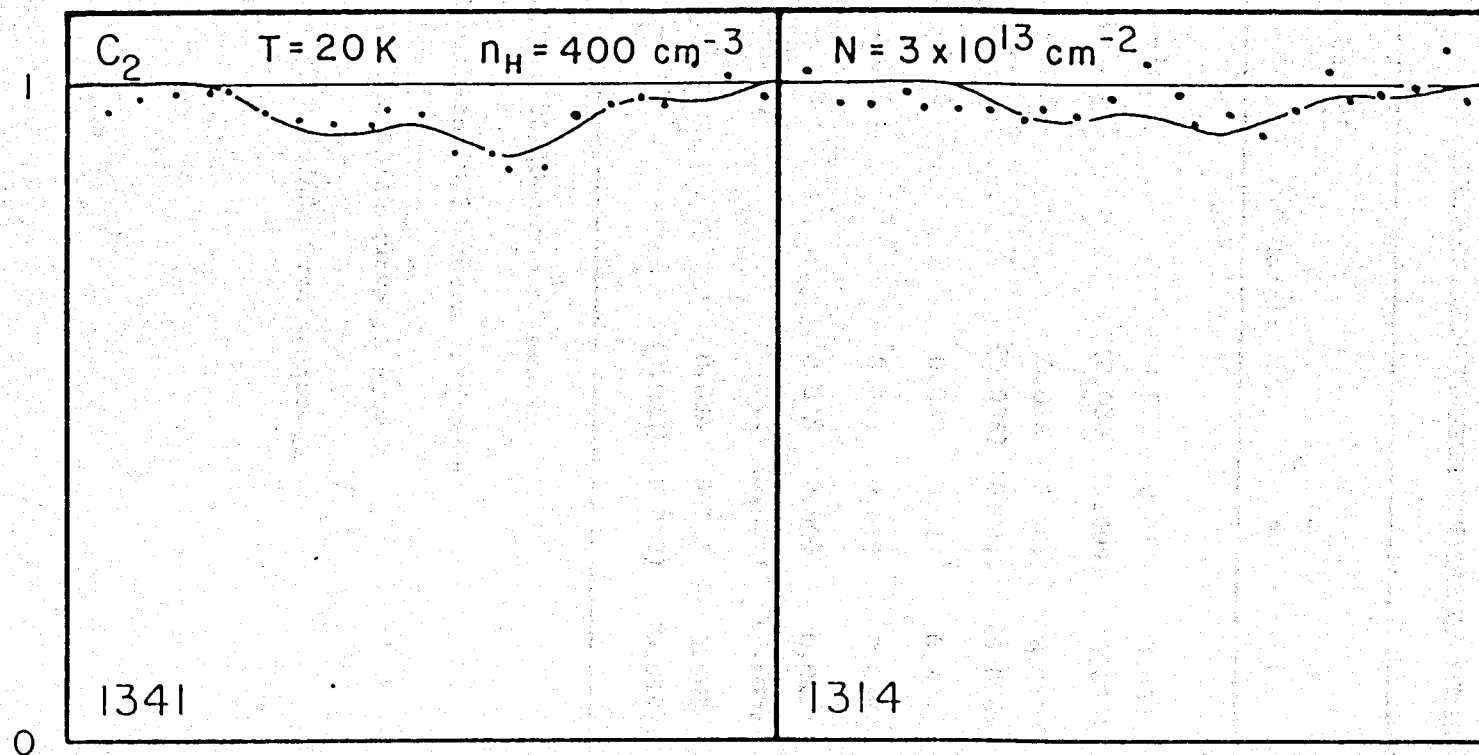


Figure 6-4. Theoretical C_2 line profiles for $N = 3 \times 10^{13} \text{ cm}^{-2}$, $T = 20 \text{ K}$, and $b = 1 \text{ km/s}$.

TABLE 6-6

ELECTRON DENSITY FROM IONIZATION EQUILIBRIUM

Element	Log $\frac{N_I}{N_{II}}$	n_e cm ⁻³		
		Model: 0	2	3
C	-2.15	0.076	0.017	0.053
	(-2.45) ^a	(0.038)	(0.009)	(0.027)
Mg	-2.25	0.016	0.008	0.012
	(-1.91) ^b	(0.036)	(0.017)	(0.026)
Si	-3.46	0.043	0.017	0.034
S	-2.75	0.048	0.012	0.033
Ca	-2.80	0.025	0.009	0.013
	(-3.10) ^c	(0.012)	(0.005)	(0.006)
Fe	-3.28	0.036	0.001	0.003
	(-2.42) ^d	(0.022)	(0.010)	(0.019)

^a n_e for CI with a 90/10 curve of growth

^b n_e for MgII with an 80/20 curve of growth

^c n_e for CaII with a 90/10 curve of growth

^d n_e for FeII with a 60/40 curve of growth

The error in the electron density is hard to assess, primarily because the exact form of the curve of growth is unknown. Additionally, the grain properties are not known which, for the models used, can alter the electron density by up to a factor of three. This is perhaps the best indication of the error in the electron density. There is very good agreement between the electron densities derived from Si, S, and C for models 2 and 3. In section 6.1, I stated that the Mg II and Fe II curves of growth must be smaller than 95/5 in order to match the depletions derived from the neutrals. Since the neutral depletions were tied to the S I depletion and the sulfur electron density matches the silicon and carbon electron densities, the Fe II curve of growth (60/40) and Mg II curve of growth (80/20) will yield electron densities which are similar. These electron densities are 0.019 cm^{-3} and 0.026 cm^{-3} for Fe and Mg, respectively. The mean electron density assuming a 95/5 curve of growth for all ions and neutrals is $\langle n_e \rangle = 0.019 \pm 0.014 \text{ cm}^{-3}$ (model 3), and $\langle n_e \rangle = 0.0087 \pm 0.0055 \text{ cm}^{-3}$ (model 2). If the curves of growth for Mg II and Fe II are different from 95/5, then $\langle n_e \rangle = 0.025 \pm 0.008 \text{ cm}^{-3}$ (model 3), $\langle n_e \rangle = 0.014 \pm 0.004 \text{ cm}^{-3}$ (model 2), and $\langle n_e \rangle = 0.035 \pm 0.010 \text{ cm}^{-3}$ (no extinction). Similarly, n_e from calcium is increased to $n_e = 0.034$ (model 3) and $n_e = 0.028 \text{ cm}^{-3}$ (model 2) for Ca II curves of growth of 60/40 and 85/15, respectively. These curves of growth also equate the neutral and dominant stage depletions (of 6.1). The mean electron densities for ζ Oph and ζ Per are $\langle n_e \rangle = 0.7$ (Morton, 1975) and $\langle n_e \rangle = 0.12$ (Snow, 1977), respectively. Crutcher and Watson (1981) suggest that for ζ Oph, $\langle n_e \rangle = 0.075 \text{ cm}^{-2}$.

Table 6-7 lists the predicted column densities for unobservable ions whose neutrals can be observed. The mean n_e from each model was used to calculate the abundances. Note that Ca II, not Ca III is the dominant stage of ionization. The implied depletions are also listed. Chlorine appears to be from two to five times overabundant from this calculation. However, the value of $\langle \Gamma \rangle$ for chlorine is extremely susceptible to the radiation field, as the ionization edge is at 958 Å. Hence, any shielding at all (eg H_2 , H I, etc) will drastically reduce the radiation field in the ISM, which is reflected in a major change in $\langle \Gamma \rangle$. δ_{Cl} could easily be an order of magnitude smaller.

Electrons in diffuse clouds come from the photoionization of trace elements (eg C, Si, etc) and the Cosmic Ray (CR) ionization of hydrogen (either atomic or molecular). For small depletions, carbon supplies most of the electrons. The contribution from other metals is insignificant. CR ionization becomes relatively more important as the extinction increases or as carbon becomes more depleted. For example, CR ionization of hydrogen contributes $\approx 50\%$ of the electrons for a hydrogen density of 100 and $\delta_C = 0.3$ and less than 1% for $\delta_C = 1.0$ ($\Gamma_0 = 10^{-16} \text{ s}^{-1}$). The hydrogen density implied by the mean electron density and the observed carbon depletion is $n_H < 100 \text{ cm}^{-3}$.

The electron density of the 10 km/s component can be obtained from the ratio $n_e(1)/n_e(10)$ (cf 5.4.1). For $T(1) = T(10)$, $n_e(10) = 0.028 \text{ cm}^{-3}$ (model 2) and $n_e(10) = 0.033 \text{ cm}^{-3}$ (model 3). For $T(10) = 200T(1)$, $n_e(10) = 2.6 \text{ cm}^{-3}$ (model 2) and $n_e(10) = 3.2 \text{ cm}^{-3}$ (model 3). The column

TABLE 6-7

COLUMN DENSITIES OF UNOBSERVABLE IONS

Element	Log Column Density (cm^{-2})			Log Depletion			Solar Abun.
	Model: 0	2	3	0	2	3	
NaII	14.77	14.68	14.75	-0.93	-1.02	-0.95	-5.7
ClII	15.98	15.20	15.60	+1.08	+0.30	+0.70	-6.5
KII	14.73	14.76	14.75	+0.13	+0.16	+0.15	-6.8
CaIII	13.53	13.22	13.48	-2.17	-2.48	-2.22	-5.7

density of hydrogen in the 10 km/s component is $1.3 \times 10^{20} \text{ cm}^{-2}$. If the hydrogen is fully ionized ($n_{\text{H}} = n_{\text{e}}$), then the thickness of this region is $\Delta R = 1.3 \times 10^{20} / n_{\text{e}} = 15 \text{ pc}$. The emission measure would be $\text{EM} = 140 \text{ cm}^{-6} \text{ pc}$. Additionally, the high electron density and temperature yield $\log(N_{\text{Si II}^*}(10)) = 11.04 \text{ cm}^{-2}$ for the column density of Si II*. The upper limit on the Si II* column density is $\log(N_{\text{Si II}^*}) < 11.6$, which is consistent with the calculated column density. Regardless of the temperature, the analysis of section 6.1 indicates that the electron density in the 10 km/s component is greater than the electron density in the 1 km/s component. This can occur if (1) the particle density is greater in the 10 km/s component or (2) the particle density in the 10 km/s is small, but with a higher fractional ionization. The ratio $n_{\text{e}}(1)/n_{\text{e}}(10)$ will increase by an amount equal to $19/R$, where R is the ratio of the fractions in the 1 km/s and 10 km/s components. For example, the 80/20 curve of growth yields $R = 4$; hence, $n_{\text{e}}(1)$ is increased by a factor of $19/4 = 4.75$. For $T(1) = T(10)$, $n_{\text{e}}(10) = 0.0059 \text{ cm}^{-3}$ and 0.0069 cm^{-3} for models 2 and 3, respectively. For $T(10) = 200T(1)$, $n_{\text{e}}(10) = 0.56 \text{ cm}^{-3}$ and 0.67 cm^{-3} for models 2 and 3, respectively. This reduces the emission measure to within the observational limits, particularly if the hydrogen in the 10 km/s component is not completely ionized. If the 10 km/s component is in the ICM at $T(10) = 200T(1)$, then the hydrogen density is greater than or equal to the electron density quoted above. Although a hydrogen density of $\approx 1 \text{ cm}^{-3}$ is large for the ICM, it is not impossible. For $T(1) = T(10)$, the hydrogen density is $\approx 10 \text{ cm}^{-3}$ for no depletion of carbon, or $\approx 40 \text{ cm}^{-3}$ for a carbon depletion of 0.3.

The results of this section are that the electron density is $\approx 0.02 \text{ cm}^{-3}$, the exact value depending on the grain scattering properties. I have also shown that the upper limits on the emission measure precludes the material in the 10 km/s component from being hot ($>10^4 \text{ K}$), unless the Mg II curve of growth is less than a 95/5 curve of growth. If the absorbing gas is behind the cloud, then the extinction could account for the emission measure limits. The smaller Mg II curve of growth also equalizes the neutral and dominant stage depletions, as well as bringing the electron density derived from the Mg I/Mg II ratio into line with other electron density indicators. If indeed the Mg II curve of growth is less than 95/5, then there is not enough information to determine whether the material is hot and diffuse ($T = 10^4 \text{ K}$, $n_{\text{H}} = 1 \text{ cm}^{-3}$), or cool and dense ($T = 50 \text{ to } 200 \text{ K}$, $n_{\text{H}} = 10 \text{ to } 40 \text{ cm}^{-3}$). The observations of highly ionized species (cf 5.2) could fit both models, although the latter suggests ionization by X-rays.

6.3.2 Hydrogen Density

If the electrons come primarily from the photoionization of carbon, then the hydrogen density is the mean electron density times the ratio of hydrogen to carbon. For $n_{\text{e}} = 0.02 \text{ cm}^{-3}$ and $\delta_{\text{C}} = 0.3$, $n_{\text{H}} = 130 \text{ cm}^{-3}$.

For a two level system, the relative populations can be determined by statistical equilibrium (BW):

$$n_1 R_{12} = n_2 R_{21} \quad (6-7a)$$

$$R_{ij} = Q_{ij} + \omega_{ij} \quad (6-7b)$$

$$Q_{ij} = \sum_k \langle \sigma v \rangle_k n_k \quad (6-7c)$$

$$Q_{12} = \frac{g_1}{g_2} Q_{21} e^{-\Delta E_{12}/kT} \quad (6-7d)$$

$$g_i = 2J_i + 1 \quad (6-7e)$$

where J is the total angular momentum of level i , ΔE is the energy (positive) difference between the two states, n_k is the density of colliding particle k , and $\langle \sigma v \rangle$ is the cross section for collisions with particle k . W_{ij} is the photoabsorption rate ($I_\nu B_{\nu 12}$) or the radiative decay rate (A_{21}). For the fine structure levels of C II and Si II, W_{12} is negligible for absorption by the 2.8 K microwave background. UV pumping can be important for the level population of the Si II fine structure level (Flannery et al. 1980). Since Si II* is not seen, this complication can be ignored. In this section, I will refer to the

colliding particle density either as n_e from electrons or as n_H for neutral species. In most cases of interest in this work, the colliding neutral particle is H_2 . The total hydrogen volume density is $2n_{H_2} + n_{HI}$. For a three level system, the population of the levels with respect to the lowest level can be shown to be (BW)

$$\frac{n_1}{n_0} = \frac{R_{01}(R_{21} + R_{20}) + R_{02}R_{21}}{R_{10}(R_{21} + R_{20}) + R_{20}R_{12}} \quad (6-8a)$$

$$\frac{n_2}{n_0} = \frac{R_{02}(R_{12} + R_{10}) + R_{01}R_{12}}{R_{20}(R_{12} + R_{10}) + R_{10}R_{21}} \quad (6-8b)$$

where the R_{ij} 's are defined through equations 6-7b-6-7e. Table 6-8 contains values of A_{ij} , $\langle\sigma v\rangle$, g_i , g_j , and ΔE_{ij} for all the levels of interest. I have also included the value of $\langle\sigma v\rangle$ for electron excitation in the form of the parameter Ω , where

$$\langle\sigma v\rangle_{21} = \frac{8.629 \times 10^{-6} \Omega}{g_2 T^{1/2}} \quad (6-9)$$

The value of $\langle\sigma v\rangle$ for collisions with hydrogen is also given. If $n\langle\sigma v\rangle \ll A_{21}$, then equation 6-7a reduces to

$$\frac{n_2}{n_1} = n_k \langle\sigma v\rangle / A_{21} \quad (6-10)$$

The problem with the fine structure lines is that the percentage in the two clouds is unknown. The C I lines have serious blending problems, and I will treat this separately at the end of this section. The other

TABLE 6-8

ATOMIC COLLISIONAL EXCITATION PARAMETERS

Elem.	St. Wt.			T_{21} (K)	T_{31} (K)	A_{21} (s^{-1})	A_{31} (s^{-1})	A_{32} (s^{-1})	σv ($cm^3 s^{-1}$)	
	g=0	1	2							
CI	1	3	5	23.6	62.4	7.9(-8) ^a	1.9(-14)	2.7(-7)	-	3.5(-8)
CII	2	4	-	91.3	—	2.36(-6)	—	—	1.33	8.4(-10)
OI	5	3	1	228.0	325.9	8.95(-5)	1.0(-10)	1.7(-5)	-	7.2(-10)
SiIII	2	4	-	413.4	—	2.17(-4)	—	—	7.7	6.1(-11)

^aThe number in parenthesis indicates the power of ten to which the number is raised

fine structure lines are the $^3P_{3/2}$ levels of C II and Si II and the 3P_0 and 3P_1 levels of O I. The 3P_2 level of O I is 325 K above the P ground state level, and I will ignore its effect, thus treating O I as a two-level system. This assumption breaks down at high densities and where UV photon pumping occurs. Since neither O I* nor O I** have been detected towards X Per, this is probably not a bad assumption.

The observed column densities of the fine structure lines of C II and Si II are $\log(N_{C II^*}) = 16.3 \text{ cm}^{-2}$ (95/5) and $\log(N_{Si II^*}) < 11.6 \text{ cm}^{-2}$. The range of electron densities for $T = 10^4 \text{ K}$ is $2.0 - 0.5 \text{ cm}^{-3}$, and depends on the Mg II curve of growth (cf 6.3.1). The predicted column densities for the fine structure lines for $T = 10^4 \text{ K}$ are $\log(N_{Si II^*}) = 10.2-10.9 \text{ cm}^{-2}$, and $\log(N_{C II^*}) = 14.4 - 15.0 \text{ cm}^{-2}$, assuming that 5% of the total column density in the ground state is in the 10 km/s component. The larger column densities are derived from the larger electron densities (larger Mg II curve of growth) The minimum observable $\log(N_{C II^*})$ is 14.7 cm^{-2} , suggesting that the observed C II* column density can be explained by a material at $T = 10^4 \text{ K}$ and $n_e > 1.0 \text{ cm}^{-3}$. Other data (emission measure and Mg II curve of growth arguments) suggest that the electron density is less than 1 cm^{-3} (cf 6.3.1). This suggests that electrons are probably not the primary excitation mechanism.

For $T = 50 \text{ K}$, $\langle \sigma v \rangle$ increases by a factor of 14 through the $T^{-1/2}$ dependence, but decreases through the exponential in equation 6-7d by factors of 3×10^3 for Si II and 6 for C II. The conclusion for the

cooler cloud is also the same, that electrons are not the primary exciting particle.

Neutral species have very low cross sections for excitation by electrons (BW). If the hydrogen density is the electron density times the H/C ratio, then $n_H \leq 130 \text{ cm}^{-3}$. The expected column densities for the fine structure lines are $\log(N_{\text{C II}^*}) = 15.46 \text{ cm}^{-2}$, $\log(N_{\text{Si II}^*}) = 7.46 \text{ cm}^{-2}$, and $\log(N_{\text{O I}^*}) = 12.01 \text{ cm}^{-2}$. The upper limit on O I* is 12.8 dex, which is consistent with the above calculation. Because of the larger separation between the fine structure levels, Si II is affected more by the electron density than the neutral density for diffuse clouds. The calculated C II* abundance is commensurate with the observed abundance for a 80/20 curve of growth. The upper limit on the hydrogen density can be found by assuming a 100/0 curve of growth for C II*. The upper limits implied by O I* and Si II* as well as C II* are $n_H(\text{O I}) < \text{cm}^{-3}$, $n_H(\text{Si II}) < 1.3 \times 10^6 \text{ cm}^{-3}$, and, $n_H(\text{C II}) < 3221 \text{ cm}^{-3}$. Clearly, the O I limits the density of the region to $< 500 \text{ cm}^{-3}$. Assuming that the collisions are primarily due to H_2 , the total volume density is 1000 cm^{-3} . The C II* column density for $n_H = 500 \text{ cm}^{-3}$ and $T = 50 \text{ K}$ is $\log(N_{\text{C II}^*}) = 15.8 \text{ cm}^{-2}$, which corresponds to a curve of growth of 85/15 for C II*.

The physical parameters of the 10 km/s cloud are not as evident as those of the 1 km/s cloud. If the 10 km/s cloud is the ICM, and is collisionally ionized at $T = 10000 \text{ K}$, then the C II and Si II fine structure lines can be used to determine the electron density. The

ratio of the log of the column densities of the fine structure levels are -3.3 and -1.6 dex for Si II and C II, respectively. The ratio for the 10 km/s cloud stays the same irrespective of the actual curve of growth used, except for a 100/0 curve of growth. This is because as the ratio decreases, the column density decreases, but the percentage in the 10 km/s cloud increases at the same rate, resulting in the same total column density. The implied electron densities are $n_e(\text{Si II}) < 0.68 \text{ cm}^{-3}$ and $n_e(\text{C II}) = 1 \text{ cm}^{-3}$. Within the errors, these numbers are probably the same, and the Si II lines should almost be observable. Indeed, on some of the individual well exposed spectra, there is a suggestion of a line at 1264 Å, which would correspond to the strongest expected Si II* line. However, the stacked spectra do not show a significant feature there. A major discrepancy is implied by this large n_e , as the emission measure, assuming no clumping, would be $260 \text{ cm}^{-6} \text{ pc}$, which is much larger than the observed value of ≈ 10 (Reynolds and Ogden, 1982). A filling factor of $5 \times 10^{-2} - 1 \times 10^{-4}$ would reduce the EM below the limits imposed by optical observations. An alternative possibility is that there is an outer shell of gas at the edge of the cloud which has a lower density and which contains a velocity parameter gradient. Since the C I line profiles need a velocity parameter component of greater than 2 km/s to account for the observations, this is a definite possibility. The temperature in this shell would be 100 K to 1000 K. The ICM would contribute nothing to the excited fine structure levels and would contribute less than 5% to the total column density. For this range in temperatures, and assuming a predominantly neutral gas, the implied electron densities would be

$n_e(\text{C II}) = 0.3$ to 0.4 , and $n_e(\text{Si II}) < 0.67$ to 0.15 cm^{-3} , and the implied hydrogen densities would be $n_H(\text{C II}) = 40$ to 90 cm^{-3} and $n_H(\text{Si II}) < 0.00056$ to 1300 cm^{-3} . The large range of n_H from Si II^* is due to the temperature dependence in equation 6-7. The smaller size of the shell and the lower n_e implied by the Si II are now consistent with the emission measure data. Unless hydrogen is mostly ionized, it makes the dominant contribution to the excitation of C II^* .

Neutral carbon has a ^3P ground state with three fine structure levels, the upper two at 24 K and 62 K above the ground state. The excitation of the C I fine structure levels as a function of density has been discussed in detail by BW, de Boer and Morton (1974), SP, and Jenkins and Shaya (1979). The data are usually not precise enough to independently determine both the temperature and the density. For X Per, the temperature is 40 K, derived by other methods (cf 6.2), and thus the C I level populations can be used to determine the density. Equation 6-7 was used to calculate the relative level populations. The atomic parameters used are listed in Table 6-8. The atomic hydrogen collisional cross sections are from Launay and Roueff (1977), and assumed to be the same for H_2 . The C I multiplets at 1660 Å, 1560 Å, 1328 Å, 1280 Å, 1277 Å, and 1260 Å were then calculated using the methods described in section 4.2. The oscillator strengths are listed in Table 6-9. Table 6-10 lists the relative strengths for each band within the multiplet. This number is multiplied by the multiplet oscillator strength to yield the oscillator strength for each

TABLE 6-9
CI MULTIPLETS

multiplet #	Term	Wavelength (Å)	$f_{\text{multiplet}}$
2	$^3P - ^3P$	1657	0.075
3	$^3P - ^3D$	1561	0.06
4	$^3P - ^3P$	1329	0.063
5	$^3P - ^3P$	1280	0.03
7	$^3P - ^3D$	1277	0.0646
9	$^3P - ^3P$	1261	0.0286

TABLE 6-10
CI RELATIVE LINE STRENGTHS

$^3P - ^3D$			$^3P - ^3P$		
J_1	J_u	f_{rel}	J_1	J_u	f_{rel}
0	1	1.0	0	1	1.0
1	1	0.251	1	0	0.333
1	2	0.751	1	1	0.250
2	1	0.010	1	2	0.417
2	2	0.151	2	1	0.250
2	3	0.840	2	2	0.750

line. The relative values are from Russell (1936). Figure 6-5 shows the comparison between the observed and calculated profiles for $N_{C I} = 3.0 \times 10^{15}$ (15.3 dex) and $n_H = 500 \text{ cm}^{-3}$. A 95/5 velocity parameter distribution was used. The 1260 Å multiplet of C I is affected by both the wing of the strong Si II 1260 Å line and an apparent stellar line, resulting in a very large error in the choice for the continuum.

The predicted CO excitation temperatures for the first three levels of CO (Smith et al. 1978) are $T_{10} = 6.3 \text{ K}$, $T_{21} = 4.8 \text{ K}$ and $T_{32} = 6.7 \text{ K}$ for $n_H = 330 \text{ cm}^{-3}$ and $T_{\text{kin}} = 40 \text{ K}$. This is reasonably close to the observed values of $T_{10} = 6.7 \text{ K}$, $T_{21} = 5.9 \text{ K}$, and $T_{32} = 4.5 \text{ K}$. The theoretical excitation temperatures for $n_H = 1000 \text{ cm}^{-3}$ and $T = 40 \text{ K}$ are $T_{10} = 18.4 \text{ K}$, $T_{21} = 6.8 \text{ K}$, and $T_{32} = 8.1 \text{ K}$. The excitation temperatures observed suggest a density between 300 and 1000 cm^{-3} . Smith et al. (1978) did not include any form of photon trapping, which would modify the level populations, especially at larger column densities (de Jong, Chu and Dalgarno, 1975; White, 1977; Leung and Liszt, 1976).

I have calculated the CO level populations with self absorption using a program developed by M. Elitzur (Elitzur, 1978). The program utilizes the Sobolev approximation for calculating the radiation transfer. My calculations agree with those of Smith et al. (1978) for optically thin CO. For column densities on the order of $1.0 \times 10^{16} \text{ cm}^{-2}$, the observed level populations are consistent with hydrogen densities of 200 cm^{-3} and 400 cm^{-3} for $T = 40 \text{ K}$, and between 100 cm^{-3} and 200 cm^{-3} for $T = 80 \text{ K}$. These results lie between the low

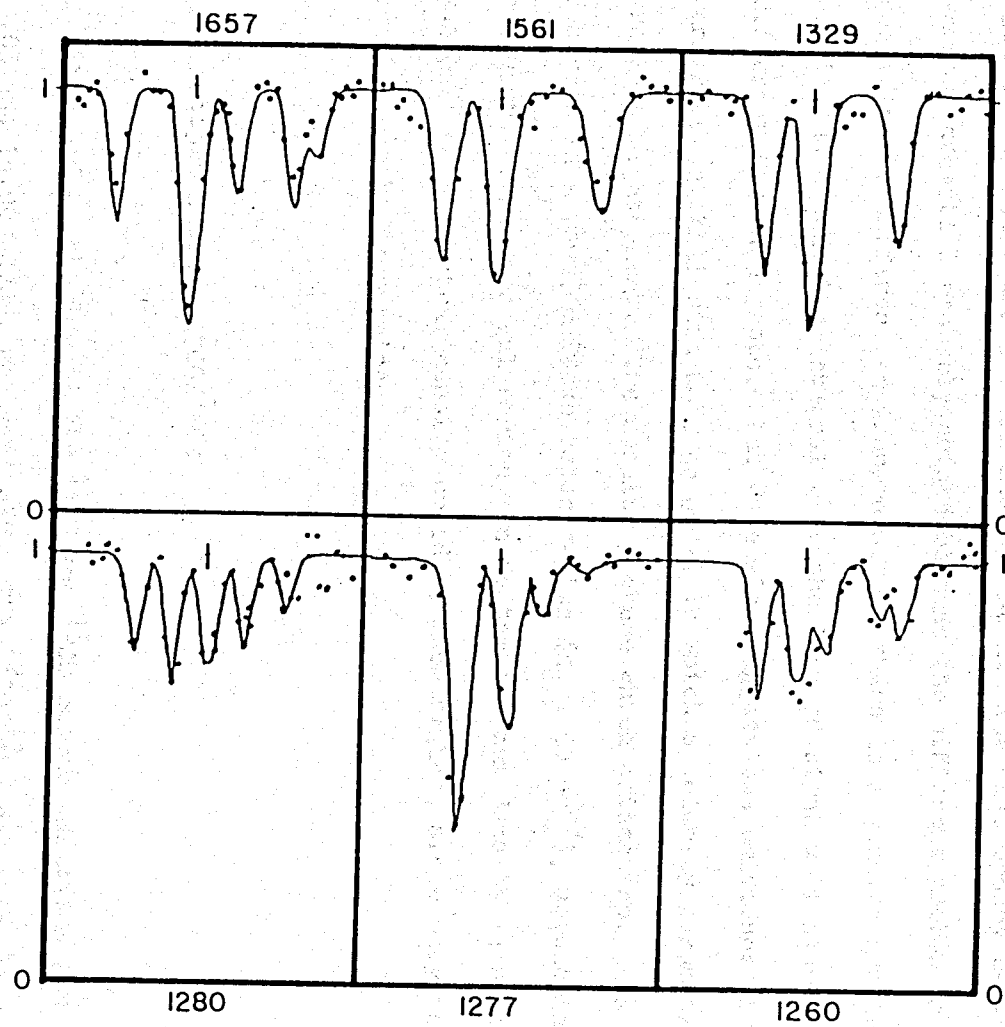


Figure 6-5. Theoretical and observed (filled circles) line profile for the strongest UV C I multiplets for $n_H = 500 \text{ cm}^{-3}$, $b = 1 \text{ km/s}$, $T = 40 \text{ K}$, and assuming a 95/5 curve of growth.

hydrogen density derived from the electron density and the higher density derived from the C I level populations.

The hydrogen volume density depends on the method used to derive it. I found that $n_{\text{H}} (n_e) < 100 \text{ cm}^{-3}$; $n_{\text{H}}(^{12}\text{CO}) = 200 \text{ to } 400 \text{ cm}^{-3}$; and $n_{\text{H}}(\text{CI}) = 500 \text{ cm}^{-3}$. All densities are for $T = 40 \text{ K}$. The discrepancy between the various densities probably arises because the different probes are sensitive to different environments. If there is a density gradient within the cloud, the integral over the line of sight will also be different for each probe. The data also suggest the existence of a warmer outer shell with $n_{\text{H}} = 50 \text{ cm}^{-3}$, in which a velocity parameter gradient might exist. The density picture which arises from this analysis is a warm, diffuse outer region ($n_{\text{H}} = 50 \text{ cm}^{-3}$), developing into a denser, cooler central region, where the maximum density is at least 500 cm^{-3} . The central density could be much higher, since only the mean density can be ascertained.

6.4 Isotopic Ratios: $^{12}\text{CO}/^{13}\text{CO}$

From 5.5.2, the log of the ^{12}CO and ^{13}CO column densities are 15.84 ± 0.05 and 14.00 ± 0.05 , respectively. The $^{12}\text{CO}/^{13}\text{CO}$ ratio is 70 ± 8 . This number is reasonably accurate, as both ^{12}CO and ^{13}CO have absorption lines which are almost optically thin. The $^{12}\text{C}/^{13}\text{C}$ ratio is not the same as the $^{12}\text{CO}/^{13}\text{CO}$ ratio, as chemical fractionation can occur (Watson et al. 1976, hereafter WAH). The relationship between

$^{12}\text{C}/^{13}\text{C}$ and $^{12}\text{CO}/^{13}\text{CO}$ is (WAH)

$$\frac{^{13}\text{CO}}{^{12}\text{CO}} = h^{-1} \frac{(1+X)}{(1+Xh^{-1})} \frac{^{13}\text{C}}{^{12}\text{C}} \quad (6-11)$$

$X = \Gamma/\alpha [^{12}\text{C}^+]$, $h^{-1} = e^{35/T}$, Γ is the CO photoionization rate, α is the reaction rate for the interchange of ^{12}C and ^{13}C , and $[^{12}\text{C}^+]$ is the volume density of singly ionized carbon (n_e).

RDF also calculated the photoionization rate of CO for their grain models. Using the methods outlined in Appendix D, I find that $\langle \Gamma \rangle = 2.02 \times 10^{-12} \text{ s}^{-1}$ for model 2 and $\langle \Gamma \rangle = 7.72 \times 10^{-12} \text{ s}^{-1}$ for model 3. With the measured reaction rate of $\alpha = 7 \times 10^{-10} \text{ cm}^3 \text{ s}^{-1}$ for equation 6-11, $X = 0.14$ and $X = 0.55$ for models 2 and 3, respectively. I have used the mean n_e for each model (Table 6-6).

For $T = 40 \text{ K}$,

$$\frac{^{12}\text{C}}{^{13}\text{C}} = \frac{h^{-1}(1+X)}{(1+Xh^{-1})} \frac{^{12}\text{CO}}{^{13}\text{CO}} = 1.94 \frac{^{12}\text{CO}}{^{13}\text{CO}} \quad (6-12a)$$

for model 2 and

$$= 1.68 \frac{^{12}\text{CO}}{^{13}\text{CO}} \quad (6-12b)$$

for model 3. For $^{12}\text{CO}/^{13}\text{CO} = 70 \pm 8$, $^{12}\text{C}/^{13}\text{C} = 136 \pm 15$ for model 2 and $^{12}\text{C}/^{13}\text{C} = 118 \pm 13$ for model 3.

Both $^{12}\text{C}/^{13}\text{C}$ ratios are above the solar value of 89. Observations of dark clouds (Wannier, 1980) suggest $^{12}\text{C}/^{13}\text{C} = 60$. The implication of this is that chemical fractionation may not be important in the diffuse cloud towards X Per. A similar conclusion was drawn by Wannier, Penzias, and Jenkins (1982) for the ζ Oph cloud. It is interesting to note that Olive and Schramm (1982) have suggested that the young solar nebula was injected with processed material from nearby supernovae (SN). Their calculations imply that the sun may have overabundances of oxygen and ^{12}C relative to their IS values.

No other isotopic species has been observed. An upper limit to the ^{18}O isotope of CO can be derived by assuming a 10 mR minimum equivalent width for the 2-0 band ($f = 0.04$), or $\log N(\text{C}^{18}\text{O}) < 1.3 \times 10^{13}$. This implies that the observed $\text{C}^{18}\text{O}/\text{C}^{16}\text{O} < 1/570$, whereas the solar value is $\approx 1/500$. A cloud with a slightly large column density of CO should make the C^{18}O detectable. Additionally, the species C^{17}O should be observable with the Space Telescope towards more heavily reddened stars.

6.5 Abundances

The existence of molecules in IS clouds indicates the existence of chemical reactions, either in the gas phase or on the surface of grains. Various reaction mechanisms have been proposed for molecular formation and destruction, and a number of authors have solved the coupled set of

linear equations for various input parameters relevant to diffuse IS clouds (Mitchell et al. 1977; Glassgold and Langer, 1974; Black and Dalgarno, 1977, Black et al. 1978; Prasad and Huntress 1980a, 1980b; and Henning, 1981). The results from each of these studies differ mainly due to the initial conditions imposed on the model. Because of this similarity, I have chosen to compare my results with those of Henning (1981). Additionally, his Model 4 matches quite closely the physical parameters which I have derived for the line of sight towards X Per ($T = 40$ K, $n_H = 1000$ cm⁻³, $\tau_V = 1.9$). The major differences are that his fractional abundance of H₂ is 0.1, whereas mine is 0.9. Henning also predicts $n_e = 0.03$, whereas I observe 0.02 cm⁻³. Table 6-11 lists the observed or upper limit of the fractional abundance of a constituent and the calculated fractional abundance. An important point in the theory is that for $2.4 < \log n < 4$, the abundances are very sensitive to the density. Henning refers to this density regime as the "Reactive Zone". For example, from $n_H = 800$ cm⁻³ to $n_H = 1400$ cm⁻³, $n(\text{H}_2\text{CO}^+)$ changes by 12 orders of magnitude. The last column in Table 6-11 lists the range which the fractional abundance takes from $n_H = 800$ cm⁻³ to 1400 cm⁻³ (eg, H₂CO⁺ would be given the value of 12 in column 3). This gives a rough estimate of the error. I have also included a number of theoretical predictions in Table 6-11 for which no observational data are available. All molecules with fractional abundances less than -10 dex have been excluded from Table 6-11. This corresponds to a column density of $< 10^{11}$ cm⁻². A footnote is used to indicate the upper limits based on Nf , where the oscillator strength is not known (cf Table 5-7).

TABLE 6-11
FRACTIONAL ABUNDANCES

T=50K $n_H=1000 \text{ cm}^{-3}$ $v=2$

Molecule	Log $\frac{n_i}{n_H}$		slope	Element	Log $\frac{n_i}{n_H}$		slope
	obs.	theory			obs.	theory	
CO	-5.5	-3.8	2	CN	-8.3	-6.7	2
CH	-7.4	-6.8	1	C ₂ H	—	-6.6	6
CH ₂	<-8.9 ^a	-6.8	1	CH ⁺	<-8.7	-11.6	1
CO ₂	—	-11.8	4	HCO	—	-8.4	6
N ₂	<-3.0	-8.0	2	NO	<-6.8	-9.4	5
H ⁺	—	-5.3	3	C ⁺	-3.7	-3.8	1
Si ⁺	-5.2	-4.5	3	HCO ⁺	—	-10.5	2
CH ₃	<-9.0 ^a	-9.4	7	C ₂ H ⁺	—	-9.8	3
C ₂	-7.9	-8.6	3	C	-5.9	-3.8	1
H ₂ CO	<-6.9	-10.0	4	C ₂ ⁺	<-10.1 ^a	-9.8	1
H ₂ O	-7.5	-9.0	4	OH	-8.0	-8.0	4
OH ⁺	—	-10.0	2	NH	—	-11.0	4
HCN	—	-9.4	8	O ₂	<-4.6	-11.4	1
CS	<-8.0	-8.3	3	SO	<-7.5	-10.4	3
S	-7.3	-5.0	2	S ⁺	-4.75	-5.0	2
HCl	<-8.1	-8.6	4				

^af value estimated at 0.1

The agreement between the observations and the data are quite good, especially when the value of the gradient is taken into account. The major discrepancy is with the prediction that the neutral and singly ionized abundances of carbon and sulfur should be equal, where I find them to be almost two orders of magnitude apart. Mitchell et al (1978) also predicts a large fraction of neutral carbon. The column density of neutral carbon could be increased if a 99/1 or 99.5/.5 curve of growth were used, but the data are not good enough to distinguish between the different curves of growth. Again, the calculated abundance of CH^+ is orders of magnitude below the observed abundance, which is not a new problem (cf Watson, 1978). The $\text{OH}/\text{H}_2\text{O}$ ratio is >1 , whereas I observe a ratio of less than 1, if my identification of H_2O is correct. My upper limit on CS is very close to the predicted limit, suggesting that perhaps the identification of the 1510 Å and 1543 Å UI lines with CS is correct. Alternatively, the large abundance of both C_2H and C_2H^+ also indicate that perhaps one of the three strong lines in the 1500 Å region could be attributed to C_2H (cf 5.12). The large abundance of HCN and HCO suggest these molecules might be observable also.

In conclusion, except for CH^+ , the observed molecular abundances can be explained by a combination of gas phase and grain induced chemical reactions. Additional evidence would be the detection in the diffuse ISM of such species as HCO, HCN, HCO^+ and C_2^+ . However, a great deal of laboratory work must be done in order to identify the spectrum and to extract quantitative values.

7. A DIFFUSE CLOUD MODEL

7.1 The Model

To a first approximation, the line of sight towards X Per contains a 0.8 pc thick cloud of gas and dust at a kinetic temperature of 40 K and a hydrogen density of 1000 cm^{-3} , with the hydrogen primarily diatomic. The question to be asked then is: Are these parameters physically possible, and do they really describe the material along the line of sight? For example, the diffuse IS radiation field decreases with depth into the cloud, which decreases the photoionization rate. If the cloud can be characterized by a single density, then the electron density will decrease towards the center, and the neutral fraction will increase. Similarly, the molecular abundance also increases towards the center, if by no other reason other than a decrease in the photodestruction rate. The temperature and density may also change as a function of depth, particularly if pressure equilibrium with the ICM is invoked and heating is due to outside sources. Clearly, serious consideration must be given to the actual meaning of the physical parameters derived from the observed column densities.

The observed column density is the integral of the volume density over the line of sight. This integral could be different for each ion because of differences in the distribution of their volume densities. Moreover, pressure indicators, such as the fine structure levels of C I

and C II, may be difficult to interpret accurately. The C I fine structure analysis of 6.3.2 has this problem, as the observed level populations cannot be described by a single density and temperature. Similarly, the differences between the hydrogen density derived from the C I fine structure levels and by scaling the electron density by the carbon to hydrogen ratio indicates that the line of sight cannot be described by a single set of parameters.

A more appropriate method for determining the physical conditions along the line of sight is to construct a model of the cloud(s), requiring it to match the observed column densities. For the line of sight towards X Per, the major observations to be explained are the diatomic hydrogen abundance, the column densities of the neutrals and their ions, and the column densities of the fine structure levels. Additional limits are suggested by the level population of C_2 ($T = 40$ K) and by the non-detection of the fine structure levels of Si II and O I.

I have constructed a simple model of the line of sight towards X Per which satisfies the above requirements. The density distribution within the cloud is described by the plane parallel cloud model of de Jong et al. (1980). They assume that the cloud is in hydrostatic equilibrium and that the cloud is supported by turbulent pressure of a gaussian nature, with a dispersion of $b/\sqrt{2}$. The central pressure is

$$P_0 = P_1 + 4.34 \times 10^4 A_{V0}^2 \text{ K cm}^{-3} \quad (7-1)$$

where P_1 is the pressure (cm^{-3}K) of the ICM, and A_{V0} is the visual extinction at the center of the cloud. The pressure at any visual extinction (A_V) into the cloud is

$$P = P_0 - 4.34 \times 10^4 (A_{V0} - A_V)^2 \text{ K cm}^{-3} \quad (7-2)$$

The density is related to the pressure by

$$n = 0.0118 \frac{P}{b^2} \text{ cm}^{-3} \quad (7-3)$$

where b is in km/s. I have used $b = 1$ km/s for all calculations; and have assumed that the density described by equation 7-3 is the particle density n ($= n_{\text{HI}} + n_{\text{H}_2}$).

The rate of formation of diatomic hydrogen is

$$n_{\text{H}} T^{1/2} K \times 10^{-18} \text{ s}^{-1} \quad (7-4)$$

(Hollenbach, Werner, and Salpeter, 1971, hereafter HWS; BD; Federman, Glassgold, and Kwan, 1979, hereafter FGK), where K is a constant used to absorb uncertainties. BD found $K = 2.86$ towards ζ Oph.

The destruction of H_2 is a two step process (Stecher and Williams, 1967; HWS). The first step involves the excitation of an electron by the absorption of a UV photon in any one of the permissible Lyman or Warner bands. The electron then decays back into the ground electronic state, where the particular vibrational band it decays to is described by the Franck-Condon principle. The decay into the ground state vibrational continuum is permissible and has a non-negligible Franck-Condon factor. This factor is then the probability that an H_2 molecule dissociates after an electron reaches the particular excited level. The total dissociation rate is then the rate of absorption to that level times the probability that the level decays to the ground state vibrational continuum, weighed by the initial population of the lower level, and summed over all possible transitions. The absorption oscillator strengths have been calculated by Allison and Dalgarno (1969), and the decay probabilities by Stephens and Dalgarno (1972). Numerically, the rate of destruction is

$$R = \sum_i h_i k_i \int_0^{\infty} G_i(\nu) \sigma_i(\nu) d\nu \quad (7.5)$$

where i signifies the appropriate quantum numbers for a single transition, $\sigma_i(\nu)$ is the cross section for excitation, normalized to

$$\int_0^{\infty} \sigma_i(\nu) d\nu = \frac{\pi e^2}{mc} f_i \quad (7.6)$$

f_i is the absorption oscillator strength, h_i is 1/4 or 3/4, depending on the symmetry of the lower rotational level, and k_i is the fractional

probability that the decay dissociates the molecule. $G(\nu)$ is the radiation field at the particular point within the cloud. The radiation field is attenuated by absorption by dust and by the absorption of line photons. HWS expresses $G(\nu)$ as

$$G(\nu) = \frac{G_0}{4\pi} \int d\Omega e^{-(\tau_g + \tau_l)} \quad (7-7)$$

where τ_{gr} is the optical depth of the dust, and τ_l is the optical depth of the line due to the surrounding H_2 . The calculation of equation 7-5 is very time consuming, as there are more than 54 B-X (Lyman) transitions from the first two rotational levels of H_2 . HWS and BD state that dissociation from C-X (Werner) transitions is negligible. BD suggested that equation 7-7 could be rewritten in terms of the equivalent width of the line. Since there exist approximations to the curve of growth, the equivalent width (W) of a line can be determined at a fraction of the cost it would take to calculate the exact line profile (cf 4.1). Equation can then be rewritten as (BD)

$$R = \sum_i \frac{W_i G_{oi}}{N_i} \quad (7-8)$$

where N_i is the column density of the molecule in the lower state of transition i , and W_i is the equivalent width of the line. FGK point out that equation 7-8 is an incorrect expansion of equation 7-5, and that $dW_i/d\tau_i$ should replace W_i in equation 7-8 for the two expressions to be equivalent. The derivative of the equivalent width can be found almost as easily as the equivalent width from approximations to the curve of

growth.

The best approximation for the curve of growth is by Rodgers and Williams (1974). They find that the equivalent width of a line can be approximated by

$$W = (W_L^2 + W_D^2 - \{W_L W_D / W_W\}^2)^{1/2} \quad (7-9)$$

where W_W is the equivalent width of an optically thin line (cf 4.1), and W_D and W_L are expansions for the equivalent width of a gaussian line profile and a Lorentz line profile, respectively. I have used equation 7-8 with the modification suggested by FGK to calculate the photodestruction rate of H_2 . I included absorption from only the $J=0$ and $J=1$ levels of H_2 . FGK show that the photodissociation rate increases by 15% to 30% when higher levels are included, especially if account is taken of the overpopulations of the higher rotational levels observed towards most reddened stars (Spitzer, 1978).

The photoionization rates for the atomic species are discussed in Appendix D, where I have used equation D-2 to describe the decrease as a function of extinction. I have only considered model 2 and model 3 (RDF, cf Appendix D) calculated for a central optical depth of 0.5. RDF point out that the photoionization rates depend not only on the specifics of the grains but also on the total extinction through the cloud. Their analysis show major variations between central optical depths of 0.3 and 0.5. From RDF, it appears then that the

photoionization rates for X Per ($T_c = 0.8$) will be lower than just a simple extension of the rates for $T_c = 0.5$. For example, the photoionization rate decreases by 50% between $T_c = 0.3$ and $T_c = 0.5$ for chlorine. This is the largest variation, the others changing by less than 20%. I have used the photoionization rates for $T_c = 0.5$, extrapolating them to $T_c = 0.8$.

Photoionization of carbon and CR ionization of hydrogen are the primary sources of electrons in diffuse clouds. At any point in the cloud,

$$\zeta_0 n_H + \Gamma n_{CI} = n_e (\alpha_H n_{HII} + \alpha_C n_{CII}) \quad (7-10)$$

where $\zeta_0 = 10^{-16} \text{ s}^{-1}$ is the CR ionization rate, Γ is the photoionization rate, and α_H and α_C are the recombination rates for hydrogen and carbon, respectively. The identities

$$n_{CI} + n_{CII} = n_C \quad (7-11)$$

and

$$n_e = n_{CII} + n_{HII} \quad (7-12)$$

can be used to express equation 7-10 in terms of n_C , n_H , and n_e

$$n_e^3 \alpha_H \alpha_C + n_e^2 \Gamma_H \alpha_H - n_e (\zeta_O \alpha_C n_H + n_C \Gamma_H \alpha_H) - \zeta_O \Gamma_H n_H = 0 \quad (7-13)$$

The electron density is the first root of equation 7-13.

The temperature of the gas is, in principle, an equilibrium between heating and cooling processes. Many of these processes have been discussed in detail by Field (1971), Dalgarno and McCray (1972), Draine (1978), and others. The important heating mechanisms appear to be photoejection of electrons from dust grains (Watson, 1972; Draine, 1978; RDF)

$$2.4 \times 10^{-26} n_H \text{ erg cm}^{-3} \text{ s}^{-1} \quad (7-14a)$$

photoionization of carbon (Field, 1971)

$$5.0 \times 10^{-22} n_e n_{\text{CII}} e^{-\tau_{\text{UV}}} T^{-0.624} \text{ erg cm}^{-3} \text{ s}^{-1} \quad (7-14b)$$

cosmic ray ionization (Field, 1971)

$$4.5 \times 10^{-27} n_H (\zeta_O / 10^{-16}) \text{ erg cm}^{-3} \text{ s}^{-1} \quad (7-14c)$$

H₂ formation (Barlow and Silk, 1976)

$$1.65 \times 10^{-28} n_H n_{HI} \text{ erg cm}^{-3} \text{ s}^{-1} \quad (7-14d)$$

and chemical heating (Dalgarno and Oppenheimer, 1974)

$$3.0 \times 10^{-29} n_{H_2} n_H e^{-\tau_{UV}} \text{ erg cm}^{-3} \text{ s}^{-1} \quad (7-14e)$$

RDF calculated the photoelectric heating for their different grain models. The heating rate for model 2 is

$$9.0 \times 10^{-27} n_H e^{-2.73\tau} \text{ erg cm}^{-3} \text{ s}^{-1} \quad (7-15a)$$

and the heating rate for model 3 is

$$4.5 \times 10^{-27} n_H e^{-0.81\tau} \text{ erg cm}^{-3} \text{ s}^{-1} \quad (7-15b)$$

The primary cooling mechanism is the energy lost by the radiative decay of the $3p_{3/2}$ level of C II, and occurs at a rate of

$$2.5 \times 10^{-24} e^{-91.3/T} n_{CII} \sum_i n_i \langle \sigma v \rangle_i \text{ erg cm}^{-3} \text{ s}^{-1} \quad (7-16a)$$

where n_i is the density of colliding particle i , $\langle \sigma v \rangle$ is the collisional cross section in units of 10^{-10} cm^2 and T is the temperature. The collisional deexcitation rates for H I are from Flower and Launay (1977a) and from Flower and Launay (1977b) for H_2 . These cross sections can be approximated quite closely by

$$\langle \sigma v \rangle = 4.83 + 0.678 \ln(T) \quad (7-16b)$$

$$\langle \sigma v \rangle = 2.53 + 0.372 \ln(T) \quad (7-16c)$$

$$\langle \sigma v \rangle = 3.05 + 0.471 \ln(T) \quad (7-16d)$$

in units of 10^{-10} cm^2 for atomic hydrogen, para- and ortho- diatomic hydrogen, respectively. The cross section for deexcitation by electrons is

$$\langle \sigma v \rangle = 5.74 \times 10^4 T^{-1/2} \quad (7-17)$$

also in units of 10^{-10} cm^2 .

If the cloud is warm, the fine structure levels of O I are efficient coolants, where the cooling rate is

$$8.4 \times 10^{-24} T^{1/6} n_{\text{H}} n_{\text{OI}} e^{-228/T} \text{ erg cm}^{-3} \text{ s}^{-1} \quad (7-18)$$

To calculate the equilibrium temperature for a given density, the heating rates are summed and equivalenced with the net cooling rate by iteratively solving for the temperature.

The cloud was separated into 50 zones of equal extinction. The input parameters are the external pressure (P_1), the depletions of the elements (C, Mg, Si, S, Ca, and Fe), the velocity parameter, and the total color excess of the cloud, where I assume $A_{V0} = 3/2E(B-V)$. At each shell, the equilibrium temperature, ionization, and H_2 abundance are calculated. I cannot fit the theory to the observations for any combination of the input parameter. This appears to be because the equilibrium temperature is too small.

To check this, I have recalculated the model with an arbitrary temperature distribution. I find that I can fit all of the observed column densities by using a linear temperature distribution of the form

$$T = T_1 - (T_1 - T_0) \frac{A_V}{A_{V0}} \quad (7-19)$$

where T_1 and T_0 are the temperatures at the edge and center of the cloud, respectively.

Table 7-1 lists the calculated column densities for a cloud with the following parameters: $b = 1$ km/s, $P_1 = 3000$ cm⁻³K, $T_1 = 200$ K, $T_0 = 35$ K, $E(B-V) = 0.52$. The depletions of the elements are $\delta_C = 0.3$, $\delta_{Mg} = 0.05$, $\delta_{Si} = 0.15$, $\delta_S = 1.0$, $\delta_{Ca} = 0.0015$, and $\delta_{Fe} = 0.0019$. The depletions for C, Si, and S are from Table 6-2, whereas the depletions for Mg II, Fe II, and Ca II are from the analysis of the electron densities (6.3.1) and the neutral depletions (6.1). The total Fe column density is (log) 14.6 cm⁻² which is 50% of the total column density from

TABLE 7-1
IS DIFFUSE CLOUD MODEL

Model Parameters: $P_1 = 3000 \text{ K cm}^{-3}$ $T = 200 \text{ to } 35 \text{ K}$ $b = 1 \text{ km/s}$ $E(B-V) = 0.52^m$		
Depletions: $C = 0.3$ $Mg = 0.05$ $Si = 0.15$ $S = 1.0$ $Ca = 0.0015$ $Fe = 0.0019$		
	Model ¹	Observed
H_{Tot}	21.4	21.4
HI	20.46	20.51
H_2	21.05	21.04
f	0.885	0.87
H_2 J=0	20.67	20.78
J=1	20.79	20.70
J=2	19.38	
J=3	18.55	
J=4	16.38	
J=5	14.78	
n_e	0.047 cm^{-3}	0.02 cm^{-3}
CII Tot	17.57	17.65
J=1/2	17.55	17.63
J=3/2	16.22	16.25
CI Tot	15.45	15.50
J=0	15.06	15.12
J=1	15.13	15.12
J=2	14.53	14.6 - 14.8

¹Except for f and n_e , the quoted numbers are $\text{Log}(\text{Column Density}) \text{ cm}^{-2}$.

TABLE 7-1 (CONT.)

	Model ¹	Observed
MgII	15.69	16.3 - 15.7 ²
MgI	14.03	14.08
SiIII Tot	16.18	16.18
J=1/2	16.17	16.18
J=3/2	10.73	12.72
SiI	12.92	12.72
SII	16.60	16.65
SI	14.06	13.90
CaIII	12.40	
CaII	12.70	13.40
CaI	10.57	10.60
FeII	14.28	15.60 - 14.3 ³
FeI	12.24	12.30

¹Except for f and n_e , the quoted numbers are Log (Column Density) cm^{-2} .

²Column density for an 70/30 curve of growth.

³Column density for a 50/50 curve of growth.

a 50/50 curve of growth. This curve of growth is consistent with the upper limits on the 2366 Å line of Fe II. The Mg column density is (log) 15.9 cm^{-2} , which is 70% of the column density of a 70/30 curve of growth. The Ca II depletion was derived empirically by finding the depletion which resulted in an accurate calculation of the Ca I column density. The corresponding Ca II curve of growth lies between an 70/30 and a 50/50 curve of growth, which is the same range as suggested in 6.1. The H_2 fudge-factor (K) was set equal to 1, although its value is probably larger, since I did not include absorptions from the higher rotational states of H_2 . If these absorptions were included, the photodissociation rate would increase, resulting in a lower H_2 column density.

The external pressure of $3000 \text{ cm}^{-3}\text{K}$ is similar to the mean ICM pressure of $\approx 10^3 \text{ cm}^{-3}\text{K}$ (Myers, 1978).

The photoionization rates from model 3 (RDF, of Appendix D) were used in the model. I cannot match the observed and theoretical column densities for any combination of input parameters using the photoionization rates of model 2. The difference between the models is that for $\lambda < 1500 \text{ Å}$, the grains of model 3 have a much higher albedo and have a large asymmetry parameter, indicating that they are strongly forward scattering. The calculated atomic and diatomic hydrogen column densities agree with the observations quite well, even though the model parameters were chosen specifically to match the column densities of the neutrals and the column densities of the C I fine structure levels.

Indeed, not only is the total H_2 column density accurately predicted, but the column densities of the $J=0$ and $J=1$ levels are within the observational errors. Figure 7-1 shows the calculated column density of the rotational levels of H_2 (scaled by their statistical weight) versus the excitation energy of the level above the ground state. The interesting feature of Figure 7-1 is the fact that the calculated populations of the H_2 rotational levels cannot be fit by a single rotational temperature. The line drawn through the first three rotational levels corresponds to a rotation temperature of 110 K, whereas the last three levels can be fit by a rotation temperature of 170 K. The latter temperature is a strong function of the choice of the initial temperature at the edge of the cloud (T_1). The upper level rotational populations will be different from those shown in Figure 7-1 if a complete analysis of the statistical equilibrium of the rotational levels were included (FGK). The H_2 level populations of ζ Oph (Morton, 1975), $^{\circ}$ Per (Snow, 1976), and ζ Per (Snow, 1977) all show the same qualitative structure as Figure 7-1. The important point is that this model reproduces the general trend of the H_2 level populations observed towards other stars without invoking an overly large radiation field. The C I level populations, neutral column densities, and hydrogen column densities remain within the observational errors if there is no temperature gradient within the cloud, and $T_1 = T_0 = 75$ K. The only real reason I include the temperature gradient is because the C_2 data cannot be explained by temperatures greater than ≈ 50 K (6.2). In this model then, the C_2 would exist only in the central core of the cloud ($T < 50$ K), and $N(C_2)/N(H) = 1 \times 10^{-7}$. For a central density of $n_H = 700$

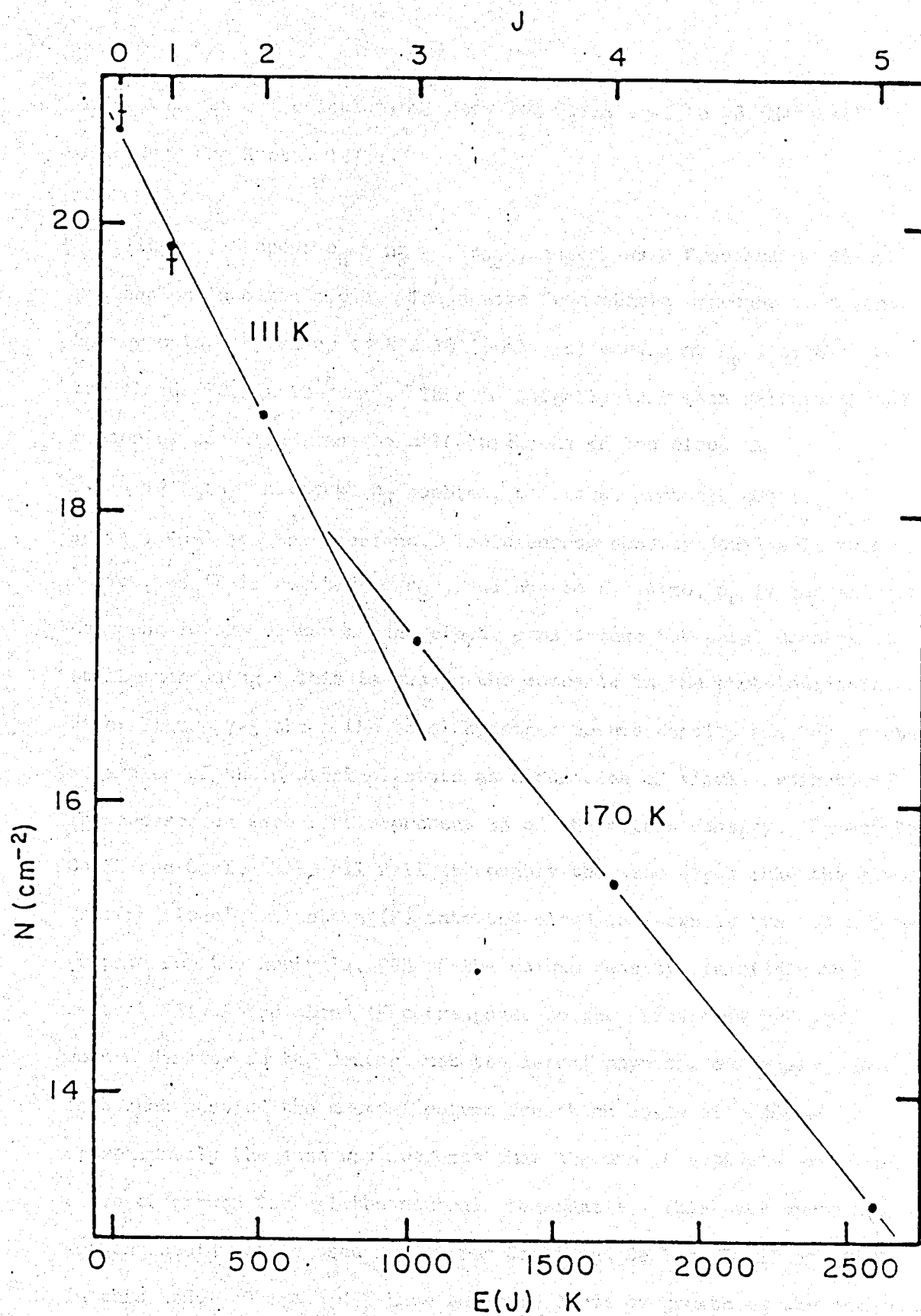


Figure 7-1. Predicted column densities from the first six rotational levels of H_2 . The observed $J=0$ and $J=1$ column densities are also indicated. The solid lines are theoretical predictions of the column densities for the indicated excitation temperatures.

cm^{-3} , theoretical calculations show $\log C_2/n_H = -6$ to -8 (Mitchell, Ginsburg, and Kuntz, 1977).

Figure 7-2 shows n_H , $n_{H I}$, n_{H_2} , and n_e as a function of visual extinction into the cloud. The change from atomic hydrogen to diatomic hydrogen is very sharp ($< 4 \times 10^{17}$ cm), and occurs at $A_V = 0.08^m$ into the cloud ($\approx 2.3 \times 10^{18}$ cm). This is slightly less than halfway to the center of the cloud, as the half-thickness of the cloud is 5.4×10^{18} cm. Although n_H doubles, the total particle density ($n_{H I} + n_{H_2}$) remains constant. The electron density doubles in this region, as it is related to n_H , and not to n . Also, n_e is beginning to decrease in the center of the cloud, even though the total density is still increasing. This is due to the decrease in the photoionization rate; Figure 7-3 shows the total hydrogen column density and the column densities of the neutral elements as a function of visual extinction. The crosses on each line represent 5% of the column density. Except for Ca II and Ca I, these all fall at roughly the same depth into the cloud. The fractional extinction (F) into the cloud is shown at the top of the graph. For the neutrals, 95% of the column density lie within the central 75% of the cloud (F corresponds to the fractional hydrogen column density to the center, not the actual physical distance). The fact that most of the neutral column densities scale with depth approximately the same way suggests that the use of a single empirical curve of growth for all the neutrals reasonable. This same curve of growth should not be used for either Ca II and Ca I or Ti II and Ti I. In this model, O I and N I have the same curve of growth as the dominant

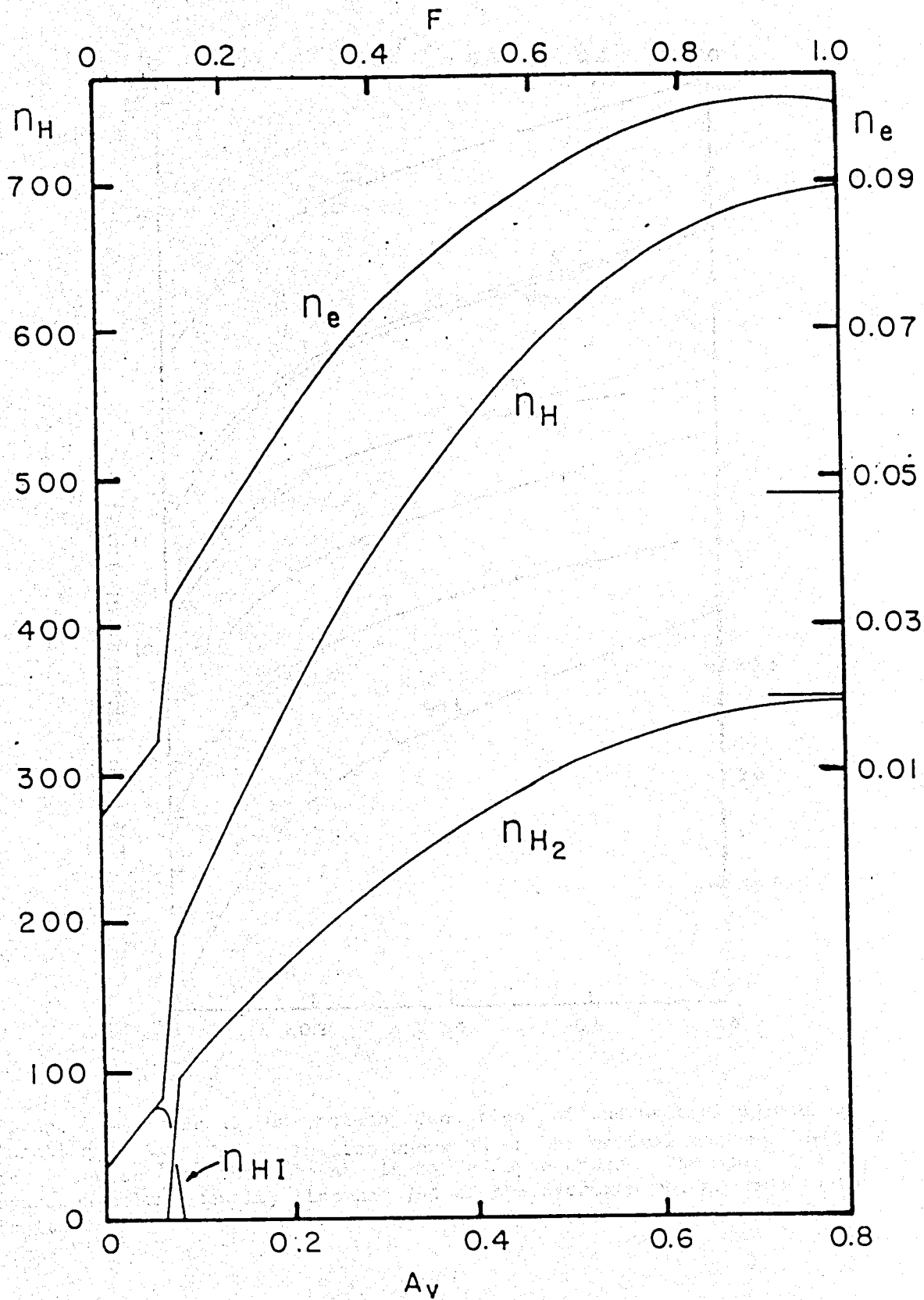


Figure 7-2. Predicted densities of n_e , n_H , n_{H_2} , and n_{HI} as a function of A_V . $F = A_V/A_{V0}$.

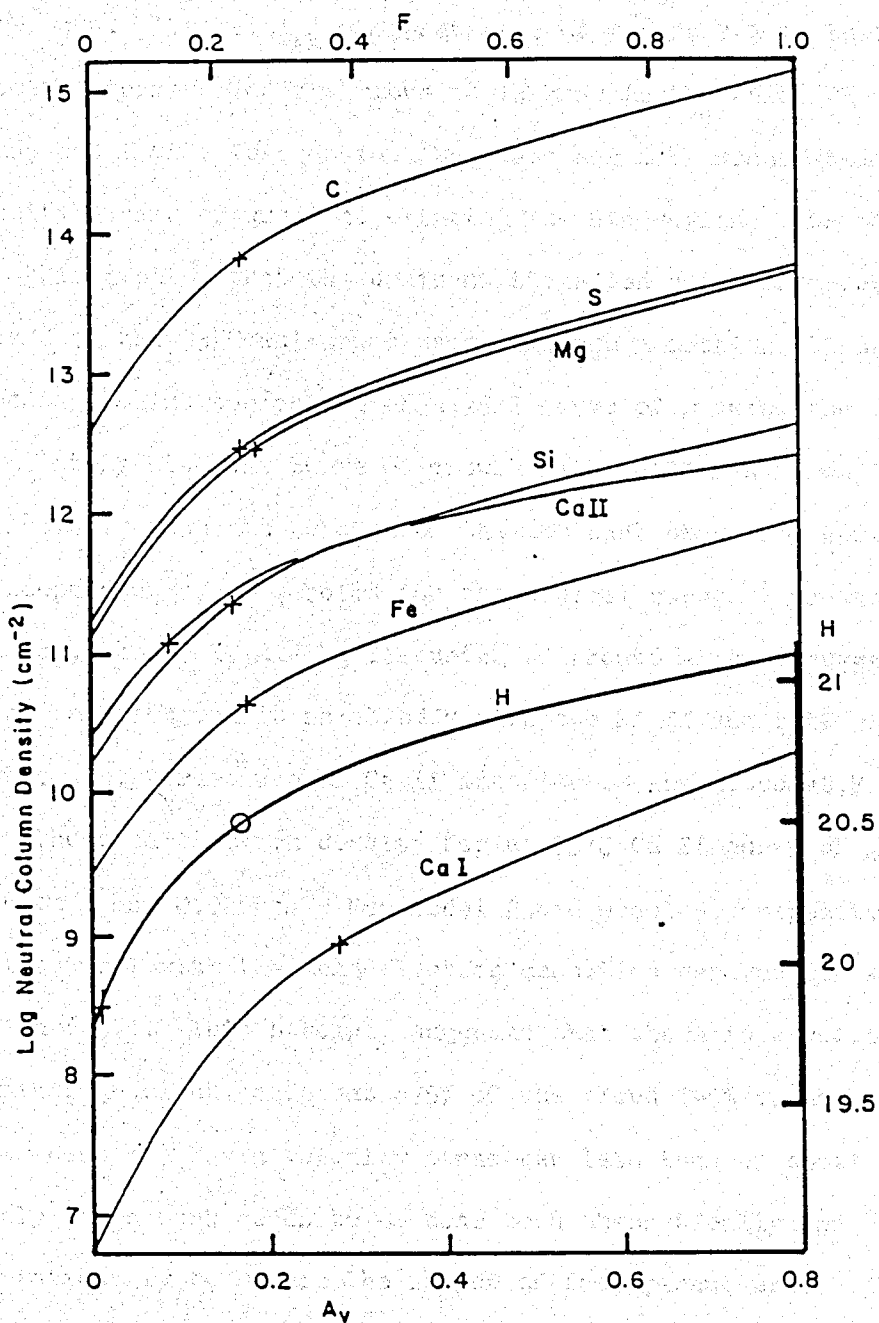


Figure 7-3. Predicted column densities of the neutral species as a function of A_V . The extinction where 5% of the neutral column density is exterior to that point is marked by a cross. The open circle on the hydrogen column density line has 74% of the hydrogen column density interior to it.

stage ions. A possible interpretation of Figure 7-3 is that the velocity parameter of the cloud is 10 km/s in the first 25 % of the cloud, and 1 km/s further in. The data are not inconsistent with a velocity parameter gradient existing in this region. The problem is that this implies that the dominant stage ion curve of growth is 75/25, instead of the 95/5 which was used. Although section 4.2 outlined the reasoning behind the choice of a 95/5 curve of growth, the data are not inconsistent with the curve of growth being different from 95/5, particularly since the choice of the dominant stage ion curve of growth is independent of the choice for the neutral curve of growth (5.1). Moreover, the Fe II and Mg II curves of growth already suggest such a reduction, although it is at odds with the Si II and S II curves of growth. The percentage of Ca II interior to the cloud at $F = 0.25$ is 85%. The mean electron density for an 85/5 Ca II curve of growth is 0.016 cm^{-3} and 0.020 cm^{-3} for model 2 and model 3, respectively. These are identical with the mean electron densities derived for each model in section 6.3.1. This strongly suggests that there is a velocity parameter gradient, and that $\approx 75\%$ of the cloud (95% of the neutral column density) has a velocity parameter less than or equal to 1 km/s. Clearly, more work needs to be done both theoretically and observationally to reduce the number of free parameters.

Figure 7-4 shows the column densities of the fine structure levels of C I (units on the left) and C II (units on the right) as a function of extinction. The tick marks again indicate the point at which 5% of the column density is on the exterior of the cloud and 95% is on the

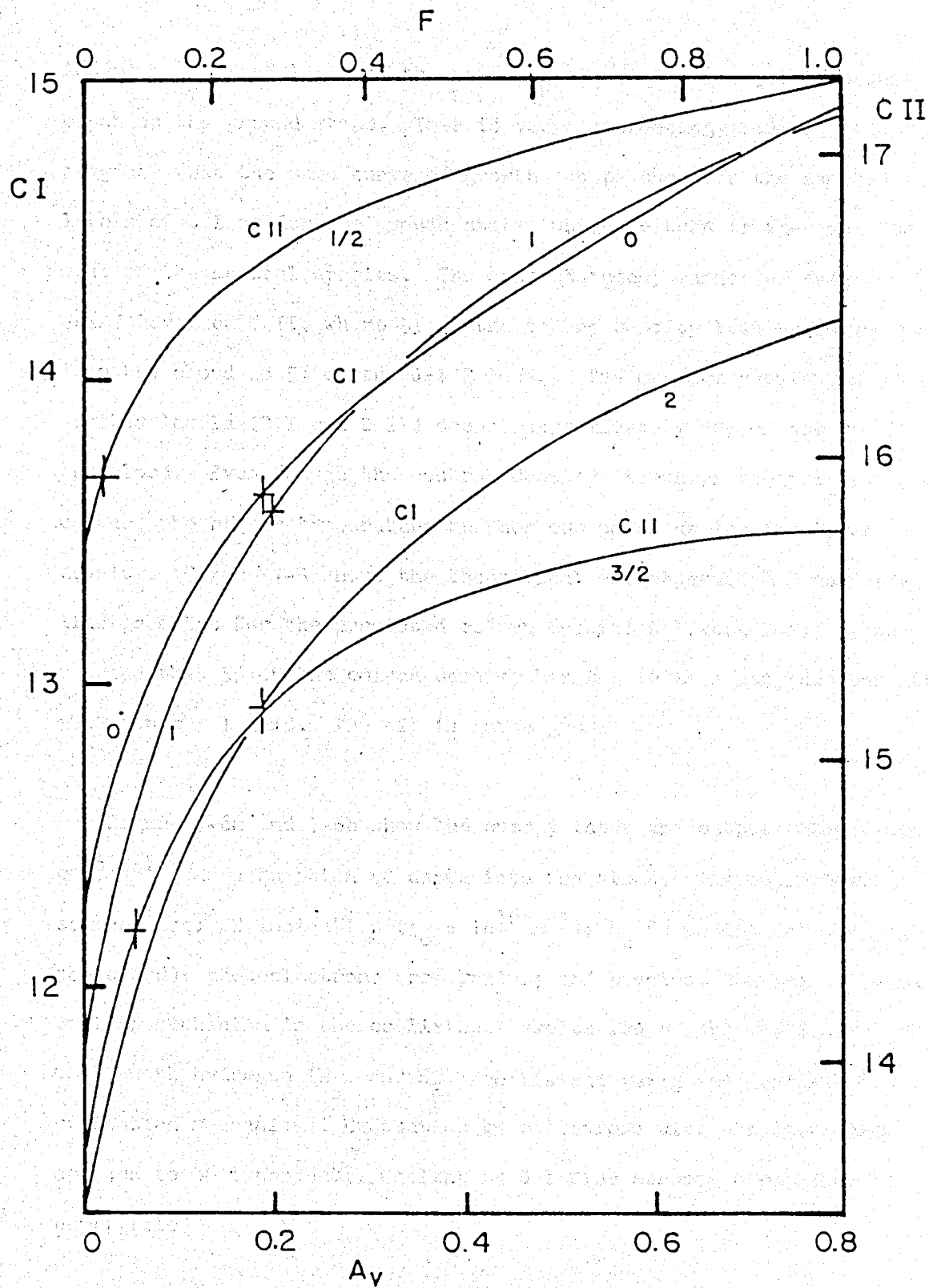


Figure 7-4. The same as Figure 7-3, except for the column density from the fine structure levels of C I and C II.

interior. The 5% level of the upper levels of C I occur at the same depth as the ground state. This is very interesting, because it suggests that the same curve of growth can be used for the excited levels of C I as for the ground state, which in turn is the same for most of the neutral species. The same statement cannot be said for the $J=3/2$ level of C II, where 5% of the column density lies twice as far into the cloud as 5% of the $J=1/2$ level. The maximum population of all excited levels (C I and C II) occurs approximately 50% of the way into the cloud. Even though the central density increases towards the center, the higher temperature further out makes up for the lower density. Figure 7-5 shows the theoretical and observed C I multiplet line profiles for the predicted column densities (Table 7-1). I have assumed that 5% of the column density has $b = 10$ km/s and the remaining 95% with $b = 1$ km/s. The fit is quite good.

Figure 7-6a and 7-6b show the energy input and output rates (ergs $\text{cm}^{-3} \text{s}^{-1}$) as a function of depth into the cloud. The major heating sources are: CR ionization ($\tau_0 = 10^{16} \text{s}^{-1}$); H_2 formation (at the edge of the cloud); photoelectrons from grains; and chemical heating. The major cooling mechanism is the collisional excitation of the $J=3/2$ level of C II, with hydrogen (H I and H_2) collisions being the dominant excitation mechanism. Excitation by collisions with electrons also appears to be important. Cooling by O I fine structure emission is negligible.

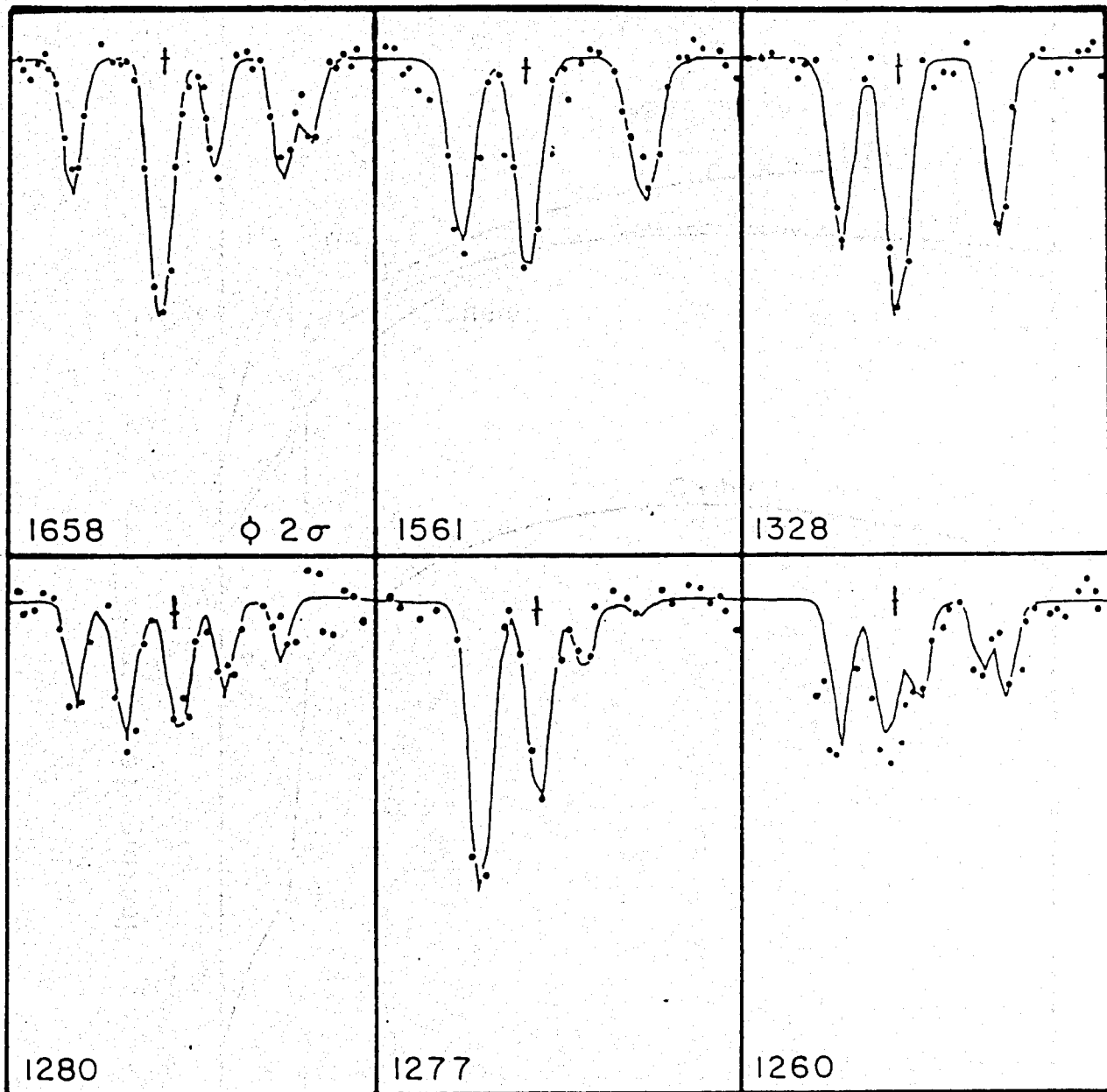


Figure 7-5. The predicted C I line profiles as compared with the observations.

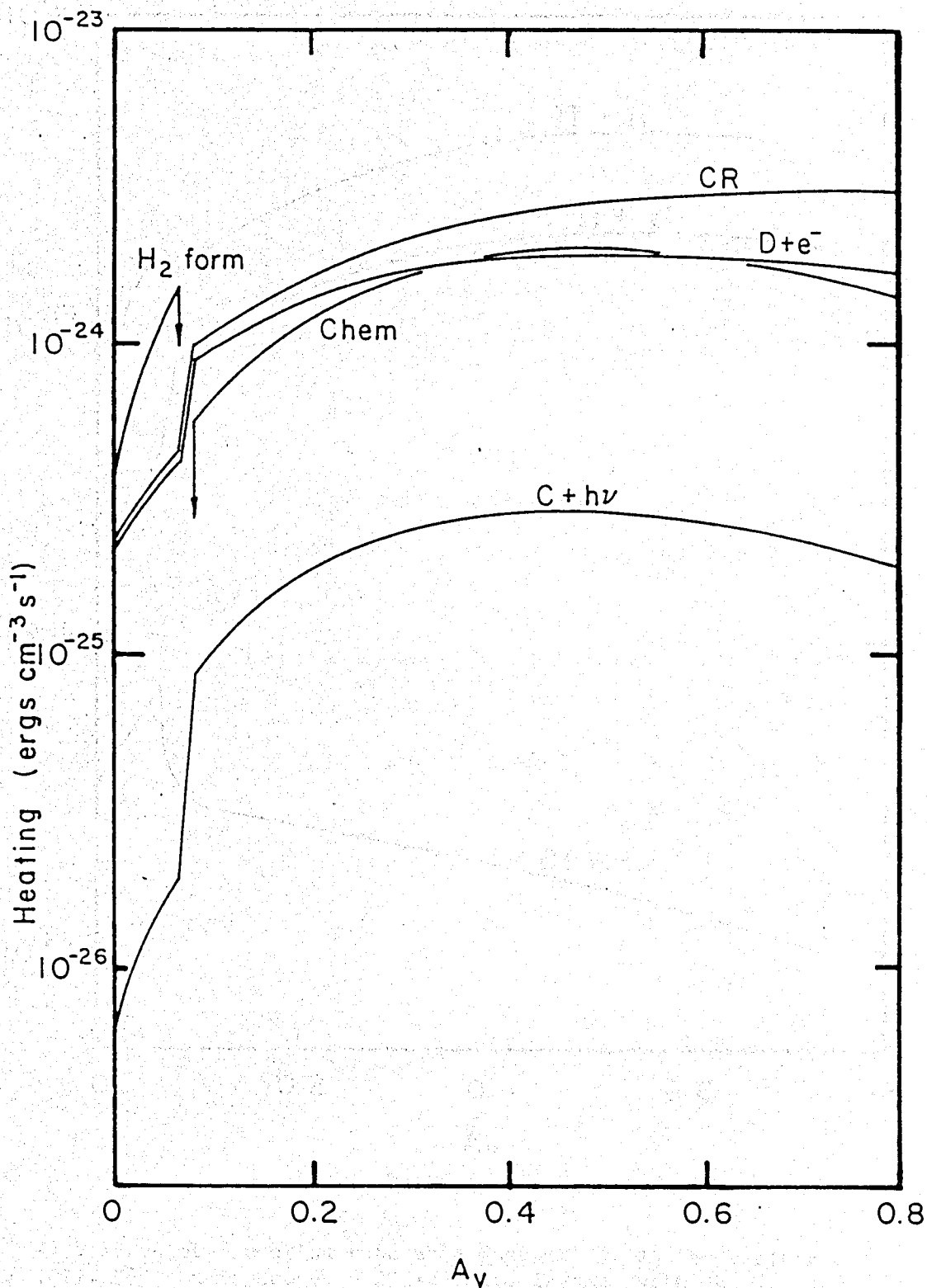


Figure 7-6a. Predicted heating rate as a function of A_v for heating by cosmic rays (CR), photoelectron ejection from dust grains ($D+e^-$), formation of H_2 (H_2 form), chemical reactions (Chem), and from the photoionization of carbon ($C+h\nu$).

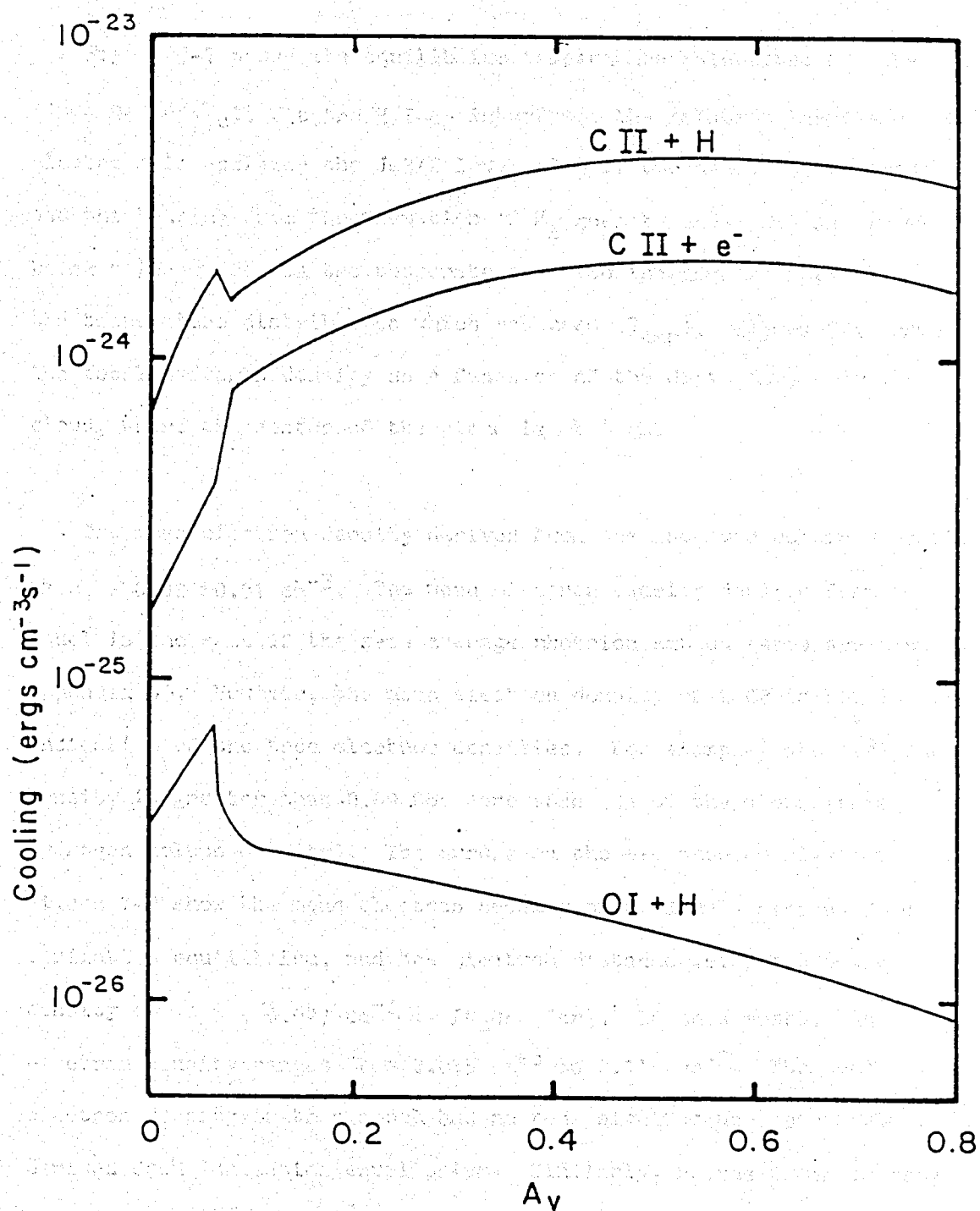


Figure 7-6b. Predicted cooling rate as a function of A_V for cooling by electron ($\text{C II} + e^-$) and hydrogen ($\text{C II} + \text{H}$) collisions with C II, and for hydrogen collisions with O I ($\text{O I} + \text{H}$).

Figure 7-7 shows the equilibrium temperature calculated for the model cloud (T_c). At the H I-H₂ interface, the relative importance of electrons in exciting the J=3/2 level of C II becomes more important, and the heating from the formation of H₂ goes to zero, the net result being a large drop in the temperature. Also included in Figure 7-7 is the temperature distribution which was used (T_{emp}). Figure 7-8 shows the total hydrogen density as a function of the depth (cm) into the cloud, where the center of the cloud is at 0 cm.

The mean electron density derived from the observed column densities is $n_e = 0.02 \pm 0.01 \text{ cm}^{-3}$. The mean electron density derived from the model is the same if the same average photoionization rates are used (cf Appendix D). However, the mean electron density of 0.02 is not at all indicative of the true electron densities. For example, the electron density is greater than 0.09 for more than 50% of the cloud (total hydrogen column density). The arrows on the electron density scale of Figure 7-2 show the mean electron density of 0.02 cm^{-3} derived from ionization equilibrium, and the electron distance-weighted electron density of $\langle n_e \rangle = 0.047 \text{ cm}^{-3}$ ($= \int n_e dr / \int dr$). In this model, the electron density ranges from 0.015 cm^{-3} to 0.111 cm^{-3} . The mean electron density in this model has no real significance, particularly if derived from ionization equilibrium. Similarly, n_H was found to range between 500 and 1000 cm^{-3} , although from Figure 7-2, the mean n_H has little meaning.

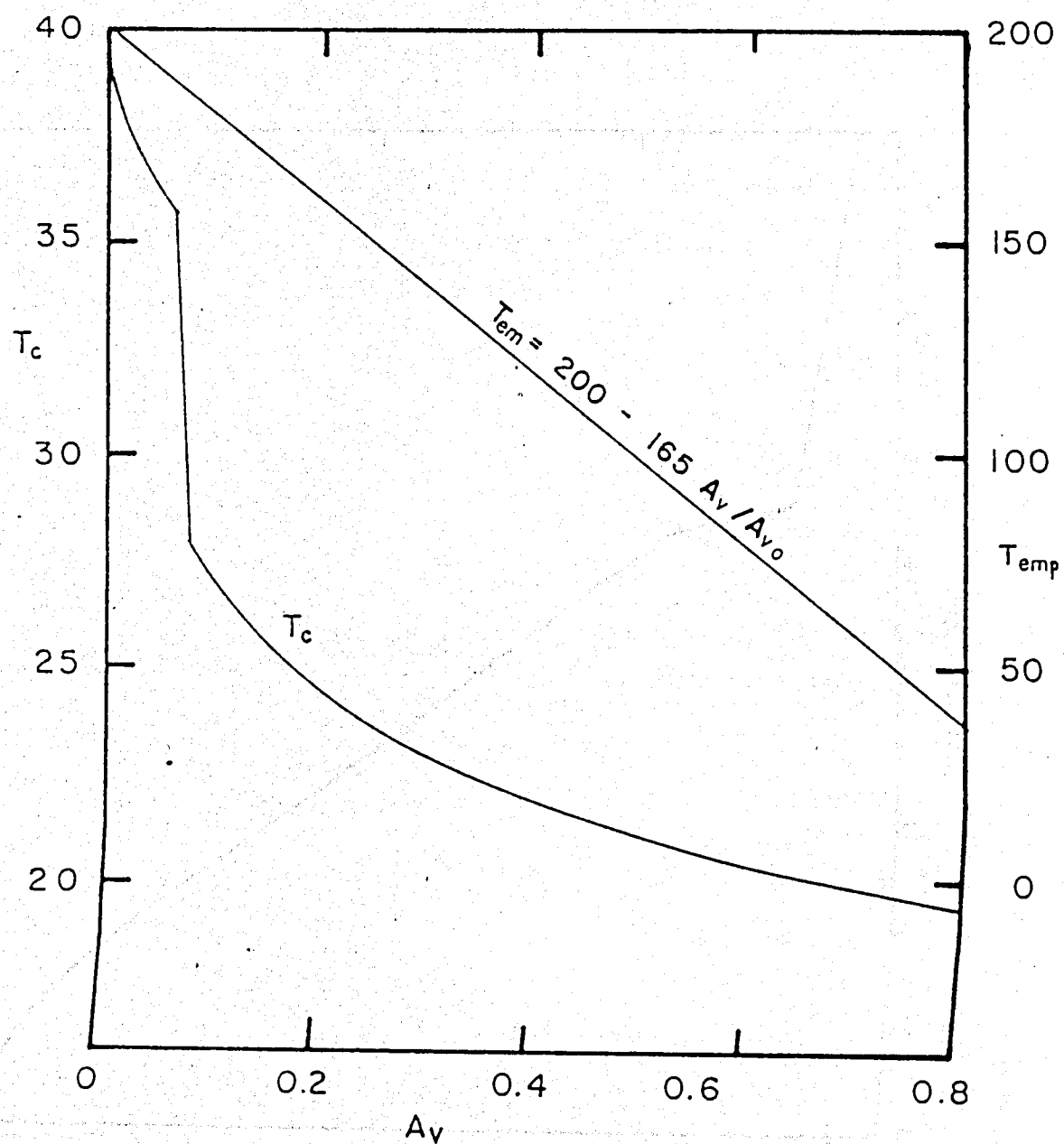


Figure 7-7. Predicted temperature from equating the heating and cooling rates (T_c). Also shown is the empirical temperature used ($Temp$; ordinate on the right).

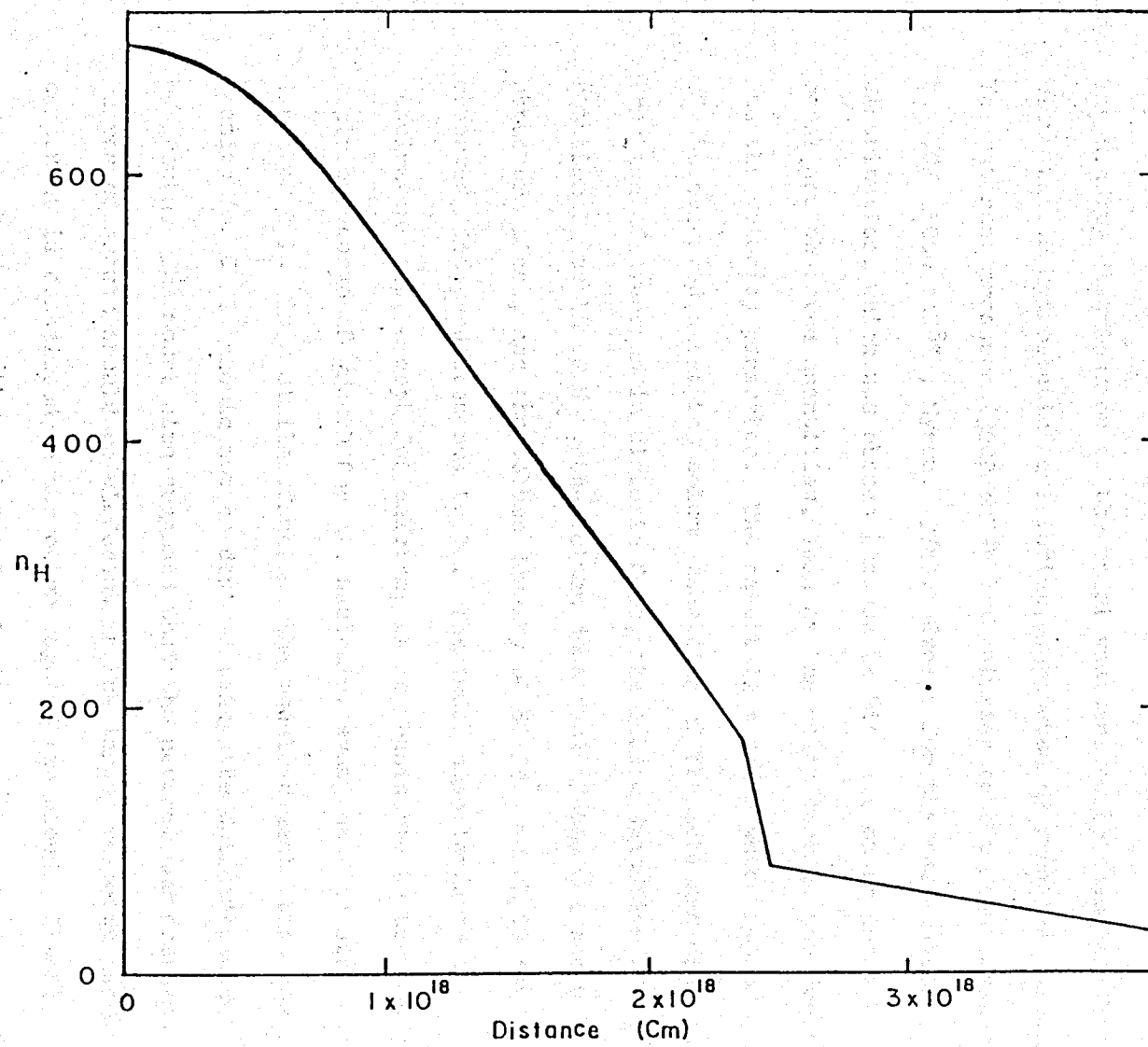


Figure 7-8. Hydrogen density as a function of linear distance out of the cloud (cloud center = 0 cm).

In this chapter, I have presented a model which accurately reproduces all of the observed ion and neutral column densities. The observed Ca II column density can be made to match the theoretical column density by reasonable arguments concerning its curve of growth. The density distribution of the model was derived by assuming that the cloud was in hydrostatic equilibrium, supported by gaussian turbulence. The external pressure ($3000 \text{ cm}^{-3} \text{ K}$) is similar to the mean pressure of the ICM ($1000 \text{ cm}^{-3} \text{ K}$, Myers, 1978). Except for the temperature distribution, which was chosen because it fit, all other input to the model are observed quantities, such as the color excess, the depletions, and the velocity parameter. The result is a model which reproduces all of the observed data: the column densities of the ions and neutrals, the fraction of hydrogen in diatomic form, the column densities of the two rotational levels of H_2 , the column densities of the C I and C II fine structure lines, and the column density of Si II^* , which is not observed, and predicted not to be. The model also leads to the conclusion that, except for calcium, it is reasonable to use the same empirical curve of growth for all neutrals, even the fine structure lines of C I. In a similar fashion, the model suggests that the column density for C II^* should not be derived using the dominant stage curve of growth. The model also suggests that the neutral and dominant stage curves of growth should be different if the larger velocity parameter component is contained in the outer edge of the cloud. Clearly, work needs to be done on the variety of velocity parameters observed along a single line of sight, particularly concerning the location of the material with the different velocity parameters.

8. SUMMARY AND CONCLUSIONS

8.1 Summary

In this dissertation, I have used UV, optical, and radio data to infer the physical conditions in the diffuse cloud along the line of sight towards X Per. Additionally, my studies have pointed out a number of problems in deriving these properties from the basic observational data.

The integrated volume densities along the line of sight towards X Per can be characterized by two velocity parameters, where $b = 1$ km/s for 95% of the material, and $b = 10$ km/s for the other 5%. For the dominant stage ions, the percentage in each component corresponds to the mass distribution of the gas with respect to the velocity parameter along the line of sight. The atomic curves of growth do not indicate whether this separation is a physical separation, where there are two distinct clouds with different velocity parameters or whether there is only one cloud with a velocity parameter gradient. The radio ^{12}CO and ^{13}CO suggest the latter, as the line widths are greater (^{12}CO) and less (^{13}CO) than 1 km/s. This could be due to optical depth effects. The analysis of the CH data indicate the need for $b = 0.75$ km/s, which is similar to the ^{13}CO line width. The CH data may have other problems, and work is in progress to determine the implications of this and other CH data. I have also constructed a model for the X Per diffuse cloud.

The model predicts that the density near the edge of the cloud is $\approx 35 \text{ cm}^{-3}$. This is very close to the hydrogen density predicted by matching the observed column densities of C IV, Si IV, N V (upper limit) with those predicted by an X-ray source embedded in the ISM. Since $b = 10 \text{ km/s}$ for the highly ionized species curve of growth, this suggests that indeed, the cloud edge has a higher velocity parameter. Alternatively, at least 1/3 of the material with $b = 10 \text{ km/s}$ can be accounted for by just the ICM along the line of sight. The data do not give an unambiguous answer for the question of the relative positions of the 1 km/s and 10 km/s velocity parameter components.

Another point brought out was that the most neutral species fit the a unique curve of growth, and that most dominant stage ions fit another curve of growth. In the case of X Per, these two curves of growth have the same shape, although this is probably not common. This conclusion was reached through ionization equilibrium calculations and by the model. The model also showed that the fine structure carbon lines used the same curve of growth as the neutral species. Ca II was shown to be an exception, both by the model and by the ionization equilibrium arguments.

I derived a mean electron density from ionization equilibrium of $n_e = 0.02 \text{ cm}^{-3}$. I found that the electron density for all observed ions and neutrals would agree if the curve of growth used to derive the Mg II, Fe II, and Ca II column densities were different from a 95/5 curve of growth. Indeed, when the depletion derived from the 1 km/s

column density of these three ions was input into the model, the neutral column densities were accurately predicted. In all three cases, the neutral column density is independent of the curve of growth used. The Ca II curve of growth can be justified by noting that Ca III is the dominant stage ion in the ICM. This clearly modifies the fraction expected in each velocity parameter component. Ti II probably behaves in a similar manner. The curves of growth for Mg II and Fe II can only be justified if Fe and Mg are preferentially depleted in the 1 km/s component. Since Si II does not show this same behavior, but is itself depleted, one can infer that the grain cores are primarily silicates, whereas the mantles appear to be Mg-Fe compounds. Clearly, other lines of sight must be analyzed to substantiate this. I have also pointed out that an incorrect curve of growth will result in a higher derived depletion, and that the depletion will appear to increase as a function of the extinction, although the specifics depend on the particular line of sight.

The difference between the photoionization rates of model 2 and model 3 (RDF, of Appendix C) is almost negligible when the rates are used to derive the electron density and describe the general ionization trends within the cloud. However, only the rates of model 3 will work in the model. The rates of model 2 result in neutral column densities which are over an order of magnitude larger than observed. The grains of model 3 have large albedoes and are strongly forward scattering shortward of 1500 \AA .

The notion of an average temperature, density, and pressure was questioned in this dissertation. For example, the electron density derived from ionization equilibrium is a factor of 5 smaller than the electron density of the region which contains the majority of the material. Indeed, the model shows that the electron density varies by over an order of magnitude from the edge of the cloud to the center. This also occurs for the hydrogen volume density. Clearly, the mean density is dependent on how the data are weighted. The mean electron density is weighed by the physical distance, and hence is a measure of the outer parts of the cloud. CO is a relatively hardy molecule and can exist near the edge. The hydrogen density from the CO data are thus weighed by both distance and density. Neutral carbon is easily destroyed, hence the fine structure lines are more indicative of the central density. I have found that in order to duplicate the temperature and density indicators, a temperature gradient must exist in the model. If I ignore the C₂ observations, I can fit all the observations to a model with T = 75 K, which is the temperature derived from the H₂ data.

Observations of H₂ along other lines of sight show two different phenomena. First, the curve of growth appears to lie between the neutral and the dominant stage ion curves of growth; and second, that the rotational temperature of the high J states is higher than the rotational temperature of the low J states. The temperature and density gradient of my model emulates this effect. There is no indication in the ¹²CO curve of growth which suggests the existence of a 10 km/s curve

of growth. This suggests that ^{12}CO and H_2 are not completely co-existent, and that the H_2 extends further from the center than the CO .

I have found a new transition of C_2 in absorption, which makes this the first conclusive detection of C_2 in the UV. I have also detected two lines of H_2O at the 1-2 level. This would be the first detection of gaseous H_2O in a diffuse cloud. The level of detection is not high enough to conclusively report a detection. I have searched unsuccessfully for a number of other molecular features, although I have detected 5 unidentified features. I have discussed the possible identifications of the three strongest lines with CS , C_2H and C_3 . As an aside, I find it very interesting that the three strongest U1 lines lie within 1 Å of a ^{12}CO band, that two of them (1419 and 1543) show definite band structure, and that each one is shaded to the red.

The only isotopic species found was ^{13}CO , and the $^{12}\text{CO}/^{13}\text{CO}$ ratio of 70 : 8 seems to suggest that chemical fractionation has not occurred, although the electron density is high enough that it should be seen.

8.2 Conclusions

Many problems still exist in our understanding of diffuse IS clouds. In this dissertation, I have pointed out many of them, and have, perhaps, answered some of them. I have also introduced a number of new questions. To answer the questions and solve the problems, it is necessary to conduct similar analyses for other diffuse clouds, as well as building more sophisticated models. I think that the next steps should be in opposite directions: an analysis of a more heavily reddened star; and the analysis of a star whose reddening is primarily due to a large pathlength through the ICM. These analyses will probably be crucial in determining the velocity parameter structure of the ISM, and perhaps the true dynamical structure of the ICM and of diffuse clouds.

APPENDIX A: Radio Data Reduction

Consider a warm, opaque cloud of IS gas. The power radiated per unit volume is given by the Planck function

$$P = \frac{8\pi h\nu^3}{c^2 (e^{h\nu/kT} - 1)} \Delta\nu \quad (\text{A-1})$$

In the limit $h\nu \ll kT$, the energy emitted per solid angle is

$$P = \frac{2kT}{\lambda^2} \Delta\nu \quad (\text{A-2})$$

often referred to as the Rayleigh-Jeans approximation. The direct relationship between the emitted energy and the temperature of the emitting cloud indicates that with proper calibration, a radio telescope measures the temperature of the emitting region, providing that it radiates like a black body. Even if the flux is non-thermal, a temperature can still be associated with the total power emitted, even though it is not the actual temperature. This temperature is referred to as the equivalent brightness temperature, and it is the temperature that that the cloud would have if it were radiating like a black body. For shorter wavelengths, the Rayleigh-Jeans approximation does not hold. In this case, equation A-1 describes the relationship between the temperature and the emitted power. Since only the exponential is affected by a change in the temperature, an effective source radiation temperature can be defined as

$$J(\nu, T) = \frac{h\nu/k}{(e^{h\nu/kT} - 1)} \quad (\text{A-3})$$

(KU, 1981). $J(\nu, T_e)$ is the parameter observed in the millimeter radio region, from which T_e can be found. Since $J(\nu, T_e)$ is usually measured as the height above the continuum, any continuum emission must be accounted for before T_e can be evaluated. At millimeter wavelengths, the major source of continuum emission is the 2.7 K ($=T_{bb}$) cosmic background radiation. For a cloud of optical depth τ , the observed line source radiation temperature J_1 is

$$J_1 = J(\nu, T_e)(1 - e^{-\tau}) + J(\nu, T_{bb})e^{-\tau} \quad ((\text{A-4}))$$

and the background source radiation temperature, J_b is

$$J_b = J(\nu, T_{bb}) \quad (\text{A-5})$$

The difference is

$$T_R = J_1 - J_b \quad (\text{A-6})$$

$$T_R = (1 - e^{-\tau})\{J(\nu, T_e) - J(\nu, T_{bb})\}$$

The observed antenna temperature is a convolution of the beam pattern and the distribution of T_R in the sky (Kraus 1966; KU). Let η be this normalized coupling factor. Then, the quantity which is observed is

$$T_R^* = \eta T_R \quad (A-7)$$

where η is often close to unity for extended sources (KU).

To get T_R^* , the output from the telescope must be corrected for the opacity of the atmosphere (τ), the forward spillover and scattering efficiency (η_{fss}), the rearward spillover and scattering efficiency (η_{rss}), and the radiation efficiency (η_r). The observed antenna temperature, T_A is

$$T_A = T_R^* e^{-\tau A} \eta_{fss} \eta_r \eta_{rss} \quad (A-8)$$

where A is the airmass. For the $J=1-0$ transition of ^{12}CO and ^{13}CO observed with the NRAO 36 foot telescope, $\eta_{fss} \eta_r \eta_{rss} = 0.71$, and for the $J=2-1$ transition of ^{12}CO observed with the MWO 16-foot telescope, the product is equal to 0.83.

Using the chopper wheel calibration method (KU), the relationship between the observed voltage and antenna temperature can be calibrated. The antenna temperature, uncorrected for the atmospheric opacity, can be written as

$$\begin{aligned} T_A^* &= T_A e^{-\tau A} \\ &= T_{\text{amb}} V_1 / V_{\text{cal}} \end{aligned} \quad (A-9)$$

where T_{amb} is the ambient temperature, V_1 is the voltage of the line, and

$$V_{\text{cal}} = G \eta_{\text{fss}} \eta_{\text{r}} (T_{\text{amb}} - T_{\text{sky}}) \quad (\text{A-10})$$

G is the gain of the receiver, T_{sky} is the temperature of blank sky, and T_{amb} is the temperature of the chopping vane. From equations (A-10), (A-9) and (A-8),

$$T_{\text{R}}^* = \frac{T_{\text{A}}^*}{\eta_{\text{fss}} \eta_{\text{r}} \eta_{\text{rss}}} \quad (\text{A-11})$$

T_{A}^* is often the reported quantity, as the product $\eta_{\text{fss}} \eta_{\text{r}} \eta_{\text{rss}}$ changes with frequency and telescope configuration.

The observation of a radio emission line yields T_{R}^* and Δv . There are two unknowns from equation A-10: T_{e} and The optical depth, τ . τ is related to the column density in the j^{th} rotational level (N_{J}) by

$$\int \tau dv = \tau_0 \Delta v \frac{v}{c} = \frac{8\pi^3 \mu^2 v}{3hc} (1 - e^{-hv/kT_{\text{e}}}) N_{\text{J}} \frac{(J+1)}{(2J+1)} \quad (\text{A-12})$$

where v is the FWHM in velocity units, μ is the dipole moment, τ_0 is the line center optical depth, and the rest of the symbols have their usual meaning. The total column density, N_{T} , is related to N_{J} by (cf Appendix C for a more complete discussion of this)

$$N_J = \frac{N_T}{Q_{\text{rot}}} (2J+1) e^{-J(J+1)B/T_e} \quad (\text{A-13})$$

where B is the rotation constant and the partition function Q is defined as

$$Q_{\text{rot}} = \sum_{J=0}^{\infty} (2J+1) e^{-J(J+1)B/T_e} \quad (\text{A-14a})$$

$$Q_{\text{rot}} \approx \frac{T_e}{B} \quad (\text{A-14b})$$

in LTE. For small T_e , equation A-14b overestimates Q. However, CO is normally not in LTE, and the population of each level will not be given by equation A-12). An alternative way of stating this non-LTE effect is that each rotational state has its own characteristic T_e , and it this $T_e(J)$ which must be used in both equations (A-12) and (A-13). Dickman (1976) calculated various values of Q for CO for various temperatures and densities. He used the large velocity gradient method (Goldreich and Kwan, 1974) to model the radiation transfer. For a wide range of temperatures and densities, equation A-14b is a better approximation than equation A-14a.

Using equation A-14b for Q, N_T can be solved for in terms of the known quantities:

$$N_T = \frac{3\tau_o \Delta v T_e h e^{J(J+1)B/T_e}}{8\pi^3 \mu^2 B(J+1)(1 - e^{-hv/kT_e})} \quad (A-15a)$$

which can be rewritten for any rotational level of CO as

$$N_T = \frac{2.309 \times 10^{14} \tau_o \Delta v T_e e^{2.767 J(J+1)/T_e}}{(J+1)(1 - e^{-hv/kT_e})} \text{ cm}^{-2} \quad (A-15b)$$

which for the J=1-0 transition is

$$N_T = \frac{2.309 \times 10^{14} \tau_o \Delta v T_e}{(1 - e^{-5.534/T_e})} \text{ cm}^{-2} \quad (A-15c)$$

For large optical depth, the exponential in equation A-6b is effectively zero, hence

$$T_R^* = J(v, T_e) - J(v, T_{bb}) \quad (A16)$$

For small optical depths, the exponential can be expanded, and equation A-6b is then

$$T_R^* = \tau \{ J(v, T_e) - J(v, T_{bb}) \} \quad (A17)$$

Clearly, an optically thick line will return the excitation temperature (equation A-16) but will not give any information about the column density of the material. An optically thin line yields a convolution of the column density and the excitation temperature (equation A-17). If the excitation temperature were known for an optically thin line, then

either equation A-6b or equation A-17 can be solved for τ_{12} , which in turn yields the column density. In practice, the ^{12}CO J=1-0 line is usually optically thick. Solving equation (A-16) for T_e yields

$$T_e = \frac{h\nu/k}{\ln\left(\frac{h\nu/k}{T_R^* + J(\nu, T_{bb})} + 1\right)} \quad (\text{A-18})$$

The ^{13}CO J=1-0 line is usually optically thin, and if the excitation temperature of the two transitions are equal, equations (A-17) and (A-15c) yield the column density for ^{13}CO . The column density of ^{12}CO is then the ^{13}CO column density times the $^{12}\text{CO}/^{13}\text{CO}$ ratio for the region (solar-89, ISM 40; Wannier, 1980). There is a useful relationship for determining the optical depth of the ^{13}CO J=1-0 line. Solving equation A-6b for τ_{13} yields

$$\tau_{13} = -\ln\left(1 - \frac{T_{R13}^*}{J(\nu_{13}, T_e) - J(\nu_{12}, T_{bb})}\right) \quad (\text{A-19})$$

where the frequency is that of the corresponding ^{12}CO line. Assuming that

$$J(\nu_{13}, T_e) - J(\nu_{13}, T_{bb}) = J(\nu_{12}, T_e) - J(\nu_{12}, T_{bb}) \quad (\text{A-20})$$

equation A-19 can be rewritten as

$$\tau_{13} = -\ln\left(1 - \frac{T_{R13}^*}{T_{R12}^*}\right) = -\ln\left(\frac{T_{R12}^*}{T_{R12}^* - T_{R13}^*}\right) \quad (\text{A-21})$$

There is an interesting relationship between the optical depths for the J=1-0 and J=2-1 transitions. Let the subscripts 1 and 2 differentiate between the two transitions. The optical depth can be written as

$$\tau_J = \frac{\nu_J(J+1)}{c} N_{\text{Tot}} e^{-J(J+1)B/T_e} \frac{8\pi^3 \mu^2 T_e}{3h B} (1 - e^{-h\nu/kT_e}) f(\nu_J) \quad (\text{A-22})$$

where $\phi(\nu_J)$ is the normalized line shape function. Since $\tau_2 = 2\tau_1$, and assuming that the line shape function does not vary between frequencies (over the interval from ν_1 to ν_2), τ_2 is related to τ_1 by

$$\tau_2 = 2\tau_1 e^{-2B/T_e} (1 - e^{-h\nu/kT_e}) \quad (\text{A-23a})$$

or since $2B = h\nu_1/k = T_1$,

$$\tau_2 = 2\tau_1 e^{-T_1/T_e} (1 - e^{-T_1/T_e}) \quad (\text{A-23b})$$

$$\tau_2 \approx 4\tau_1 \quad (\text{A-23c})$$

as $T_e \rightarrow \infty$. Figure A-1 shows τ_2/τ_1 as a function of T_e . Note that for $T_e = 5$, $\tau_2 = \tau_1$.

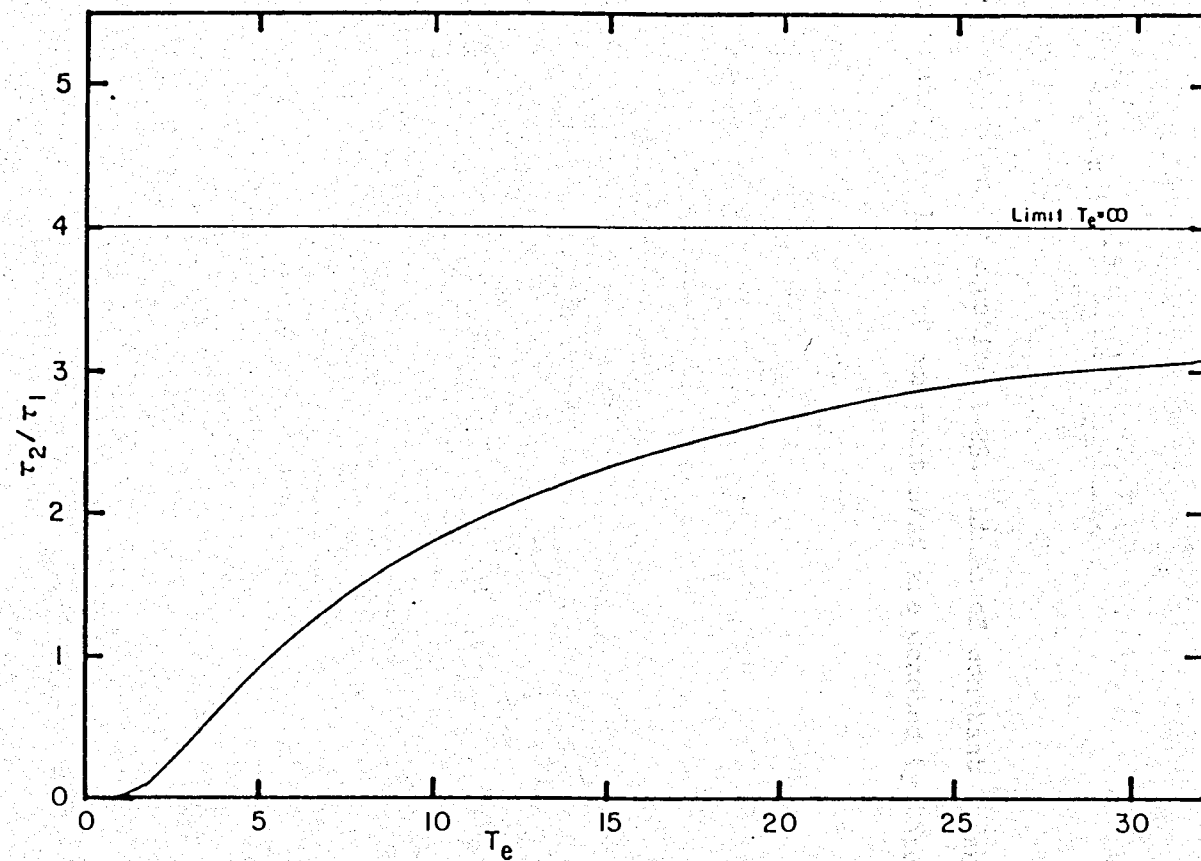


Figure A-1. The ratio of the J=1-0 and J=2-1 optical depths as a function of the excitation temperature. The limit for large T_e is indicated.

In a similar fashion, $J(\nu, T) = 2 J(\nu, T) / (1 + e^{T_1/T_e})$. Figure A-2 is a plot of T_R^* versus T_R^* for various values of T_e and $N/\Delta V$, where $T_{bb} = 2.8$ K. T_R^* was calculated using equation A-6b, and

$$\tau_1 = 4.33 \times 10^{-15} \frac{N}{\Delta v} \frac{(1 - e^{-T_1/T_e})}{T_e} \quad (A-24)$$

and τ_2 is given by equation A-23. Lines of constant T_e are denoted by thin lines, and lines of constant $N/\Delta V$ are denoted by thick lines.

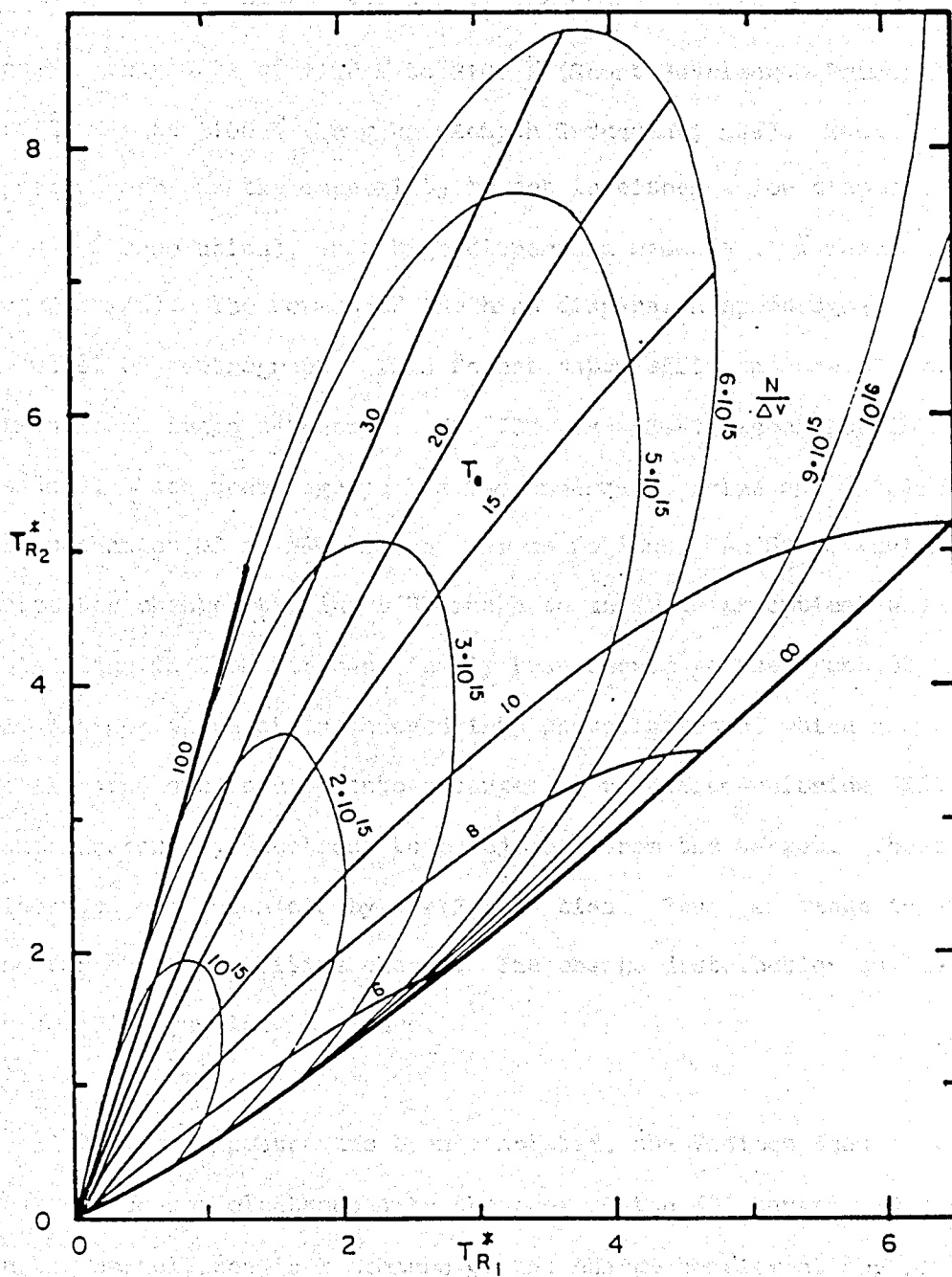


Figure A-2. T_{R1}^* versus T_{R2}^* for different values of T_e (thick lines) and N/v (thin lines). The heaviest line on the right corresponds to an infinite column density.

APPENDIX B: The IUE Satellite

The IUE has two spectrographs, which effectively cover the wavelength ranges of 1190 Å to 2100 Å (Short Wavelength Prime; SWP), and 2000 Å to 3100 Å (Long Wavelength Redundant; LWR). Each spectrograph has the capability to act in either a low dispersion mode (6 to 8 Å resolution), or a high dispersion mode (≈ 0.1 Å resolution, or ≈ 25 km/s). The format of the high dispersion spectrograph is that of an echelle spectrograph. This format makes efficient use of two dimensional image detectors. The IUE uses SEC-Vidicons for imaging and readout. Each spectrograph has two cameras, a Prime and a Redundant. The mechanics of an SEC vidicon are as follows. An UV to visible converter changes the input UV image to an image at optical wavelengths. This image is then fiber-optically transferred to the front of the SEC-Vidicon where it is changed into photoelectrons, which are then accelerated and focused onto a target of potassium-chloride (KCl) which causes secondary electrons to be ejected from the target. These electrons are drawn off by a +12 volt bias. Thus, an image is stored on the target as a positive charge. The charge distribution on the target is roughly gaussian in nature.

After the exposure has been completed, the Vidicon sends a pulsed beam of focused electrons onto the back of the KCl target. The change in the capacitance is a measure of the charge density at the position of the electron beam, which in turn is a measure of the intensity at the

front of the UV-to-Visual converter. A set of flat field exposures of varying intensities gives the relationship between the measured charge and the input flux. The Vidicon scans the KCl target in a grid of 768 by 768 positions. Each capacitance is converted into an integer from 0 to 255 and is telemetered in real time. The data are collected and processed at either GSFC or VILSPA, Spain.

The current (April, 1982; see IUE Newsletter #18 for new processing techniques) processing technique is as follows. Because of the distortions inherent in magnetically and electrostatically focused image tubes, the output array of data numbers (DN) are distorted with respect to the input image. To determine the magnitude of this distortion, the fiber-optics between the ultraviolet to visual converter and the image tube contain a set of black reseaux, whose relative positions are accurately known. A bilinear interpolation is then performed on the array of DN's, which then corrects the image for all geometric distortions. A set of exposures of known intensities is used to construct an intensity transfer function (ITF). Each pixel has its own ITF, and due to the nature of the KCl target, adjacent pixels can have significantly different ITF's. The result of the ITF acting on a DN is a flux number (FN), which is the relatively calibrated IUE flux. Depending on the nature of the spectrum (high or low dispersion, point source, trailed spectrum or extended object), the next procedure is to extract the intensity at each point along a given order. This is done by passing a "pseudo-slit" across the image, along an order. This slit consists of summing the intensities of the three pixels on either side

of the central pixel, perpendicular to the direction of the dispersion (the number on either side depends on the type of spectrum; the examples being given are for a high dispersion spectrum of a point source). Added to this is the average of the two columns of pixels on either side and parallel to the previous column of pixels. This is done from one end of each order to the other.

A previous exposure to a platinum hollow cathode lamp allows the position of the slit to be associated with a wavelength. All SWP wavelengths are vacuum wavelengths, and all LWR wavelengths are air wavelengths.

The interorder background for the high dispersion spectra is obtained by taking the average of two pixels halfway between the order being measured and the two adjacent orders. These background data are scaled to the same slit area (9 square pixels) as the extraction slit, and eventually are smoothed by a median filter before being subtracted from the "gross" spectrum to yield the "net" spectrum. The photometric quality of certain pixels is known to be rather poor. This can occur for pixels near a reseau and overexposed pixels. These pixels are marked by giving them a quality factor. This quality factor, often called an "Epsilon", indicates to the guest observer that the net flux may be in error.

The basic IUE data reduction procedure is as follows. After the image has been converted to relative flux units (FN), the pseudo-slit is passed along each order. The result is six arrays for each order. Each array index corresponds to the same wavelength along the order. The arrays consist of the gross flux, the background flux, the wavelength associated with each pixel, the quality control value (epsilon), the net flux (gross-background), and the net flux corrected for the echelle ripple.

The current (January, 1982) data extraction procedures were used to produce the magnetic tape given to the guest observer (Turnrose et al. 1979). All spectra have been processed with the current (June, 1980) ITF. The normal procedure is to subtract the background flux (B) from the gross flux (G), yielding the net flux (N) for each wavelength point. These fluxes can be obtained from the extracted spectrum file on the data tape. Fluxes derived in this manner, however, tend to be too low. Boggess et al. (1979) noted that the equivalent widths of IS absorption features in the spectrum of Zeta Oph were larger than those published by Morton (1975). Because of the proximity of the orders near the short wavelength range of each camera, the position used to extract the background flux is contaminated by the spectrum. Thus, it is more correct to think of the background as being too large than as the net flux being too small. This conclusion is evidenced by the existence of zero or negative residual fluxes for strong, narrow (FWHM \approx 10km/s) IS absorption lines which are not resolved by the IUE (FWHM \approx 25km/s).

In order to quantify the effects of the excess background, I have made a detailed comparison between IUE and Copernicus observations of Zeta Oph (Morton, 1975), Zeta Per (Snow, 1977), and Omicron Per (Snow, 1975, 1976). Using the definition of the equivalent width and assuming that both the continuum and background flux do not vary across the absorption feature, one can show that the background which should be subtracted from the gross IUE flux such that the resultant equivalent width agrees with the published Copernicus data is

$$B = G \left(1 - \frac{W_g}{W_c} \right) \quad (B-1)$$

where G is the IUE continuum from the gross flux, W_g is the equivalent width calculated from the gross flux, and W_c is the published Copernicus equivalent width. It is interesting to note that the value of B obtained from (B-1) is greater than the extracted background flux, B_0 , for all lines measured and for both cameras. The only exception is the Al II line at 1670 Å, where $B < 0$ for Zeta Oph. The result of the analysis was that the IUE and Copernicus equivalent could be equated within the observational error if the background were modified by:

$$B_t = C + f(B_0 - C) \quad (B-2)$$

B_t is the "true" background which should be used instead of the observed background, B_0 . C is the value of B_0 at the long wavelength end of each order, and f is a constant, equal to 0.7 for both cameras. The equivalent widths extracted from the modified net spectrum for each of

the three stars were within the observational error of the published values. The B_0-C term in (B-2) is a measure of the amount of order-overlap and scattering which is affecting the background. For large C (long exposures), $B_t = B_0$. However, for small C (short exposures), the order overlap and scattering are the largest contributors to the observed background and are correspondingly reduced by (B-2). Equation 2 is the same form as the equation used by Lien et al. (1980), which was derived by equating the values of the equivalent widths of lines which were measured in more than one order of the program star spectra. Lien et al. found a value of 0.6 for f by comparing the equivalent widths of the same line observed in two orders. Since this was an internal calibration, the errors are larger, and $f = 0.7$ is the preferred value. All equivalent widths quoted in this analysis have been extracted from the net flux modified by subtracting the altered background from the gross flux.

The potassium-chloride (KCl) target coupled with the Vidicon scanner seems to produce systematic noise features in the extracted fluxes. Hence, the signal-to-noise ratio (S/N) resulting from co-adding spectra will only increase to the point where these systematic features are the major contributors to the RMS noise. Even though the S/N will become a constant, weak features can be detected if the position of these features can be determined. Independently, Jura and York (1982) and I have found that these features are not only time dependent but may also be position dependent. Jura and York suggested observing a standard star of little reddening to help identify and correct for these

features.

Probably the best way to detect and account for these noise features is to make multiple exposures of the same star through different positions in the large aperture. This has the effect of shifting the stellar and interstellar lines in wavelength. Noise features inherent to the KCl target will remain at the same physical position, and, hence, at the same absolute wavelength as defined by the weekly comparison spectrum exposure. Exposures taken at different times of the year will also yield the same result, in that a weak feature can be identified as noise if it does not appear in both spectra. Since the projected velocity towards the star is probably different between the two exposures, the spectral lines will also be shifted with respect to each other. Again, this aids in determining whether a feature is real. A few weak features towards X Per have been conclusively identified as real or artificial by using a combination of these three identification methods.

Figure B-1 shows a theoretical view of the face of the KCl target. The grid is a representation of the horizontal and vertical scans the Vidicon camera makes on the target. The dashed lines are the centers of the orders (for specific order numbers labeled alongside the line; SWP and LWR in parenthesis). The orders are inclined at an angle of about 50° with respect to the horizontal scan lines. The thick semi-rectangle is the representation of the slit on the camera face. The single cross-hatching indicates the pixels with a weight of $1/2$, and the full

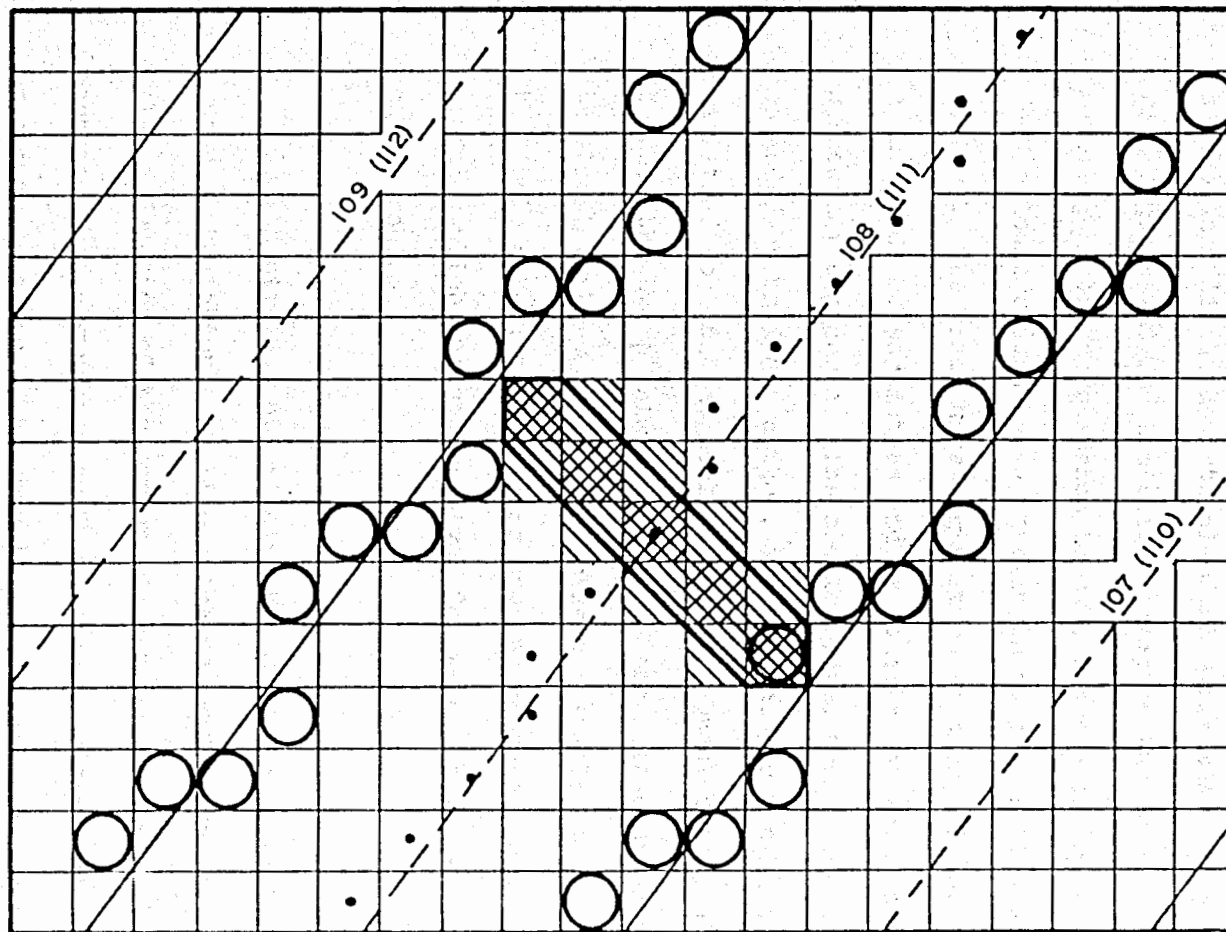


Figure B-1. Idealized representation of the KCl target. The grid represents the individual pixels; the dashed lines and solid lines indicate the center and edge of an echelle order, respectively. The order number is indicated for the SWP and for the LWR in parenthesis. The filled dots and open circles represent the center pixel of the slit and the position of the background pixels, respectively. The thick line represents the outline of the pseudo-slit, where the hatching indicates pixels given a weight of 1/2, and the full cross hatching indicates pixels with a weight of unity.

hatching is for pixels whose intensities are given full weight (unity). The dark dots indicate the center of the slit as it "moves" along an order, and the open circles show the position of the pixels used for the background. Because the orders are not at an angle of 45° with respect to the scan lines, a vertical pixel shift must occur every few wavelength steps for the slit to stay on the order. The normal wavelength step corresponds to $d\sqrt{2}$, where d is the width of a pixel. The periodic upstep has a wavelength step of half the normal step-size ($d\sqrt{2}/2$). The exact wavelength at which this half-step occurs depends on a multitude of parameters and is usually not even constant for sequential exposures. The problem comes from the fact that spectra are co-added by an index number, and are not the absolute wavelength. This will tend to broaden the line profile, particularly since the flux between the two pixels separated by the half-step have similar fluxes, as almost a third of the slit pixels are added into both slits. Over the whole order, this binning problem averages out. It is only for line profiles which are not resolved for which this line broadening is a major problem.

Qualitatively, this binning broadens the wings and flattens the cores of the absorption line. The net effect on the line profile is also a function of the number of co-added spectra. In practice, it appears that a gaussian profile adequately represents the instrumental response function. The gaussian can be characterized by a dispersion σ .

I determined the dispersion (which is a function of wavelength) by first fitting gaussians to the emission line wavelength calibration spectra. I then modified the dispersions to the summed data by fitting the line profile to weak, neutral IS features. For the LWR camera,

$$\sigma_{\text{LWR}} = 0.174 \text{ \AA} \quad (\text{B-3a})$$

and

$$\sigma_{\text{SWP}} = 8.936 \times 10^{-5} \lambda - 0.0358 \text{ \AA} \quad (\text{B-3b})$$

for the SWP camera. Although no formal errors were calculated, I estimate that the error is less than 0.025 Å.

APPENDIX C: Molecular Band Structure

Most of the following material on molecular structure is taken from Herzberg (1950, 1971).

The ground state of a simple diatomic molecule is that state where the electron distribution has its lowest possible total energy. If the molecule were to rotate, solutions to the Schroedinger equation imply that there are only discrete energies which the molecule may have. Similarly, if the molecule were to vibrate along its internuclear axis, only discrete vibrational periods are allowed. Different electronic energy levels exist when the total energy of the electronic distribution is non-zero. Molecular electronic states are similar to the atomic energy levels delineated by the quantum numbers n and L .

The vector sum of the individual components of the electronic angular momentum projected onto the internuclear axis is called the total orbital angular momentum, Λ . Λ is an integer when expressed in units of h , and is denoted by Σ, Π, Δ for $= 0, 1,$ and 2 . Since Λ is the vector projection of the orbital angular momentum onto the internuclear axis, for $\Lambda \neq 0$, the electronic state is doubly degenerate.

The spins of the individual electrons also add vectorially, and the magnitude of the resultant spin vector is denoted by S . S can take on half or whole integral values, depending on whether the number of

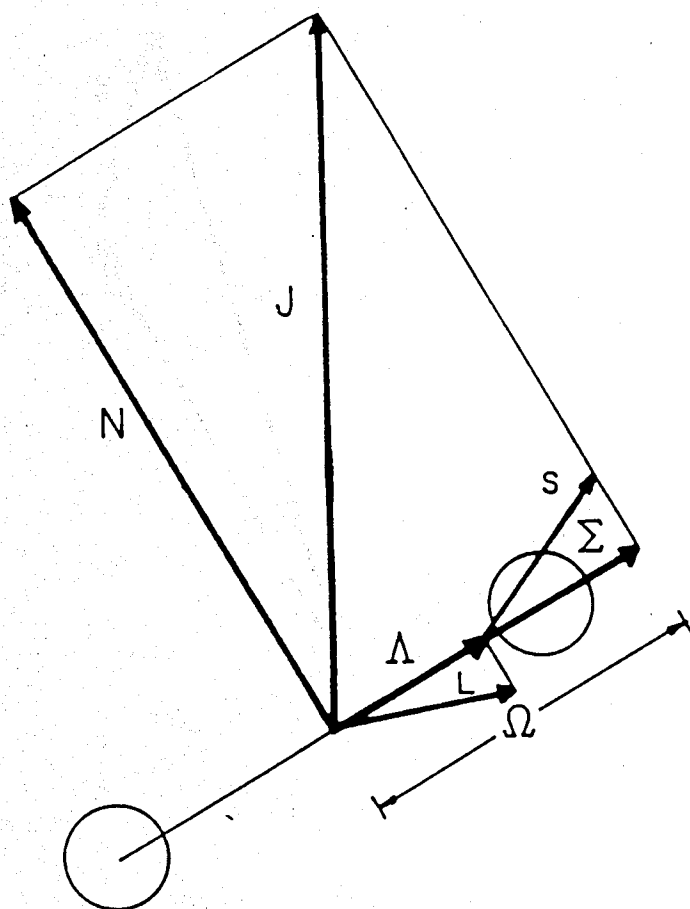
electrons in the valence orbital is odd or even, respectively. S also determines the multiplicity $(2S+1)$ of the electronic state. For homonuclear diatomic molecules, the electronic eigenfunctions are either even (g) or odd (u), depending on whether there is an even or odd number of antisymmetric orbitals. If the electronic wave function is symmetric (antisymmetric) with respect to reflection by any plane through the internuclear axis, then it is denoted as + (-). For $\Lambda \neq 0$, each state is doubly degenerate, where one degeneracy has a + character, and the other a - character. For example, the ground state of the diatomic carbon molecule (C_2) is designated as $X^1\Pi_g^+$, where $S = 0$ ($2S+1 = 1$), and $\Lambda = 0$ (Σ).

The individual rotational levels are characterized by their parity: a rotational level is positive (+) or negative (-) depending on whether the sign of the total electronic eigenfunction remains the same or changes under the inversion operator. For Σ states, the rotational levels alternate between + and -. The character of the lowest rotational level is determined by whether the state is a Σ^+ or Σ^- . For $\Lambda \neq 0$, each rotational level has both parities. The form of the coupling between the orbital motions of the electrons and the rotation of the molecule can split this degeneracy. This splitting is known as Λ -type doubling. Each split level then has either a + parity or a - parity.

There are two major ways in which the spin and the total angular electronic angular momentum can couple. The first (Hund's case a) is where both the spin and orbital angular momentum couple to the internuclear axis (Figure C-1). The net angular momentum is $\Omega = \Sigma + \Lambda$. The rotational angular momentum (N) couples to Ω to form the total angular momentum (J). J can take on values $\Omega + N$, where $N=1, 2, 3, \dots$. Clearly, J is never less than Ω . An example of the ground state of a Hund's case a molecule is the $X^2\Pi$ ground state of CH (Figure 5-15). The multiplicity is two, hence CH has two "ladders", a $^2\Pi_{3/2}$ and a $^2\Pi_{1/2}$. OH is another example, except that the $^2\Pi_{3/2}$ has the lower energy. OH is an example of an inverted Hund's case a.

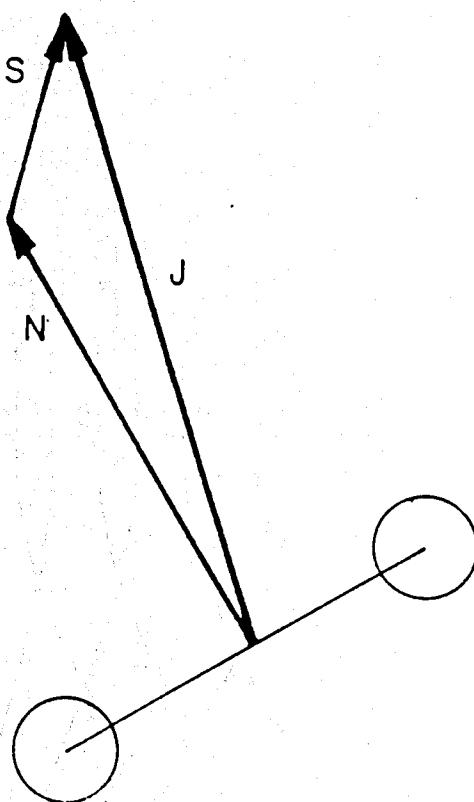
The second case (Hund's case b) occurs when the spin is coupled to the rotational angular momentum instead of the internuclear axis (Figure C-2). The resultant momentum vector is called J , which can take on values from $N-S$ to $N+S$. All states are by definition case b, since there is no electronic angular momentum for the spin to couple to. Examples of Hund's case b are the $B^2\Sigma^-$ and the $C^2\Sigma^+$ systems of CH (Figure 5-15), where each N is split into two components ($S = 1/2$; $2S+1 = 2$).

Most states ($\Lambda \neq 0$) are intermediate between case a and case b. The ratio $Y=A/B$, where A is the coupling constant and B is the rotational constant, can be used to measure the amount of coupling. Figure C-3 shows how the various levels correlate as Y ranges from 0 (case b) to large values (case a).



Hund's case (a)

Figure C-1. Vector representation of Hund's case (a). The symbols are defined in the text.



Hund's case (b)

Figure C-2. Vector representation of Hund's case (b). The symbols are defined in the text.

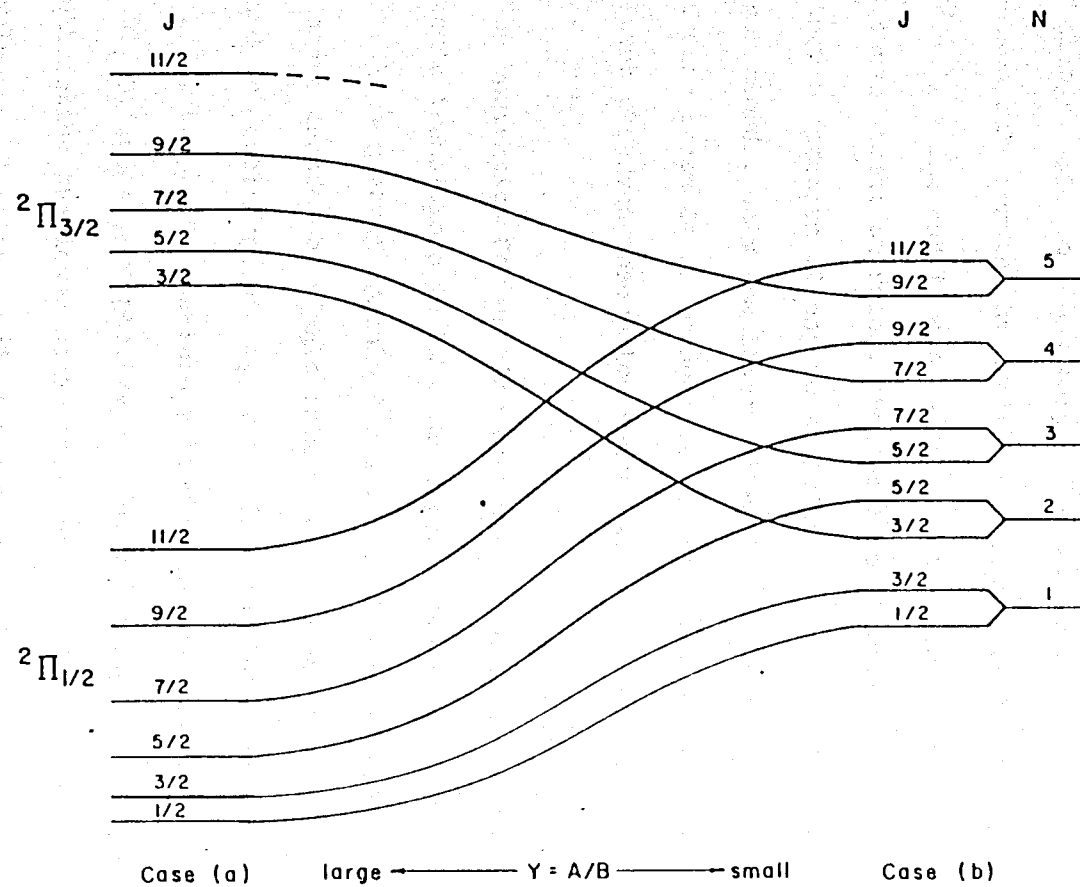


Figure C-3. Conversion from Hund's case (a) into Hund's case (b) as a function of the ratio of the spin splitting (A) and the rotational (B) constants.

The selection rules for electric dipole transitions between electronic states are: $\Delta\Lambda = 0, \pm 1$ and $\Delta\Sigma = 0$. For transitions between electronic states, there is no restriction on the change in the vibrational quantum number (Δv). For rotational transitions, $\Delta J = 0, \pm 1$, except $J=0 \rightarrow J=0$, and $J=0$ does not exist for $\Sigma-\Sigma$ transitions. The parity must change sign, i.e. $+\leftrightarrow -$ only. For homonuclear diatomics, $g \leftrightarrow u$. The selection rule for the hyperfine components is $\Delta F = 0, \pm 1$, $F=0 \rightarrow F=0$, where $F = J + I_1 + I_2$, and I_1 and I_2 are the nuclear spins of the two atoms. With these selection rules, the total rotational, vibrational and electronic spectrum of any molecule can be predicted. For studies of diffuse clouds, only the lowest vibrational level ($v=0$) in the ground electronic state is of importance, which greatly simplifies the resultant observed absorption spectrum.

The convention for writing molecular transitions differs from that of atomic transitions in that the upper state is written first, then the lower. If a general formula for a transition is written, the upper states are denoted by single primes (eg, v') and the lower states are denoted by double primes (eg, v''). From the rotational selection rule $\Delta J = 0, \pm 1$, the three possible values of ΔJ are indexed P, Q, and R for $\Delta J = -1, 0$, and $+1$, respectively. The difference is always calculated by subtracting the lower state from the upper state (eg, $\Delta J = J' - J''$). The value of J'' is enclosed in parenthesis: R(3), where $J' = 4$ and $J'' = 3$.

The particular vibrational transition is usually written as (v', v'') . Each electronic state can be describe by its electronic orbital angular momentum (Λ), its multiplicity ($= 2S+1$), and, for case b, $\Omega (= \Lambda + \Sigma)$. Since many different states within a molecule can have the same term structure, the different electronic states are also indexed with a capitol letter (for states with the same multiplicity as the ground state). X is reserved for the ground electronic state. For example, the absorption line of CH^+ at 4232 \AA is written as $R(0) (0,0) A^1 \Pi - X^1 \Sigma^+$. I have described the term structure of some of the molecules studied in Chapter 5.

Since an electronic transition in a diatomic molecule is split into vibrational and rotational terms, it seems reasonable that the oscillator strengths, which determine the efficiency of absorption, are also split into rotational and vibrational terms.

Let f_{el} be the electronic oscillator strength for a transition between two electronic states. The strength of a particular vibrational band is determined by the square of the overlap of the eigenfunctions of the upper and lower vibrational states:

$$q_{v', v''} = |\langle \psi_{v'} | \psi_{v''} \rangle|^2 \quad (\text{C-1})$$

$q_{v', v''}$ is called the Franck-Condon factor and has the property that

$\sum q_{v', v''} = 1$. The oscillator strength for each vibrational band is then

$$f_{v',v''} = f_{el} q_{v',v''} \quad (C-2)$$

Equation (C-1) is only valid if the Born-Oppenheimer approximation is valid. Unfortunately, the Born-Oppenheimer approximation is usually not a good approximation over all vibrational bands. Hence, first order estimates are all that equation C-1 is useful for. Kuznetsova et al. (1974) and Kuznetsova et al. (1979) have published values for f_{el} for many systems of astronomical interest. Nicholls (1962) presents a bibliography of Franck-Condon factors of astrophysical interest, and Nicholls (1973) presents an approximation formula for calculating $q_{v',v''}$. The useful quantity, and the one usually reported in the literature, is $f_{v',v''}$.

Whiting and Nicholls (1974) define a rotational line as the sum of all Zeeman components between two J levels. A very important point is that the Λ doublet is made up of two rotational lines. This definition of a rotational level corresponds to the definition of an atomic line (Condon and Shortley, 1935; p237). The oscillator strength of an atomic line within a multiplet is just the multiplet oscillator strength times some normalized line strength factor (Russell, 1936). In a similar fashion, the oscillator strength for a rotational line is $f_{v',v''}$ times a normalized line strength factor, called the Honl-London factor (HLF). Whiting and Nicholls (1974) show that the sum of all possible rotational transitions to (or from) all rotational levels with a given J" is

$$\sum_{p''} \sum_{J''} \sum_{\Sigma''} S_{\Sigma J p} = (2 - \delta_{0, \Lambda'' + \Lambda''}) M'' (2J'' + 1) \quad (C-3)$$

where $M'' = 2S + 1$ and $S_{\Sigma J p}$ is the HLF for the rotational line. Schadee (1975) noted that both M'' and the HLFs for the first rotational lines of some transitions change due to the fact that there are fewer than $2S + 1$ rotational levels for the lowest J value. The lowest rotational level of CH falls into this category, Schadee (1975) showed that for $\Lambda - S \leq J < \Lambda + S$, $M'' = J + S + 1 + \Lambda$, and if $J < S - \Lambda$, $M'' = 2J + 1$, otherwise, $M'' = 2S + 1$. The oscillator strength for a single rotational line, characterized by the electronic orbital angular momentum (Λ), the vibrational quantum number (v), the spin (Σ), the rotational quantum number (J), and the parity (p) is

$$f_{\Lambda'' v'' \Sigma'' J'' p''} = \frac{(2 - \delta_{0, \Lambda''}) f_{v'' v''}}{(2 - \delta_{0, \Lambda'' + \Lambda''}) (2J'' + 1)} S_{\Sigma'' J'' p''} \quad (C-4)$$

where $S_{\Sigma J p}$ is the normalized HLF (equation C-3). Tables of HLFs are given in Kovacs (1969), Tatum (1967), Schadee (1964). Most of the tabulated HLFs are not normalized.

The column density found from using the oscillator strength from equation C-4 in the curve of growth analysis (cf Section 4.1) is not the total column density of the molecule. Rather, it is the column density of the number of molecules within a particular rotational level. To determine total column density of a particular species, the relative population of all rotational levels must be known. Tatum (1967) discusses in detail the relative population of rotational, vibrational

and electronic states in diatomic molecules. He points out that the angular momentum coupling case (Hund's case a or b) determines the exact form of the statistical weights used in the Boltzmann equation. For electronic state n , vibrational state v , spin state Σ , rotational levels N and J , and parity p , the population of a single rotational line for case a is

$$\frac{N(nv\Sigma Jp)}{N_{\text{Tot}}} = \frac{(2-\delta_{o,\Lambda}) \phi(2S+1)(2J+1)e^{-\frac{hc}{kT}(T_e+G(v)+A\Sigma\Lambda+F(J))}}{Q_{\text{el}}Q_{\text{vib}}Q_{\text{rot}}(a)} e^{-\frac{hc}{kT}A\Sigma\Lambda} \quad (\text{C-5})$$

and for case b is

$$\frac{N(nvN Jp)}{N_{\text{Tot}}} = \frac{(2-\delta_{o,\Lambda}) \phi(2N+1) \left| \frac{(2J+1)}{(2S+1)(2N+1)} \right| e^{-hc/kT(T_e+G(v)+F(N))}}{Q_{\text{el}}Q_{\text{vib}}Q_{\text{rot}}(b)} \quad (\text{C-6})$$

where for $N=0$ of a Σ state, the quantity in square brackets in equation C-6 is 1. T_e , $G(v)$, $F(N)$, and $F(J)$ have their usual meanings (Herzberg, 1950), and are expressed in cm^{-1} . The unit of hc/k is cm . For equations (C-5) and (C-6), the partition functions (Q) are

$$Q_{\text{el}} = \sum_{\text{all states}} (2 - \delta_{o,\Lambda})(2S+1) \quad (\text{C-7})$$

$$Q_{\text{vib}} = \sum_{v=0}^v e^{-hc/kT G(v)} \quad (\text{C-8})$$

$$Q_{\text{rot}}(a) = \sum_{J=|\Lambda+\Sigma|}^{\infty} (2J+1) e^{-hc/kT F(J)} \quad (\text{C-9a})$$

$$Q_{\text{rot}}(b) = \sum_{N=\Lambda}^{\infty} (2N+1) e^{-hc/kT F(N)} \quad (\text{C-9b})$$

$\phi = 1/2$ ($=1$) for heteronuclear molecules with $\Lambda \neq 0$ ($=0$). For homonuclear molecules, alternates with symmetric (s) and antisymmetric (a) rotational levels. For integral nuclear spin,

$$\phi = \frac{I+1}{2I+1} \quad (\text{s}); \quad \phi = \frac{I}{2I+1} \quad (\text{a}) \quad (\text{C-10a})$$

For half integral nuclear spin,

$$\phi = \frac{I}{2I+1} \quad (\text{s}); \quad \phi = \frac{I+1}{2I+1} \quad (\text{a}) \quad (\text{C-10b})$$

For homonuclear molecules, both $Q_{\text{rot}}(a)$ and $Q_{\text{rot}}(b)$ are split into two separate sums, one for antisymmetric levels, the other for symmetric levels. ϕ must also be incorporated into the rotational partition function. The total partition function is the sum of the symmetric and antisymmetric partial partition functions. Under usual diffuse cloud conditions, a diatomic molecule is in its ground electronic state and its lowest vibrational level, with only spin splitting (case a) and rotational terms to consider. Equations (C-5) and (C-6) can thus be rewritten as

$$\frac{N(nv\Sigma Jp)}{N_{\text{Tot}}} = \frac{\phi(2J+1) e^{-hc/kT(A\Sigma\Lambda + F(J))}}{Q_{\text{rot}}(a) \sum_{\Sigma}^{+s} e^{-hc/kT A\Sigma\Lambda}} \quad (C-11)$$

$\Sigma = -s$

for case a, and

$$\frac{N(nvN Jp)}{N_{\text{Tot}}} = \frac{\phi(2N+1) \left| \frac{(2J+1)}{(2N+1)(2S+1)} \right| e^{-hc/kT F(N)}}{Q_{\text{rot}}(b)} \quad (C-12)$$

for case b. The quantity in square brackets is 1 for $N=0$ of a Σ state.

For cases intermediate between case a and case b, $F(N)$ should be replaced by $F(J)$ until the spin splitting (A) becomes large. For small A (close to case b), $\sum_{\Sigma}^{+s} e^{hc/k(A\Sigma\Lambda)} = 2S+1$, hence the two forms are equivalent in the limit.

For low excitation temperatures and unresolvable doublets, equations (C-11) and (C-12) reduce to

$$\frac{N(nvJ)}{N_{\text{Tot}}} = \frac{(2J+1) e^{-hc/kT F(J)}}{Q_{\text{rot}}(a)} \quad (C-13)$$

for case a, and

$$\frac{N(nvN J)}{N_{\text{Tot}}} = \frac{(2J+1) e^{-hc/kT F(N)}}{(2S+1) Q_{\text{rot}}(b)} \quad (C-14)$$

for case b, where $(2J+1)/(2S+1) = 1$ for $N=0$ of a Σ state. For case b, if the spin splitting is small, then the J levels will be unresolvable, hence

$$\frac{N(nvN)}{N_{\text{Tot}}} = (2N+1) \frac{e^{-hc/kT} F(N)}{Q_{\text{rot}}(b)} \quad (\text{C-15})$$

Equations (C-13) or (C-15) are the Boltzmann equations usually found in the literature.

The rotational temperature between two levels can be found by taking the ratio

$$\frac{N(nv\dots J')}{N(nv\dots J'')} = \frac{\phi_{J'}(2J'+1) e^{-hc/kT(F(J') - F(J''))}}{\phi_{J''}(2J''+1)} \quad (\text{C-16})$$

and solving for the temperature, T . Because of the low densities in diffuse clouds, spontaneous emission depopulates the upper rotational levels faster than collisions populate them, hence the rotational temperature is usually less than the kinetic temperature.

APPENDIX D: Photoionization and Recombination in the ISM

Most of the first thirty elements of the periodic table have first ionization potentials less than 13.6 eV. Consequently, most elements exist as singly ionized atoms in diffuse clouds. The photoionization rate is

$$\Gamma = c \int_{\nu_0}^{\nu_{912}} \frac{\sigma(\nu) \mu(\nu)}{h\nu} d\nu \quad (D-1)$$

where ν_0 is the photoionization edge, μ_ν ($\text{erg cm}^{-3} \text{ Hz}^{-1}$) is the energy density of the IS radiation field, and σ_ν is the photoionization cross section (cm^2).

The evaluation of equation D-1 is difficult because (1) the photoionization cross section (σ_ν) is often either not well known or not known at all; and (2) the absolute value and functional form of the IS radiation field is not well known, particularly shortward of 1500 Å (de Boer et al. 1973; RDF). Using the radiation field of Witt and Johnson (1973), de Boer et al (1973) calculated the photoionization rates for a number of elements whose cross sections were known in 1973. BD and BHD used the results of de Boer et al. to calculate the photoionization rate as a function of optical depth into a cloud which was assumed to be made up of isotropically scattering grains. They found that the photoionization at any depth could be written as

$$\Gamma = \Gamma_0 e^{-\tau A} s^{-1} \quad (D-2)$$

where Γ_0 is the photoionization rate for the undiluted radiation field, and A is a constant for the particular element.

RDF have re-analyzed the photoionization rate in diffuse clouds using a more detailed radiative transfer approach, and including more realistic grain properties, such as anisotropic scattering. They used the IS radiation field described by Draine (1978).

RDF show that the photoionization rate is a function of the grain properties (albedo (w_λ), extinction (τ_λ), and asymmetry parameter (g_λ)), and more surprisingly, on the optical depth to the center of the cloud (T_c). The dependence on T_c has the effect of making the value A in equation D-2 a function of T_c . RDF calculated the photoionization rate for three different grain models. Of these, model 2 and model 3 are suggested to be the most appropriate for diffuse IS clouds. Model 3 and model 2 have equivalent extinctions and equivalent values of w and g from $\lambda = 4000 \text{ \AA}$ to 1500 \AA . For $\lambda < 1500 \text{ \AA}$, model 3 has $g_\lambda \rightarrow 1.0$ very quickly (strongly forward scattering grains) and the albedo goes from 0.6 to 0.8. For model 2, the albedo remains constant at 0.6, and g_λ , the asymmetry parameter, drops to and remains constant at 0.5. Table D-1 lists the undiluted IS photoionization rates (Γ_0), and the value of A in equation D-2 for $T_c = 0.5$ for both models 2 and 3. For X Per, $E(B-V) = 0.52$, which corresponds to $A_V = 0.78$ or $T_c = 0.84$. From the discussion of RDF, the photoionization rates calculated for $T_c = 0.8$

TABLE D-1

PARAMETERS FOR PHOTOIONIZATION AND RECOMBINATION RATES

Element	Γ_{01} (s^{-1})	A(2)	A(3)	α_0 ($cm^3 s^{-1}$)	η
C	1.58×10^{-10}	3.08	0.91	4.7×10^{-13}	0.624
Na	2.51×10^{-11}	3.68	2.30	2.1×10^{-13}	0.75
Mg	4.47×10^{-11}	1.61	0.69	1.4×10^{-13}	0.855
Si	2.00×10^{-9}	1.98	0.56	5.9×10^{-13}	0.601
S	3.54×10^{-10}	2.94	0.82	4.1×10^{-13}	0.63
Cl ^a	1.26×10^{-11}	4.05	1.20	2.50×10^{-13}	0.7
K	3.55×10^{-11}	1.89	0.74	2.11×10^{-13}	0.77
Ca	2.51×10^{-10}	2.12	1.47	1.12×10^{-13}	0.9
Ca ⁺	1.26×10^{-12}	3.41	1.15	6.8×10^{-13}	0.8
Fe	1.12×10^{-10}	1.70	0.41	1.42×10^{-13}	0.891

^a Assumed values for recombination coefficient

will be smaller than the rates calculated for 0.5 or 0.3 (The only two central optical depths published by RDF). Since the extrapolation of the A values of equation D-2 to higher values of T_c is difficult from the published data, I have used the values of A corresponding to $T_c = 0.5$ for all photoionization calculations

Table D-1 also contains values for the recombination coefficient α (cm^3s^{-1}). The recombination coefficients are a function of the temperature, and are tabulated in Table D-1 as α_0 and η , where

$$\alpha = \alpha_0 \left(\frac{T}{10^4}\right)^{-\eta} \quad \text{cm}^3 \text{ s}^{-1} \quad (\text{D-3})$$

T is in Kelvins. All recombination coefficients are from Shull and van Steenberg (1982), except for K and Na, which are from Jenkins and Shaya (1978).

Observationally, what is observed is the integral of the volume density over the thickness of the cloud: $\int n dl$. Ionization equilibrium relates the density in two adjacent stages of ionization to the photoionization rate the recombination coefficient and the electron density

$$n_I = n_{II} \frac{\alpha(T)}{\Gamma(s)} n_e \quad (\text{D-4})$$

The neutral column density to the center of the cloud is

$$N_I = \int_0^L n_I ds = \int_0^L n_{II} n_e \alpha(T) / \Gamma(s) ds \quad (D-5)$$

If n_{II} , n_e and $\alpha(T)$ are constant, and the photoionization rate is written as

$$\Gamma(s) = \Gamma_0 e^{-AT_c s/L} \quad (D-6)$$

then

$$\begin{aligned} N_I &= n_{II} n_e \frac{\alpha(T)}{\Gamma_0} \int_0^L e^{AT_c s/L} ds \quad (D-7) \\ &= \frac{N_{II} n_e}{AT_c} \frac{\alpha(T)}{\Gamma_0} (e^{AT_c} - 1) \end{aligned}$$

If the cloud is symmetrical about its center, equation D-7 is the same for the whole cloud. Equation D-7 can be re-written in terms of the mean photoionization rate ($\langle \Gamma \rangle$),

$$N_I = N_{II} n_e \frac{\alpha(T)}{\langle \Gamma \rangle} \quad (D-8)$$

where

$$\langle \Gamma \rangle = \frac{\Gamma_0 AT_c}{(e^{-AT_c} - 1)} \quad (D-9)$$

Table D-2 lists $\langle \Gamma \rangle$ for the elements of Table D-1 for models 2 and 3, along with values for Γ_0/α and $\langle \Gamma \rangle/\alpha$ for $T = 50$ K and $T_c = 0.8$, corresponding to the 1 km/s component towards X Per.

TABLE D-2
IONIZATION EQUILIBRIUM PARAMETERS

Element	$\langle \Gamma \rangle$			$\langle \Gamma \rangle / \alpha(40K)$	
	Model: 2	3	0	2	3
C	3.6×10^{-11}	1.1×10^{-10}	10.8	2.4	7.5
Na	4.1×10^{-12}	8.7×10^{-12}	1.13	0.37	0.78
Mg	2.2×10^{-11}	3.3×10^{-11}	2.9	1.40	2.10
Si	8.2×10^{-10}	1.6×10^{-9}	123	50.3	98.2
S	8.8×10^{-11}	2.5×10^{-10}	27	6.6	18.8
Cl	1.7×10^{-12}	7.5×10^{-12}	2.1	0.14	0.63
K	1.5×10^{-11}	2.6×10^{-11}	2.8	1.2	2.1
Ca	9.6×10^{-11}	1.3×10^{-10}	15.6	5.9	8.1
Ca ⁺	2.4×10^{-13}	7.7×10^{-13}	0.022	0.0043	0.014
Fe	5.3×10^{-11}	9.5×10^{-11}	5.8	2.7	4.9

BIBLIOGRAPHY

- Adams, W. S. 1949, Ap.J. 109, 354.
- Allison, A. C. and Dalgarno, A. 1969, Atomic Data, 1, 289.
- Anderson, R. C., Henry, R. L., and Fastie, W. G. 1982, Ap.J. 259, 573.
- Asbrink, H., Fridh, P. R., Lindholm, A., and Codling, K. 1974, Phys. Scripta 10, 183.
- Armstrong, B. H. 1967, J. Quant. Spect. Rad. Trans. 7, 61.
- Bahcall, J. N. and Wolf, R. A. 1968, Ap.J. 152, 701 (BW).
- Ballik, E. A. and Ramsay, D. A. 1963, Ap.J. 137, 84.
- Barlow, J. and Silk, J. 1976, Ap.J. 207, 131.
- Blaauw, A. 1950, B.A.N., 11, 405.
- Black, J. H. and Dalgarno, A. 1977, Ap.J. Suppl. 34, 405 (BD).
- Black, J. H., Hartquist, T. W., and Dalgarno, A. 1978, Ap.J. 224, 448 (BHD).
- Black, J. H., Dupree, A. K., Hartmann, L. W., and Raymond, J. C. 1980 Ap.J. 239, 502 (BDHR).
- Boggess, A. et al 1979, Nature, 275, 372.
- Braes, L. L. E. and Miley, G. K. 1972, Nature, 235, 273.
- Brucatan, R. J. and Kristian, J. 1972, Ap.J. 173, L105.
- Bruhweiler, F. C., Kondo, Y., and McCluskey, G. F. 1980, Ap.J. 237, 19.
- Bruhweiler, F. C. and Kondo, Y. 1982, Ap.J. 259, 232.
- Chaffee, F. H., Jr. 1974, Ap.J. 189, 427.
- Chaffee, F. H., Jr., Lutz, B. L., Black, J. H., Vanden Bout, P. A., and Snell, R. L. 1980, Ap.J. 236, 474.
- Chaffee, F. H., Jr. and White, R. E. 1982, Ap.J. Suppl. 50, 169.
- Chu, S.-I., and Dalgarno, A. 1975, Ap.J. 199, 637.
- Cohen, J. G. 1973, Ap.J. 186, 149.
- Condon, E. U. and Shortley, G. H. 1935, The Theory of Atomic Spectra. (1967 printing; London: Cambridge University Press).

- Cowan, R. D., Hobbs, L. M., and York, D. G. 1982, Ap.J. 257, 373.
- Cowie, L. L., Taylor, W., and York, D. G. 1982, Ap.J. 248, 528 (CTY).
- Crutcher, R. M. 1975, Ap.J. 200, 625.
- Crutcher, R. M. 1976, Ap.J. 206, L171.
- Crutcher, R. M. 1978, Ap.J. 219, 72.
- Crutcher, R. M. 1980, private comm.
- Crutcher, R. M. 1981, Ap.J. 244, 855.
- Crutcher, R. M. and Watson, W. D. 1976, Ap.J. 203, L123..
- Crutcher, R. M. and Watson, W. D. 1981, Ap.J. 244, 855.
- Czyzak S. J., Hirth, J. P., and Tabak, R. G. 1982, Vistas in Astronomy 25, 337.
- Dalgarno, A. and McCray, R. 1972, Ann. Rev. Ast. Astrophys. 10, 375.
- Dalgarno, A. and Oppenheimer, A. 1974, Ap.J. 192, 597.
- de Boer, K. S. 1979, Ap.J. 229, 132.
- de Boer, K. S. 1981, Ap.J. 244, 848.
- de Boer, K. S., Koppenaal, K. and Pottasch, S. R. 1973, Astr.Ap. 28, 145.
- de Boer, K. S. and Morton, D. C. 1974, Astr.Ap. 37, 305.
- de Jong, T., Chu, S.-I., and Dalgarno, A. 1975, Ap.J. 199, 69.
- de Jong, T., Dalgarno, A., and Boland, W. 1980, Astr.Ap. 91, 68.
- Delhaye, J. and Blaauw, A. 1953, B.A.N., 12, 72.
- Dickman, R. L. 1976, Ph.D. Thesis, Columbia University.
- Dickman, R. L., Somerville, W. B., Whittet, D. C. B., McNally, D., and Blades, J. C., 1982, Preprint.
- Donovan, R. J., Hussain, D., and Stevenson, C. D. 1970. Tr. Far. Soc. 66, 1.
- Draine, B. T. 1978, ApJ. Suppl. 36, 595.
- Drayson, S. R. 1976, J. Quant. Spect. Rad. Trans. 16, 611.

- Duley, W. W. 1982, Preprint.
- Elitzur, M. 1978, Private Communication.
- Engvold, O. 1977, Phys. Scripta 16, 48.
- Federman, S. R. 1980, Ap.J. 241, L109.
- Federman, S. R., Glassgold, A. E., and Kwan, J. 1979, Ap.J. 227, 466 (FGK).
- Federman, S. R., Glassgold, A. E., Jenkins, E. B., and Shaya, E. J. 1980, Ap.J. 242, 545.
- Ferlet, R., Vidal-Madjar, A., and Laurent, C. 1980, Ap.J. 242, 576.
- Field, G. 1971, Ann. Rev. Ast. Astrophys. 9, 227.
- Flannery, B. P., Rybicki, G. B., and Sarazin, C. L. 1980. Ap.J. Suppl. 44, 539.
- Flower, D. R. and Launay, J. M. 1977a, J.Phys.B. 10, 879.
- Flower, D. R. and Launay, J. M. 1977b, J.Phys.B. 10, 3673.
- Frisch, P. C. 1979, Ap.J. 227, 474.
- Frisch, P. C. 1980, Ap.J. 241, 697.
- Frontera, F., Fuligni, F., Morelli, E., and Ventura, G. 1979, Ap.J. 229, 291.
- Garavoglia, M. and Treves, A. 1976, Astr.Ap. 49, 235.
- Glassgold, A. E. and Langer, W. D. 1974, Ap.J. 193, 73.
- Green, S. 1980, Ap.J. Suppl. 42, 103.
- Greenberg, J. M. 1974, Ap.J. 189, L81.
- Goldreich, P. and Kwan, J. 1974, Ap.J. 189, 441.
- Harris, D. L. 1956, Ap.J. 123, 371.
- Henning, K. 1981, Astr.Ap.Suppl. 44, 405.
- Herbig, G. H. 1968, Zeit. f. Astr. 68, 243.
- Herzberg, G. 1950 Molecular Spectra and Molecular Structure. I. Spectra of Diatomic Molecules. (2d ed., Princeton: Van Nostrand).

- Herzberg, G. 1971 *The Spectra and Structure of Simple Free Radicals*. (New York: Cornell University Press)
- Herzberg, G. and Johns, J. W. C. 1969 *Ap.J.* 158, 399.
- Herzberg, G., Lagerquist, A., and Malmberg, C. 1969, *Can. J. Phys.* 47, 2735.
- Hill, R. M. 1979, *J. Quant. Spect. Rad. Trans.* 21, 19.
- Hillier, I. H., Kendrick, J., and Guest, M. F. 1975, *Mol. Phys.* 30, 1138.
- Hiltner, W. A. 1954, *Ap.J.* 120, 454.
- Hjalmarson, A., Sume, A., Ellder, J., Rydbeck, O. E. H., Moore, E. L., Huguenin, G. R., Sandqvist, A., Linblad, P. O., and Lindroos, P. 1977, *Ap.J. Suppl.* 35, 263.
- Hobbs, L. M. 1974, *Ap.J.* 191, 381.
- Hobbs, L. M. 1979a, *Ap.J.* 229, L129.
- Hobbs, L. M. 1979b, *Ap.J.* 232, L175.
- Hobbs, L. M. 1981, *Ap.J.* 243, 485.
- Hollenbach, D., Werner, M. W., and Salpeter, E. E. 1971, *Ap.J.* 163, 155 (HWS).
- Huber, K. P. and Herzberg, G. 1979, *Molecular Spectra and Molecular Structure. IV. Constants of Diatomic Molecules* (Van Nostrand: Princeton).
- Humlicek, J. 1979, *J. Quant. Spect. Rad. Trans.* 21, 309.
- Hutchings, J. B. 1977, *M.N.R.A.S.* 181, 619.
- Jansson, P. A. and Korb, C. L. 1968, *J. Quant. Spect. Rad. Trans.* 8, 1399.
- Jenkins, E. B. and Shaya, E. J. 1979, *Ap.J.* 231, 55.
- Johns, J. W. C. 1963, *Can. J. Phys.* 41, 209.
- Jura, M. and Smith, W. H. 1981, *Ap.J.* 251, L43.
- Kallman, T. R. and McCray, R. 1982 *Ap.J. Suppl.* 50, 263 (KM).
- Kemp, J. 1982, private comm.
- Knapp, G. R. and Jura, M. 1976, *Ap.J.* 209, 782.

- Kovacs, I. 1969. Rotational Structure in the Spectra of Diatomic Molecules (London: Adam Hilger Ltd.).
- Kraus, J. 1966, Radio Astronomy (New York: McGraw-Hill).
- Kurucz, R. L. 1982, S.A.O. Report 390.
- Kutner, M. L. and Ulich, B. L. 1981, Ap.J. 250, 341.
- Kuz'menko, N. E., Kuznetsova, L. A., Monyakin, A. P., Kuzyakov, Yu. Ya., and Plastinin, Yu. A. 1979, Sov. Phys. Usp. 22, 160.
- Kuznetsova, L. A., Kuz'menko, N. E., Kuzyakov, Yu. Ya., and Plastinin, Yu. A. 1974, Sov. Phys. Usp. 17, 405.
- Lassertte, E. N. and Skerbele, A. 1971, J.C.P. 54, 1957.
- Launay, J. M. and Roueff, J. M. 1977, Astr.Ap. 56, 289.
- Leung, C. M. and Liszt, H. S. 1976, Ap.J. 208, 732.
- Lien, D. J., Buhl, D., Crutcher, R. M., Donn, B. D., Smith, A. M., Snyder, L. E., and Stief, L. J. 1980, The Universe in Ultraviolet Wavelengths: The First Two Years of IUE. NASA CP-2171 pp. 581.
- Liszt, H. S. 1979, Ap.J. 233, L147.
- Liszt, H. S. 1981, Ap.J. 246, L147.
- Lugger, P., Barker, E., York, D. G., and Oegerle, W. 1982, Ap.J. 259, 67.
- Mason, K. O., White, N. E., Sanford, P. W., Hawkins, F. J. 1976, M.N.R.A.S., 176, 193.
- McCray, R. 1982, Private Communication.
- McCray, R., Wright, C., and Hatchet, S. 1977, Ap.J. 211, L29.
- Mendoza, E. E. V. 1958, Ap.J. 128, 207.
- Mitchell, G. F., Ginsburg, J. L., and Kuntz, P. J. 1973 Ap.J. 212, 71.
- Moffat, A. F. J., Haupt, W., Schmidt-Kalar, Th. 1973, Astr.Ap. 23, 433.
- Morton, D. C. 1975, Ap.J. 197, 85.
- Morton, D. C. and Hu, E. M. 1975, Ap.J. 202, 638.
- Mushotzky, R. F., Roberts, D. H., Baiity, W. A., and Peterson, L. E. 1977, Ap.J. 211, L129.

- Myers, P. C. 1978, Ap.J. 225, 380.
- Nicholls, R. W. 1962, J. Quant. Spect. Rad. Trans. 2, 433.
- Nicholls, R. W. 1973, J. Quant. Spect. Rad. Trans. 13, 1059.
- Olive, K. A. and Schramm, D. N. 1982 Ap.J. 257, 276.
- Olivero, J. J. and Longbothum, R. L. 1977, J. Quant. Spect. Rad. Trans. 17, 233.
- Penner, S. S. 1969, Quantitative Molecular Spectroscopy and Gas Emissivities. (Reading: Addison-Wesley).
- Pierluissi, J. H., Vanderwood, P. C., and Gomez, R. B. 1977 J. Quant. Spect. Rad. Trans. 18 555.
- Platt, J. R. 1956, Ap.J. 123, 486.
- Posener, D. W. 1959, Aust. J. Phys. 12 184.
- Prasad, S. S. and Huntress, W. T. 1980a, Ap.J. Suppl. 43, 1.
- Prasad, S. S. and Huntress, W. T. 1980b, Ap.J. 239, 151.
- Ramsey, J. 1950, Ap.J. 111, 434.
- Reynolds, R. J. and Ogden, P. M. 1982, Wisc. Astr., Vol. 144.
- Roberge, W. G., Dalgarno, A., and Flannery, B. P. 1981, Ap.J. 243, 817 (RDF).
- Rodgers, C. D., and Williams, A. P. 1974, J. Quant. Spect. Rad. Trans. 14, 319.
- Rogerson, J. B., Spitzer, L., Drake, J. F., Dressler, K., Jenkins, E. B., Morton, D. C., and York, D. G. 1973, Ap.J. 181, L97.
- Romelt, J. Peyerimhoff, S., and Buenker, R. J. 1978, Chem. Phys. Lett. 58, 197.
- Russell, H. N. 1936, Ap.J. 83, 129.
- Rydbeck, O. E. H., Kollberg, E., Hjalmarson, A., Sume, A., and Ellder, J. 1976, Ap.J. Suppl. 31, 333.
- Sancisi, R., Goss, W. M., Anderson, C. Johansson, L. E. B., and Winnberg, A. 1974, Astr.Ap. 35, 445.
- Savage, B. D. and Bohlin, R. C. 1979, Ap.J. 229, 136.
- Savage, B. D. and Mathis, J. S. 1979, Ann. Rev. Astr. Ap. 17,73.

- Schadee, A. 1964, B.A.N. 5, 311.
- Schadee, A. 1975, Astr.Ap 41, 203.
- Shih, S. K., Peyerimhoff, S., and Buenker, R. J. 1978, J. Mol. Spect. 74, 124.
- Shull, J. M. 1980, Ap.J. 238, 560.
- Shull J. M. and van Steenberg, M. 1982, Ap.J. Suppl. 48, 95.
- Shulman, S., Bortolot, V. J., and Thaddeus, P. 1974, Ap.J. 193, 97.
- Simmons, J.D., Bass, A. M., and Tilford, S. G. 1969, Ap.J. 155, 345.
- Smeding, A. G. and Pottasch, S. R. 1979. Astr.Ap. Suppl. 35, 257 (SP).
- Smith, A. M. 1974, Ap.J. 190, 565.
- Smith, A. M., Krishna-Swamy, K. S., and Stecher, T. P. 1978, Ap.J. 220, 138.
- Smith, W. H. and Snow, T. P. 1978, Ap.J. 228, 435.
- Smith, P. L., Yoshino, K., Griesinger, H. E., and Black, J. H. 1981,
- Snow, T. P. 1975, Ap.J. 201, L21.
- Snow, T. P., Jr. 1976, Ap.J. 204, 759.
- Snow, T. P., Jr. 1977, Ap.J. 216, 724.
- Snow, T. P., Jr. 1978, Ap.J. 220, L93.
- Snow, T. P., Jr. and Meyers, K. A. 1979, Ap.J. 229, 545.
- Snow, T. P. and Dodgen, M. 1980, Ap.J. 237, 708.
- Snow, T. P. and Smith, W. H. 1981, Ap.J. 250, 163. Ap.J. 250, 166.
- Spitzer, L. E. 1978, Physical Processes in the Intestellar Medium (New York: Wiley).
- Spitzer, L. and Zweibel, E. 1974, Ap.J. 191, L127.
- Stecher, T. P. and Williams, A. 1967, Ap.J. 149, L29.
- Stephens, T. L. and Dalgarno, A. 1972, J. Quant. Spect. Rad. Trans. 12, 599.
- Tatum, J. B. 1967, Ap.J. Suppl. 14, 21.

- Thompson, H. W. 1936, Proc. Roy. Soc. Lond. Ser. A. 157, 331.
- Turnrose, B. E., Harvel, C. A., and Perry, P. M. 1979, IUE Imaging Processing Information Manual, NASA TM-79/6077.
- Ulich, B. L. and Haas, R. W. 1976, Ap.J. Suppl. 30, 247.
- Van de Hulst, H. C. and Reesnick, J. J. M. 1947, Ap.J. 106, 121.
- Vanden Bout, P. A. and Snell, R. L. 1980, Ap.J. ,236, 460.
- Vanden Bout, P. A. and Snell, R. L. 1981, Ap.J. 246, 460.
- Van den Bergh, 1972, Nature, 235, 273.
- van Dishoeck, E. F. and Black, J. H. 1982, Ap.J. 258, 533 (vDB).
- Wannier, P. G. 1980, Ann. Rev. Astr. Astrophys. 18, 399.
- Wannier, P. G., Penzias, A. A., and Jenkins, E. B. 1982, Ap.J. 254, 100.
- Watson, W. D. 1972, Ap.J. 176, 103.
- Watson, W. D., Anicich, V. G., and Huntress, W. T., Jr. 1976, Ap.J. 205, L165 (WAH).
- White, R. E. 1977, Ap.J. 211, 744.
- White, N. E., Swank, J. H., Holt, S. S., and Parmer, A. N. 1982, NASA TM 83929.
- Whiting, E. E. 1968, J. Quant. Spect. Rad. Trans. 8, 1379.
- Whiting, E. E. and Nicholls, R. W. 1974, Ap.J. Suppl. 27, 1.
- Witt, A. N. and Johnson, M. W. 1973, Ap.J. 181, 363.
- Wooten, A., Bozyan, E. P., Garrett, D. B., Loren, R. B., and Snell, R. L. 1980, Ap.J. 239, 844.
- York, D. G. 1975a, Ap.J. 196, L103.
- York, D. G. 1975b, Mem. Soc. Astr. It. 5, 493.
- York, D. G. and Jura, M. 1982, Ap.J. 254, 88.

VITA

David Jeffrey Lien

Office: Department of Astronomy
1011 W. Springfield Ave.
University of Illinois
Urbana, IL 61801
(217) 333-2316

Home: 1006 W. Springfield Ave
Urbana, IL 61801
(217) 367-3554

Date and Place of Birth
November 28, 1954; Milwaukee, WI (U. S. Citizen)

Education: BS (1977) University of Wisconsin, Madison, WI;
MS (1979) University of Illinois Urbana, IL;
PhD (1982, expected) University of Illinois, Urbana, IL

Professional Experience:

Teaching Assistant, Department of Astronomy, Univ. of Illinois,
Academic years 1977, 1978, 1979, 1981, 1982.
Research Assistant, Department of Astronomy, Univ. of Illinois,
Academic year 1982, Summers 1978, 1979, 1980 (work done at
Goddard Space Flight Center), 1981, 1982.

Professional and Academic Societies:

Sigma Pi Sigma
American Astronomical Society